Charge Transfer of Transition Metal Ions for Flow Battery Applications

by

Harsh Agarwal

A dissertation submitted in partial fulfillment
of the requirements for the degree of
Doctor of Philosophy
(Chemical Engineering)
in the University of Michigan
2022

Doctoral Committee:

Assistant Professor Nirala Singh, Chair
Assistant Professor Bryan R. Goldsmith
Professor Nicholas A. Kotov
Professor Vincent L. Pecoraro

“Success is not final; failure is not fatal: it is the courage to continue that counts.”

Harsh Agarwal

agharsh@umich.edu

ORCID iD: 0000-0002-5237-4819

Dedication

To my family.

Acknowledgements

As I reflect over my PhD journey, the one person who stands out amongst everyone is my advisor Professor Nirala Singh. Professor Singh served as my pillar of support throughout my time here at University of Michigan. I am grateful to Professor Singh for considering me good enough to be a part of first cohort of graduate students he chose to advise. Because of that, I got the invaluable experience of setting up of a new experimental lab from scratch that I hope to put in use someday. Professor Singh not only trained me to become an independent researcher and critical thinker, but also taught valuable life lessons along the way. He provided me the freedom to pursue several research directions and involved me in a wide variety of projects that helped me expand my research skills. Over the years, his work ethics have inspired me, and I hope I can emulate them as I move forward in my career. I could not have asked for a better mentor than Professor Singh and I hope to keep learning from him well beyond my time here.

I am also extremely grateful to Professor Bryan Goldsmith for his support and guidance over the years. He always believed in me and pushed me to become a better experimentalist. Working with him over the last five years has taught me how experimental and computational researchers can work together in harmony for the advancement of science. He was very kind to share his experiences along the way and I hope his mentorship would continue in the years to come. I am very thankful to Professor Vincent Pecoraro for always finding time to meet me whenever I had any questions. The Inorganic Chemistry course that I did under his guidance played a huge role in the way I started thinking about transition metal ion chemistry. Thank you very

much Professor Pecoraro and I hope I didn't bother you too much! I am also thankful to Professor Nicholas Kotov for agreeing to serve on my committee and asking good questions that helped me grow as a researcher. I would also like to express my gratitude to Professor Stephen Maldonado for teaching and making me fell in love with electrochemistry during my first year.

This dissertation could not have been completed without the contribution of Jacob Florian, a brilliant undergraduate student who worked in Professor Bryan Goldsmith's lab. Thank you for always being ready to try out new things and the effort you put in Jacob! I am glad I got the opportunity to work alongside you and apologize for being "rate determining" in all the publications. I am also grateful to all the other masters and undergraduate students I worked with over the years: Jiun-Yeu Chang, Austin Shelton, Angeline Monitello, Analeigh Majewski, and Daniel Pert. Each one of them made a positive influence in my research and helped me grow as an individual, thank you!

I had the pleasure to work with some wonderful collaborators over the years and share resources available in different labs across the university. Special thanks to Dr. John Fulton (PNNL), Dr. Mahalingam Balasubramanian (ORNL, previously APS), and Dr. Niranjan Govind (PNNL) for being patient in teaching me XAFS. I learned a lot from interacting with them, thank you very much to you all! I am grateful to Professor Syed Mubeen (University of Iowa) for always being available to answer questions related to surface enhanced Raman and encouraging me every step along with the way. I am also thankful to Professor Jovan Kamcev for sharing his insights with me about the development of membranes. Thanks to Professor Suljo Linic for allowing me to use their UV-vis instrument during my first two years and all his students (Dr. Umar Aslam, Dr. Steven Chavez, Dr. Valentina Igenegbai. Dr. Sean Dix, Dr. Ali Hussain Motagamwala, Rawan Almallahi, and Rachel Elias) for always being willing to help. I am very grateful to Dr. Matthew

Oonk, Dr. Pilar Herrera-Fierro, and Dr. Sandrine Martin at the Lurie Nanofabrication Facility for always being available to answer questions related to metal depositions. Thanks to Professor Adam Matzger for allowing me to use their Raman equipment over the last year and providing guidance along the way.

I am grateful to all the past and present members of the Singh Lab for all the love, affection, and support over the years. They were like my extended family away from home during my stay here. I want to thank Danielle Richards, Cailin Buchanan, James Akinola, Claire Yin, Jared Arkfeld, Wendy Wu, Dr. Libo Yao, Dr. Gyan Sharma, Dr. Zixuan Wang, Dr. Benjamin Silcox, Takaaki Miki, and Cem Komurcuoglu. Special thanks to Danielle and Zixuan for always being available for long discussions regarding anything, James for tolerating me as his office mate for few years and making me laugh during all times, Cailin for serving as an epitome of punctuality, and Claire for teaching me a little of American slang. Special mention to Jared who took out time to read significant portions of the dissertation and provided helpful feedback. I could not have done anything without you all and will miss working alongside you.

I am appreciative to the Chemical Engineering Administrative Staff who does a lot of work behind the scenes to make the graduate degree enjoyable. I would especially like to express my gratitude to Susan Hamlin who was always available to share her wisdom and wealth of knowledge regarding university resources. Thanks to Barbara Perry for processing hundreds of my orders over the last five years to keep the research continue without any delay.

I am thankful to all my friends here at Michigan and back in India, especially Dr. Vishnu Chipade, Dr. Vivek Ojha, Dr. Kunal Garg, Gurmeet Singh, Dr. Aaditya Lakshmanan, Aditya Sundar, Anjali Mittal, Adarsh Bhat, and Amit Gupta for being always there for me, for tolerating me over the years, and never making me feel home sick. I cannot even begin to describe how

grateful I am to Vishnu who was my constant roommate for the last five years. He very patiently listened to me, provided me good advice, and along the way fed me with some delicious Indian food. I will miss our long discussions about life Vishnu as we move to different cities.

Finally, I would like to thank the most important people in my life, my parents and my sisters. The immense sacrifices my parents have made over the years so that all their kids get the best opportunities inspires me to work hard and make my presence count wherever I go. They taught me the importance of being persistent and hard-working, and at the same time be a good human being. My sisters have been my support system over the years who have ensured that I don't have to worry about anything happening back at home. They have always motivated me to push my boundaries. The enormous trust they have shown in my skills and capabilities has helped me become a confident person.

Table of Contents

Dedication ..... **ii**

Acknowledgements ..... **iii**

List of Tables ..... **xii**

List of Figures ..... **xiii**

List of Schemes ..... **xvi**

Abstract ..... **xvii**

Chapter 1: Introduction **1**

1.1 Importance of Energy Storage 1

1.2 Redox Flow Batteries: Operation and Different Types 4

1.2.1 Inorganic Redox Flow Batteries 5

1.2.2 Organic Redox Flow Batteries 8

1.3 Voltage Losses in Redox Flow Batteries 10

1.4 Electrolytes and Electrode Treatments for Vanadium Redox Flow Batteries 13

1.5 Dissertation Overview 16

1.6 Dissertation Outline 17

1.7 References 19

Chapter 2: Electrochemical and Spectroscopy Techniques for Probing Charge Transfer Mechanisms **28**

2.1 Summary 28

2.2 Charge Transfer Mechanisms 28

2.3 Techniques to Identify the Structure of Ions in Solution 30

2.3.1 Ultraviolet-visible Spectroscopy 31

2.3.2 X-ray Absorption Fine Structure Spectroscopy 34

2.4 Techniques to Measure Electrochemical Kinetics 37

2.4.1 Steady State Current Measurements 37

2.4.2 Electrochemical Impedance Spectroscopy 42

2.5 Measurement of Electrochemically Active Surface Area 45

2.5.1 Cyclic Voltammetry Capacitance Method 46

2.5.2 Underpotential Deposition 48

2.5.3 Hydrogen Evolution Reaction Currents 51

2.6 References 54

Chapter 3: V^{2+}/V^{3+} Reaction Kinetics on Glassy Carbon in Sulfuric, Hydrochloric, and Mixed Acid Electrolytes for Vanadium Redox Flow Batteries 57

3.1 Summary 57

3.2 Introduction 58

3.3 Results and Discussions 59

3.4 Conclusions 74

3.5 Supporting Information 75

3.5.1 Starting Electrolyte Preparation 75

3.5.2 Electrochemical Cell Assembly and Setup 75

3.5.3 Pre-electrolysis to Produce V^{2+} and Oxidizing Back to V^{3+} to Reach Desired States of Charge 76

3.5.4 Theoretical UV-vis spectra Calculations 77

3.5.5 Predicting the Number of Anions in V^{3+} Inner-Coordination Sphere Using UV-vis 79

3.5.6 Supporting Figures 81

3.6 References 82

Chapter 4: The Effect of Anion Bridging on V^{2+}/V^{3+} Charge Transfer 87

4.1 Summary 87

4.2 Introduction 87

4.3 Results and Discussions 90

4.3.1 V^{2+}/V^{3+} Reaction Kinetics on Glassy Carbon 90

4.3.2 Influence of Sulfate Anions on V^{2+}/V^{3+} Reaction Kinetics 94

4.3.3 Structures of V^{2+} and V^{3+} in $HClO_4$, H_2SO_4, and HCl, using EXAFS and MD-EXAFS.. 96

4.3.4 Proposed Inner Sphere Mechanism and Kinetic Model for V^{2+}/V^{3+} Reaction in Different Electrolytes 104

4.3.5 Energies of V^{2+}/V^{3+} Complexes and Anions Adsorbed on Glassy Carbon 105

4.4 Conclusions 109

4.5 Supporting Information 110

4.5.1 Experimental Details 110

4.5.2 Rate Law for V^{2+}/V^{3+} Reaction in Presence of Anions 110

4.5.3 Molecular Dynamics (MD) Simulations for Extended X-ray Absorption Fine Structure (EXAFS) for V^{2+} and V^{3+} Complexes 116

4.5.4 Ligand-Exchange Free Energies for V^{2+}/V^{3+} Complexes 117

4.5.5 DFT Modeling of Adsorbed Intermediates 119

4.5.6 Coverage of Anions on Glassy Carbon 120

4.5.7 Supporting Figures and Tables 123

4.6 References 130

Chapter 5: Understanding Influence of Halides on Metal Ion Charge Transfer Reactions 134

5.1 Summary 134

5.2 Introduction 134

5.3 Results and Discussion 140

5.3.1 V^{2+}/V^{3+} Reaction on Graphite Edge Plane 140

5.3.2 V^{2+}/V^{3+}, Cr^{2+}/Cr^{3+}, and Cd^{0}/Cd^{2+} Reaction on Mercury 143

5.4 Conclusions 148

5.5 Supporting Information 150

5.5.1 Rate Constants for Metal Ion Redox Couples 150

5.5.2 Electrochemical Kinetic Measurements on EPPG 152

5.5.3 Computational Methods and Simulation Cell Setup for Metadynamics 153

5.6 References 156

Chapter 6: Understanding Influence of Electrode on Charge Transfer Reactions of Transition Metal Ions. 162

6.1 Summary 162

6.2 Introduction 163

6.3 Results and Discussion 168

6.3.1 V^{2+}/V^{3+} Reaction Kinetics on Metal Electrodes 168

6.3.2 Correlating V^{2+}/V^{3+} Reaction Kinetics with the *d*-band Center of the Electrode . 176

6.3.3 *d*-band Center as a Descriptor for Heterogeneous Inner Sphere Charge Transfer of Fe-, Co-, Cr- Metal Ions 178

6.4 Conclusions 182

6.5 Supporting Information 183

6.5.1 Preparation of Metal Electrodes 183

6.5.2 Rate Laws to Identify Rate Determining Step of V^{2+}/V^{3+} Reaction 183

6.5.3 Supporting Figures and Tables 191

6.6 References 195

Chapter 7: Conclusions, Future Directions, and Outlook 198

7.1 Summary and Conclusions 198

7.2 Limitations of the Work and Future Directions 202

7.2.1 Experimental Evidence of Adsorbed Metal Ion Intermediate 202

7.2.2 Extension of Findings to Carbon Felt Electrodes 204

7.2.3 Similarity in Charge Transfer Mechanism of Transition Metal Ion and Organic Redox Couples..... 204

7.3 Outlook..... 207

7.4 References 208

List of Tables

Table 4.1. Reaction Orders for V^{2+}/V^{3+} on Glassy Carbon in H_2SO_4 and HI by Regression 93

Table S4.1. Reaction Orders for V^{2+}/V^{3+} in H_2SO_4, HCl, HBr, $HClO_4$, and HI with H_2SO_4 or $HClO_4$ on Counter Electrode Calculated using Regression……..127

Table S4.2. Structural Parameters from Model Fits to Experimental EXAFS Spectra of V^{2+} and V^{3+} in $HClO_4$, H_2SO_4, and HCl for Two and Multiple Leg Scattering Paths 127

Table S4.3. DFT-calculated Free Energies of Ligand Exchange Reactions (ΔG_L) at 298 K and 1 M Solute Concentration. 129

Table S4.4. Free Energies for Proposed Vanadium-anion Intermediates Calculated with either the B3LYP-D3 or M06-2X-D3 Functional. 129

Table S5.1. Standard Rate Constants for Metal Ion Redox Couples With and Without Halide Anions 150

Table S6.1. Reaction Orders for V^{2+}/V^{3+} Reaction in H_2SO_4 on Au, Ag, Cu, Bi, and W Metal Electrodes using Regression 194

Table S6.2. Experimental Observed and Predicted Trends for Various Reaction Mechanisms of V^{2+}/V^{3+} Reaction 194

Table S6.3. Electronic Properties of Different Metal Electrodes 194

List of Figures

Figure 1.1. Distribution of Global Energy Storage Technologies and Installed Pumped Hydroelectric Capacity over Time 2

Figure 1.2. Installed Capacity of Electrochemical Energy Storage Over the Last Seven Years ... 3

Figure 1.3. Classes of Organic Molecules used in Organic Redox Flow Batteries based on their Molecular Structure 9

Figure 1.4. Cell Voltage vs Current Density During Charging and Discharging of a Redox Flow Battery Showing Different Voltage Losses 12

Figure 2.1. UV-vis Spectra of V^{2+} and V^{3+} in H_2SO_4 and HCl at Different Total Vanadium Concentrations 32

Figure 2.2. UV-vis Spectra of V^{2+} and V^{3+} in HBr, HI, and $HClO_4$ at Different Total Vanadium Concentrations 33

Figure 2.3. Gaussian Fits from the Model Used to Estimate V^{2+} and V^{3+} Concentrations in a Mixture of Vanadium Ions 34

Figure 2.4. Identifying Optimum Rotation Rate for No Mass Transfer Limitations for V^{2+}/V^{3+} Measurements on Glassy Carbon in HI 41

Figure 2.5. Methodology Used to Obtain V^{2+}/V^{3+} Kinetic Parameters on Edge Plane Pyrolytic Graphite and Metal Electrodes 42

Figure 2.6. ECSA of Edge Plane Pyrolytic Graphite in H_2SO_4 using CV Capacitance Method . 47

Figure 2.7. Copper Underpotential Deposition on a Gold Electrode 49

Figure 2.8. Lead Underpotential Deposition on a Silver and Copper Electrode 51

Figure 2.9. HER Calibration to Obtain ECSA of Bismuth Electrodes 53

Figure 2.10. HER Calibration to Obtain ECSA of Tungsten Electrodes 54

Figure 3.1. V^{2+}/V^{3+} Kinetics on Glassy Carbon in H_2SO_4 at Room Temperature 62

Figure 3.2. V^{2+}/V^{3+} Exchange Current Densities on Glassy Carbon as a Function of State of Charge in HCl, H_2SO_4, and mixed HCl/H_2SO_4 Electrolytes 64

Figure 3.3. Apparent Activation Energies for the V^{2+}/V^{3+} Redox Reaction on Glassy Carbon in H_2SO_4 and HCl Electrolytes 66

Figure 3.4. UV-vis Absorbance as a Function of Wavelength for V^{3+} in HCl, H_2SO_4, and mixed HCl/H_2SO_4 Electrolytes 67

Figure S3.1. Tafel Slopes of V^{2+}/V^{3+} Reaction on Glassy Carbon in H_2SO_4, HCl/H_2SO_4, and HCl 81

Figure S3.2. Exchange Current Density of V^{2+}/V^{3+} Reaction on Glassy Carbon in HCl/H_2SO_4 Using Two Independent Methods 81

Figure S3.3. UV-vis Spectra of V^{3+} at Varying Concentrations of SO_4^{2-} and Cl^- 82

Figure 4.1. Kinetic Parameters for V^{2+}/V^{3+} Reaction on Glassy Carbon in $HClO_4$, H_2SO_4, HCl, HBr, and HI Acidic Electrolytes 91

Figure 4.2. Influence of Sulfate on V^{2+}/V^{3+} Kinetics in HI on Glassy Carbon 96

Figure 4.3. Structures of Hydrated V^{2+} and V^{3+} using EXAFS 98

Figure 4.4. Structure of V^{3+} in H_2SO_4 and HCl with Changing Anion Concentrations using EXAFS 102

Figure S4.1. V^{2+}/V^{3+} Reaction Kinetics in HBr on Glassy Carbon using Two Independent Methods 123

Figure S4.2. V^{2+}/V^{3+} Reaction Kinetics on Glassy Carbon in Various Acidic Electrolytes at Different Temperatures using Two Independent Methods 124

Figure S4.3. Tafel Slopes for V^{2+}/V^{3+} Reaction on Glassy Carbon in Various Acidic Electrolytes 125

Figure S4.4. UV-vis Spectra of V^{3+} at High Concentrations of Br^- and I^- 125

Figure S4.5. Graphene Cluster used as a Model Carbon Surface 126

Figure S4.6. Coverage of Halides on Glassy Carbon as a Function of Electrode Potential 126

Figure 5.1. Effect of Halides on Metal Ion Charge Transfer Kinetics for Multitude of Redox Couples 135

Figure 5.2. Computational Metadynamics of V^{3+}-anion Complexes on Graphite and Experimental Kinetic Measurements of V^{2+}/V^{3+} Reaction on Edge Plane Pyrolytic Graphite 141

Figure 5.3. Desorption Barriers and Kinetics in the Presence of Halides of Metal Complexes on Mercury Electrode 145

Figure 5.4. Desorption Barriers of Fe^{3+}-anion Complexes on Gold Electrode 147

Figure 5.5. Rate Constants vs Desorption Barrier on Different Electrodes for V^{2+}/V^{3+} Redox Couple 148

Figure S5.1. Kinetic Parameters of V^{2+}/V^{3+} Reaction on Edge Plane Pyrolytic Graphite in H_2SO_4, HCl, and HI Evaluated using Tafel Method vs Desorption Barriers 152

Figure S5.2. Kinetic Parameters of V^{2+}/V^{3+} Reaction on Edge Plane Pyrolytic Graphite in H_2SO_4, HCl, and HI Evaluated using Charge Transfer Resistance Method vs Desorption Barriers 153

Figure S5.3. Simulation Cell for $[X{-}Cr(H_2O)_5]^{2+}$ Complex on Hg(111) used for Calculating Desorption Barriers 154

Figure S5.4. Simulation cell for $[X{-}Fe(H_2O)_5]^{2+}$ complex on Au(111) used for Calculating Desorption Barriers 155

Figure S5.5. Two-dimensional Contour Plot Showing the Free Energy Surface of the Desorption of $*[I{-}Cr(H_2O)_5]^{2+}$ when Biasing Both Coordination Number of Water and Cr^{3+}-Hg Distance 156

Figure 6.1. Kinetic Parameters for the V^{2+}/V^{3+} Reaction in H_2SO_4 on Metal and Carbon Electrodes 173

Figure 6.2. V^{2+}/V^{3+} Kinetic Parameters in H_2SO_4 Compared to Desorption Barrier of Proposed Intermediate on Metals 175

Figure 6.3. Relationship between Exchange Current Density of V^{2+}/V^{3+} Reaction in H_2SO_4, *d*-Band Center, Desorption Barrier, and Metal-Hydrogen Bond Strength 177

Figure 6.4. Correlation between Kinetics of Inner Sphere Charge Transfer Reactions of Transition Metal Ions and Electrode Properties 180

Figure S6.1. Exchange Current Density of V^{2+}/V^{3+} Reaction in H_2SO_4 for Au, Ag, Cu, and Bi Metal Electrodes by Two Independent Methods 191

Figure S6.2. Kinetic Trends for a Reaction Mechanism with Desorption Step as RDS 192

Figure S6.3. Kinetic Trends for Reaction Mechanism with Electron Transfer Step as RDS 192

Figure S6.4. Kinetic Trends for Reaction Mechanism with Adsorption Step as RDS 193

Figure S6.5. Free Energy Profiles of $*[O{-}V(H_2O)_4SO_4]$ Intermediate on Au, Ag, Cu, Bi, and W Metals 193

List of Schemes

Scheme 1.1. Schematic showing Different Components of a Redox Flow Battery 5

Scheme 2.1. Outer and Inner Sphere Charge Transfer of Transition Metal Ions at Electrodes ... 29

Scheme 2.2. Excited State Decay Mechanisms in XAFS 35

Scheme 2.3. Modified Randles Circuit Used for Fitting Nyquist Plots of All the EIS measurements for V^{2+}/V^{3+} reaction in Different Electrodes and Electrolytes 45

Scheme 3.1. Proposed Catalytic Cycle of V^{2+} Oxidation to V^{3+} on Glassy Carbon in H_2SO_4, HCl/H_2SO_4, and HCl Electrolytes..... 73

Scheme 4.1. Two Possible Causes for the Anion Effect on Charge Transfer Kinetics of Various Transition Metal Ion Redox Couples including V^{2+}/V^{3+} on Electrodes (e.g., Glassy Carbon) 88

Scheme 4.2. Proposed Reaction Energy Diagram for the V^{2+}/V^{3+} Redox Reaction at 50% State of Charge and V^{2+}/V^{3+} Standard Redox Potential Considering Two Possible Mechanisms to Explain the Effect of Anions on Redox Kinetics 107

Scheme 5.1. Reaction Energy Diagram and Predicted Trends for Kinetic Parameters with Varying Desorption Barriers 138

Scheme 6.1. Inner Sphere Charge Transfer Reactions of Transition Metal Ions in Solution and at Electrode 165

Scheme 7.1. Effect of Anions on the Reaction Energy Profile of V^{2+}/V^{3+} on Glassy Carbon... 199

Scheme 7.2. Influence of Desorption Barriers on V^{2+}/V^{3+} Reaction Kinetics on Edge Plane Pyrolytic Graphite 200

Scheme 7.3. Effect of the Electronic Structure of Electrode on Heterogeneous Charge Transfer Kinetics of Transition Metal Ions 201

Scheme 7.4. Proposed Charge Transfer Mechanism in Quinones Used in Aqueous Organic Redox Flow Batteries 206

Abstract

Redox flow batteries (RFBs) are one of the most promising technologies for grid scale energy storage. RFBs store and release energy by charge transfer (CT) reactions in active species flown on electrode surface. Over the years, many RFBs using transition metal ions as active species have been demonstrated, among which vanadium RFBs (VRFBs: VO_2^+/VO^{2+} // V^{2+}/V^{3+}) are the most commercialized. The slow CT kinetics of transition metal ions at electrodes introduces voltage losses that lower RFBs energy storage efficiency, thereby increasing RFBs costs. More than 70 electrolyte and electrode treatments have been shown to improve the CT kinetics of vanadium redox couples used in VRFBs alone over the last two decades. However, there is still a lack of mechanistic understanding of how CT of transition metal ions occurs, which has prevented a targeted approach for rational design of materials that enhance CT kinetics to lower RFBs cost.

In this dissertation, I present my efforts to understand the CT mechanism of transition metal ions at the electrode surface and identify electrode and electrolyte properties that can be tailored to design materials with improved CT kinetics of transition metal ions for development of low-cost RFBs. I use V^{2+}/V^{3+} as the probe redox couple because the slow V^{2+}/V^{3+} kinetics is shown to in part limit the performance of most commercialized VRFBs. I elucidate the structure of hydrated and complexed vanadium ions in different acidic electrolytes. I identify two key properties using kinetic and spectroscopic measurements, microkinetic modeling, and adsorption energy calculations that act as descriptors of V^{2+}/V^{3+} kinetics. I demonstrate that the identified descriptors also explain CT kinetics of several other transition metal ion redox couples used in RFBs.

I conduct V^{2+}/V^{3+} kinetic measurements in different acidic electrolytes (H_2SO_4, HCl, HBr, HI, and $HClO_4$) to isolate the effect of anions and on different metal electrodes (Au, Ag, Cu, Bi, and W) to isolate the effect of the electrode on CT kinetics. I show that the V^{2+}/V^{3+} is an inner sphere reaction and the V^{2+}/V^{3+} kinetics in different acidic electrolytes correlates with the calculated adsorption energy and desorption barrier of the vanadium intermediate. The anions in the electrolyte serve as bridges for CT between the electrode and the vanadium ions, altering the energy of the vanadium intermediate. I show that the *d*-band center of the electrode linearly correlates with V^{2+}/V^{3+} kinetics on different metal electrodes. The *d*-band electronic structure controls the kinetics by changing the adsorption energy and desorption barrier of the vanadium intermediate.

I demonstrate that the desorption barrier of the transition metal ion intermediate correlates with the kinetics of several other metal ion redox couples including Cr^{2+}/Cr^{3+}, Cd^{0}/Cd^{2+}, and Fe^{2+}/Fe^{3+} in the presence of anions and serves as a descriptor to understand the influence of anions on transition metal ion CT kinetics. I show that the *d*-band center linearly correlates with CT kinetics of several Cr, Fe, and Co-based complexes on metal electrodes, indicating *d*-band center is a descriptor for transition metal ion CT kinetics on electrodes. The desorption barrier of the transition metal ion intermediate can be tuned by altering metal ions' coordination structure and *d*-band center of the electrode can be modified by alloying or nano structuring and can serve as design principles for development of new electrolytes and electrodes with enhanced transition metal ion CT kinetics for low-cost RFBs.

Chapter 1 : Introduction

1.1 Importance of Energy Storage

The global energy demand is expected to rise by ~50 % from the current levels by 2050 due to the continuous increase in the world's population and improvement in standard of living.[1] This rising energy demand is currently met by burning fossil fuels that emit carbon dioxide (~35 billion metric tons in 2020),[1] which has led to a rise in the Earth's temperature by ~0.40 °C in the past two decades,[2] causing harmful climate change and a huge loss to biodiversity. A sustainable way to meet the growing energy needs is to utilize the energy from clean renewables like solar and wind, which are expected to grow five-fold from the current levels and supply ~35 % of the global electricity demand by 2050.[1] However, solar and wind are both intermittent in nature and hence their energy needs to be stored to match demand for effective utilization. With the fraction of energy coming from intermittent renewable sources projected to increase, energy storage will be required to store the energy for long durations (from several days to months) to keep the grid stable, i.e., 20 % intermittent renewables is generally viewed as an upper limit before significant grid destabilization.[3] In developing countries of South Asia, power disruptions due to grid destabilizations have hindered the development of rural communities and account for ~5 % loss of the gross domestic product, which would worsen unless cheap energy storage technologies are developed.[4]

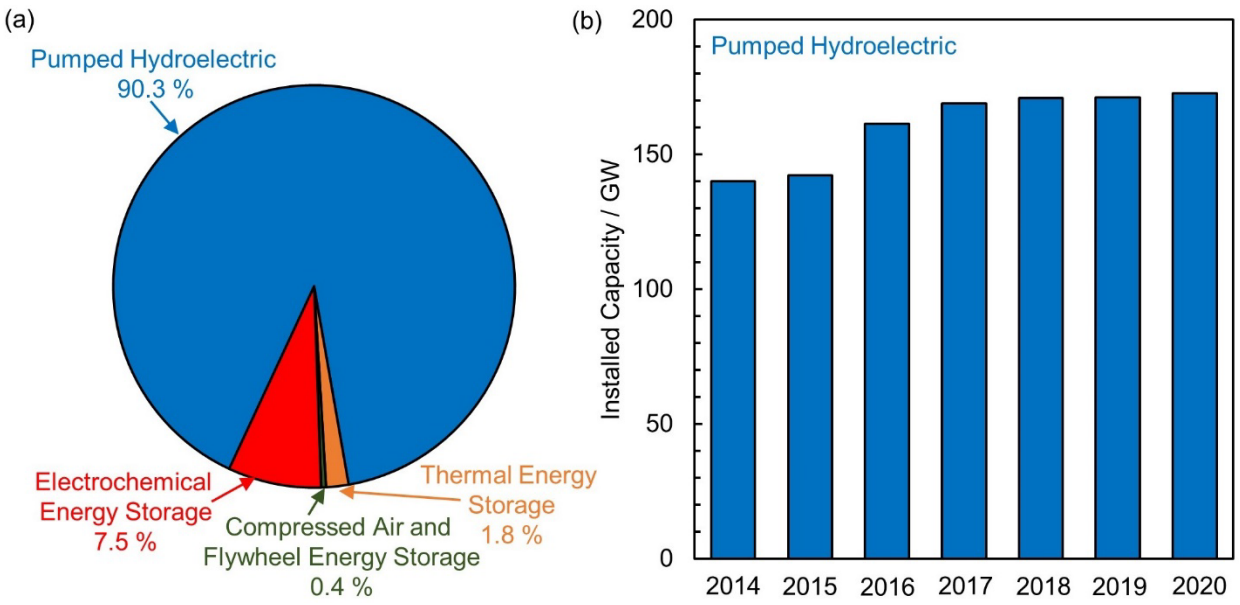

Figure 1.1. Distribution of Global Energy Storage Technologies and Installed Pumped Hydroelectric Capacity over Time. (a) Global energy storage distribution of various technologies at the end of 2020. **(b)** Installed capacity of pumped hydroelectric over the last seven years. The figure is adapted from reference 5.

The technologies that can be used for large scale energy storage include physical energy storage through pumped hydroelectric, compressed air, and flywheels, thermal energy storage by heating or melting materials, and electrochemical energy storage like batteries.[5] **Figure 1.1a** shows the global distribution of installed energy storage technologies. Pumped hydroelectric is currently the top choice of electrical energy storage and accounts for 90.3 % of the total installed energy capacity (172.5 GW),[5] however there are only limited regions where pumped hydroelectric is geographically feasible. Resultantly, the installations of pumped hydroelectric have grown slowly over the past few years as shown in **Figure 1.1b**.[5] Compressed air energy storage is affected by the geological conditions and requires high pressure-bearing capacity equipment. Flywheel energy storage needs vacuum environment for proper operation making flywheels costly and unsuitable for large scale long duration energy storage. The geographical limitations of compressed air energy storage and the need of large vacuum environments for flywheel energy storage are in part responsible for such small contributions of compressed air and flywheels in the global energy storage (**Figure 1.1a**). On the contrary, electrochemical energy storage constitutes 7.5 % (14.2

GW) of the installed energy storage technologies (**Figure 1.1a**), with an annual increase of 49.3 % as shown in **Figure 1.2**.

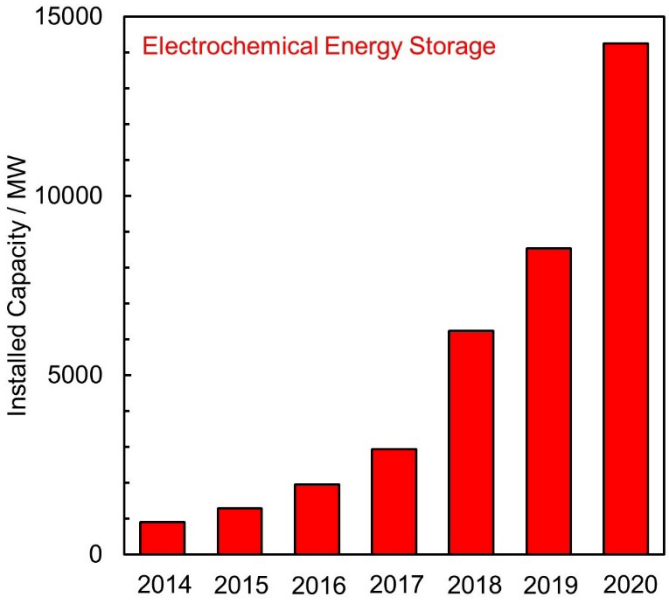

Figure 1.2. Installed Capacity of Electrochemical Energy Storage Over the Last Seven Years. There has been an exponential growth in the installations of the electrochemical energy storage technologies. The figure is adapted from reference 5.

Electrochemical energy storage technologies such as super-capacitors and batteries provide desirable features like high round trip efficiency, long lifetimes, and low maintenance.[6] Super-capacitors store energy by forming an electrochemical double layer at the electrode-electrolyte interface but are only suitable for applications where short discharge times (from μs to s) are required.[6] Batteries like Li-ion and redox flow batteries (RFBs) store energy by chemical changes in active species with discharge durations ranging from several hours to days making them suitable for storing energy from renewable sources. Li-ion batteries are shown to be cost competitive with pumped hydroelectric for storing energy for discharge durations of a few hours and have found extensive applications in automotive industry due to their high energy and power densities. RFBs are shown to hold promise for grid scale energy storage that requires discharge durations ranging from several days to months due to their very high electrode lifetimes and stability; however RFBs

still suffer from high costs.[7–9] The details of operation and different types, voltage losses, and treatments to facilitate charge transfer (CT) reaction in RFBs are discussed in sections below.

1.2 Redox Flow Batteries: Operation and Different Types

Redox flow batteries (RFBs) are one of the promising ways of storing energy electrochemically and have received a widespread interest since their inception in 1974 by Thaller because of RFBs ability to decouple energy and power.[10] An RFB consists of an electrochemical cell and two tanks which contain electrolytes with redox active species dissolved in them. These electrolytes with redox active species are circulated from the tanks to the electrodes in the electrochemical cell using pumps. The electrodes transfer electrons to/from the active species based on the species' redox potential to store or release energy. The redox active species with a lower standard redox potential reacts reversibly at the "negative electrode", and the redox active species with a higher standard redox potential reacts reversibly at the "positive electrode".[3,6,11,12] The two electrodes where CT reactions occur are separated by a separator or an ion-conducting membrane that allows ionic charge carriers to pass through, completing the circuit and maintaining charge balance. Carbon felts are the most commonly used electrodes in RFBs due to their high surface area and conductivity and low cost. The schematic of an RFB is shown in **Scheme 1.1**. The energy and power of an RFB can be controlled independently of each other. The energy can be controlled by changing the concentration of active species and volume of the electrolyte in the tanks, while the power can be controlled by changing the total surface area of the electrodes.[6] This ability of RFBs to decouple energy and power along with high current densities (~1 A cm^{-2}),[13] high power densities (~2.78 W cm^{-2}),[13] and long electrode lifetimes (>20,000 cycles,[13] >20 years) provide them high flexibility and scalability, making them suitable for grid energy storage applications.[14]

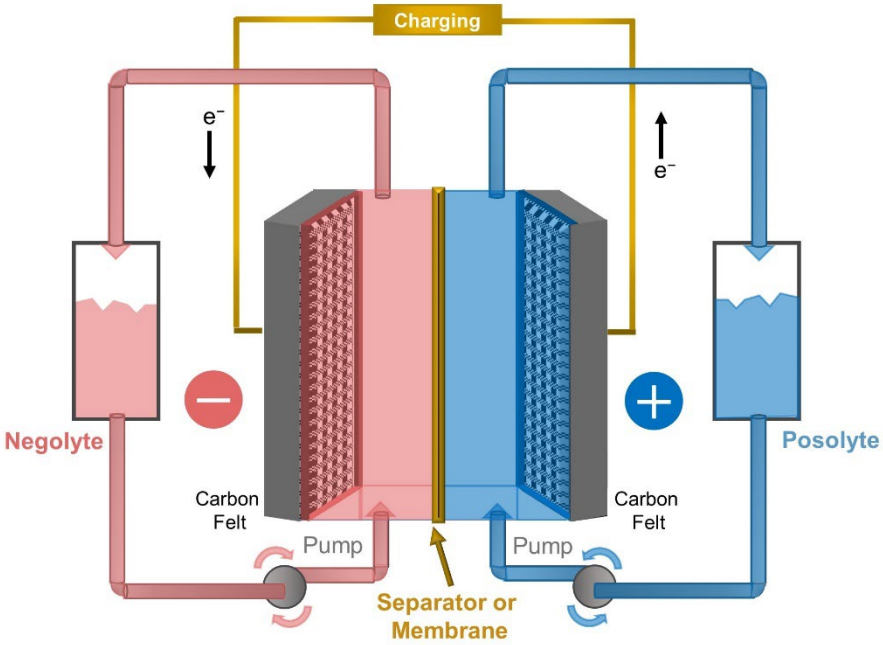

Scheme 1.1. Schematic showing Different Components of a Redox Flow Battery. The electron flows from the positive to the negative electrode during the charging of the battery. The two electrodes are separated by a separator or a membrane that allows the ionic charge carriers to pass through to complete the electrical circuit. The negolyte and posolyte are pumped to the negative and positive electrodes respectively using pumps, where reduction and oxidation reactions occur during charging.

RFBs are classified into inorganic and organic based on the nature of the redox active species used as energy carriers as discussed in **Sections 1.2.1** and **1.2.2**.

1.2.1 Inorganic Redox Flow Batteries

Inorganic RFBs involve CT in different oxidation states of transition metal ions dissolved in water to store and release energy. Even though certain non-aqueous solvents have also been used as electrolytes for inorganic RFBs, these studies are very limited due to the low solubility of transition metal ions in non-aqueous solvents. Transition metal ions spanning the entire *3d* block (Ti to Zn) have been demonstrated for use in RFBs.[15,16] These transition metal ions are coordinated by ligands (e.g., water, anions) in the electrolyte which influence the metal ions structure and reactivity. The inorganic RFB chemistries that are commercialized or have shown promise at the laboratory scale are discussed below:

a) All Vanadium Redox Flow Battery

The Vanadium Redox Flow Battery (VRFB) has been the most commercialized inorganic RFB technology with 209.8 MWh of energy capacity installed till date.[17] VRFBs (VO_2^+/VO^{2+} // V^{2+}/V^{3+}), invented in early 1980s by Prof. Maria Skyllas-Kazacos, have received the most interest among RFBs because of the use of same active element on both sides of the battery. The use of the same element on both sides eliminates cross-contamination and reduces the capacity fade due to crossover extending the lifetime of the battery. Sulfuric acid (H_2SO_4) is the most commonly used electrolyte in VRFBs because of its low cost. The CT reactions occurring in VRFBs during discharge are shown below:

$$V^{2+} \leftrightarrows V^{3+} + e^- \qquad E^o = -0.25 \text{ V vs SHE}$$

$$VO_2^+ + e^- \leftrightarrows VO^{2+} \qquad E^o = 1.0 \text{ V vs SHE}$$

Here E^o is the standard redox potential for the reactions and SHE is standard hydrogen electrode. The standard cell potential provided by VRFB is 1.25 V.

b) Iron–Chromium Redox Flow Battery

Iron–chromium (Fe–Cr) RFBs were the first investigated RFBs because of the low material cost of active species due to the abundance of the chromite ore. Fe–Cr RFBs involves Fe and Cr redox species dissolved in hydrochloric acid (HCl). Fe–Cr RFBs use HCl instead of H_2SO_4 due to the higher solubility of Fe and Cr salts in HCl compared to H_2SO_4.[18] The CT reactions in Fe–Cr RFB during discharge are shown below:

$$Cr^{2+} \leftrightarrows Cr^{3+} + e^- \qquad E^o = -0.41 \text{ V vs SHE}$$

$$Fe^{3+} + e^- \leftrightarrows Fe^{2+} \qquad E^o = 0.77 \text{ V vs SHE}$$

The standard cell potential provided by Fe–Cr RFB is 1.18 V, which is lower in comparison to VRFB. Recently, chelating of Fe and Cr ions has been used as a strategy to alter the redox potential and solubility of ions leading to improved RFB performance.[19,20]

c) All Copper and All Iron Redox Flow Battery

All copper (Cu) RFBs utilize the different oxidation states of copper dissolved in HCl to store and release energy.[21] Due to the use of the active species of same element on both halves, all Cu RFBs have an added advantage of reduced capacity fade due to crossover like VRFBs. The CT reactions in an all Cu RFB during discharge are shown below:

$$Cu^0 \leftrightarrows Cu^+ + e^- \qquad E^o = -0.52 \text{ V vs SHE}$$

$$Cu^{2+} + e^- \leftrightarrows Cu^+ \qquad E^o = 0.15 \text{ V vs SHE}$$

The standard cell potential provided by an all Cu RFB is 0.77 V, much smaller in comparison to Fe–Cr RFB and VRFB.

All iron (Fe) RFBs are based on a similar concept as all Cu RFBs and utilizes different oxidation states of iron (Fe^{3+}/Fe^{2+} // Fe^0/Fe^{2+}). The standard redox potential of an all Fe RFB is 1.21 V.[22] Recently, similar to Fe–Cr flow battery, changing the coordination environment of Fe has been shown to expand the cell voltage of an all Fe RFB to 1.34 V.[23]

d) Manganese-based Redox Flow Battery

Manganese-based RFBs involve Mn^{2+}/Mn^{3+} redox couple at the positive electrode due to high redox potential of Mn^{2+}/Mn^{3+}. H_2–Mn and Ti–Mn RFBs use Mn^{2+}/Mn^{3+} dissolved in H_2SO_4 coupled with H^+/H_2 or TiO^{2+}/Ti^{3+} redox couple, yielding a total standard cell potential between 1.4−1.5 V.[24,25] Even though the standard cell potentials of manganese-based RFBs are higher than VRFBs, the Mn^{3+} undergoes disproportionation reaction to form insoluble MnO_2 along with Mn^{2+}, which blocks the electrodes reducing the overall efficiency.

e) Vanadium–Cobalt Redox Flow Battery

Vanadium–Cobalt (V–Co) RFBs involve replacing the VO_2^+/VO^{2+} at the positive half of VRFB with Co^{3+}/Co^{2+} redox couple dissolved in H_2SO_4. The standard cell potential of 2.35 V is achieved in V–Co RFBs, much higher in comparison to VRFBs.[26] However, more work is needed to demonstrate the V–Co RFBs performance for longer durations at high current densities. Additionally, the capacity decay due to crossover needs to be examined.

f) Other Inorganic Transition Metal Ion-based Chemistries for RFBs

Several other inorganic RFBs involving *3d* transition metal ions including Zn–Ni,[27] Zn–Fe,[28] Zn–Ce,[29] Zn–halide,[30] V–halide,[31] and V–Ce,[32] have also been demonstrated. However, all these chemistries face significant challenges for commercial implementation. The Zn^{2+}/Zn^0 redox reaction in the negative half of Zn-based RFBs forms Zn dendrites during continuous cycling that causes the Zn-based RFBs to short circuit. RFBs with halide redox couples (Cl^-/Cl_2, Br^-/Br_2) have safety concerns due to the toxic and corrosive nature of halides. Ce-based RFBs are promising due to the high standard redox potential of Ce^{3+}/Ce^{4+} redox couple, but the low solubility of Ce in acids is a concern.

1.2.2 Organic Redox Flow Batteries

Organic RFBs use organic molecules as active species to store and release energy. These organic molecules are prepared from earth abundant materials, thereby reducing the material cost of RFBs. The structure of these organic molecules can be tailored to improve their solubility and undergo multiple charge transfers to increase the battery capacity.

The active species used in organic RFBs are classified in five broad classes based on their molecular structure as shown in **Figure 1.3**. These five broad classes are (1) quinones, (2) organometallic coordination complexes, (3) nitroxide radical derivatives, (4) viologens, and (5) all

other aromatic heterocycles that does not belong to the classes (1), (3), and (4). These organic molecules degrade with continuous charging/discharging of battery to form irreversible products lowering the battery efficiency. Resultantly, a lot of research over the last decade has been conducted to understand degradation mechanisms of organic molecules and if CT reactions in these organic molecules can be done reversibly with high efficiency.[33,34] Organic RFBs are generally operated in non-symmetric condition, i.e., with different class or derivatives of same class of organic molecules as redox couples on the positive and negative half.

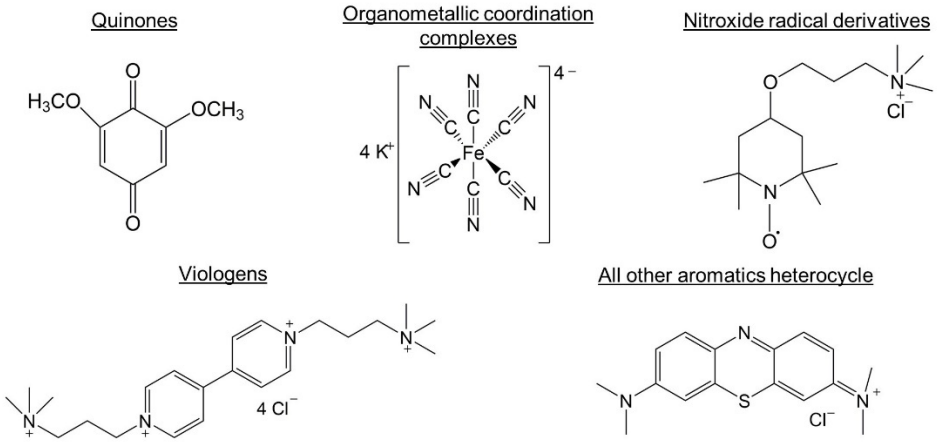

Figure 1.3. Classes of Organic Molecules used in Organic Redox Flow Batteries based on their Molecular Structure. A representative molecule for each class is shown, DMBQ for quinones, $K_4Fe(CN)_6$ for organometallic coordination complexes, TMAP-TEMPO for nitroxide radical derivatives, BTMAP-Vi for Viologens, and MB for all other aromatic heterocycles. Here, DMBQ is dimethyl benzoquinone, $K_4Fe(CN)_6$ is potassium hexacyanoferrate, TMAP-TEMPO is 4-[3-(trimethylammonio)propoxy]-2,2,6,6-tetramethylpiperidine-1-oxyl, BTMAP-Vi is bis(3-trimethylammonio)- propyl viologen tetrachloride, and MB is methylene blue.

Based on the nature of the solvent used, organic RFBs are generally classified into two broad categories, aqueous organic and non-aqueous organic.[16] Aqueous organic RFBs use organic molecules dissolved in aqueous solutions. Aqueous organic RFBs can operate over the entire pH range, contrary to inorganic based aqueous RFBs which operate mostly under acidic environments. The aqueous electrolytes are cheap, non-flammable, and have high conductivity. However, the aqueous organic RFBs are limited by the narrow electrochemical window of water splitting. Non-aqueous organic RFBs have organic molecules dissolved in non-aqueous electrolytes like dimethyl

sulfoxide, acetonitrile instead of water, providing an added advantage of expanded electrochemical window of operation. However, the low conductivities of non-aqueous electrolytes along with faster chemical degradation of organic molecules and capacity fade due to crossover makes the cycling performance of non-aqueous RFBs worse than aqueous organic RFBs.

1.3 Voltage Losses in Redox Flow Batteries

The slow CT kinetics, resistances in the cell, and concentration gradient of active species between the electrode and bulk electrolyte lead to voltage losses in RFBs. The thermodynamic voltage that can be obtained from a battery is the difference in the standard redox potential of the reactions occurring at the two electrodes. However, due to the inefficiencies in RFBs, the charging of the battery requires more voltage than the thermodynamic voltage. Similarly, the battery delivers less voltage than the thermodynamic voltage during discharging. This excess voltage required for charging or lost during discharging of the battery is called the overvoltage (η). The overvoltage will generally increase with increasing current density. The total overvoltage has contributions from kinetic, ohmic, and mass transfer overvoltage as discussed below:[35]

1) *Kinetic or activation overvoltage* (η_{kinetic}): Overvoltage that arises from slow CT kinetics of reactions occurring at the electrode surface. η_{kinetic} can be reduced by using catalysts that enhance CT kinetics. That is, some catalysts will allow you to operate at the same current density, but lower η_{kinetic}. The current density or the CT reaction rate increases exponentially with increase in η_{kinetic} as discussed in detail in **Chapter 2**.
2) *Ohmic overvoltage* (η_{ohmic}): Overvoltage that arises from resistances throughout the cell, including resistance from solution, membrane, and electrical connections. The conductivity and hydrophilicity of the electrode can be improved to reduce η_{ohmic}. η_{ohmic} is linearly

related to current density, through Ohm's law (i.e., $\eta_{ohmic} = iR$, where i is the operating current density and R is the cell resistance).

3) *Mass transfer or concentration overvoltage* (η_{MT}): Overvoltage that arises from the gradient in concentration of active species between the electrode surface and the electrolyte bulk. These gradients arise when the CT reaction rate is faster than the transport rate to replenish the active species via diffusion at the electrode surface. η_{MT} can be reduced by using active species with high diffusivities, increasing the flow rates of the electrolytes, and using less porous electrodes.

Figure 1.4 shows the cell voltage as a function of current density during charging and discharging of an RFB. At low operating current densities, diffusion of active species to reach the electrode surface is much faster compared to the CT rate of reactions occurring at the electrode surface. Resultantly, there is no concentration gradient of active species between the electrode surface and bulk electrolyte due to which η_{MT} is negligible. The contributions of η_{ohmic} are small due to minor iR drop at low operating current densities for a fixed cell resistance. Resultantly, $\eta_{kinetic}$ dominates the overall voltage losses at low current densities. $\eta_{kinetic}$ is larger with slower CT kinetics because more driving force is required for CT reaction to occur at desired rates for achieving the same operating current density. These low current densities at which $\eta_{kinetic}$ dominates are often called kinetic current densities. At moderate operating current densities, the iR drop due to resistances in the cell starts to become more significant and contribute along with the $\eta_{kinetic}$, while η_{MT} is still negligible due to the absence of active species concentration gradient. The shape of the cell voltage vs current density appears linear in the region of moderately operating current densities because the additional increase in current density from the kinetic current densities is mostly dominated by ohmic losses in the cell and hence η_{ohmic}. At extremely high

operating current densities, the CT reaction rate is much faster (because of the exponential dependence of CT reaction rate on overpotential as discussed in **Chapter 2**) than the diffusion of active species to reach the electrode surface, which gives rise to a concentration gradient. Consequently, the current drawn out of the battery is limited by the active species reaching the electrode surface for CT giving rise to η_{MT}. These extremely high operating current densities where η_{MT} limits the battery performance is called limiting current densities.

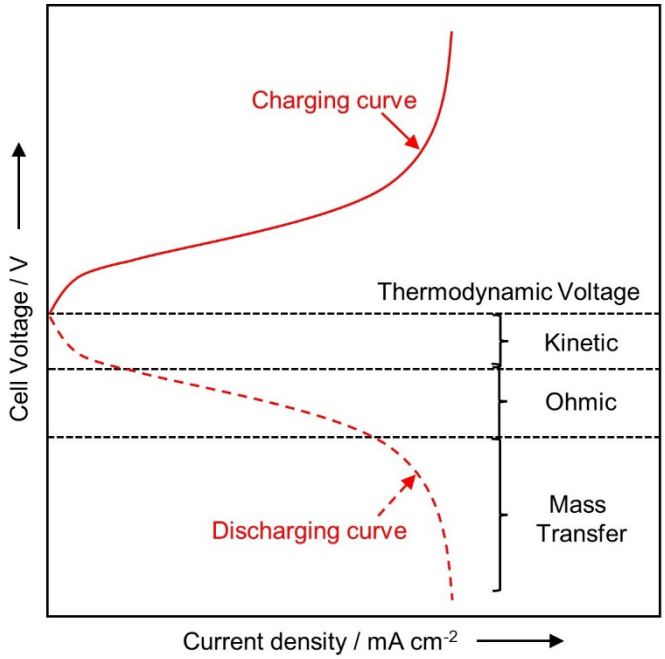

Figure 1.4. Cell Voltage vs Current Density During Charging and Discharging of a Redox Flow Battery Showing Different Voltage Losses. Cell voltage with varying operating current density showing contributions from kinetic, ohmic, and mass transfer overvoltages during discharging in a redox flow battery. The overvoltages during charging can be same or different in magnitude than those in discharging based on the kinetic reversibility of the charge transfer reactions and the properties of oxidants and reductants.

The voltage losses in the RFB reduce the round-trip energy efficiency (EE) of the battery. The EE of the battery is defined as the product of voltage efficiency (VE) and coulombic efficiency (CE). VE is defined as the ratio of the discharging to the charging voltage. The voltage losses decrease the discharging voltage and increase the charging voltage, thereby reducing the VE. CE is defined as the ratio of output charge to the input charge of the battery. CE is reduced due to enhancement of side reactions with larger voltage losses.

Although the organic RFBs provide some significant advantages over inorganic RFBs, organic RFBs are still in the early stages of development and more research is needed to develop organic molecules that are chemically stable over long periods of RFB operation. On the contrary, active species in inorganic RFBs are chemically stable over long operations. However, the kinetic overvoltage dominates the overall voltage losses in inorganic RFBs and lowers their energy storage efficiency. The large voltage losses due to slow CT kinetics prevents inorganic RFBs from operating at high current densities and limits their performance, thereby increasing their overall costs. Hence, the understanding of the CT reactions in redox couples employed in inorganic RFBs forms the focus of this dissertation.

The electrolyte and the electrode play a crucial role in the CT reactions occurring in RFBs. The anions present in the electrolyte can alter the coordination sphere of the transition metal ion reaching the electrode surface. The nature of the transition metal ion complex formed in the electrolyte depends on the *d* electronic configuration of the central metal ion and the nature of the ligands present in the solution.[36] The anions from the electrolyte can also adsorb on the electrode surface under reaction conditions. The electrode itself can also be functionalized using various treatments to provide different active sites for CT. Thus, it is necessary to understand the structure of the metal ions and the nature of the electrode surface under reaction conditions to understand the CT reactions of transition metal ions.

1.4 Electrolytes and Electrode Treatments for Vanadium Redox Flow Batteries

Many inorganic RFBs have been demonstrated as discussed in **Section 1.2.1**, however, the most extensive work to improve the CT kinetics by electrolyte and electrode engineering is conducted for V^{2+}/V^{3+} and VO_2^+/VO^{2+} redox couple used in VRFBs because of their enormous potential for large scale commercialization. These studies are typically conducted in half-cell to

show the kinetic enhancement using cyclic voltammetry and electrochemical impedance spectroscopy, while full-cell configurations are used to compare the overall VRFB performance. Since these half- and full-cell studies are conducted in very differing experimental conditions, inferring mechanistic insights and comparing among different electrode and electrolyte treatments is very challenging. In this section, I summarize the major electrolyte and electrode treatments conducted for VRFBs, identify which half of the battery is improved kinetically (*superscript* '*' *= positive half (VO_2^+/VO^{2+}), superscript* '$' *= negative half ($V^{2+}/V^{3+}$), and superscript* '#' *= both positive and negative half*), and whether both full- and half-cell studies (*superscript 'a' = Only full-cell and no half-cell studies, superscript 'b' = only half-cell and no full-cell studies, no superscript = Both half- and full-cell studies*) are conducted showing the improvement in performance.

The introduction of several anions in the traditionally used H_2SO_4 electrolyte for VRFBs have been shown to improve the kinetics of CT and solubility of vanadium ions. HCl[#],[31,37,38] mixed acid electrolytes like HCl and H_2SO_4[#],[39–41] phosphoric acid (H_3PO_4) and H_2SO_4[#],[42,43] and addition of magnesium chloride ($MgCl_2$) and di-ammonium hydrogen phosphate ($(NH_4)_2HPO_4$)[a] to H_2SO_4 have been shown to improve performance for VRFBs.[44] However, how these anions influence the structure of vanadium ions and impacts the CT kinetics is not understood.

The carbon felts used as electrodes in VRFBs are often 1) treated or 2) loaded with electrocatalysts to improve the overall battery performance. More than 50 treatments and 20 electrocatalysts for VRFBs have been reported till date showing improvement; however, there is still a lack of understanding of what electrode property controls CT kinetics. The carbon felt treatments can be classified based on the nature of treatment in various categories as discussed below:

1) Acid/Base Treatments: H_2SO_4[#,45] HNO_3[#,45] Aqua Regia[#,46] KOH[a, 47]
2) Thermal Treatment: Air[#,48–55] O_3[#,52] CO_2[*,56] Ar[a, 57]
3) Plasma Treatment: N_2[#,58,59] O_2[#,50,51,58,60] Ar[# 58]
4) Electrochemical Oxidation: Oxidative potential[#,61,62] Square wave pulse[# 63]
5) Microwave[*, 64] and Gamma Ray[a,50] Treatment
6) Corona Discharge[#,65] H_2O_2[#,60,65–67] HF[*, 66]
7) Doped with Elements: N[#,68–79] B[#,53] O[#,53,74] S[#,75,77,80] P[#,57,71,81] and Halogens[#] (Cl, Br, I)[82]
8) Porous Electrodes by Chemical Reaction: NiO/Ni[#,83] K_2FeO_4[$, 84]
9) Carbon-based Electrocatalysts: Graphite oxide nanoplatelets[#,82,85] Graphite- carbon nanotubes (CNTs)[#], Single-walled CNTs (SWCNTs)[#,86] Multi-walled CNTs (MWCNTs)[#,76–78,80,81,87–90] Carbon dots[#,91] Carbon nanofiber/CNT composite[#,92] Graphite/Graphite oxide[#,93] Carbon black[#,70] Carbon Nano-[#] and Micro-spheres[*,71,79] Graphite oxide based graphene[*, 93,94]

Similar to the carbon felt treatments, several metal/metal oxide based electrocatalysts are loaded on carbon felts using techniques like wet impregnation, electrodeposition, and hydrothermal method and have shown to improve the performance of VRFBs. The metal/metal oxide based electrocatalysts tested for VRFBs are summarized below:

1) Metals: Bi[#,95–99] Sn[#,100] Sb[#,101] Ag[$,102] Cu[$,103] RuSe[*,104] Prussian Blue[*,105] Pt[#,b,106] $CuPt_3$[#,b,107] Ir[#,b,106] Mn[#,b,106] Te[#,b,106] In[#,b,106] Pd[#,b,106] Au[#,b,106]
2) Metal oxides and others: Nb_2O_5[#,108] ZrO_2[#,109] Mn_3O_4[#,110] WO_3[#,111] SnO_2[#,112] CeO_2[#,113,114] NiO[#,115,116] Co_3O_4[#,117] Nd_2O_3[#,118] MoO_3[#,119] $KMnO_4$[#,120] TiO_2[$,121,122] H: TiO_2[$,123] IrO_2[*,124] Cr_2O_3[*,125] CoO[*,116] $NiCoO_2$[*,116] Ta_2O_5[*,126] PbO_2[*,127] RuO_2[a, 128]

Several other metal nitrides and carbides (TiN[#], TiC[#])[129–132] have also shown to improve the performance of VRFBs.

1.5 Dissertation Overview

Even though the development of inorganic RFBs dates to early 1970s and many strategies have been implemented to improve the CT of transition metal ions (as discussed in **Section 1.4** for VRFBs), there is still a lack of fundamental understanding of how these CT reactions occur and why these treatments improve CT kinetics. The ways in which coordination structure of the transition metal ions in solution can be tuned to improve CT kinetics is underexplored. The lack of understanding of the coordination structure of transition metal ions in solution and the reaction mechanism has prevented a targeted approach to identify material properties that can be tailored to design efficient electrodes and electrolytes to minimize the voltage losses due to CT to improve RFBs performance and lower their costs. Additionally, given the CT reactions of *3d* transition metal ions also have applications in fields of corrosion, electrodeposition, chemical sensors, and naturally occurring processes like photosynthesis and respiration, an improved understanding of the CT mechanism will also serve as a major leap in making these processes more efficient.

This dissertation identifies certain electrolyte and electrode properties that can be tailored to control CT reactions of transition metal ions used in RFBs. These properties are identified by conducting extensive studies to understand the structure of ions in solution and isolating the effect of anions and electrode on reaction kinetics. I use the V^{2+}/V^{3+} redox couple for detailed study in this dissertation because the slow CT kinetics of V^{2+}/V^{3+} has been shown to in part limit VRFBs performance. In existing VRFB systems, eliminating the V^{2+}/V^{3+} redox couple overvoltage alone by improving the V^{2+}/V^{3+} redox kinetics could increase this efficiency from 77% to ~86%.[133] I clearly show how the findings V^{2+}/V^{3+} redox couple are generalizable and can be extended to

understand CT of other transition metal ions. The work done in this dissertation opens an avenue to design new electrolytes and electrodes with higher CT rates of transition metal ions having far ranging applications, from development of low-cost energy storage technologies to more efficient electrochemical processes. The dissertation is divided into seven chapters as outlined below.

1.6 Dissertation Outline

Chapter 1 provides an introduction to the energy storage technologies and highlights the importance of the development of RFBs for grid scale energy storage. This chapter provides an overview of various transition metal ion chemistries used in RFBs and explains how slow CT introduces voltage losses in the battery increasing RFBs costs. Additionally, this chapter discusses a wide variety of electrolytes and electrode treatments that have been shown to improve CT kinetics for VRFBs despite of which there is a lack of mechanistic understanding, motivating the need to understand the CT reactions at a fundamental level for a more targeted approach to design materials for low-cost RFBs.

Chapter 2 provides a background of the different mechanisms through which CT at electrode surface can take place. This chapter discusses the theory and experimental details of different techniques used in this dissertation to identify the structure of transition metal ions in solution and measuring electrochemical kinetic parameters. I also review the different methods used to measure electrochemically active surface area of electrodes for normalizing measured kinetic parameters.

Chapter 3 discusses V^{2+}/V^{3+} reaction kinetics on a glassy carbon electrode in HCl, H_2SO_4 and mixed HCl/H_2SO_4 electrolyte used for VRFBs. I show that the V^{2+}/V^{3+} reaction is an inner sphere reaction with an adsorbed intermediate and the kinetics are faster in HCl compared to H_2SO_4 and HCl/H_2SO_4. I identify the structure of V^{2+} and V^{3+} ions in these electrolytes using UV-vis

spectroscopy. Using two independent experimental techniques of measuring kinetics in conjunction, I show V^{2+}/V^{3+} reaction is an overall two electron reaction in HCl.

Chapter 4 builds on the findings of **Chapter 3** and discusses the influence of anions (ClO_4^-, SO_4^{2-}, Cl^-, Br^-, and I^-) on V^{2+}/V^{3+} CT kinetics on glassy carbon electrode. I show that the adsorption strength of the vanadium intermediate controls V^{2+}/V^{3+} reaction kinetics, rather than the changes in anion coverage. I show conclusively that SO_4^{2-} has an inhibiting effect on the V^{2+}/V^{3+} CT kinetics. I identify the structures of V^{2+} and V^{3+} ions in different electrolytes under electrochemical conditions using extended x-ray absorption spectroscopy. I demonstrate that the adsorption strength of the vanadium intermediate correlates with free anion polarizability rationalizing the use of anion polarizability in the existing literature to explain kinetic trends in presence of anions of several other *3d* transition metal ion redox couples.

Chapter 5 identifies the desorption barrier of metal ion intermediate as a descriptor of reaction kinetics of metal ions in the presence of anions. I show that the desorption barrier of vanadium intermediate correlates with the V^{2+}/V^{3+} reaction kinetics in different electrolytes on edge plane pyrolytic graphite. I further demonstrate that the desorption barrier of the metal ion intermediate also correlates with the kinetics of V^{2+}/V^{3+}, Cr^{2+}/Cr^{3+}, and Cd^0/Cd^{2+} in the presence of anions.

Chapter 6 isolates the effect of the electrode on kinetics to show that *d*-band center of the electrode correlates with CT kinetics of transition metal ions. The V^{2+}/V^{3+} kinetics correlates with the desorption barrier of vanadium intermediate on metal electrodes, which in turn correlates with the *d*-band center of the electrode. I extend this study to identify that the *d*-band center of electrode also correlates with kinetics of several Fe, Co, Cr-based complexes on metal electrodes. The *d*-band center as a descriptor for CT reactions at electrode surface is similar to *d*-electronic

configuration as a descriptor of CT of transition metal ions in solution phase based on the analogous CT mechanisms in both phases.

Chapter 7 summarizes the major findings of the dissertation and elaborates how these findings can have an influence in the field of energy storage. I discuss the limitations of the work in this dissertation and propose some future directions to address these limitations. Finally, I provide an outlook highlighting the importance of standardization to measure CT kinetics and RFB performance as the field of RFB moves forward in the coming future.

1.7 References

(1) US Energy Information Administration. *International Energy Outlook 2021*; 2021.
(2) NASA. Global Temperature | Vital Signs – Climate Change: Vital Signs of the Planet https://climate.nasa.gov/vital-signs/global-temperature/ (accessed Nov 28, 2020).
(3) Gür, T. M. Review of Electrical Energy Storage Technologies, Materials and Systems: Challenges and Prospects for Large-Scale Grid Storage. *Energy Environ. Sci.* **2018**, *11*, 2696–2767.
(4) Zhang, F. *In the Dark : How Much Do Power Sector Distortions Cost South Asia?*; Washington, DC: World Bank, 2019.
(5) Huang, Z.; Mu, A.; Wu, L.; Yang, B.; Qian, Y.; Wang, J. Comprehensive Analysis of Critical Issues in All-Vanadium Redox Flow Battery. *ACS Sustain. Chem. Eng.* **2022**.
(6) Dunn, B.; Kamath, H.; Tarascon, J.-M. Electrical Energy Storage for the Grid : A Battery of Choices. *Sci. Mag.* **2011**, *334* (6058), 928–935.
(7) Hunter, C. A.; Penev, M. M.; Reznicek, E. P.; Eichman, J.; Rustagi, N.; Baldwin, S. F. Techno-Economic Analysis of Long-Duration Energy Storage and Flexible Power Generation Technologies to Support High-Variable Renewable Energy Grids. *Joule* **2021**, *5* (8), 2077–2101.
(8) Albertus, P.; Manser, J. S.; Litzelman, S. Long-Duration Electricity Storage Applications, Economics, and Technologies. *Joule* **2020**, *4* (1), 21–32.
(9) Dowling, J. A.; Rinaldi, K. Z.; Ruggles, T. H.; Davis, S. J.; Yuan, M.; Tong, F.; Lewis, N. S.; Caldeira, K. Role of Long-Duration Energy Storage in Variable Renewable Electricity Systems. *Joule* **2020**, *4* (9), 1907–1928.
(10) Thaller, L. H. Electrically Rechargeable Redox Flow Cells. In *Intersociety Energy Conversion Engineering Conference, 9th, Proceedings. (A75-10476 01-44)*; San Francisco, 1974; pp 924–928.
(11) Nguyen, T.; Savinell, R. F. Flow Batteries. *Electrochem. Soc. Interface* **2010**, *19* (3), 54–56.
(12) Ding, C.; Zhang, H.; Li, X.; Liu, T.; Xing, F. Vanadium Flow Battery for Energy Storage: Prospects and Challenges. *J. Phys. Chem. Lett.* **2013**, *4* (8), 1281–1294.
(13) Jiang, H. R.; Sun, J.; Wei, L.; Wu, M. C.; Shyy, W.; Zhao, T. S. A High Power Density and Long Cycle Life Vanadium Redox Flow Battery. *Energy Storage Mater.* **2020**, *24*, 529–

540.
(14) Wei, X.; Duan, W.; Huang, J.; Zhang, L.; Li, B.; Reed, D.; Xu, W.; Sprenkle, V.; Wang, W. A High-Current, Stable Nonaqueous Organic Redox Flow Battery. *ACS Energy Lett.* **2016**, *1*, 705–711.
(15) Agarwal, H.; Florian, J.; Goldsmith, B. R.; Singh, N. The Effect of Anion Bridging on Heterogeneous Charge Transfer for V^{2+}/V^{3+}. *Cell Reports Phys. Sci.* **2021**, *2* (1), 100307.
(16) Luo, J.; Hu, B.; Hu, M.; Zhao, Y.; Liu, T. L. Status and Prospects of Organic Redox Flow Batteries toward Sustainable Energy Storage. *ACS Energy Lett.* **2019**, *4*, 2220–2240.
(17) Vanadium Is the Latest Beneficiary of the Battery Craze. *The Economist*. 2018, pp 1–3.
(18) Pawar, S. H.; Madhale, R. D.; Patil, P. S.; Lokhande, C. D. *Studies on Iron-Chromium Redox Storage System*; 1988; Vol. 10.
(19) Waters, S. E.; Robb, B. H.; Marshak, M. P. Effect of Chelation on Iron−Chromium Redox Flow Batteries. *ACS Energy Lett.* **2020**, *5*, 1758–1762.
(20) Robb, B. H.; Farrell, J. M.; Marshak, M. P. Chelated Chromium Electrolyte Enabling High-Voltage Aqueous Flow Batteries. *Joule* **2019**, *3*, 2503–2512.
(21) Sanz, L.; Lloyd, D.; Magdalena, E.; Palma, J.; Kontturi, K. Description and Performance of a Novel Aqueous All-Copper Redox Flow Battery. *J. Power Sources* **2014**, *268*, 121–128.
(22) Hruska, L. W.; Savinell, R. F. Investigation of Factors Affecting Performance of the Iron-Redox Battery. *J. Electrochem. Soc.* **1981**, *128* (1), 18–25.
(23) Gong, K.; Xu, F.; Grunewald, J. B.; Ma, X.; Zhao, Y.; Gu, S.; Yan, Y. All-Soluble All-Iron Aqueous Redox-Flow Battery. *ACS Energy Lett.* **2016**, *1*, 89–93.
(24) Rubio-Garcia, J.; Kucernak, A.; Zhao, D.; Li, D.; Fahy, K.; Yufit, V.; Brandon, N.; Gomez-Gonzalez, M. Hydrogen/Manganese Hybrid Redox Flow Battery. *J. Phys. Energy* **2019**, *1* (1), 015006.
(25) Dong, Y. R.; Kaku, H.; Hanafusa, K.; Moriuchi, K.; Shigematsu, T. A Novel Titanium/Manganese Redox Flow Battery. *ECS Trans.* **2015**, *69* (18), 59–67.
(26) Kocyigit, N.; Gencten, M.; Sahin, M.; Sahin, Y. A Novel Vanadium/Cobalt Redox Couple in Aqueous Acidic Solution for Redox Flow Batteries. *Int. J. Energy Res.* **2020**, *44* (1), 411–424.
(27) Cheng, J.; Zhang, L.; Yang, Y.-S.; Wen, Y.-H.; Cao, G.-P.; Wang, X.-D. Preliminary Study of Single Flow Zinc-Nickel Battery. *Electrochem. commun.* **2007**, *9*, 2639–2642.
(28) Gong, K.; Ma, X.; Conforti, K. M.; Kuttler, K. J.; Grunewald, J. B.; Yeager, K. L.; Bazant, M. Z.; Gu, S.; Yan, Y. A Zinc–Iron Redox-Flow Battery Under $100 per KW h of System Capital Cost. *Energy Environ. Sci* **2015**, *8*, 2941–2945.
(29) Leung, P. K.; Ponce-de-León, C.; Low, C. T. J.; Shah, A. A.; Walsh, F. C. Characterization of a Zinc–Cerium Flow Battery. *J. Power Sources* **2011**, *196* (11), 5174–5185.
(30) Zhang, J.; Jiang, G.; Xu, P.; Kashkooli, A. G.; Mousavi, M.; Yu, A.; Chen, Z. An All-Aqueous Redox Flow Battery with Unprecedented Energy Density. *Energy Environ. Sci* **2018**, *11*, 2010–2015.
(31) Skyllas-Kazacos, M. Novel Vanadium Chloride/Polyhalide Redox Flow Battery. *J. Power Sources* **2003**, *124*, 299–302.
(32) Leung, P. K.; Mohamed, M. R.; Shah, A. A.; Xu, Q.; Conde-Duran, M. B. A Mixed Acid Based Vanadium–Cerium Redox Flow Battery with a Zero-Gap Serpentine Architecture. *J. Power Sources* **2015**, *274*, 651–658.
(33) Kwabi, D. G.; Ji, Y.; Aziz, M. J. Electrolyte Lifetime in Aqueous Organic Redox Flow Batteries: A Critical Review. *Chem. Rev.* **2020**, *120*, 6467–6489.

(34) Luo, J.; Hu, B.; Hu, M.; Zhao, Y.; Liu, T. L. Status and Prospects of Organic Redox Flow Batteries toward Sustainable Energy Storage. *ACS Energy Lett.* **2019**, *4*, 2220–2240.
(35) Bard, A. J.; Faulkner, L. R. *Electrochemical Methods: Fundamentals and Applications*; John Wiley & Sons, Inc.: New York, 2001.
(36) Ribas Gispert, J. *Coordination Chemistry*, 1st ed.; Wiley-VCH: Weinheim, Germany, 2008.
(37) Kim, S.; Vijayakumar, M.; Wang, W.; Zhang, J.; Chen, B.; Nie, Z.; Chen, F.; Hu, J.; Li, L.; Yang, Z. Chloride Supporting Electrolytes for All-Vanadium Redox Flow Batteries. *Phys. Chem. Chem. Phys.* **2011**, *13*, 18186–18193.
(38) Wang, W.; Kim, S.; Chen, B.; Nie, Z.; Zhang, J.; Xia, G.-G.; Li, L.; Yang, Z. A New Redox Flow Battery Using Fe/V Redox Couples in Chloride Supporting Electrolyte. *Energy Environ. Sci.* **2011**, *4*, 4068–4073.
(39) Viswanathan, V.; Crawford, A.; Stephenson, D.; Kim, S.; Wang, W.; Li, B.; Coffey, G.; Thomsen, E.; Graff, G.; Balducci, P.; et al. Cost and Performance Model for Redox Flow Batteries. *J. Power Sources* **2014**, *247*, 1040–1051.
(40) Li, L.; Kim, S.; Wang, W.; Vijayakumar, M.; Nie, Z.; Chen, B.; Zhang, J.; Xia, G.; Hu, J.; Graff, G.; et al. A Stable Vanadium Redox-Flow Battery with High Energy Density for Large-Scale Energy Storage. *Adv. Energy Mater.* **2011**, *1* (3), 394–400.
(41) Vijayakumar, M.; Wang, W.; Nie, Z.; Sprenkle, V.; Hu, J. Elucidating the Higher Stability of Vanadium(V) Cations in Mixed Acid Based Redox Flow Battery Electrolytes. *J. Power Sources* **2013**, *241*, 173–177.
(42) Holland-Cunz, M. V.; Friedl, J.; Stimming, U. Anion Effects on the Redox Kinetics of Positive Electrolyte of the All-Vanadium Redox Flow Battery. *J. Electroanal. Chem.* **2018**, *819*, 306–311.
(43) Oldenburg, F. J.; Bon, M.; Perego, D.; Polino, D.; Laino, T.; Gubler, L.; Schmidt, T. J. Revealing the Role of Phosphoric Acid in All-Vanadium Redox Flow Batteries with DFT Calculations and In Situ Analysis. *Phys. Chem. Chem. Phys* **2018**, *20*, 23664–23673.
(44) Murugesan, V.; Nie, Z.; Zhang, X.; Gao, P.; Zhu, Z.; Huang, Q.; Yan, L.; Reed, D.; Wang, W. Accelerated Design of Vanadium Redox Flow Battery Electrolytes through Tunable Solvation Chemistry. *Cell Reports Phys. Sci.* **2021**, *2*, 100323.
(45) Sun, B.; Skyllas-Kazacos, M. Chemical Modification of Graphite Electrode Materials for Vanadium Redox Flow Battery Application—Part II. Acid Treatments. *Electrochim. Acta* **1992**, *37* (13), 2459–2465.
(46) Yue, L.; Li, W.; Sun, F.; Zhao, L.; Xing, L. Highly Hydroxylated Carbon Fibres as Electrode Materials of All-Vanadium Redox Flow Battery. *Carbon N. Y.* **2010**, *48* (11), 3079–3090.
(47) Zhou, X. L.; Zhao, T. S.; Zeng, Y. K.; An, L.; Wei, L. A Highly Permeable and Enhanced Surface Area Carbon-Cloth Electrode for Vanadium Redox Flow Batteries. *J. Power Sources* **2016**, *329*, 247–254.
(48) Sun, B.; Skyllas-Kazacos, M. Modification of Graphite Electrode Materials for Vanadium Redox Flow Battery Application-I. Thermal Treatment. *Electrochim. Acta* **1992**, *7*, 1253–1260.
(49) Ghimire, P. C.; Schweiss, R.; Scherer, G. G.; Lim, T. M.; Wai, N.; Bhattarai, A.; Yan, Q. Optimization of Thermal Oxidation of Electrodes for the Performance Enhancement in All-Vanadium Redox Flow Battery. *Carbon N. Y.* **2019**, *155*, 176–185.
(50) Kim, K. J.; Kim, Y.-J.; Kim, J.-H.; Park, M.-S. The Effects of Surface Modification on Carbon Felt Electrodes for Use in Vanadium Redox Flow Batteries. *Mater. Chem. Phys.* **2011**, *131* (1–2), 547–553.

(51) Dixon, D.; Babu, D. J.; Langner, J.; Bruns, M.; Pfaffmann, L.; Bhaskar, A.; Schneider, J. J.; Scheiba, F.; Ehrenberg, H. Effect of Oxygen Plasma Treatment on the Electrochemical Performance of the Rayon and Polyacrylonitrile Based Carbon Felt for the Vanadium Redox Flow Battery Application. *J. Power Sources* **2016**, *332*, 240–248.
(52) Kil, D.; June Lee, H.; Park, S.; Kim, S.; Kim, H. Synthesis of Activated Graphite Felts Using Short-Term Ozone/Heat Treatment for Vanadium Redox Flow Batteries. *J. Electrochem. Soc.* **2017**, *164* (13), A3011–A3017.
(53) Kim, H.; Yi, J. S.; Lee, D. Marked Electrocatalytic Effects of Two-Step Boron and Oxygen Atomic Doping of Carbon Electrodes for Vanadium Redox Flow Battery. *ACS Appl. Energy Mater* **2021**, *4*, 425–433.
(54) Liu, Y.; Shen, Y.; Yu, L.; Liu, L.; Liang, F.; Qiu, X.; Xi, J. Holey-Engineered Electrodes for Advanced Vanadium Flow Batteries. *Nano Energy* **2018**, *43*, 55–62.
(55) Pezeshki, A. M.; Clement, J. T.; Veith, G. M.; Zawodzinski, T. A.; Mench, M. M. High Performance Electrodes in Vanadium Redox Flow Batteries Through Oxygen-Enriched Thermal Activation. *J. Power Sources* **2015**, *294*, 333–338.
(56) Chang, Y. C.; Chen, J. Y.; Kabtamu, D. M.; Lin, G. Y.; Hsu, N. Y.; Chou, Y. S.; Wei, H. J.; Wang, C. H. High Efficiency of CO_2-Activated Graphite Felt as Electrode for Vanadium Redox Flow Battery Application. *J. Power Sources* **2017**, *364*, 1–8.
(57) Kim, K. J.; Lee, H. S.; Kim, J.; Park, M. S.; Kim, J. H.; Kim, Y. J.; Skyllas-Kazacos, M. Superior Electrocatalytic Activity of a Robust Carbon-Felt Electrode with Oxygen-Rich Phosphate Groups for All-Vanadium Redox Flow Batteries. *ChemSusChem* **2016**, *9* (11), 1329–1338.
(58) Bellani, S.; Najafi, L.; Prato, M.; Oropesa-Nuñ Ez, R.; Martín-García, B.; Gagliani, L.; Mantero, E.; Marasco, L.; Bianca, G.; Zappia, M. I.; et al. Graphene-Based Electrodes in a Vanadium Redox Flow Battery Produced by Rapid Low-Pressure Combined Gas Plasma Treatments. *Chem. Mater* **2021**, *33*, 4106–4121.
(59) Chen, J. Z.; Liao, W. Y.; Hsieh, W. Y.; Hsu, C. C.; Chen, Y. S. All-Vanadium Redox Flow Batteries with Graphite Felt Electrodes Treated by Atmospheric Pressure Plasma Jets. *J. Power Sources* **2015**, *274*, 894–898.
(60) Estevez, L.; Reed, D.; Nie, Z.; Schwarz, A. M.; Nandasiri, M. I.; Kizewski, J. P.; Wang, W.; Thomsen, E.; Liu, J.; Zhang, J. G.; et al. Tunable Oxygen Functional Groups as Electrocatalysts on Graphite Felt Surfaces for All-Vanadium Flow Batteries. *ChemSusChem* **2016**, *9* (12), 1455–1461.
(61) Li, X.; Huang, K.; Liu, S.; Tan, N.; Chen, L. Characteristics of Graphite Felt Electrode Electrochemically Oxidized for Vanadium Redox Battery Application. *Trans. Nonferrous Met. Soc. China (English Ed.* **2007**, *17* (1), 195–199.
(62) Zhang, W.; Xi, J.; Li, Z.; Zhou, H.; Liu, L.; Wu, Z.; Qiu, X. Electrochemical Activation of Graphite Felt Electrode for VO_2^+/VO^{2+} Redox Couple Application. *Electrochim. Acta* **2013**, *89*, 429–435.
(63) He, Z.; Jiang, Y.; Zhou, H.; Cheng, G.; Meng, W.; Wang, L.; Dai, L. Graphite Felt Electrode Modified by Square Wave Potential Pulse for Vanadium Redox Flow Battery. *Int. J. Energy Res.* **2017**, *41* (3), 439–447.
(64) Wu, X.; Xu, H.; Xu, P.; Shen, Y.; Lu, L.; Shi, J.; Fu, J.; Zhao, H. Microwave-Treated Graphite Felt as the Positive Electrode For All-Vanadium Redox Flow Battery. *J. Power Sources* **2014**, *263*, 104–109.
(65) Kim, K. J.; Lee, S. W.; Yim, T.; Kim, J. G.; Choi, J. W.; Kim, J. H.; Park, M. S.; Kim, Y.

J. A New Strategy for Integrating Abundant Oxygen Functional Groups into Carbon Felt Electrode for Vanadium Redox Flow Batteries. *Sci. Rep.* **2014**, *4* (1), 1–6.
(66) He, Z.; Jiang, Y.; Meng, W.; Jiang, F.; Zhou, H.; Li, Y.; Zhu, J.; Wang, L.; Dai, L. HF/H_2O_2 Treated Graphite Felt as the Positive Electrode for Vanadium Redox Flow Battery. *Appl. Surf. Sci.* **2017**, *423*, 111–118.
(67) Gao, C.; Wang, N.; Peng, S.; Liu, S.; Lei, Y.; Liang, X.; Zeng, S.; Zi, H. Influence of Fenton's Reagent Treatment on Electrochemical Properties of Graphite Felt for All Vanadium Redox Flow Battery. *Electrochim. Acta* **2013**, *88*, 193–202.
(68) Wu, T.; Huang, K.; Liu, S.; Zhuang, S.; Fang, D.; Li, S.; Lu, D.; Su, A. Hydrothermal Ammoniated Treatment of PAN-Graphite Felt for Vanadium Redox Flow Battery. *J. Solid State Electrochem.* **2012**, *16*, 579–585.
(69) He, Z.; Shi, L.; Shen, J.; He, Z.; Liu, S. Effects of Nitrogen Doping on the Electrochemical Performance of Graphite Felts for Vanadium Redox Flow Batteries. *Int. J. Energy Res.* **2015**, *39* (5), 709–716.
(70) Park, M.; Ryu, J.; Kim, Y.; Cho, J. Corn Protein-Derived Nitrogen-Doped Carbon Materials with Oxygen-Rich Functional Groups: A Highly Efficient Electrocatalyst for All-Vanadium Redox Flow Batteries. *Energy Environ. Sci.* **2014**, *7*, 3727–3735.
(71) He, Z.; Jiang, Y.; Wei, Y.; Zhao, C.; Jiang, F.; Li, L.; Zhou, H.; Meng, W.; Wang, L.; Dai, L. N,P Co-Doped Carbon Microsphere as Superior Electrocatalyst for VO_2^+/VO^{2+} Redox Reaction. *Electrochim. Acta* **2018**, *259*, 122–130.
(72) Flox, C.; Skoumal, M.; Rubio-Garcia, J.; Andreu, T.; Morante, J. R. Strategies for Enhancing Electrochemical Activity of Carbon-Based Electrodes for All-Vanadium Redox Flow Batteries. *Appl. Energy* **2013**, *109*, 344–351.
(73) Park, S.; Kim, H. Fabrication of Nitrogen-Doped Graphite Felts as Positive Electrodes Using Polypyrrole as a Coating Agent in Vanadium Redox Flow Batteries. *J. Mater. Chem. A* **2015**, *3*, 12276–12283.
(74) Lee, M. E.; Jin, H. J.; Yun, Y. S. Synergistic Catalytic Effects of Oxygen and Nitrogen Functional Groups on Active Carbon Electrodes for All-Vanadium Redox Flow Batteries. *RSC Adv.* **2017**, *7* (68), 43227–43232.
(75) Shah, A. B.; Wu, Y.; Joo, Y. L. Direct Addition of Sulfur and Nitrogen Functional Groups to Graphite Felt Electrodes for Improving All-Vanadium Redox Flow Battery Performance. *Electrochim. Acta* **2019**, *297*, 905–915.
(76) Wang, S.; Zhao, X.; Cochell, T.; Manthiram, A. Nitrogen-Doped Carbon Nanotube/Graphite Felts as Advanced Electrode Materials for Vanadium Redox Flow Batteries. *J. Phys. Chem. Lett* **2012**, *3*, 34.
(77) Li, C.; Xie, B.; Chen, J.; He, J.; He, Z. Enhancement of Nitrogen and Sulfur Co-Doping on the Electrocatalytic Properties of Carbon Nanotubes for VO_2^+/VO^{2+} Redox Reaction. *RSC Adv.* **2017**, *7* (22), 13184–13190.
(78) Shin, M.; Noh, C.; Chung, Y.; Kim, D.-H.; Kwon, Y. Vanadium Redox Flow Battery Working Even at a High Current Density by the Adoption of Tris(Hydroxymethyl) Aminomethane Functionalized Acidified Carbon Nanotube Catalyst. *Appl. Surf. Sci.* **2021**, *550*, 148977.
(79) Wu, L.; Shen, Y.; Yu, L.; Xi, J.; Qiu, X. Boosting Vanadium Flow Battery Performance by Nitrogen-Doped Carbon Nanospheres Electrocatalyst. *Nano Energy* **2016**, *28*, 19–28.
(80) He, Z.; Cheng, G.; Jiang, Y.; Wang, L.; Dai, L. Sulfonated Carbon Nanotubes as Superior Catalysts towards V^{3+}/V^{2+} Redox Reaction for Vanadium Redox Flow Battery. *J.*

Electrochem. Soc. **2018**, *5*, A932–A938.
(81) Noh, C.; Kwon, B. W.; Chung, Y.; Kwon, Y. Effect of the Redox Reactivity of Vanadium Ions Enhanced by Phosphorylethanolamine Based Catalyst on the Performance of Vanadium Redox Flow Battery. *J. Power Sources* **2018**, *406*, 26–34.
(82) Park, M.; Jeon, I. Y.; Ryu, J.; Jang, H.; Back, J. B.; Cho, J. Edge-Halogenated Graphene Nanoplatelets with F, Cl, or Br as Electrocatalysts for All-Vanadium Redox Flow Batteries. *Nano Energy* **2016**, *26*, 233–240.
(83) Park, J. J.; Park, J. H.; Park, O. O.; Yang, J. H. Highly Porous Graphenated Graphite Felt Electrodes with Catalytic Defects for High-Performance Vanadium Redox Flow Batteries Produced via NiO/Ni Redox Reactions. *Carbon N. Y.* **2016**, *110*, 17–26.
(84) Lv, Y.; Li, Y.; Han, C.; Chen, J.; He, Z.; Zhu, J.; Dai, L.; Meng, W.; Wang, L. Application of Porous Biomass Carbon Materials in Vanadium Redox Flow Battery. *J. Colloid Interface Sci.* **2020**, *566*, 434–443.
(85) Sankar, A.; Michos, I.; Dutta, I.; Dong, J.; Angelopoulos, A. P. Enhanced Vanadium Redox Flow Battery Performance Using Graphene Nanoplatelets to Decorate Carbon Electrodes. *J. Power Sources* **2018**, *387*, 91–100.
(86) Li, W.; Liu, J.; Yan, C. The Electrochemical Catalytic Activity of Single-Walled Carbon Nanotubes towards VO_2^+/VO^{2+} and V^{3+}/V^{2+} Redox Pairs for an All Vanadium Redox Flow Battery. *Electrochim. Acta* **2012**, *79*, 102–108.
(87) Li, W.; Liu, J.; Yan, C. Multi-Walled Carbon Nanotubes Used as an Electrode Reaction Catalyst for VO_2^+/VO^{2+} for a Vanadium Redox Flow Battery. *Carbon N. Y.* **2011**, *49*, 3463–3470.
(88) NanotubesWei, G.; Jia, C.; Liu, J.; Yan, C. Carbon Felt Supported Carbon Nanotube Catalysts Composite Electrode For Vanadium Redox Flow Battery Application. *J. Power Sources* **2012**, *220*, 185–192.
(89) Yang, H.; Fan, C.; Zhu, Q. Sucrose Pyrolysis Assembling Carbon Nanotubes on Graphite Felt Using for Vanadium Redox Flow Battery Positive Electrode. *J. Energy Chem.* **2018**, *27* (2), 451–454.
(90) Chang, Y.-C.; Shih, Y.-C.; Chen, J.-Y.; Lin, G.-Y.; Hsu, N.-Y.; Chou, Y.-S.; Wang, C.-H. High Efficiency of Bamboo-like Carbon Nanotubes on Functionalized Graphite Felt as Electrode in Vanadium Redox Flow Battery. *RSC Adv.* **2016**, *6*, 102068–102075.
(91) Zhou, Y.; Liu, L.; Shen, Y.; Wu, L.; Yu, L.; Liang, F.; Xi, J. Carbon Dots Promoted Vanadium Flow Batteries for All-Climate Energy Storage. *Chem. Commun.* **2017**, *53* (54), 7565–7568.
(92) Park, M.; Jung, Y.; Kim, J.; il Lee, H.; Cho, J. Synergistic Effect of Carbon Nanofiber/Nanotube Composite Catalyst on Carbon Felt Electrode for High-Performance All-Vanadium Redox Flow Battery. *Nano Lett.* **2013**, *13*, 4833–4839.
(93) Hu, G.; Jing, M.; Wang, D. W.; Sun, Z.; Xu, C.; Ren, W.; Cheng, H. M.; Yan, C.; Fan, X.; Li, F. A Gradient Bi-Functional Graphene-Based Modified Electrode for Vanadium Redox Flow Batteries. *Energy Storage Mater.* **2018**, *13*, 66–71.
(94) González, Z.; Botas, C.; Blanco, C.; Santamaría, R.; Granda, M.; Álvarez, P.; Menéndez, R. Graphite Oxide-Based Graphene Materials as Positive Electrodes in Vanadium Redox Flow Batteries. *J. Power Sources* **2013**, *241*, 349–354.
(95) Li, B.; Gu, M.; Nie, Z.; Shao, Y.; Luo, Q.; Wei, X.; Li, X.; Xiao, J.; Wang, C.; Sprenkle, V.; et al. Bismuth Nanoparticle Decorating Graphite Felt as a High-Performance Electrode for an All-Vanadium Redox Flow Battery. *Nano Lett.* **2013**, *13* (3), 1330–1335.

(96) Yang, X.; Liu, T.; Xu, C.; Zhang, H.; Li, X.; Zhang, H. The Catalytic Effect of Bismuth for VO_2^+/VO^{2+} and V^{3+}/V^{2+} Redox Couples in Vanadium Flow Batteries. *J. Energy Chem.* **2017**, *26* (1), 1–7.
(97) Liu, T.; Li, X.; Nie, H.; Xu, C.; Zhang, H. Investigation on the Effect of Catalyst on the Electrochemical Performance of Carbon Felt and Graphite Felt for Vanadium Flow Batteries. *J. Power Sources* **2015**, *286*, 73–81.
(98) Liu, Y.; Liang, F.; Zhao, Y.; Yu, L.; Liu, L.; Xi, J. Broad Temperature Adaptability of Vanadium Redox Flow Battery–Part 4: Unraveling Wide Temperature Promotion Mechanism of Bismuth for V^{2+}/V^{3+} Couple. *J. Energy Chem.* **2018**, *27* (5), 1333–1340.
(99) Lv, Y.; Zhang, J.; Lv, Z.; Wu, C.; Liu, Y.; Wang, H.; Lu, S.; Xiang, Y. Enhanced Electrochemical Activity of Carbon Felt for V^{2+}/V^{3+} Redox Reaction via Combining KOH-Etched Pretreatment with Uniform Deposition of Bi Nanoparticles. *Electrochim. Acta* **2017**, *253*, 78–84.
(100) Mehboob, S.; Mehmood, A.; Lee, J.-Y.; Shin, H.-J.; Hwang, J.; Abbas, S.; Ha, H. Y. Excellent Electrocatalytic Effects of Tin Through In Situ Electrodeposition on the Performance of All-Vanadium Redox Flow Batteries. *J. Mater. Chem. A* **2017**, *5*, 17388–17400.
(101) Shen, J.; Liu, S.; He, Z.; Shi, L. Influence of Antimony Ions in Negative Electrolyte on the Electrochemical Performance of Vanadium Redox Flow Batteries. *Electrochim. Acta* **2015**, *151*, 297–305.
(102) Zhang, Q.; Liu, T.; Zhang, H.; Li, X. Highly Active Ag Nanoparticle Electrocatalysts toward V^{2+}/V^{3+} Redox Reaction. *ACS Appl. Energy Mater.* **2021**, *4*, 3913–3920.
(103) Wei, L.; Zhao, T. S.; Zeng, L.; Zhou, X. L.; Zeng, Y. K. Copper Nanoparticle-Deposited Graphite Felt Electrodes for All Vanadium Redox Flow Batteries. *Appl. Energy* **2016**, *180*, 386–391.
(104) Han, P.; Wang, X.; Zhang, L.; Wang, T.; Yao, J.; Huang, C.; Gu, L.; Cui, G. RuSe/Reduced Graphene Oxide: An Efficient Electrocatalyst for VO_2^+/VO^{2+} Redox Couples in Vanadium Redox Flow Batteries. *RSC Adv.* **2014**, *4*, 20379–20381.
(105) Xia, L.; Long, T.; Li, W.; Zhong, F.; Ding, M.; Long, Y.; Xu, Z.; Lei, Y.; Guan, Y.; Yuan, D.; et al. Highly Stable Vanadium Redox-Flow Battery Assisted by Redox-Mediated Catalysis. *Small* **2020**, *16* (38), 2003321.
(106) Sun, B.; Skyllas-Kazacds, M. Chemical Modification and Electrochemical Behaviour of Graphite Fibre in Acidic Vanadium Solution. *Electrochim. Acta* **1991**, *36* (3/4), 513–517.
(107) Flox, C.; Rubio-Garcia, J.; Nafria, R.; Zamani, R.; Skoumal, M.; Andreu, T.; Arbiol, J.; Cabot, A.; Morante, J. R. Active Nano-$CuPt_3$ Electrocatalyst Supported on Graphene for Enhancing Reactions at the Cathode in All-Vanadium Redox Flow Batteries. *Carbon*. Elsevier Ltd May 1, 2012, pp 2372–2374.
(108) Li, B.; Gu, M.; Nie, Z.; Wei, X.; Wang, C.; Sprenkle, V.; Wang, W. Nanorod Niobium Oxide as Powerful Catalysts for an All Vanadium Redox Flow Battery. *Nano Lett.* **2014**, *14* (1), 158–165.
(109) Zhou, H.; Shen, Y.; Xi, J.; Qiu, X.; Chen, L. ZrO_2-Nanoparticle-Modified Graphite Felt: Bifunctional Effects on Vanadium Flow Batteries. *ACS Appl. Mater. Interfaces* **2016**, *8* (24), 15369–15378.
(110) Kim, K. J.; Park, M.-S.; Kim, J.-H.; Hwang, U.; Lee, N. J.; Jeong, G.; Kim, Y.-J. Novel Catalytic Effects of Mn_3O_4 for All Vanadium Redox Flow Batteries. *Chem. Commun* **2012**, *48*, 5455–5457.

(111) Yao, C.; Zhang, H.; Liu, T.; Li, X.; Liu, Z. Carbon Paper Coated with Supported Tungsten Trioxide as Novel Electrode for All-Vanadium Flow Battery. *J. Power Sources* **2012**, *218*, 455–461.
(112) Mehboob, S.; Ali, G.; Shin, H. J.; Hwang, J.; Abbas, S.; Chung, K. Y.; Ha, H. Y. Enhancing the Performance of All-Vanadium Redox Flow Batteries by Decorating Carbon Felt Electrodes with SnO_2 Nanoparticles. *Appl. Energy* **2018**, *229*, 910–921.
(113) Zhou, H.; Xi, J.; Li, Z.; Zhang, Z.; Yu, L.; Liu, L.; Qiu, X.; Chen, L. CeO_2 Decorated Graphite Felt as a High- Performance Electrode for Vanadium Redox Flow Batteries. *RSC Adv.* **2014**, *4*, 61912.
(114) Jing, M.; Zhang, X.; Fan, X.; Zhao, L.; Liu, J.; Yan, C. CeO_2 Embedded Electrospun Carbon Nanofibers as the Advanced Electrode with High Effective Surface Area For Vanadium Flow Battery. *Electrochim. Acta* **2016**, *215*, 57–65.
(115) Yun, N.; Jin, J.; Park, O. O.; Bong, K.; Hoon, J. Electrocatalytic Effect of NiO Nanoparticles Evenly Distributed on a Graphite Felt Electrode for Vanadium Redox Flow Batteries. *Electrochim. Acta* **2018**, *278*, 226–235.
(116) Xiang, Y.; Daoud, W. A. Binary $NiCoO_2$-Modified Graphite Felt as an Advanced Positive Electrode for Vanadium Redox Flow Batteries. *J. Mater. Chem. A* **2019**, *7* (10), 5589–5600.
(117) You, D.; Lou, J.; Li, X.; Zhou, Y.; Sun, X.; Wang, X. Investigation of Advanced Catalytic Effect of Co3O4 Nanosheets Modified Carbon Felts as Vanadium Flow Battery Electrodes. *J. Power Sources* **2021**, *494*, 229775.
(118) Fetyan, A.; El-Nagar, G. A.; Derr, I.; Kubella, P.; Dau, H.; Roth, C. A Neodymium Oxide Nanoparticle-Doped Carbon Felt as Promising Electrode for Vanadium Redox Flow Batteries. *Electrochim. Acta* **2018**, *268*, 59–65.
(119) Cao, L.; Skyllas-Kazacos, M.; Wang, D.-W. Modification Based on MoO_3 as Electrocatalysts for High Power Density Vanadium Redox Flow Batteries. *ChemElectroChem* **2017**, *4* (8), 1836–1839.
(120) Jiang, H. R.; Shyy, W.; Ren, Y. X.; Zhang, R. H.; Zhao, T. S. A Room-Temperature Activated Graphite Felt as the Cost-Effective, Highly Active and Stable Electrode for Vanadium Redox Flow Batteries. *Appl. Energy* **2019**, *233–234*, 544–553.
(121) He, Z.; Li, M.; Li, Y.; Zhu, J.; Jiang, Y.; Meng, W.; Zhou, H.; Wang, L.; Dai, L. Flexible Electrospun Carbon Nanofiber Embedded with TiO_2 as Excellent Negative Electrode for Vanadium Redox Flow Battery. *Electrochim. Acta* **2018**, *281*, 601–610.
(122) Tseng, T.-M.; Huang, R.-H.; Huang, C.-Y.; Liu, C.-C.; Hsueh, K.-L.; Shieu, F.-S. Carbon Felt Coated with Titanium Dioxide/Carbon Black Composite as Negative Electrode for Vanadium Redox Flow Battery. *J. Electrochem. Soc.* **2014**, *161* (6), A1132–A1138.
(123) Vázquez-Galván, J.; Flox, C.; Fàbrega, C.; Ventosa, E.; Parra, A.; Andreu, T.; Morante, J. R. Hydrogen-Treated Rutile TiO_2 Shell in Graphite-Core Structure as a Negative Electrode for High-Performance Vanadium Redox Flow Batteries. *ChemSusChem* **2017**, *10* (9), 2089–2098.
(124) Wang, W. H.; Wang, X. D. Investigation of Ir-Modified Carbon Felt as the Positive Electrode of an All-Vanadium Redox Flow Battery. *Electrochim. Acta* **2007**, *52*, 6755–6762.
(125) Xiang, Y.; Daoud, W. A. Cr_2O_3-Modified Graphite Felt as a Novel Positive Electrode for Vanadium Redox Flow Battery. *Electrochim. Acta* **2018**, *290*, 176–184.
(126) Bayeh, A. W.; Kabtamu, D. M.; Chang, Y.-C.; Chen, G.-C.; Chen, H.-Y.; Lin, G.-Y.; Liu, T.-R.; Wondimu, T. H.; Wang, K.-C.; Wang, C.-H. Ta_2O_5 -Nanoparticle-Modified Graphite

Felt As a High-Performance Electrode for a Vanadium Redox Flow Battery. *ACS Sustain. Chem. Eng.* **2018**, *6* (3), 3019–3028.
(127) Wu, X.; Xu, H.; Lu, L.; Zhao, H.; Fu, J.; Shen, Y.; Xu, P.; Dong, Y. PbO_2-Modified Graphite Felt as the Positive Electrode for an All-Vanadium Redox Flow Battery. *J. Power Sources* **2014**, *250*, 274–278.
(128) Fabjan, C.; Garche, J.; Harrer, B.; Jö Rissen, L.; Kolbeck, C.; Philippi, F.; Tomazic, G.; Wagner, F. The Vanadium Redox-Battery: An Efficient Storage Unit for Photovoltaic Systems. *Electrochim. Acta* **2001**, *47* (5), 825–831.
(129) Ghimire, P. C.; Schweiss, R.; Scherer, G. G.; Wai, N.; Lim, T. M.; Bhattarai, A.; Nguyen, T. D.; Yan, Q. Titanium Carbide-Decorated Graphite Felt as High Performance Negative Electrode in Vanadium Redox Flow Batteries. *J. Mater. Chem. A* **2018**, *6* (15), 6625–6632.
(130) Yang, C.; Wang, H.; Lu, S.; Wu, C.; Liu, Y.; Tan, Q.; Liang, D.; Xiang, Y. Titanium Nitride as an Electrocatalyst for V(II)/V(III) Redox Couples in All-Vanadium Redox Flow Batteries. *Electrochim. Acta* **2015**, *182*, 834–840.
(131) Wei, L.; Zhao, T.; Zeng, L.; Zhou, X.; Zeng, Y. Titanium Carbide Nanoparticle-Decorated Electrode Enables Significant Enhancement in Performance of All-Vanadium Redox Flow Batteries. *Energy Technol.* **2016**, *4* (8), 990–996.
(132) Wei, L.; Zhao, T. S.; Zeng, L.; Zeng, Y. K.; Jiang, H. R. Highly Catalytic and Stabilized Titanium Nitride Nanowire Array-Decorated Graphite Felt Electrodes for All Vanadium Redox Flow Batteries. *J. Power Sources* **2017**, *341*, 318–326.
(133) Roznyatovskaya, N.; Noack, J.; Mild, H.; Fühl, M.; Fischer, P.; Pinkwart, K.; Tübke, J.; Skyllas-Kazacos, M. Vanadium Electrolyte for All-Vanadium Redox-Flow Batteries: The Effect of the Counter Ion. *Batteries* **2019**, *5* (1), 13.

Chapter 2 : Electrochemical and Spectroscopy Techniques for Probing Charge Transfer Mechanisms

2.1 Summary

This chapter discusses the approach followed in this dissertation to understand charge transfer mechanism of transition metal ions. **Section 2.2** discusses different types of charge transfer mechanisms. **Section 2.3** discusses spectroscopic techniques used to identify the structure of transition metal ions and **Section 2.4** provides overview of the electrochemical techniques used to measure reaction kinetic parameters. **Section 2.5** discusses the measurement of electrochemically active surface area (ECSA). The ECSA is used to normalize reaction kinetic parameters measured in **Section 2.4**. In each of the section, I also provide the experimental details of techniques used in the various chapters of this dissertation.

2.2 Charge Transfer Mechanisms

Charge transfer (CT) reaction at electrode interfaces involves transfer of electrons from the electrode to the reactant or vice versa. The oxidation state of the transition metal ion reactant is either decreased (reduction) or increased (oxidation) depending on the direction of flow of electrons. The electrochemical potential (E) of the electrode can be used to change the Fermi level of transferable electrons and control the direction of the flow of electrons. If E is more negative than the standard redox potential of the metal ion (E_{eq}), the Fermi level of electrons in the electrode is high enough for transfer to solution causing metal ion reduction and vice versa for oxidation.[1]

CT reaction of transition metal ions can occur either through outer or inner sphere reaction mechanism.[1–3] In an outer sphere CT reaction, electron transfer between the electrode and the metal ion takes place at the plane separated by at least a solvent layer from the electrode which is called the outer Helmholtz plane (OHP). Since there is no direct contact between the metal ion and the electrode, the reactant−electrode interactions are weak. On the contrary, in an inner sphere CT reaction, the ligand of the coordinated metal ion is chemically bound to the electrode surface in the inner Helmholtz plane (IHP) serving as a bridge to form an adsorbed intermediate for electron transfer. Resultantly, the electrode has a huge influence on rate constants of inner sphere CT (several orders of magnitude), as opposed to 3−8 times for outer sphere CT.[3–6] **Scheme 2.1** depicts the outer and inner sphere CT mechanisms of transition metal ions.

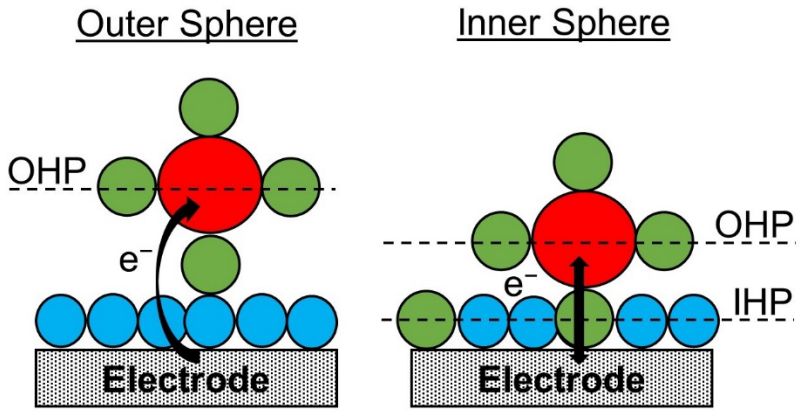

Scheme 2.1. Outer and Inner Sphere Charge Transfer of Transition Metal Ions at Electrodes. The ligand of the transition metal ion is chemically bound to the electrode in inner sphere charge transfer, while there is no direct interaction of the transition metal ion ligand and the electrode in outer sphere charge transfer. Here OHP and IHP are outer and inner Helmholtz plane respectively. Color legend: Red = Transition Metal Ion, Green = Ligand, and Blue = Solvent.

The understanding of CT of transition metal ions in solution phase needs to be translated to the CT at electrode surface. Several generalizable theories have been developed for outer sphere CT showing comparisons between reaction kinetic parameters in solution phase and at electrode surface. The reaction rates for outer sphere CT in both solution and at electrode surface are described well by the energy associated with the reorganization of the solvent molecules and

ligands in the coordination sphere of metal ion. However, these studies emphasize the need to consider the double layer coulombic interactions to obtain reasonable estimates of kinetics for reactions taking at electrode surface.[7–10] On the contrary, there is a lack of any such theory for inner sphere CT that identifies the similarities and accounts for the differences between inner sphere CT in solution phase and at electrode surface to explain the reaction kinetics trends. This lack of a generalizable theory for inner sphere CT arises partially due to the complexity of the reaction mechanism and the difficulty in identifying the structure of formed intermediates.

In this dissertation, to distinguish the CT mechanism of transition metal ions occurring at electrodes, I use V^{2+}/V^{3+} reaction as a probe reaction and identify the structures of reacting ions and evaluate kinetic parameters in different electrolytes and electrodes using techniques discussed in **Section 2.3** and **2.4** respectively. I develop microkinetic models for outer and inner sphere CT. I identify the CT mechanism by looking at the impact of electrolyte and electrode on measured rate constants and comparing the predicted kinetic trends with observed kinetic trends. The microkinetic models are discussed in **Chapters 3, 4, 5,** and **6** and the derivations are included in the **Supporting Information** sections of respective chapters wherever needed. In **Chapter 6**, I propose a unique analogy between inner sphere CT in solution phase and at electrode surface to explain the kinetic trends.

2.3 Techniques to Identify the Structure of Ions in Solution

The transition metal ions are coordinated by either water or complexed with other ligands present in the electrolyte. I use spectroscopic techniques to identify the complexation of vanadium ions in the presence of different anions in various electrolytes as discussed below. The identification of structures of vanadium ions in different electrolytes provide us the information about the reactants and products formed in the reaction.

2.3.1 Ultraviolet-visible Spectroscopy

Ultraviolet-visible (UV-vis) spectroscopy involves exciting an electron from the ground to an excited state by passing a beam of polychromatic ultraviolet and visible radiation through the sample. The intensity of light is measured by a sensor after passing through the sample to estimate absorbance (A), which is related to incident light intensity (I_o) by **eq. 2.1** as follows:

$$A = \log\left(\frac{I_o}{I}\right) \qquad \text{(eq. 2.1)}$$

Here I is the intensity of light after passing through the sample. The energy of the excitation is inversely proportional to the wavelength of light based on Planck's equation.[11]

The degenerate *d* orbitals of transition metal ions are split into various electronic energy states with their splitting dependent on the strength of the electric field created when the ligand approaches the metal ion (i.e., ligand field strength). The number of distinct electronic energy states are dictated by the *d* electron configuration of the metal ion, symmetry of the ligand field, and the relative magnitudes of spin-orbit coupling and interelectron interactions.[2] The peaks in UV-vis spectra of transition metal ions can have different origins: (1) *d-d* transitions in the different electronic energy states of central transition metal ion discussed above that generally give rise to broad peaks in visible region, (2) electronic transitions between the central ion and ligand that lead to intense peaks in ultraviolet region, and (3) electronic transitions in the ligands (mostly observed in organic ligands).[2]

I use the shift in the peak locations of the *d-d* transitions in the different electronic energy states of V^{2+} and V^{3+} to understand the structure of vanadium ions in various electrolytes (H_2SO_4, HCl, $HClO_4$, HBr, and HI) in **Chapters 3** and **4**. The peak locations of these *d-d* transitions are dependent on the magnitude of splitting in the electronic energy states which is controlled by the ligand field strength. The spectrochemical series groups ligands based on their ligand field strength

and shifts in peaks of *d-d* transitions can be qualitatively compared in different electrolytes to understand anion complexation.[2] For instance the ligand field strength of anions used in this dissertation follow the order $SO_4^{2-} > Cl^- > Br^- > I^-$ from the spectrochemical series. Thus, if the vanadium ions complex with these anions, the peak location of *d-d* transitions in vanadium ions will shift the most for SO_4^{2-}, followed by Cl^-, Br^-, and then least for I^-.[2]

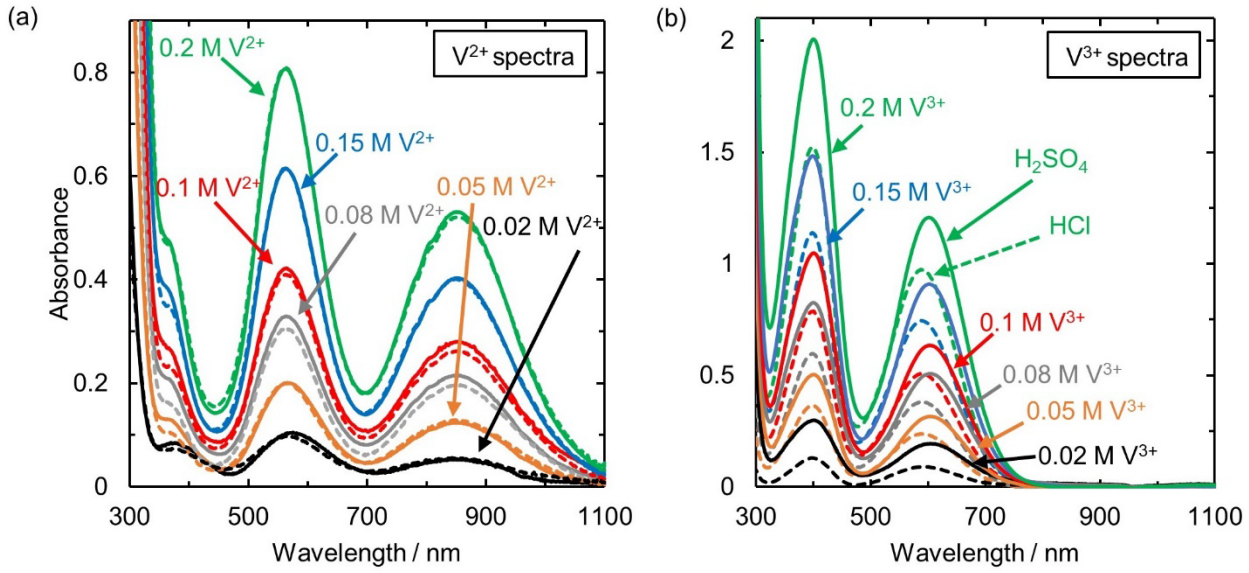

Figure 2.1. UV-vis Spectra of V^{2+} and V^{3+} in H_2SO_4 and HCl at Different Total Vanadium Concentrations. Comparison of UV-vis absorbance as a function of wavelength for various **(a)** V^{2+} and **(b)** V^{3+} concentrations: 0.2 M, 0.15 M, 0.1 M, 0.08 M, 0.05 M and 0.02 M. Solutions are obtained by reducing VCl_3 to V^{2+} and then reoxidizing to V^{3+}. Supporting electrolyte is 0.5 M H_2SO_4 (solid lines) or 1 M HCl (dashed lines) at room temperature (T = 23.3 °C).

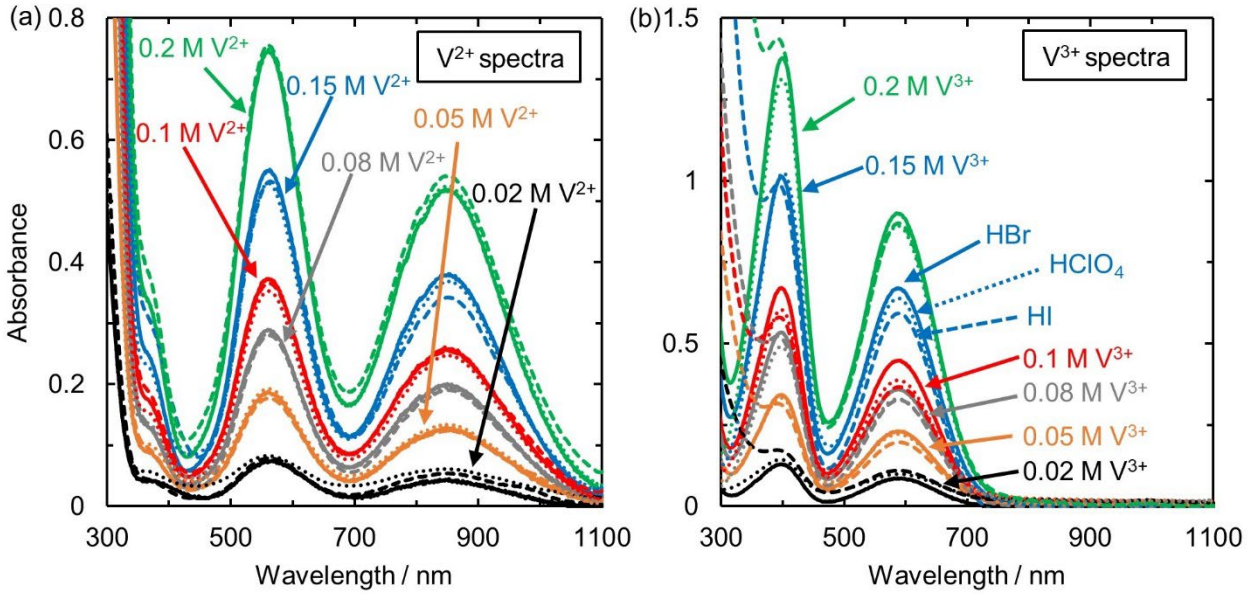

Figure 2.2. UV-vis Spectra of V^{2+} and V^{3+} in HBr, HI, and $HClO_4$ at Different Total Vanadium Concentrations. Comparison of UV-vis absorbance as a function of wavelength for various **(a)** V^{2+} and **(b)** V^{3+} concentrations: 0.2, 0.15, 0.1, 0.08, 0.05, and 0.02 M. Solutions are obtained by reducing V_2O_5 to V^{2+} and then reoxidizing to V^{3+}. Supporting electrolyte is 1 M HBr (solid lines), 1 M HI (dashed lines), or 1 M $HClO_4$ (dotted lines) at room temperature (T = 23.3 °C).

I also use UV-vis spectroscopy to measure concentrations of V^{2+} and V^{3+} ions and confirm the desired states of charge $\left(\mathrm{SoC} = \frac{[V^{2+}]}{[V^{2+}]+[V^{3+}]}\right)$ are reached for kinetic measurements discussed throughout the dissertation. UV-vis spectra are obtained at various known concentrations of V^{2+} and V^{3+} in different electrolytes (**Figures 2.1** and **2.2**). The baseline for each UV-vis spectrum measurement is the supporting electrolyte solution (i.e., solution without vanadium ions) whose contribution is removed to obtain the spectra associated solely with the vanadium complexed species. A quartz cuvette with path length of 1 cm is used. The Curve Fitting feature of MATLAB is used to fit the spectra as a sum of Gaussian functions in the range of 350–1100 nm. The V^{2+} spectrum is fitted as a sum of three Gaussian functions, whereas the V^{3+} spectrum is fitted as a sum of two Gaussian functions to obtain calibration standards at different concentration of V^{2+} and V^{3+} ions. The total absorbance A_{total} is related to the contribution of absorbance from individual

ions ($A_{V^{2+}}/A_{V^{3+}}$).[12] For a mixture of ions, the root-mean-square error in total absorbance is minimized over the wavelengths of interest to approximate the concentrations (**Figure 2.3**).

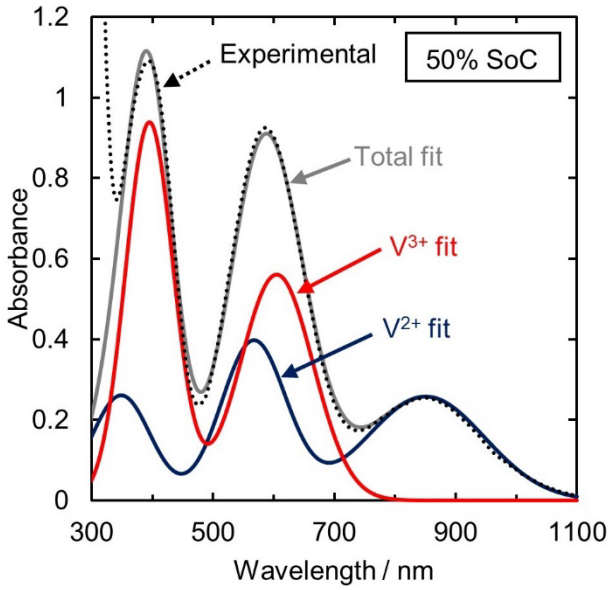

Figure 2.3. Gaussian Fits from the Model Used to Estimate V^{2+} and V^{3+} Concentrations in a Mixture of Vanadium Ions. UV-vis absorbance as a function of wavelength at room temperature (T = 23.3 °C) for an unknown total vanadium ion concentration. Individual concentrations of V^{2+} and V^{3+} are deconvoluted by fitting to Gaussian peaks based on the calibration standards.

2.3.2 X-ray Absorption Fine Structure Spectroscopy

X-ray absorption fine structure (XAFS) spectroscopy involves excitation of the core level electron using x-rays with energy greater than or equal to the electronic binding energy. Due to the absorption of x-ray, a photo-electron is ejected into the continuum, leaving the atom in excited state with a hole at the core level. The excited state decays within a few femtoseconds of absorption via two primary mechanisms, x-ray fluorescence and the Auger effect as shown in **Scheme 2.2**. X-ray fluorescence involves a higher energy core-level electron filling the hole and ejecting a characteristic x-ray. The Auger effect on the other hand involves a higher energy electron filling the hole with a second electron ejected into the continuum.[13]

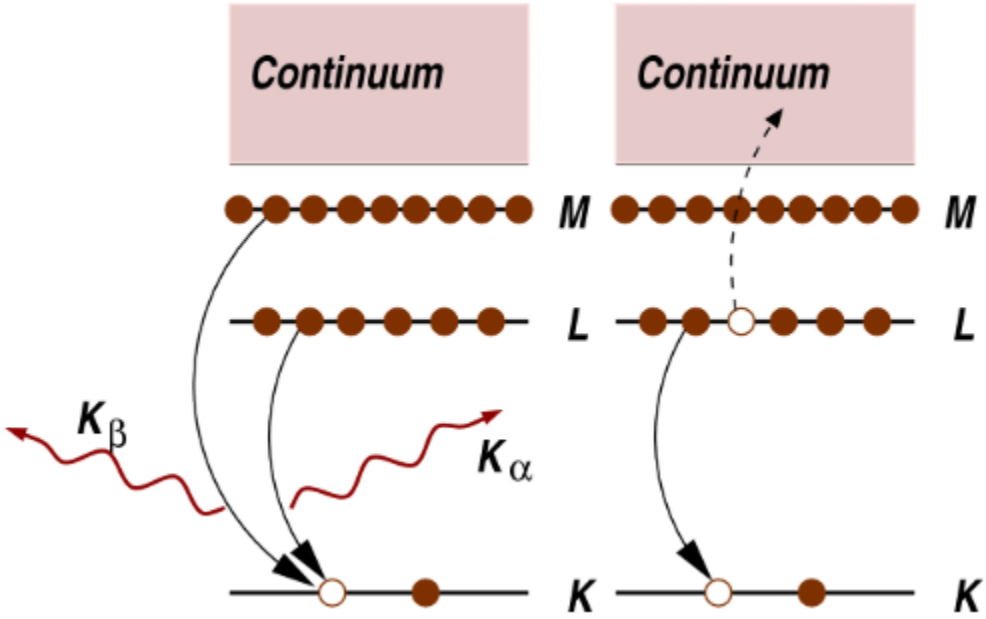

Scheme 2.2. Excited State Decay Mechanisms in XAFS. X-ray fluorescence (left) showing electron in higher energy core level (L or M) filling the hole and releasing characteristic K_α or K_β x-rays and Auger effect (right) showing higher energy core level (L) filling the hole along with ejecting another electron in continuum. The scheme is taken from reference 13.

The characteristic x-ray signals measured using detectors are scattered from the surrounding atoms and can be processed to get XAFS spectrum which contains information regarding the oxidation state, coordination number, bond lengths, and identity of surrounding atoms. XAFS spectrum is divided into near-edge (XANES) and extended (EXAFS) regions. The XANES spectral region extends from about −20 to 50 eV about the absorption edge and the EXAFS region typically extends 1 keV beyond the XANES.[13,14]

In **Chapter 4**, I use EXAFS to identify the structures of V^{2+} and V^{3+} ions in $HClO_4$, H_2SO_4, and HCl with changing anion concentrations under electrochemical conditions. The XAFS measurements are carried out at ambient conditions on a bending magnet beamline (sector 20) at the Advanced Photon Source (APS) facility in Argonne National Lab in fluorescence mode. An electrochemical XAFS cell designed previously is used for the measurements.[15] A circular Nafion 117 membrane (presoaked in water) is used to electrically isolate the working and counter

electrodes and provide a seal between the two cell compartments. A carbon felt (Alfa Aesar) supported on an isomolded graphite rod (1.57 mm outer diameter, Graphtek LLC) is used as the working electrode for large surface areas, while an isomolded graphite rod alone is used as the counter electrode. The liquid compartments for the working and counter electrodes are independently fed with electrolyte from separate syringes using a dual syringe pump at the rate of 0.5 mL min^{-1} (Langer Instruments). The electrolyte in the syringe at the working electrode compartment is the electrochemically prepared V^{2+} or V^{3+} solution in different electrolytes, which is degassed before it is connected to the XAFS cell. The syringe at the counter electrode compartment is supporting electrolyte without any vanadium ions. A leakless Ag/AgCl electrode (Warner Instruments) is used as the reference electrode. At least four scans are collected, which are then averaged to get the final reported XAFS spectra. The potential is maintained at open circuit voltage (OCV) using SP-150 (Biologic Instruments, USA) potentiostat to prevent the change in oxidation state of vanadium ions.

The raw XAFS data is processed using the ATHENA software.[16,17] Because the data collection is in fluorescence mode, absorption coefficient μ(E) is obtained by taking the logarithmic ratio of incident intensity (I_o) and the fluorescence intensity (I_f). The V^{2+} and V^{3+} threshold energy (E_o) is set to 5472 and 5479 eV based on the inflection point in the absorption edge energy spectrum. The μ(E) normalization is done by removing the background by setting a Fourier cutoff of $R_{bkg} = 1$, over a *k*-range from 2.2–12.5 $Å^{-1}$, with specifications of the region of energy where the pre-edge and post-edge starts and ends. More details of ATHENA processing are available elsewhere.[18]

After normalization in ATHENA, the V^{2+} and V^{3+} EXAFS data, is analyzed using the software program ARTEMIS.[16,17] The R range of the fit for V^{2+} and V^{3+} is 1.0 to 4.4 Å. The data

is k^2-weighted and windowed using a Hanning window with $dk = 1$ Å^{-1} in with range of 2.2 to 12.5 Å^{-1}, at the K-edge. The *xyz* coordinates from the density functional theory (DFT) predicted structures of vanadium complexes are used to generate scattering paths using FEFF9 with SCF in JFEFF.[19] The paths for V^{2+} and V^{3+} are selected based on a previous study involving transition metal ions.[20] I included an additional V-S path to consider sulfate complexation in H_2SO_4 and a V-Cl path to take into account the chloride complexation in HCl apart from the paths used for fitting in $HClO_4$. More details regarding ARTEMIS fitting are available elsewhere.[18]

2.4 Techniques to Measure Electrochemical Kinetics

The CT kinetics of transition metal ions are influenced by the electrolyte and electrode as discussed in **Chapter 1**. I use a rotating disk electrode (RDE) setup for conducting V^{2+}/V^{3+} kinetic measurements in different electrolytes and electrodes. An RDE assembly involves a disk of electrode material imbedded in a rod whose rotation is controlled using a rotation control unit.[1] The kinetics parameters are evaluated using steady state current measurements and electrochemical impedance spectroscopy techniques as discussed below.

2.4.1 Steady State Current Measurements

Cyclic voltammetry (CV), which involves cycling in a range of potentials at a specific scan rate, is the most common technique to measure instantaneous oxidation and reduction currents that are used to estimate kinetic parameters. Even though CVs are fast, CVs do not represent true steady state; thus, the extracted kinetic parameters and obtained mechanistic insights from CVs are erroneous and misleading.[21] Consequently, for the work conducted in this dissertation, I use steady state current measurements that involves applying fixed voltages for longer period of times until the currents reach steady state. The duration of the steady state current measurement at a fixed

potential is dependent on the electrode, i.e., I observed steady state is reached within a minute on glassy carbon, while reaching steady state can take anytime up to 90 minutes on metal electrodes.

In **Chapters 3, 4, 5,** and **6**, I evaluate V^{2+}/V^{3+} reaction kinetic parameters using steady state current measurements. Steady state current measurements are conducted between +350 mV and −100 mV overvoltages for different SoC (100, 80, 50, 30, and 10 %) at various rotation rates (ω). The overvoltage (η) is the difference between the applied voltage (E) and the thermodynamic voltage (E_{eq}), **eq. 2.2**.

$$\eta = E - E_{eq} \qquad \text{(eq. 2.2)}$$

These measured steady state currents are normalized by ECSA to obtain steady state current densities (i). The measurement of ECSA of different electrodes is discussed in **Section 2.5**.

The hydrodynamic equations and the convective-diffusion equations have been solved rigorously for steady state for RDEs, allowing deconvolution of the kinetic (i_k) and mass transfer limiting current density (i_l) from steady state current density i.[1] The i_k is dictated by the CT kinetics that controls the kinetic overvoltage (η_{kinetic}), while the i_l is dictated by concentration gradient of active species at the electrode surface and the bulk electrolyte that controls the mass transfer overvoltage (η_{MT}). Hence, i_k (and not total i) should be used to evaluate kinetic parameters. The individual contributions from i_k and i_l are obtained by using Koutecky-Levich analysis (**eq. 2.3**).[1]

$$\frac{1}{i} = \frac{1}{i_k} + \frac{1}{i_l} \qquad \text{(eq. 2.3)}$$

On an RDE, i_l is proportional to $\omega^{1/2}$ (**eq. 2.4**). The intercept of the plot of $1/i$ vs $\omega^{-1/2}$ is used to estimate $1/i_k$.

$$i_l = 0.62nFD_O^{2/3}\omega^{1/2}\nu^{-1/6}C_O^* \quad \text{(eq. 2.4)}$$

Here n is the total number of electrons involved in the reaction, F is the Faraday constant, D_O and C_O^* are the diffusivity and bulk concentration of the oxidant (here V^{3+}) respectively, and ν is the kinematic viscosity. If i is independent of ω, i_l is very large and the measured i is equal to i_k. Therefore, there is no need to conduct steady state measurements at multiple ω.

The kinetic current density, i_k, is evaluated using the above process for the overvoltages between 117–300 mV. The ohmic overvoltage (η_{ohmic}) losses from the total overvoltage are compensated manually during data analysis using the cell resistance measured from electrochemical impedance spectroscopy as discussed in **Section 2.4.2**. In this range of overvoltages, the i is less than 80 % of i_l, which is proposed to be the region where errors in Koutecky-Levich analysis is shown to be minimum.[22] The accuracy of the obtained i_k in this region of overvoltages can be observed by unchanging slopes of $1/i$ vs $\omega^{-1/2}$ plot at different voltages for irreversible reactions.[22]

The Butler-Volmer (BV) equation (**eq. 2.5**) relates i_k from both forward and reverse reactions with the η_{kinetic}. Here I use $\eta = \eta_{\text{kinetic}}$ for simplicity because only i_k (and not total i) is used for analysis:[1]

$$i_k = i_o\left(\frac{C_O(0,t)}{C_O^*}e^{-\frac{n_k\alpha F\eta}{RT}} - \frac{C_R(0,t)}{C_R^*}e^{\frac{n_k(1-\alpha)F\eta}{RT}}\right) \quad \text{(eq. 2.5)}$$

where

$$i_o = nFk^o C_O^{*(1-\alpha)}C_R^{*\alpha} \quad \text{(eq. 2.6)}$$

Here i_o is the exchange current density (in mA cm^{-2}) by state current measurements, $C_O(0,t)$ and $C_R(0,t)$ (and C_O^* and C_R^*) are the concentrations of oxidant and reductant (here V^{2+}) at the electrode

surface (and bulk) respectively, n_k is the total number of electrons involved in the rate determining step (RDS), k^o is the standard rate constant, α is the CT coefficient, R is the universal gas constant (8.314 J/mol K), and T is temperature (in K). The i_o gives an estimate of CT kinetics at the electrode and hence can be used to compare the activity in different electrolytes and electrodes (larger i_o implying a more active electrolyte or electrode).

For large absolute values of η (> 118 mV at 25 °C)[1] with no mass transfer limitations ($C_O(0,t) = C_O^* \; and \; C_R(0,t) = C_R^*$), the BV equation reduces to the Tafel equation (**eq. 2.7**).[23–25]

$$i_k = i_o e^{\eta/b} \qquad \text{(eq. 2.7)}$$

$$\ln(i_k) = \ln(i_o) + \frac{\eta}{b} \qquad \text{(eq. 2.8)}$$

$$b = \frac{2.303\,RT}{n_k \alpha F} \qquad \text{(eq. 2.9)}$$

Here b is the Tafel slope in mV decade^{-1} i.e., mV of kinetic overvoltage needed to change the current by a factor of 10. The Tafel plot is obtained by plotting $\ln|i_k|$ (or $\log|i_k|$) vs η. The slope of the linear region (η > 118 mV) of the Tafel plot yields Tafel slope and the *y*-intercept extrapolated to zero overvoltage is used to estimate i_o. The Tafel plot deviates from linear behavior as η approaches zero because the reverse reaction starts to contribute significantly to i_k and the Tafel approximation is no longer valid.

For V^{2+}/V^{3+} kinetic measurements on glassy carbon in various electrolytes discussed in **Chapters 3** and **4**, I observed that the measured i (and estimated i_o) is independent of ω beyond 1500−2000 rpm (ω_{min}) depending on the electrolyte, indicating no mass transfer limitations and $i = i_k$. Hence, I used $\omega \geq \omega_{min}$ for all studies on glassy carbon. **Figure 2.4** illustrates the case of V^{2+}/V^{3+} kinetic measurements on glassy carbon in HI, where measured i (and i_o in inset) is

independent of $\omega \geq 2000$ rpm. Consequently, the kinetic parameters in HI are estimated using ω of 2000 rpm.

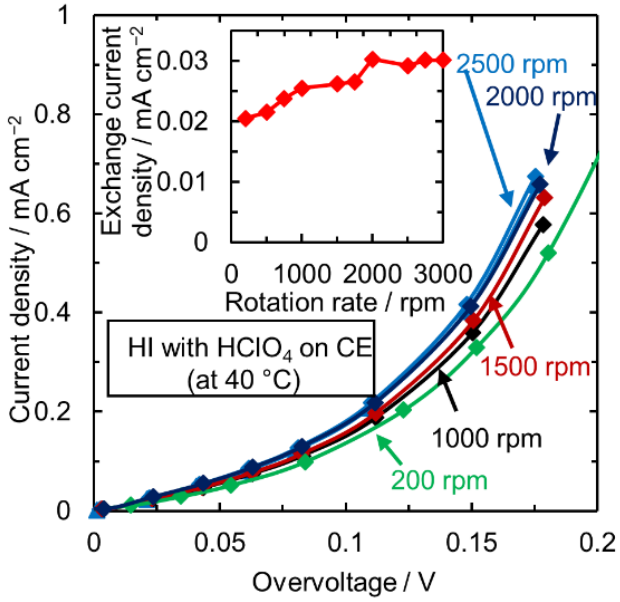

Figure 2.4. Identifying Optimum Rotation Rate for No Mass Transfer Limitations for V^{2+}/V^{3+} Measurements on Glassy Carbon in HI. Current densities vs overvoltage at 80 ± 2% state of charge with glassy carbon at various rotation rates (ω) in HI electrolyte (0.1 M V_2O_5 + 1 M HI) at T = 40 °C. Inset figure shows exchange current densities evaluated by using Tafel equation and y-intercept of extrapolated log of oxidation current densities vs rotation rates. ω is chosen as 2000 rpm for all electrochemical measurements to avoid mass transfer limitations.

For kinetic measurements on edge plane pyrolytic graphite (EPPG) and metal electrodes discussed in **Chapters 5** and **6**, I observed that the steady state current densities are dependent on ω (**Figure 2.5a**). Resultantly, I used Koutecky-Levich analysis to deconvolute contributions of i_k and i_l (**Figure 2.5b**). i_k is then used to construct a Tafel plot to estimate kinetic parameters (**Figure 2.5c**).

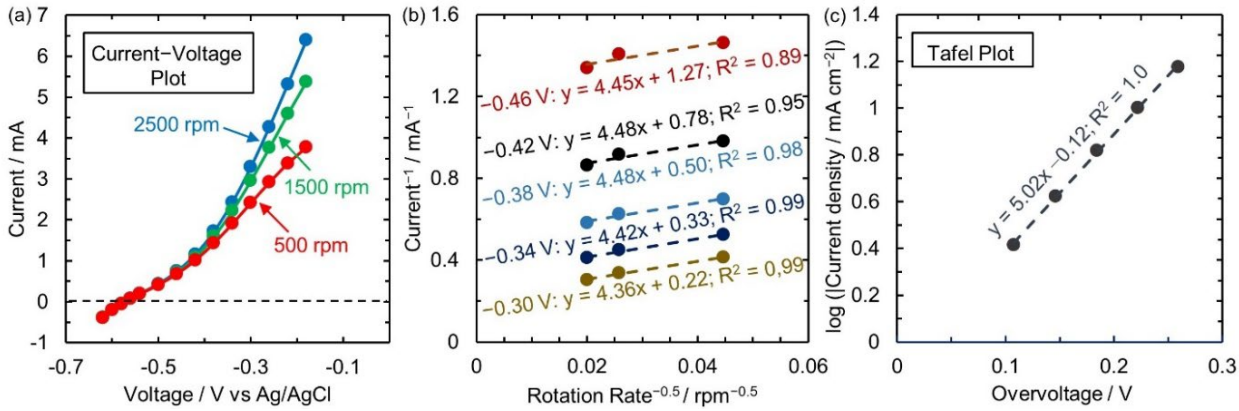

Figure 2.5. Methodology Used to Obtain V^{2+}/V^{3+} Kinetic Parameters on Edge Plane Pyrolytic Graphite and Metal Electrodes. V^{2+}/V^{3+} steady state current measurements taking Ag electrode at a particular state of charge as an example. **(a)** Current vs voltage (V vs Ag/AgCl) plot for at different rotation rates. **(b)** Koutecky-Levich plot at fixed voltages of −0.30, −0.34, −0.38, −0.42, and −0.46 V vs Ag/AgCl, which lie in the overvoltage range between 117–300 mV. The inverse of the intercept is used to estimate kinetic current which is normalized by ECSA to obtain kinetic current density, i_k. **(c)** Log (i_k) vs overvoltage plot between 117–300 mV extrapolated to zero overvoltage to obtain exchange current density from Tafel method (i_o) and Tafel slope (b).

2.4.2 Electrochemical Impedance Spectroscopy

Most electrochemical processes occurring at the electrode surface can be modeled as an electrical circuit containing resistors, capacitors, inductors, etc. based on the physical interpretation of the process. On applying voltage at the electrode, the charged species in the electrolyte are attracted towards the electrode surface forming a double layer which is modeled as a capacitor (C_{dl}). This visible current is not responsible for causing any chemical changes and is referred to as non-Faradaic current. After formation of the double layer, these currents can cause chemical changes, resistance to which is called the CT resistance (R_{ct}). Thus, once the current reaches the electrode surface, it can either go to charging of the double layer or for driving the electrochemical reaction, making C_{dl} and R_{ct} in parallel configuration. The current must pass through the solution, the membrane, and any other components in the path to reach the electrode surface, which offers some resistance (R_s) leading to the ohmic drop. The circuit described for the above electrochemical process involving a single reaction at electrode is the Randles circuit. More complex processes

(e.g., multiple chemical reactions at electrode) will require adding electrical components to modify the Randles circuit to closely resemble the process.

Electrochemical impedance spectroscopy (EIS) is a measurement in frequency domain conducted by applying excitation voltage (generally sinusoidal) of very low amplitude and looking at the impedance response. The impedance (Z) is a measure of the resistance to the flow of electrons and at a given frequency (f) is related to the processes occurring at time scales of $1/f$. For a sinusoidal excitation voltage V with amplitude $\mathrm{V_o}$ given by $\mathrm{V} = \mathrm{V_o}\sin(2\pi ft)$ and a current response shifted by phase ϕ with amplitude I_o given by $I = I_o \sin(2\pi ft + \phi)$, the impedance is $Z = \frac{\mathrm{V_o}\sin(2\pi ft)}{I_o \sin(2\pi ft+\phi)}$. Z can be expressed as a complex function and the real (Z_{real}) and imaginary (Z_{img}) impedance contributions can be deconvoluted. Similarly, the different components used to model the process as electrical circuit in EIS also have Z_{real} and Z_{img} contributions. For instance, a resistor has only real impedance and is equal to its resistance i.e., $Z_{resistor} = Z_{real} = R$. On the other hand, a capacitor (C) has completely imaginary impedance given by $Z_{capacitor} = Z_{img} = 1/2\pi f\mathrm{C}$. For a circuit with R and C in series, the total impedance is $Z_{resistor} + Z_{capacitor}$ with both real and imaginary contributions. The Nyquist plot is obtained by plotting the real vs the imaginary contributions of the measured impedance and is fitted to the impedance obtained from processes modeled as electrical circuits (e.g., Randles circuit) to obtain information of the electrochemical process occurring at the electrode like double layer capacitance, CT kinetics, and solution resistance. EIS has found the most extensive use in fields of corrosion and chemical sensors.

EIS can also be used to estimate kinetic parameters since the current-overvoltage relations are linear at low overvoltages. The BV equation in the region where η approaches zero yields the

CT resistance (R_{ct}), which is a measure of the resistance associated with electron transfer. Under no mass transfer limitations, **eq. 2.5** transforms to:

$$i_k = i_o\left(e^{-\frac{n_k\alpha F\eta}{RT}} - e^{\frac{n_k(1-\alpha)F\eta}{RT}}\right)$$

Using expansion $e^{-x} = 1 - x$ to expand around $\eta = 0$, we get:

$$i_k = i_o\left(1 - \frac{n_k\alpha F\eta}{RT} - 1 - \frac{n_k(1-\alpha)F\eta}{RT}\right)$$

and simplifying:

$$i_k = -i_o\frac{n_k F\eta}{RT}$$

The ratio of η to i_k is the R_{ct} (Ω cm^2), as shown in **eq. 2.10**:

$$R_{ct} = -\frac{\eta}{i_k} = \frac{RT}{n_k F i_o} \qquad (\text{eq. } 2.10)$$

On comparing **eq. 2.6** with **eq. 2.10**, we get an expression of exchange current density from CT resistance method, i.e., $i_{o,R_{ct}}$:

$$i_{o,R_{ct}} = \frac{RT}{n_k F R_{ct} n} \qquad (\text{eq. } 2.11)$$

Thereby, comparing i_o and $i_{o,R_{ct}}$, we can get additional information pertaining to total number of electrons in the reaction.

In **Chapters 3, 4, 5,** and **6**, EIS measurements are conducted at OCV before beginning of steady state current measurement at a particular ω. An overlaid of 10 mV amplitude sine wave is applied within a frequency range of 500 kHz to 100 mHz (with six points per decade). The OCV is equilibrated for 15 seconds before each EIS measurement. R_s is evaluated as the x-intercept in the high frequency region of Nyquist plots. The R_s is the total cell resistance with contributions of resistance from solution, membrane, and electrical connections and allows to account for the η_{ohmic} losses in steady state current measurements discussed above. The Nyquist plots obtained

from EIS measurements are fitted to a modified Randles circuit (**Scheme 2.3**), using Zfit application of EC-Lab Software V11.52. A constant phase element (Q_{CPE}) is used instead of C_{dl}, because Q_{CPE} fits the data points well and mimics real systems more accurately.[26,27] Warburg element for convective diffusion (W_d) is introduced to take into account the mass transfer at low frequencies. The R_{ct} obtained by fitting is used to evaluate $i_{o,R_{ct}}$ (**eq. 2.11**).

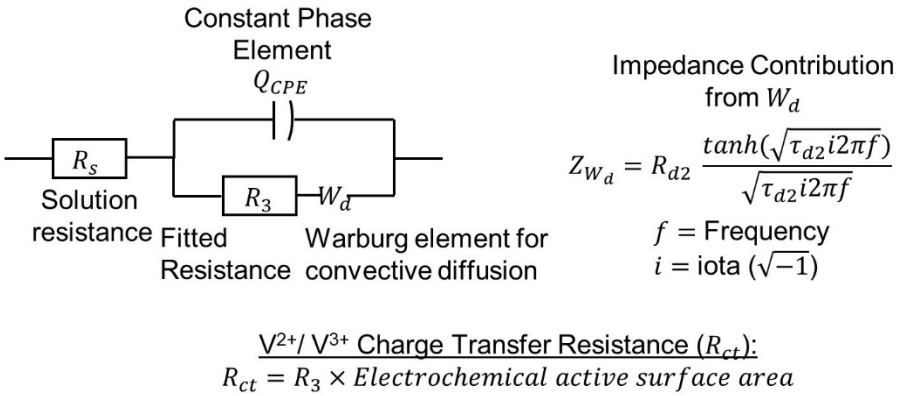

Scheme 2.3. Modified Randles Circuit Used for Fitting Nyquist Plots of All the EIS measurements for V^{2+}/V^{3+} reaction in Different Electrodes and Electrolytes. R_s is the total cell resistance with contributions of resistance from solution, membrane, and electrical connections, Q_{CPE} is the constant phase element, R_{ct} is the charge transfer resistance for V^{2+}/V^{3+} redox reaction obtained by multiplying fitted R_3 with the electrochemically active surface area, and W_d is the Warburg element for convective diffusion to account for the mass transfer at low frequencies. Impedance from W_d (Z_{W_d}) is a function of resistance R_{d2} and time constant τ_{d2}. R_s, Q_{CPE}, R_3, R_{d2}, and τ_{d2} are obtained by the Zfit application of EC-Lab Software V11.18.[28]

i_o and $i_{o,R_{ct}}$ are used to evaluate apparent activation energies by Tafel (E_a) and CT resistance ($E_{a,R_{ct}}$) methods respectively using the Arrhenius relationship given by **eq. 2.12**. The proportionality constant in **eq. 2.12** is the apparent frequency factor.

$$i_o \propto \exp\left(-\frac{E_a}{RT}\right) \qquad (\text{eq. } 2.12)$$

2.5 Measurement of Electrochemically Active Surface Area

The steady state currents and the CT resistance measured from EIS are normalized by ECSA to get intrinsic normalized kinetic parameters (i_o, E_a, and apparent frequency factors). It is imperative to normalize the measured kinetic parameters by ECSA instead of geometric surface area because the exposed surface area available for reaction can be much higher than the geometric

surface area due to electrode roughness, electrocatalysts' shape, size, and stability. The ECSA of the electrodes is measured using either CV capacitance method, underpotential deposition (UPD), or normalizing by currents of hydrogen evolution reaction as discussed below.

2.5.1 Cyclic Voltammetry Capacitance Method

CV capacitance method uses capacitance of the electrochemical double layer to estimate the ECSA. The capacitance is obtained by conducting CVs at various scan rates in the non-Faradaic region to ensure the currents are coming from the formation of the double layer. The charging of the capacitor is given by the **eq. 2.13**:

$$\mathrm{Q} = \mathrm{CV} \qquad (\mathrm{eq.}\,2.13)$$

Here Q is the charge associated with charging of double layer, C is the capacitance, and V is the applied voltage. Taking the derivative of **eq. 2.13** with respect to time yields **eq. 2.14**:

$$\frac{\mathrm{dQ}}{\mathrm{dt}} = \mathrm{C}\frac{\mathrm{dV}}{\mathrm{dt}}$$

$$i = \mathrm{C}\nu \qquad (\mathrm{eq.}\,2.14)$$

Here ν is the scan rate. Thus, the slope of i vs ν can be used to estimate the capacitance. The capacitance is normalized by the specific capacitance ($\mathrm{C_{specific}}$) to estimate the ECSA. One of the major drawbacks of this method to estimate ECSA is choosing the value of $\mathrm{C_{specific}}$ because $\mathrm{C_{specific}}$ is highly dependent on the electrode and the electrolyte.

In **Chapter 5**, CV capacitance method is used to evaluate the ECSA of the EPPG. CVs, 10 cycles each, at different scan rates (10, 20, 50, 80, 100, 150, and 200 mV/s) are conducted in the non-Faradaic region between −0.1 to 0.4 V (vs Ag/AgCl) in 1 M H_2SO_4. The difference in the current at 0.15 V (vs Ag/AgCl) during the increasing and decreasing voltage sweeps from the 10^{th} cycle is plotted against the scan rate. Since the current is the difference between oxidative and reductive sweeps of CV, the slope of the corresponding line passing through the origin is twice the

capacitance corresponding to the electrochemical double layer. Using a $C_{specific}$ of 40 μF cm^{-2} for carbon surfaces in H_2SO_4,[29,30] the ECSA is determined. **Figure 2.6** illustrates the use of CV capacitance method to estimate ECSAs.

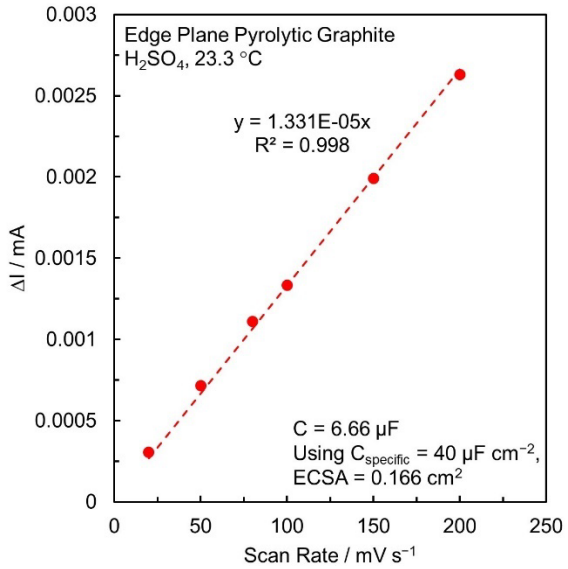

Figure 2.6. ECSA of Edge Plane Pyrolytic Graphite in H_2SO_4 using CV Capacitance Method. Variation of ΔI vs scan rate on EPPG electrode in 1 M H_2SO_4. ΔI is obtained by taking the difference between the currents in the oxidation and reduction sweeps of 10th cycle in CVs in the non-Faradaic region at different scan rates. The slope of ΔI vs scan rate plot is equal to twice the capacitance. The capacitance can be normalized by specific capacitance to estimate ECSA. The measurements are conducted at room temperature (T = 23.3 °C).

For ECSA measurements of EPPG used for kinetic measurements in HCl and HI, I measure the ECSA in 1 M $HClO_4$ instead of 1 M HCl or 1 M HI due to the possibility of specific adsorption of Cl^- and I^- anions, respectively, on electrode surface during cycling and having impact on measured kinetics. Additionally, H_2SO_4 is not used to prevent the introduction of any SO_4^{2-} due to their inhibiting effect on V^{2+}/V^{3+} reaction kinetics as discussed in **Chapter 4**.[23] To consider the change in $C_{specific}$ with change in electrolyte, the ECSA of EPPG is measured in 1 M H_2SO_4, followed by 1 M $HClO_4$, and then again in 1 M H_2SO_4, assuming the same $C_{specific}$. I observe that the ECSAs in 1 M H_2SO_4 initially and after measurements in 1 M $HClO_4$ are within ±2%, indicating that the EPPG surface is unchanged after using it for measurements in 1 M $HClO_4$. Further, on comparing the ECSA in 1 M H_2SO_4 to 1 M $HClO_4$ using the same $C_{specific}$, ECSAs

are observed to be ~15% higher in 1 M $HClO_4$ compared to 1 M H_2SO_4. As a result, to compensate for this effect, the $C_{specific}$ of 46 μF cm^{-2} (~15% higher than in 1 M H_2SO_4) is used to evaluate the ECSA in 1 M $HClO_4$.

2.5.2 Underpotential Deposition

Underpotential Deposition (UPD) is based on the principle that certain metals or species (like H) are reduced on some other metal substrates at a potential less negative than the Nernst potential for the reduction of the metal or species onto itself. This metal or species reduction at a potential less negative than the Nernst potential means that the reduction onto the host metal is more favorable, which allows the formation of a monolayer or submonolayer coverage of the secondary metal or species.[31,32] This deposited monolayer or submonolayer of the secondary metal or species can be stripped off by applying an oxidative potential. The charge associated with stripping the monolayer or submonolayer can be used to estimate ECSA of the host metal assuming the number of monolayers of secondar metal or species and the number of atoms per unit area of host metal are known. One of the most critical aspects of UPD is to identify the potential beyond which bulk deposition occurs, so that only the charge associated with the monolayer or submonolayer is considered for estimating ECSA. In **Chapter 6**, the ECSA of Au electrodes is measured using copper UPD (Cu UPD) and Ag and Cu electrodes by lead UPD (Pb UPD) whose experimental details are discussed below.

2.5.2.1 Gold Electrode ECSA using Copper Underpotential Deposition

The ECSA of the polycrystalline Au electrode is obtained by Cu UPD. Initially, the background current is obtained in 0.1 M sulfuric acid (H_2SO_4, 99.999%, Sigma Aldrich) by holding the potential at 0.1 V vs Ag/AgCl for 1 min (chronoamperometry, CA), followed by conducting linear scan voltammetry (LSV) from 0.1 to 1 V vs Ag/AgCl at 20 mV s^{-1}. The retention

time at 0.1 V is varied from 1–8 min until a stable background LSV (i.e., unchanged with retention time) is obtained. LSVs generally remain unchanged after CA with retention time ≥ 3 min. This stable LSV current is integrated to get the background charge.

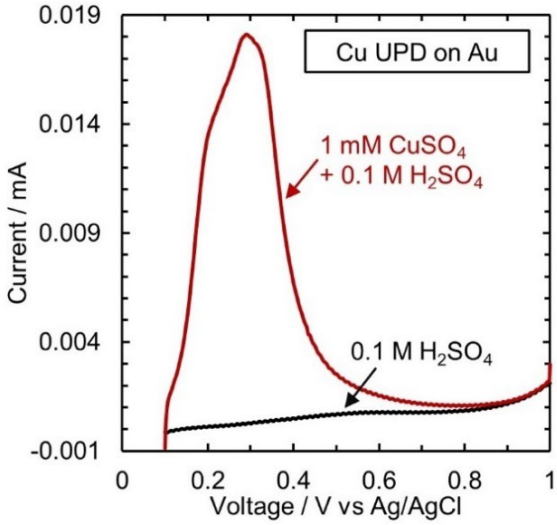

Figure 2.7. Copper Underpotential Deposition on a Gold Electrode. Linear Scan Voltammetry of a polycrystalline Au electrode in 0.1 M H_2SO_4 at 20 mV s^{-1} to obtain the background charge (black line) and after adding 1 mM $CuSO_4$ (red line) to obtain the charge associated with stripping of Cu monolayer between 0.1 to 1.0 V vs Ag/AgCl. The difference in charge associated with Cu compared to the background is attributed to stripping a Cu monolayer on Au and is normalized by the surface charge density of Cu on polycrystalline Au to obtain the ECSA. All measurements are conducted at room temperature (T = 23.3°C).

After obtaining the background charge associated with the Au electrode, 1 mM copper sulfate ($CuSO_4$ anhydrous, ≥ 99.99% trace metals basis, Sigma Aldrich) is added to the solution. CA at 0.1 V vs Ag/AgCl followed by LSV between 0.1–1.0 V vs Ag/AgCl, using the same potential range as the background is conducted with varying retention times (1–8 min), until a LSV that is independent of the retention time is obtained (**Figure 2.7**). I observe that LSVs remain unchanged after CA with retention time ≥ 3 min, indicating a monolayer of Cu has been formed on the surface. The potential of 0.1 V vs Ag/AgCl used for CAs and as the onset point for LSVs is the most reducing potential at which stable LSVs with increasing retention times are obtained indicating that at potentials beyond 0.1 V vs Ag/AgCl, bulk Cu deposition begins to occur. The upper limit of 1.0 V vs Ag/AgCl is decided because the currents from Cu stripping starts to overlay

with the background current (as in 0.1 M H_2SO_4) indicating that all the Cu is stripped from the Au surface. This Au electrode after the measurement of ECSA is taken out from the solution while applying an oxidative potential of 1.0 V vs Ag/AgCl, and then dipped in 0.1 M H_2SO_4 for 10 min to remove any Cu adatoms remaining on the surface. The background charge is subtracted from the oxidative charge obtained from stripping the monolayer of Cu to obtain the charge associated with Cu UPD. This Cu UPD charge is normalized using a surface charge density of 405 μC cm^{-2},[33] associated with Cu monolayer deposition on polycrystalline Au, to obtain the ECSA of the Au electrode.

2.5.2.2 Silver and Copper Electrode ECSA by Lead Underpotential Deposition

The ECSAs of the polycrystalline Ag and the polycrystalline Cu electrodes are obtained by lead underpotential deposition (Pb UPD) following a similar approach used for measuring the ECSA of the Au electrode via Cu UPD. Initially, the background current is obtained in 0.1 M perchloric acid ($HClO_4$, 60%, Fisher Chemical) by conducting CA at −0.34 V for Ag (−0.40 V for Cu) vs Ag/AgCl for 1 min, followed by a LSV from −0.34 to 0.05 V for Ag (−0.40 V to 0 V for Cu) vs Ag/AgCl at 20 mV s^{-1}. The retention time is varied from 1–5 min until a stable background LSV is obtained. This stable LSV is integrated to get the background charge. This process is repeated after adding 5 mM lead perchlorate trihydrate ($Pb(ClO_4)_2.3H_2O$, ACS Reagent, Fisher Scientific) to obtain the charge associated with Pb stripping (**Figure 2.8**). Bulk Pb deposition is observed at potentials below −0.34 V for Ag (−0.40 V for Cu) vs Ag/AgCl, and the background current overlaps with the current from Pb stripping at potentials more oxidative than 0.05 V for Ag (0 V for Cu) vs Ag/AgCl indicating that all Pb is stripped off from the electrode surface. After the measurement of ECSA, the electrode is held at 0.05 V for Ag (0 V for Cu) while removing from solution, and then dipped in 0.1 M $HClO_4$ for 10 min to remove of any Pb adatoms remaining

on the surface. The difference between the oxidative charge obtained from Pb stripping and the background charge is normalized using surface charge density of 280 μC cm^{-2} (302 μC cm^{-2} for Cu), associated with Pb sub monolayer on polycrystalline Ag[35–38] (or Cu),[39–41] to obtain ECSA of Ag (or Cu) electrode.

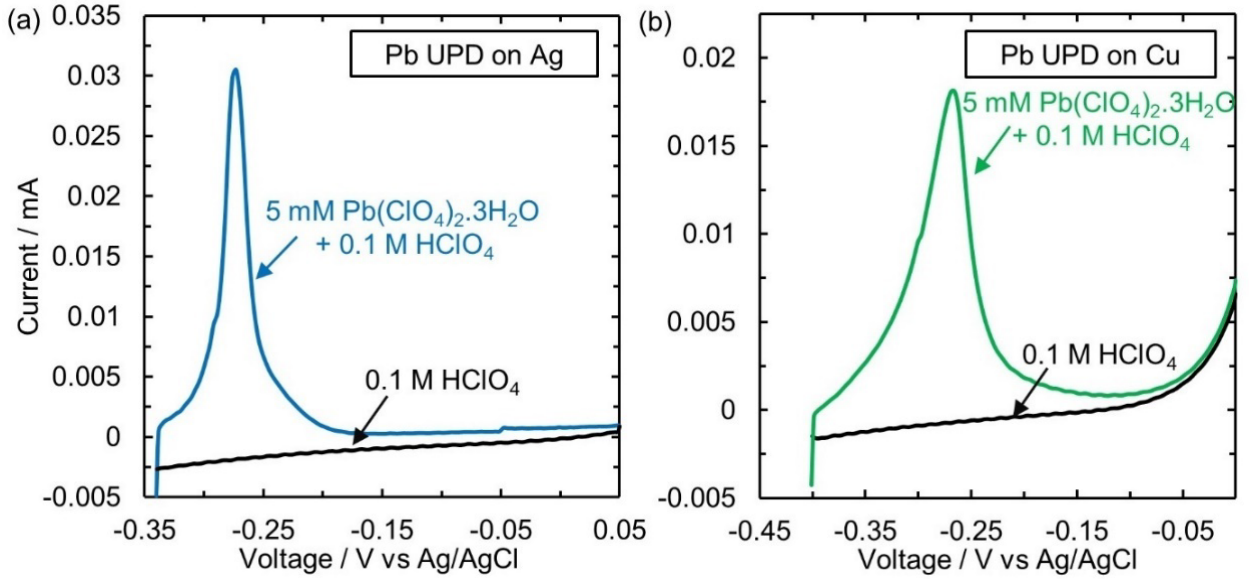

Figure 2.8. Lead Underpotential Deposition on a Silver and Copper Electrode. Linear Scan Voltammetry of polycrystalline **(a)** Ag electrode and **(b)** Cu electrode in 0.1 M $HClO_4$ at 20 mV s^{-1} to obtain the background charge (black lines) and after adding 5 mM $Pb(ClO_4)_2.3H_2O$ (blue and green lines) to obtain the charge associated with stripping of a Pb sub-monolayer. The difference in charge associated with background from Pb stripping is normalized by the surface charge density of Pb on polycrystalline Ag or Cu to obtain the ECSA. All measurements are conducted at room temperature ($T = 23.3$°C).

2.5.3 Hydrogen Evolution Reaction Currents

ECSA measurement by hydrogen evolution reaction (HER) currents involves measuring the HER currents at a fixed potential on desired electrodes and comparing to the HER currents on atomically smooth electrodes (roughness factor of one) of different sizes at the same potential. The ECSA of polycrystalline Bi and W could not be measured using Pb or Cu UPD. Resultantly, I use HER activity to measure the ECSA of Bi and W electrodes as discussed below.

2.5.3.1 Bismuth Electrode ECSA by Normalizing to Hydrogen Evolution Currents on Smooth Bismuth Films

The atomically smooth polycrystalline Bi films are prepared by electron beam evaporating 300 nm of Bi on Si wafers. A stack of Ni-Cr alloy (20 nm thick) followed by Au (50 nm thick) is used as a seed layer for depositing Bi films.[42] The films are characterized by Atomic Force Microscopy to verify that films have roughness factor close to one. The Si wafers with deposited Bi is diced using a diamond cutter, and a prepared electrode is shown in **Figure 2.9a**. The exposed geometric area of the electrode is controlled by covering the electrode with an electrochemically inert tape with a circular opening made by a hole punch of different desired sizes.[43] HER current of electrodes with different geometric area (**Figure 2.9c**) is measured by conducting steady state measurements at −0.55 V vs. RHE in 1 M H_2SO_4 to identify how the HER current of Bi varies with geometric area. The potentials are compensated 85% internally for solution resistance during the measurement. The potential loss due to 15% of the remaining solution resistance is < 2 mV and is not accounted for. The solution is continuously stirred at 800 rpm to ensure there are no mass transfer limitations (**Figure 2.9b**). The HER current of a Bi rotating disk electrode with unknown surface roughness is measured at −0.55 V vs. RHE in 1 M H_2SO_4 at 2500 rpm (using RDE setup) and the relationship obtained in **Figure 2.9c** is used to obtain the ECSA.

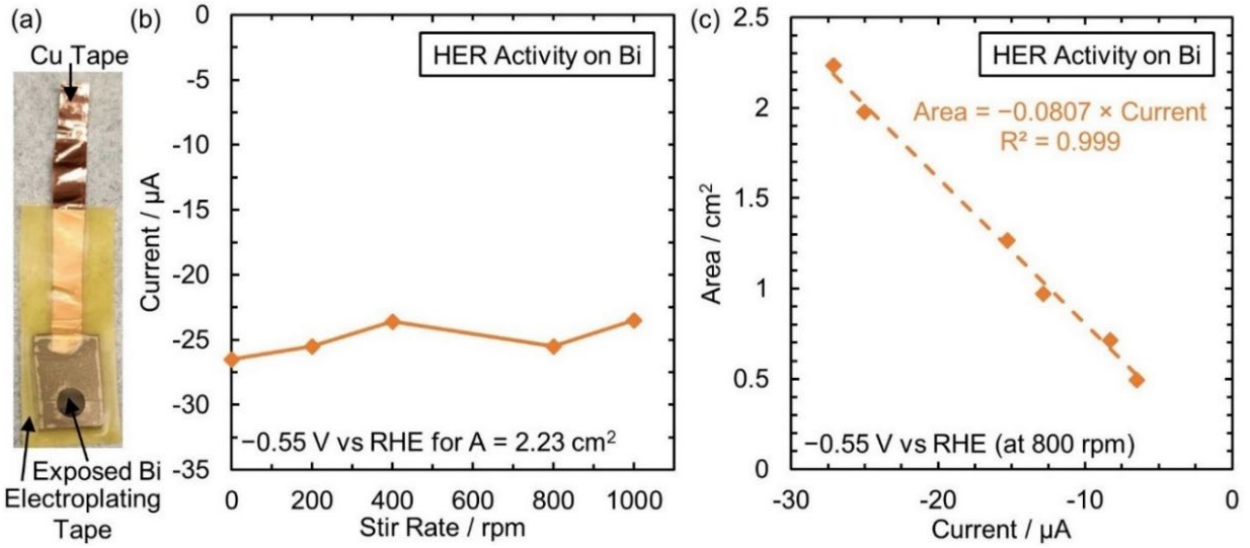

Figure 2.9. HER Calibration to Obtain ECSA of Bismuth Electrodes. (a) Electrodes prepared from Bi deposited on Si wafer used to measure the hydrogen evolution reaction (HER) current. **(b)** Currents for the largest geometric area electrode (area = 2.23 cm^2) at different stir rates to identify the optimal stir rate at which there are no mass transport limitations. **(c)** Currents due to HER on Bi electrodes with different geometric sizes at the chosen potential of −0.55 V vs RHE in 1 M H_2SO_4 with a stir rate of 800 rpm. All measurements are conducted at room temperature (T = 23.3°C).

2.5.3.2 Tungsten Electrode ECSA by Normalizing to Hydrogen Evolution Currents on Smooth Tungsten Films

The atomically smooth polycrystalline W films are formed by sputtering 300 nm of W on Si wafers. Ti (30 nm thick) is used as a seed layer for depositing W films. The roughness factor of W films is evaluated using AFM and is close to one. Electrodes of smooth W films with different geometric area are prepared and steady state currents due to HER at −0.2 V vs RHE are measured to identify how the HER currents varies with surface area (**Figure 2.10b**). The solution is continuously stirred at 750 rpm to eliminate mass transfer limitations (**Figure 2.10a**). The HER currents on W disk electrode of unknown roughness are measured at −0.2 V vs RHE, which is used to obtain ECSA using the relationship obtained in **Figure 2.10b**.

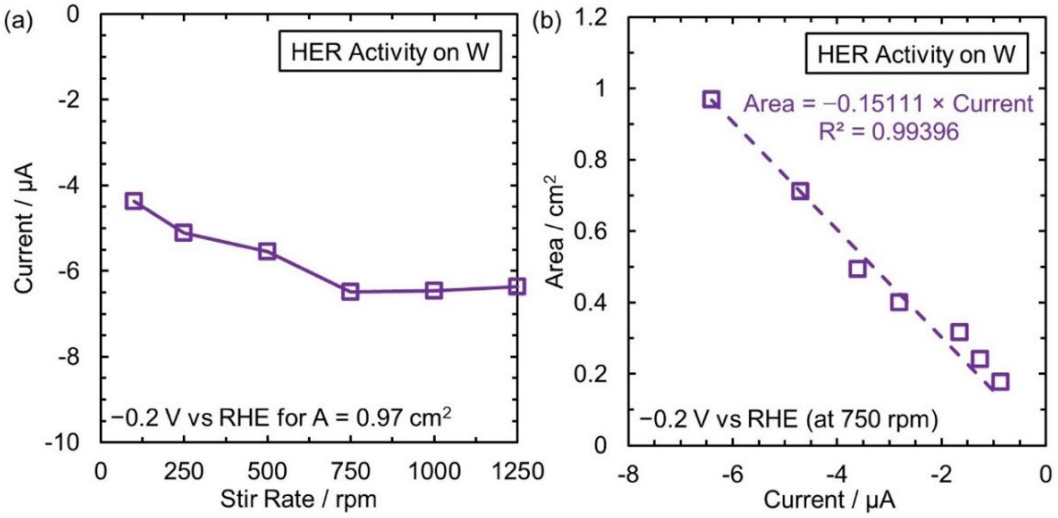

Figure 2.10. HER Calibration to Obtain ECSA of Tungsten Electrodes. (a) Current for the largest geometric area electrode (area = 0.97 cm^2) at different stir rates to identify the optimal stir rate at which there are no mass transport limitations in 1 M H_2SO_4. **(b)** Current attributed to HER on W electrodes with different geometric sizes at −0.2 V vs RHE in 1 M H_2SO_4 with a stir rate of 750 rpm. All measurements are conducted at room temperature (T = 23.3°C).

2.6 References

(1) Bard, A. J.; Faulkner, L. R. *Electrochemical Methods: Fundamentals and Applications*; John Wiley & Sons, Inc.: New York, 2001.

(2) Ribas Gispert, J. *Coordination Chemistry*, 1st ed.; Wiley-VCH: Weinheim, Germany, 2008.

(3) Tanimoto, S.; Ichimura, A. Discrimination of Inner and Outer Sphere Electrode Reactions by Cyclic Voltammetry Experiments. *J. Chem. Educ.* **2013**, *90* (6), 778–781.

(4) Kuhn, A. T.; Randle, T. H. Effect of Oxide Thickness on the Rates of Some Redox Reactions on a Platinum Electrode. *J. Chem. Soc., Faraday Trans. I* **1985**, *81*, 403–419.

(5) Iwasita, T.; Schmickler, W.; Schultze, J. W. The Influence of the Metal on the Kinetics of Outer Sphere Redox Reactions. *Ber. Bunsenges. Phys. Chem.* **1985**, *89* (2), 138–142.

(6) Velmurugan, J.; Sun, P.; Mirkin, M. V. Scanning Electrochemical Microscopy with Gold Nanotips: The Effect of Electrode Material on Electron Transfer Rates. *J. Phys. Chem. C* **2009**, *113*, 459–464.

(7) Weaver, M. J. Correlations between Electrochemical and Homogeneous Redox Reactivity. Quantitative Comparisons of Rate Constants and Activation Parameters for Some Inorganic Outer-Sphere Reactions. *J. Phys. Chem* **1980**, *84*, 568–576.

(8) Parsons, R. The Effect of Specific Adsorption on the Rate of an Electrode Process. *J. Electroanal. Chem. Interfacial Electrochem.* **1969**, *21* (1), 35–43.

(9) Henstridge, M. C.; Batchelor-Mcauley, C.; Gusmão, R.; Compton, R. G. Marcus-Hush-Chidsey Theory of Electron Transfer to and from Species Bound at a Non-Uniform Electrode Surface: Theory and Experiment. *Chem. Phys. Lett.* **2011**, *517*, 108–112.

(10) Laborda, E.; Henstridge, M. C.; Batchelor-Mcauley, C.; Compton, R. G. Asymmetric Marcus-Hush Theory for Voltammetry. *Chem. Soc. Rev* **2013**, *42*, 4905.

(11) Perkampus, H.-H. *UV-VIS Spectroscopy and Its Applications*; Springer Berlin Heidelberg, 1992.

(12) Skoog, D. A.; West, D. M.; Holler, F. J.; Crouch, S. R. *Fundamentals of Analytical Chemistry*, 9th ed.; Brooks/Cole: Belmont, 2013.

(13) Newville, M. Fundamentals of XAFS. *Rev. Mineral. Geochemistry* **2014**, *78*, 33–74.
(14) Ravel, B. Quantitative EXAFS Analysis. In *X-Ray Absorption and X-Ray Emission Spectroscopy: Theory and Applications*; Van Bokhoven, J. A., Lamberti, C., Eds.; John Wiley & Sons Ltd.: Chichester, UK, 2016; pp 281–302.
(15) Singh, N.; Nguyen, M.-T.; Cantu, D. C.; Mehdi, B. L.; Browning, N. D.; Fulton, J. L.; Zheng, J.; Balasubramanian, M.; Gutiérrez, O. Y.; Glezakou, V.-A.; et al. Carbon-Supported Pt during Aqueous Phenol Hydrogenation With and Without Applied Electrical Potential: X-Ray Absorption and Theoretical Studies of Structure and Adsorbates. *J. Catal.* **2018**, *368*, 8–19.
(16) Newville, M. IFEFFIT: Interactive XAFS Analysis and FEFF Fitting. *J. Synchrotron Radiat.* **2001**, *8*, 322–324.
(17) Ravel, B.; Newville, M. ATHENA, ARTEMIS, HEPHAESTUS: Data Analysis for X-Ray Absorption Spectroscopy Using IFEFFIT. *J. Synchrotron Rad* **2005**, *12*, 537–541.
(18) Agarwal, H.; Florian, J.; Goldsmith, B. R.; Singh, N. The Effect of Anion Bridging on Heterogeneous Charge Transfer for V^{2+}/V^{3+}. *Cell Reports Phys. Sci.* **2021**, *2* (1), 100307.
(19) Rehr, J. J.; Kas, J. J.; Vila, F. D.; Prange, M. P.; Jorissen, K. Parameter-Free Calculations of X-Ray Spectra with FEFF9. *Phys. Chem. Chem. Phys.* **2010**, *12*, 5503–5513.
(20) Fulton, J. L.; Bylaska, E. J.; Bogatko, S.; Balasubramanian, M.; Cauët, E.; Schenter, G. K.; Weare, J. H. Near-Quantitative Agreement of Model-Free DFT-MD Predictions with XAFS Observations of the Hydration Structure of Highly Charged Transition-Metal Ions. *J. Phys. Chem. Lett* **2012**, *3*, 2588–2593.
(21) Anantharaj, S.; Noda, S.; Driess, M.; Menezes, P. The Pitfalls of Using Potentiodynamic Polarization Curves for Tafel Analysis in Electrocatalytic Water Splitting . *ACS Energy Lett.* **2021**, *6*, 1607–1611.
(22) Wang, H.; Sayed, Y. S.; Luber, E. J.; Olsen, B. C.; Shirurkar, S. M.; Venkatakrishnan, S.; Tefashe, U. M.; Farquhar, A. K.; Smotkin, E. S.; McCreery, R. L.; et al. Redox Flow Batteries: How to Determine Electrochemical Kinetic Parameters. *ACS Nano* **2020**, *14*, 2575–2584.
(23) Guidelli, R.; Compton, R. G.; Feliu, J. M.; Gileadi, E.; Lipkowski, J.; Schmickler, W.; Trasatti, S. Defining the Transfer Coefficient in Electrochemistry: An Assessment (IUPAC Technical Report). *Pure Appl. Chem.* **2014**, *86* (2), 245–258.
(24) Talivaldis, B.; Delahay, P. Theory of Irreversible Polarographic Waves-Case of Two Consecutive Electrochemical Reactions. *J. Am. Chem. Soc.* **1953**, *75* (22), 5716–5720.
(25) Song, C.; Zhang, J. Electrocatalytic Oxygen Reduction Reaction. In *PEM Fuel Cell Electrocatalysts and Catalyst Layers*; Springer London: London, 2008; pp 89–134.
(26) Brug, G. J.; van den Eeden, A. L. G.; Sluyters-Rehbach, M.; Sluyters, J. H. The Analysis of Electrode Impedances Complicated By the Presence of a Constant Phase Element. *J. Electroanal. Chem. Interfacial Electrochem.* **1984**, *176* (1–2), 275–295.
(27) Hsu, C. H.; Mansfeld, F. Technical Note: Concerning the Conversion of the Constant Phase Element Parameter Y_0 into a Capacitance. *Corros. Sci. Sect.* **2001**, *57* (9), 747–748.
(28) *EC-Lab Software User's Manual*; 10.38, Ed.; BioLogic Science Instruments, 2014.
(29) Randin, J. P.; Yeager, E. Differential Capacitance Study on the Edge Orientation of Pyrolytic Graphite and Glassy Carbon Electrodes. *J. Electroanal. Chem.* **1975**, *58* (2), 313–322.
(30) Iamprasertkun, P.; Hirunpinyopas, W.; Keerthi, A.; Wang, B.; Radha, B.; Bissett, M. A.; Dryfe, R. A. W. Capacitance of Basal Plane and Edge-Oriented Highly Ordered Pyrolytic

Graphite: Specific Ion Effects. *J. Phys. Chem. Lett.* **2019**, *10*, 617–623.
(31) Herrero, E.; Buller, L. J.; Abruña, H. D. Underpotential Deposition at Single Crystal Surfaces of Au, Pt, Ag and Other Materials. *Chem. Rev.* **2001**, *101* (7), 1897–1930.
(32) Wang, C. J.; Shapiro, E. F.; Personick, M. L. Halide Ions on Metal Nanoparticles for Shape- and Composition-Controlled Synthesis. In *Reference Module in Materials Science and Materials Engineering*; Elsevier, 2022.
(33) Santos, M. C.; Mascaro, L. H.; Machado, S. A. S. Voltammetric and Rotating Ring-Disk Studies of Underpotential Deposition of Ag and Cu on Polycrystalline Au Electrodes in Aqueous H_2SO_4. *Electrochim. Acta* **1998**, *43*, 2263–2272.
(34) Hachiya, T.; Honbo, H.; Itaya, K. Detailed Underpotential Deposition of Copper on Gold(111) in Aqueous Solutions. *J. Electroanal. Chem.* **1991**, *315*, 275–291.
(35) Cleve, T. Van; Gibara, E.; Linic, S. Electrochemical Oxygen Reduction Reaction on Ag Nanoparticles of Different Shapes. *ChemCatChem* **2016**, *8*, 256–261.
(36) Kirowa-Eisner, E.; Bonfil, Y.; Tzur, D.; Gileadi, E. Thermodynamics and Kinetics of UPD of Lead on Polycrystalline Silver and Gold. *J. Electroanal. Chem.* **2003**, *552*, 171–183.
(37) Vitanov, T.; Popov, A.; Staikov, G.; Budevski, E.; Lorenz, W. J.; Schmidt, E. Slow Transformation Phenomena of Lead Adsorbates on Electrolytically Grown Ag(111) and Ag(100) Electrode Surfaces. *Electrochim. Acta* **1986**, *31*, 981–989.
(38) Bort, H.; Juttner, K.; Lorenz, W. J.; Schmidt, E. Lead Adsorption on Silver Single Crystal Surfaces. *J. Electroanal. Chem* **1978**, *90*, 413–424.
(39) Siegenthaler, H.; Juttner, K. Voltammetric Investigation of Lead Adsorption on Cu(111) Single Crystal Substrates. *J. Electroanal. Chem.* **1984**, *163*, 327–343.
(40) Brisard, G. M.; Zenati, E.; Gasteiger, H. A.; Marković, N. M.; Ross, P. N. Underpotential Deposition of Lead on Cu(100) in the Presence of Chloride: Ex-Situ Low-Energy Electron Diffraction, Auger Electron Spectroscopy, and Electrochemical Studies. *Langmuir* **1997**, *13*, 2390–2397.
(41) Brisard, G. M.; Zenati, E.; Gasteiger, H. A.; Marković, N. M.; Ross, P. N. Underpotential Deposition of Lead on Copper (111): A Study Using a Single-Crystal Rotating Ring Disk Electrode and Ex Situ Low-Energy Electron Diffraction and Auger Electron Spectroscopy. *Langmuir* **1995**, *11*, 2221–2230.
(42) Gades, L. M.; Cecil, T. W.; Divan, R.; Schmidt, D. R.; Ullom, J. N.; Madden, T. J.; Yan, D.; Miceli, A. Development of Thick Electroplated Bismuth Absorbers for Large Collection Area Hard X-Ray Transition Edge Sensors. *IEEE Trans. Appl. Supercond.* **2017**, *27* (4), 2101105.
(43) 3M™ Electroplating/Anodizing Tape 484 | 3M United States https://www.3m.com/3M/en_US/p/d/b40074778/ (accessed Feb 20, 2022).

Chapter 3 : V^{2+}/V^{3+} Reaction Kinetics on Glassy Carbon in Sulfuric, Hydrochloric, and Mixed Acid Electrolytes for Vanadium Redox Flow Batteries*

* This chapter is adapted with permission from Agarwal, H.; Florian, J.; R. Goldsmith, B.; Singh, N. V^{2+}/V^{3+} Redox Kinetics on Glassy Carbon in Acidic Electrolytes for Vanadium Redox Flow Batteries. *ACS Energy Lett.* **2019**, *4*, 2368–2377. The computational portion of the work is conducted by Jacob Florian.

3.1 Summary

In this chapter, we elucidate the impact of anion complexation on V^{2+}/V^{3+} kinetics on a glassy carbon electrode in three common electrolytes: hydrochloric acid, sulfuric acid, and mixed HCl/H_2SO_4. The V^{2+}/V^{3+} kinetics are ~2.5 times faster in HCl and have lower apparent activation energies than in H_2SO_4 or HCl/H_2SO_4. We also identify the presence of $[V(H_2O)_4Cl_2]^+$ species in HCl by UV-vis spectroscopy. We confirm the V^{2+}/V^{3+} reaction proceeds via an adsorbed intermediate and propose a bridging mechanism through adsorbed *Cl (in HCl) and *OH (in H_2SO_4 or HCl/H_2SO_4). A bridging mechanism through *Cl is supported by even faster redox kinetics in HBr than HCl, possibly due to the higher polarizability of *Br. By measuring the exchange current densities using steady state current measurements and impedance spectroscopy, we show that the overall reaction is a two-electron process in HCl as opposed to a one-electron process in H_2SO_4 and HCl/H_2SO_4.

3.2 Introduction

Despite vanadium redox flow batteries (VRFBs) being the most well-developed redox flow battery and closest to commercial implementation for large-scale energy storage, there is a lack of fundamental understanding of V^{2+}/V^{3+} redox couple chemistry, particularly the role of electrolyte on the redox couple and the associated charge transfer (CT). VRFBs with carbon electrodes employing HCl[1–3] or mixed acid electrolytes (i.e., HCl/H_2SO_4)[4–6] have higher current densities and greater vanadium ion stability compared with the traditionally used H_2SO_4 electrolyte. The structure of the vanadium ion complexes in these electrolytes is not well understood and it is unclear if the improved current densities are related to kinetics (as opposed to mass transport or conductivity). The V^{2+} and V^{3+} ions in pure water or in non-complexing electrolytes such as perchloric acid exist as $[V(H_2O)_6]^{2+}$ and $[V(H_2O)_6]^{3+}$ respectively, with each of the six water molecules located at the ends of an octahedron (O_h symmetry) constituting the first coordination sphere around the vanadium ion.[7,8] In certain acidic electrolytes (e.g., HCl, H_2SO_4, and H_3PO_4), anions can replace water molecules in the first coordination sphere of V^{2+} and V^{3+} as shown in previous studies.[9–13] Because the choice of electrocatalyst has been shown qualitatively to impact the V^{2+}/V^{3+} kinetics,[14–19] the V^{2+}/V^{3+} reaction has been postulated to involve inner sphere CT. However, further quantitative work is needed to confirm whether the CT is inner or outer sphere, and to understand the structure of the vanadium complexes in acidic electrolytes used in VRFBs. Here we show new evidence that the V^{2+}/V^{3+} reaction involves inner sphere CT and link the kinetics of the V^{2+}/V^{3+} reaction on a carbon electrode with the vanadium complex structure in three commonly used electrolytes—hydrochloric acid, sulfuric acid, and mixed HCl/H_2SO_4.

In this chapter, we identify the V^{2+} and V^{3+} complexes using UV-vis and examine V^{2+}/V^{3+} redox kinetics on a glassy carbon electrode. The V^{2+}/V^{3+} redox kinetics are enhanced in HCl

compared with H_2SO_4 or HCl/H_2SO_4 mixtures, based on our higher measured exchange current densities (i_o) and lower apparent activation energies (E_a) from both steady state current measurements and electrochemical impedance spectroscopy. These rates and activation energies depend on the V^{2+} and V^{3+} concentrations, with a negative order in V^{3+} that supports the hypothesis of an inner sphere, adsorption-mediated step in all electrolytes. From experimental UV-vis studies, we confirm that V^{2+} exists as $[V(H_2O)_6]^{2+}$ in all electrolytes, with no anions in the first coordination shell. Our experimental and computational UV-vis measurements show that V^{3+} exists as a distribution of complexes, with a majority of water/sulfate-complexed species, $[V(H_2O)_5SO_4]^+$, and a minority of water-complexed species, $[V(H_2O)_6]^{3+}$, in both H_2SO_4 and HCl/H_2SO_4. In HCl, V^{3+} exists as a majority of water-complexed species, $[V(H_2O)_6]^{3+}$, and a minority of water/chloride-complexed species, $[V(H_2O)_4Cl_2]^+$. We propose that the enhanced V^{2+}/V^{3+} kinetics in HCl compared with H_2SO_4 and HCl/H_2SO_4 are due to the CT proceeding through chloride bridges (*Cl) on the glassy carbon surface in HCl, instead of through surface-bound hydroxyl (*OH) groups[20,21] in H_2SO_4 and HCl/H_2SO_4. This hypothesis of CT through bridges is supported by the faster V^{2+}/V^{3+} redox kinetics we measure in HBr compared with HCl. This enhancement is expected for a bridging mechanism due to the greater deformability of the bromide (*Br) bridges than *Cl bridges,[22] which accelerates the CT between the adsorbed species and the electrode through the bridge.

3.3 Results and Discussions

The redox kinetics of V^{2+}/V^{3+} are examined in three electrolytes: "HCl" (0.2 M VCl_3 + 1 M HCl), "H_2SO_4" (0.2 M $VOSO_4$ + 0.5 M H_2SO_4) and "HCl/H_2SO_4" (0.2 M VCl_3 + 0.5 M H_2SO_4) to analyze how different anions (Cl^- and SO_4^{2-}) impact the kinetics of the V^{2+}/V^{3+} redox couple on a glassy carbon surface. Either VCl_3 or $VOSO_4$ is used to avoid the presence of any sulfate or

chloride anions in the HCl and H_2SO_4 electrolyte, respectively. We also study the kinetics in HBr to test the bridging mechanism hypothesis proposed in this work. Electrolytes in non-complexing perchloric acid ($HClO_4$) are prepared to serve as standards for UV-vis measurements. The State of Charge $\left(\mathrm{SoC} = \frac{[V^{2+}]}{[V^{2+}]+[V^{3+}]}\right)$ is controlled by electrochemically oxidizing or reducing the working electrolyte. V^{2+} and V^{3+} concentrations are confirmed using UV-vis spectroscopy by fitting Gaussian peaks to calibration standards as discussed in **Chapter 2**. The details of preparing these electrolytes are discussed in the Supporting Information (SI). Time dependent density functional theory (TDDFT) is used to predict UV-vis spectra of different V^{3+} complexes. All TDDFT methodology details are available in the SI. A glassy carbon electrode is selected for kinetic measurements because of its high conductivity and controlled electrochemical surface area as compared with traditionally used porous graphite felts, which suffer from large ohmic resistances.[23,24] The glassy carbon disk electrode is polished with a 0.05 μm alumina slurry followed by sonication in deionized water before each electrochemical experiment. Consistent kinetic parameters from multiple runs confirm the reproducibility of this cleaning process. The reference electrode is a single junction Ag/AgCl electrode calibrated to the Reversible Hydrogen Electrode (RHE), and the counter electrode is a graphite rod that is separated from the working electrolyte compartment by a Nafion 117 membrane. The electrochemical cell is continuously blanketed with N_2 gas during all electrochemical kinetic measurements, which are conducted at room temperature (T = 23.3 °C) unless indicated otherwise.

The intrinsic activities in different electrolytes are measured by two independent methods: (1) steady state current measurements to estimate exchange current densities using the Tafel equation (i_o) and (2) electrochemical impedance spectroscopy (EIS) to first estimate the V^{2+}/V^{3+} CT resistances (R_{ct}) at open circuit voltage (OCV), then calculate exchange current densities from

R_{ct} ($i_{o,R_{ct}}$) using **eq. 3.1** below (derived in **Chapter 2**). The i_o values are determined from the y-intercept of the log of oxidation current densities ($V^{2+} \rightarrow V^{3+} + e^-$). We use the oxidation rather than the reduction currents for i_o to avoid the convoluting effect of hydrogen evolution in the reduction currents. We confirm that we are not limited by mass transport by operating at a sufficiently high rotation speed where $i_{o,}$ is unaltered with further increase in rotation rates.

An example of a Tafel plot for different total vanadium concentrations at 30% SoC in H_2SO_4 that we used to extract the i_o values is shown in **Figure 3.1a**. The Tafel plots at other SoCs in H_2SO_4 are also obtained. The OCV and i_o in H_2SO_4 are found to be independent of total vanadium ion concentration but dependent on SoC, **Figure 3.1b**. The shift in OCV towards more positive potential with decrease in SoC in **Figure 3.1b** is expected from the Nernst equation and confirms our SoC measurements by UV-vis. The i_o values obtained for glassy carbon in H_2SO_4 at 50% SoC ($(2.89 \pm 0.01) \times 10^{-3}$ mA cm^{-2}) are in close agreement with previously reported values on carbon electrodes in H_2SO_4 ($(1.76–2.28) \times 10^{-3}$ mA cm^{-2}).[25,26] The Tafel slopes (b) in **Figure 3.1c**, ranging from 120–140 mV decade^{-1}, correspond to a rate-determining step (RDS) with one electron transfer, that is, $n_k = 1$. The nearly constant Tafel slopes indicates no change in mechanism at different total vanadium ion concentrations and SoC.

The dependence of the exchange current density on the V^{2+} and V^{3+} concentrations serves as new evidence to support the hypothesis that V^{2+}/V^{3+} is an inner sphere reaction on carbon. A kinetic model of the form $i_o \propto [V^{2+}]^{\alpha}[V^{3+}]^{-\alpha}$, where α is the (positive) reaction order in V^{2+} and $-\alpha$ is the (negative) reaction order in V^{3+}, can be used to describe the observed behavior of i_o. This kinetic model captures both the i_o independence of total vanadium ion concentration and the increase with SoC (i.e., greater V^{2+} concentration) shown in **Figure 3.1b**. The negative order dependence of i_o in [V^{3+}] indicates an adsorption event in the reaction mechanism.[27] This presence

of an adsorption event corroborates previous reports that the V^{2+}/V^{3+} redox reaction is an inner sphere CT reaction.[14–19]

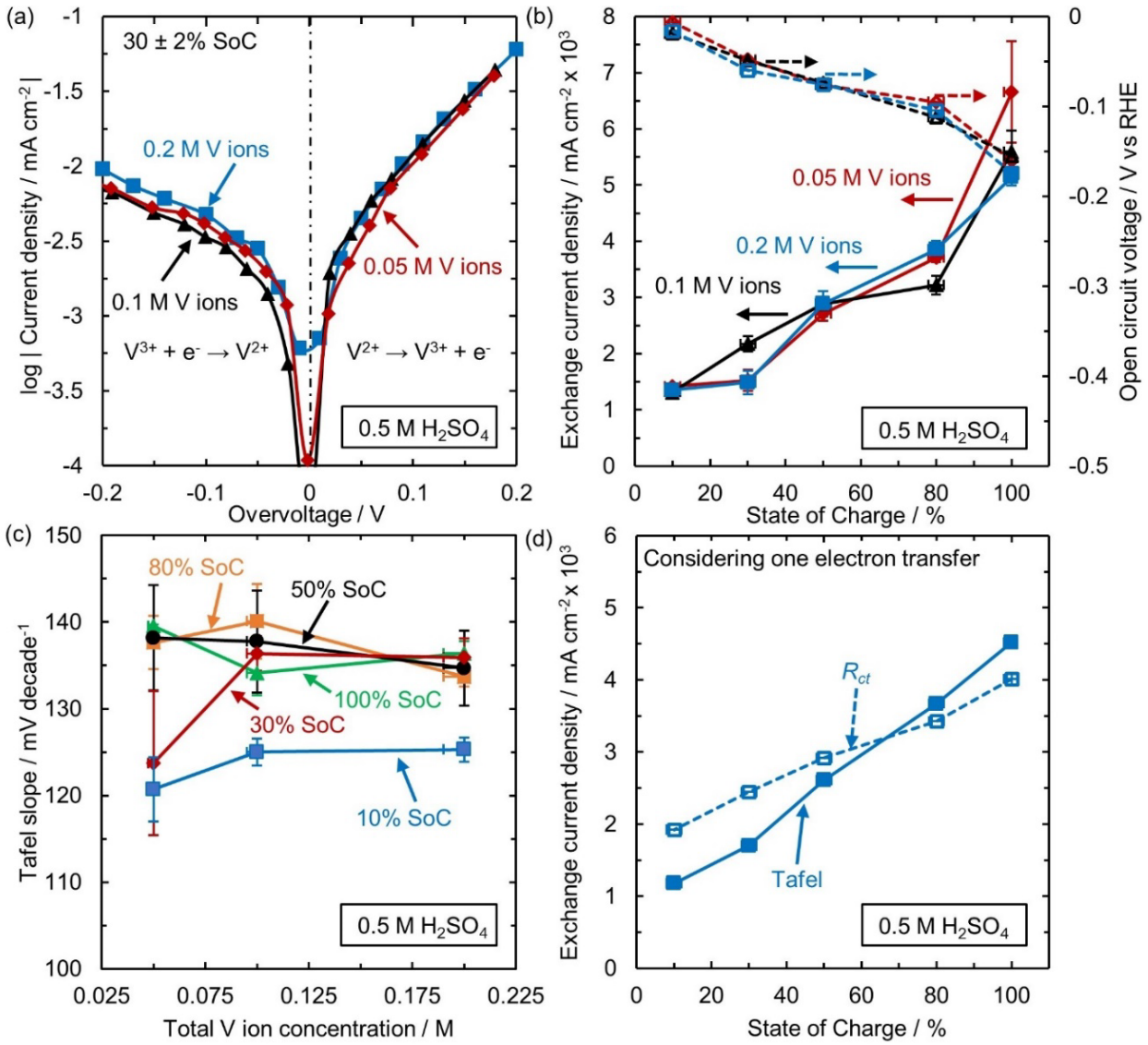

Figure 3.1. V^{2+}/V^{3+} Kinetics on Glassy Carbon in H_2SO_4 at Room Temperature. (a) Log of absolute value of current densities vs overvoltage at 30% State of Charge (SoC) for 0.05, 0.1, and 0.2 M total vanadium concentration. **(b)** Exchange current densities obtained by using the Tafel equation plotted as a function of SoC for 0.05, 0.1, and 0.2 M total vanadium. The open circuit voltages (OCV) vs RHE as a function of SoC are also shown. **(c)** Tafel slope as a function of SoC for 0.05, 0.1, and 0.2 M total vanadium. **(d)** Exchange current densities as a function of SoC for 0.2 M total vanadium by two independent methods: (i) (solid line) Using the Tafel equation as in (b) and (ii) (dashed line) Charge transfer resistance at OCV using potentiostatic electrochemical impedance measurements assuming a total of one electron transfer. The supporting electrolyte is 0.5 M H_2SO_4 and a glassy carbon working electrode disk rotating at ω = 1500 rpm is used to remain in the kinetic regime. All measurements are conducted at T = 23.3 °C.

The i_o (in mA cm^{-2}) can also be evaluated using R_{ct} (in Ω cm^2)[28] from **eq. 3.1**:

$$i_{o,R_{ct}} = \frac{RT}{n_k F R_{ct} n} \quad \text{(eq. 3.1)}$$

where n_k is the number of electrons in the RDS, n is the total number of electrons involved in the overall reaction, F is Faraday's constant, R is the universal gas constant and T is the temperature in K. From fitting the EIS data at OCV to determine R_{ct} and assuming $n = 1$, the $i_{o,R_{ct}}$ values are in close quantitative agreement with the i_o values in H_2SO_4, **Figure 3.1d**, confirming the accuracy of the measurements of the exchange current densities by both methods. The $i_{o,R_{ct}}$ and i_o values have similar magnitudes and show the same variation with SoC at elevated temperatures as well, with a percentage root mean square error (RMSE) of ~24%.

To probe the impact of anions on the intrinsic V^{2+}/V^{3+} redox kinetics, we conducted rate measurements in HCl/H_2SO_4 and HCl on glassy carbon to compare with H_2SO_4. The $i_{o,Tafel}$ in **Figure 3.2a**, b (**Figure S3.1**) and $i_{o,R_{ct}}$ (**Figure S3.2**) are the same in HCl/H_2SO_4 as H_2SO_4, indicating the same reaction mechanism involving one electron transfer ($n = 1$). In HCl, however, i_o is ~2.5 times higher than in H_2SO_4 or HCl/H_2SO_4, **Figure 3.2a**, but shows the same dependence on SoC. The $i_{o,R_{ct}}$ in HCl is larger than i_o in HCl when assuming a total of one electron transfer ($n = 1$), but if we instead assume the V^{2+}/V^{3+} overall reaction involves two-electron transfer when converting from R_{ct} to $i_{o,R_{ct}}$ ($n = 2$) using **eq. 3.1**, the values of $i_{o,R_{ct}}$ and i_o in HCl match, as shown in **Figure 3.2b**. The $i_{o,R_{ct}}$ and i_o are also in close agreement in HCl at different temperatures with a percentage RMSE of ~12.5%, only if $n = 2$. The Tafel slopes in HCl (**Figure S3.1**) are similar to H_2SO_4 and HCl/H_2SO_4, both corresponding to a RDS involving one electron transfer ($n_k = 1$). Note that this observation is not necessarily inconsistent, as the Tafel slope corresponds to the electron transfer in the RDS, whereas the value of $n = 2$ corresponds to the total number of

electrons transferred in the reaction. However, regardless of whether $n = 1$ or $n = 2$, $i_{o,R_{ct}}$ in HCl is larger than the $i_{o,R_{ct}}$ in H_2SO_4 and HCl/H_2SO_4, confirming the faster kinetics determined from i_o values shown in **Figure 3.2a**.

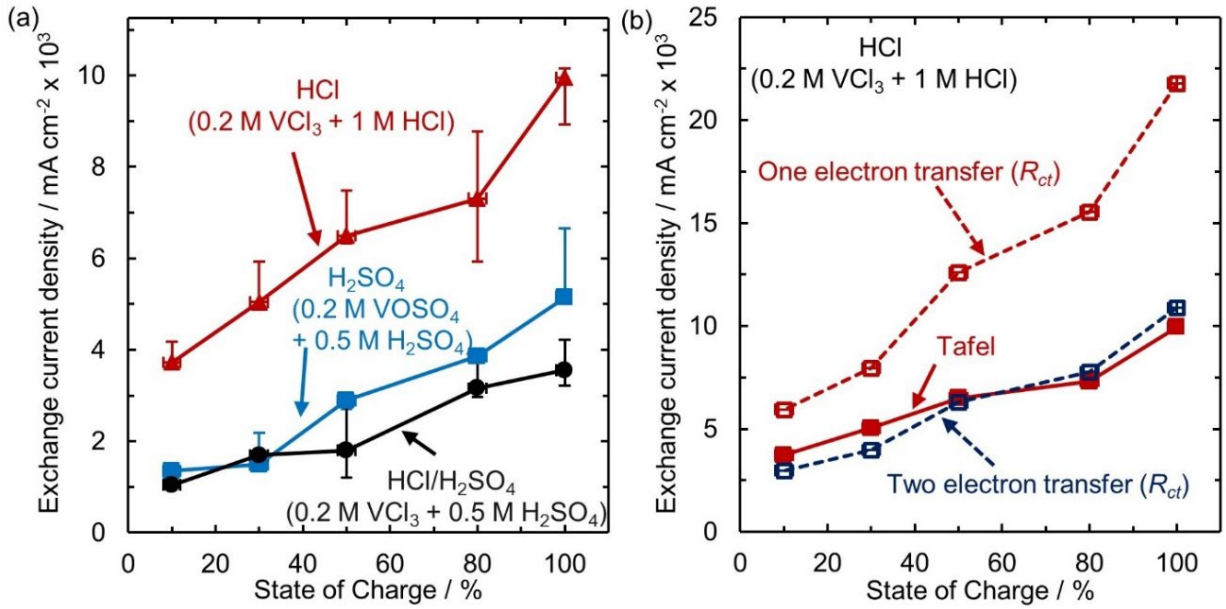

Figure 3.2. V^{2+}/V^{3+} Exchange Current Densities on Glassy Carbon as a Function of State of Charge in HCl, H_2SO_4, and mixed HCl/H_2SO_4 Electrolytes. (a) Evaluated using the Tafel equation in HCl (0.2 M VCl_3 + 1 M HCl), H_2SO_4 (0.2 M $VOSO_4$ + 0.5 M H_2SO_4), and HCl/H_2SO_4 (0.2 M VCl_3 + 0.5 M H_2SO_4). **(b)** Evaluated in HCl from two independent methods: (i) (solid line) Using the Tafel equation for the reaction: $V^{2+} \rightarrow V^{3+} + e^-$ and (ii) (dashed lines) Charge transfer resistance at open circuit voltage assuming a total of one and two electron transfer.

The various kinetic parameters evaluated in HCl compared to HCl/H_2SO_4 and H_2SO_4 suggests a change in mechanism on glassy carbon in HCl. From the agreement of i_o and $i_{o,R_{ct}}$ with $n = 2$ in HCl, but with $n = 1$ in HCl/H_2SO_4 and H_2SO_4, the total number of electrons transferred appears to change. However, the number of electrons in the RDS remains the same, based on the similar Tafel slopes in all three electrolytes. Because of the dependence of i_o on SoC in all three electrolytes, it is likely that the mechanism proceeds through an inner sphere adsorbate-mediated step in all three electrolytes; however, the increase in exchange current densities in HCl may be a result of a change in the adsorbed intermediate species.

Further support for a different mechanism in HCl comes from the lower apparent activation energies (E_a) in HCl compared to H_2SO_4 at a given SoC. E_a values evaluated from i_o (from steady state rate measurements) and $i_{o,R_{ct}}$ (from EIS) are consistent with one another for a given electrolyte, and both indicate lower activation energies for the V^{2+}/V^{3+} reaction in HCl as shown in **Figure 3.3**.

The variation of E_a with SoC also supports our hypothesis of V^{2+}/V^{3+} reaction being an inner sphere reaction involving an adsorption event, as opposed to an outer sphere reaction where E_a is expected to be independent of SoC.[29] The E_a increases with decreasing SoC (**Figure 3.3**) in HCl and H_2SO_4, which supports our previously discussed observations of increasing i_o with SoC (**Figure 3.2a**). The decrease in the apparent activation energies in HCl corresponds qualitatively to an increase in i_o and decrease of R_{ct} in HCl compared with H_2SO_4. However, quantitatively, the ~2.5-times rate enhancement in HCl is ~10^2 orders lower than would be expected from the decrease in E_a (~17 kJ mol^{-1} decrease for 50% SoC evaluated by i_o) in comparison to H_2SO_4, assuming the sole difference in rate is from the activation energies (i.e., no change in the pre-exponential factor). To understand whether changes in mechanism in HCl compared with H_2SO_4 and HCl/H_2SO_4 could arise from differences in the vanadium-complex structure that can alter the adsorbed intermediate, we examine the structure of V^{2+} and V^{3+} complexes.

We use UV-vis to identify the vanadium complexes formed in bulk solutions of different electrolytes and to probe whether the complex's structure is responsible for the rate enhancement of V^{2+}/V^{3+} in HCl. The UV-vis of V^{2+} and V^{3+} in non-interacting $HClO_4$ are used as a reference for the water-only complexes,[13] to enable a comparison to V^{2+} and V^{3+} spectra in the presence of other anions (Cl^- and SO_4^{2-}). The UV-vis of V^{2+} shows the same peak intensities and locations in HCl, H_2SO_4, HCl/H_2SO_4, and $HClO_4$ (**Figures 2.1** and **2.2** in **Chapter 2**), indicating there is no

difference in the first coordination sphere of V^{2+} in the four acidic electrolytes. As H_2O is the only common ligand in all four electrolytes of HCl, H_2SO_4, HCl/H_2SO_4, and $HClO_4$, we conclude that the $[V(H_2O)_6]^{2+}$ proposed in previous studies[12,13] is the dominant V^{2+} species in all electrolytes used in our kinetic studies.

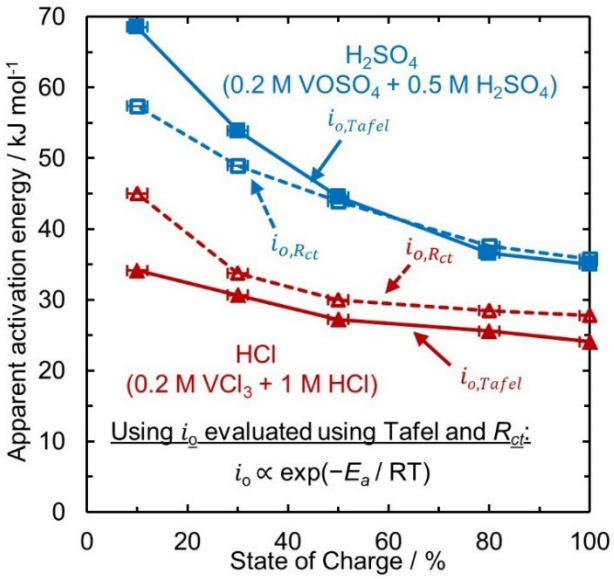

Figure 3.3. Apparent Activation Energies for the V^{2+}/V^{3+} Redox Reaction on Glassy Carbon in H_2SO_4 and HCl Electrolytes. Apparent activation energies (E_a) on glassy carbon working electrode as a function of State of Charge for H_2SO_4 (0.2 M $VOSO_4$ + 0.5 M H_2SO_4) and HCl (0.2 M VCl_3 + 1 M HCl) from: (solid lines) Exchange current densities obtained by using the Tafel equation (i_o) and (dashed lines) Charge transfer resistance ($i_{o,R_{ct}}$) at open circuit voltage. The i_o and $i_{o,R_{ct}}$ were evaluated at each SoC at T = 23.3, 30.0, 35.0, and 40.0 °C.

Unlike V^{2+}, the UV-vis spectra of V^{3+} changes with electrolyte, where the peak location of the lower energy $^3T_{1g} \rightarrow {}^3T_{2g}$ transition[30,31] is at 588 nm in HCl and $HClO_4$ and 605 nm in HCl/H_2SO_4 and H_2SO_4, shown in **Figure 3.4a**. The peak corresponding to a higher energy transition ($^3T_{1g}$ (F) $\rightarrow {}^3T_{1g}$ (P)) shifts less than the $^3T_{1g} \rightarrow {}^3T_{2g}$ on anion complexation in both experimental (**Figure 3.4a**) and computational (**Figure 3.4c**) V^{3+} UV-vis spectra. The dependence of the peak location on the electrolyte implies that unlike V^{2+}, the V^{3+} coordinates with anions in at least one of the electrolytes, **Figure 3.4a**.

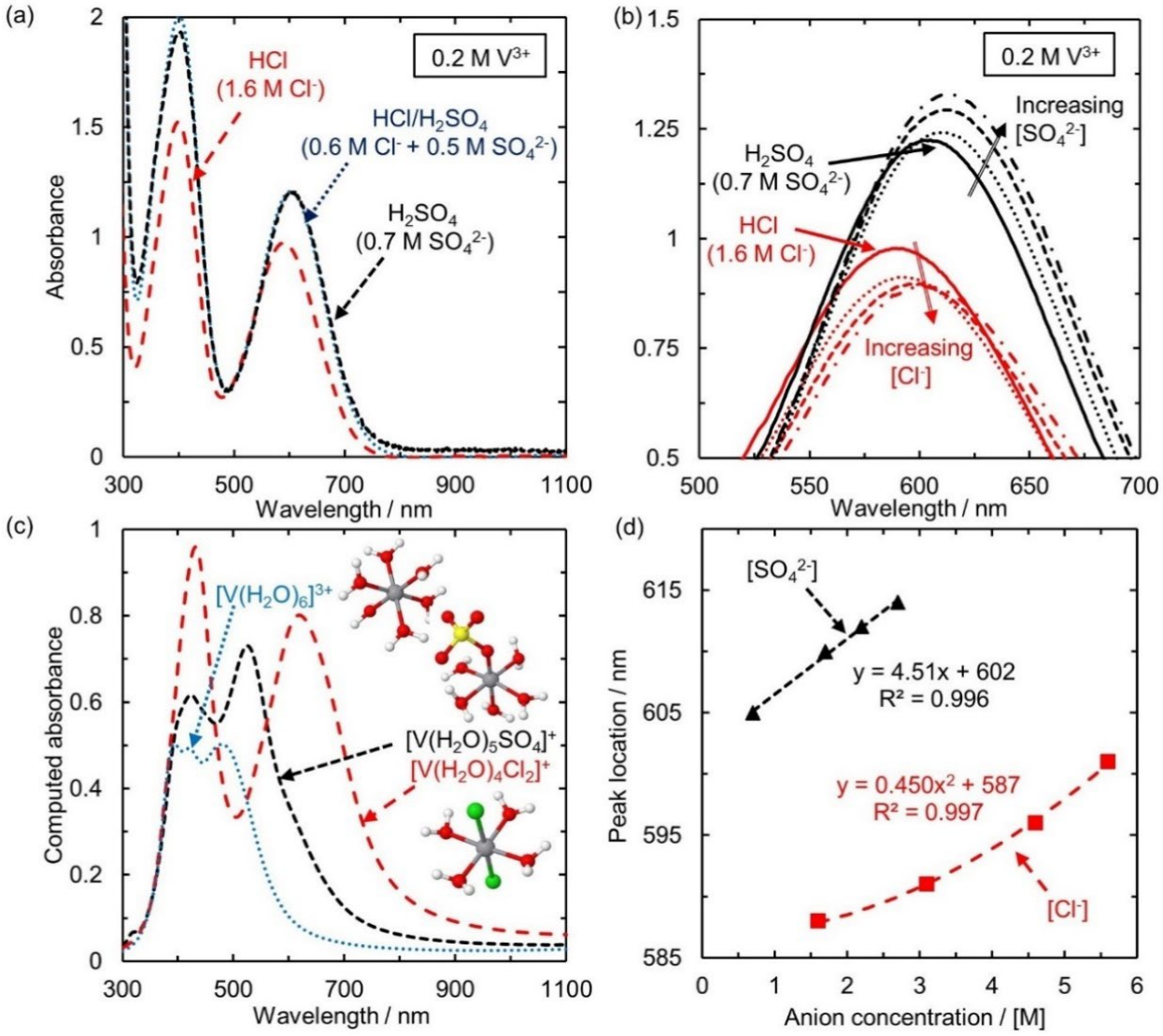

Figure 3.4. UV-vis Absorbance as a Function of Wavelength for V^{3+} in HCl, H_2SO_4, and mixed HCl/H_2SO_4 Electrolytes. (a) Experimental V^{3+} spectra for HCl (0.2 M VCl_3 + 1 M HCl), H_2SO_4 (0.2 M $VOSO_4$ + 0.5 M H_2SO_4), and HCl/H_2SO_4 (0.2 M VCl_3 + 0.5 M H_2SO_4) obtained by reducing vanadium salt (either $VOSO_4$ or VCl_3) completely to V^{2+} and oxidizing back to V^{3+}. **(b)** The $^3T_{1g} \rightarrow {}^3T_{2g}$ transition peak for V^{3+} obtained as in (a) for solutions by addition of sodium sulfate and sodium chloride separately to obtain spectra at various SO_4^{2-} (0.7, 1.7, 2.2, and 2.7 M SO_4^{2-}) and Cl^- (1.6, 3.1, 4.6, and 5.6 M Cl^-) concentrations. **(c)** Theoretical V^{3+} spectra of complexes: $[V(H_2O)_6]^{3+}$, $[V(H_2O)_5SO_4]^+$, and $[V(H_2O)_4Cl_2]^+$ obtained by TDDFT. For atom/ions in complex, grey depicts vanadium, red for oxygen, white for hydrogen, green for chloride and yellow for sulfur. **(d)** Experimental peak location of $^3T_{1g} \rightarrow {}^3T_{2g}$ transition for V^{3+} complex at various SO_4^{2-} and Cl^- concentrations (as in (b)) showing first order dependence on $[SO_4^{2-}]$ and second order dependence on $[Cl^-]$.

The peak locations in the V^{3+} spectra in HCl (1.6 M Cl^-) appear at ~400 nm ($^3T_{1g}$ (F) $\rightarrow$ $^3T_{1g}$ (P))[30,31] and ~588 nm ($^3T_{1g} \rightarrow {}^3T_{2g}$)[30,31] and resemble the spectra of $[V(H_2O)_6]^{3+}$ with only the perchlorate anion present (**Figures 2.1** and **2.2** in **Chapter 2**).[13] As the Cl^- concentration is increased from 1.6 M to 5.6 M, the $^3T_{1g} \rightarrow {}^3T_{2g}$ peak shifts to higher wavelengths, **Figure 3.4b**, in

agreement with previous studies of V^{3+} at high Cl^- concentrations.[13,32] We attribute this shift to an increase in the fraction of V^{3+} complexes with Cl^- in the V^{3+} coordination sphere rather than only water. Our theoretical UV-vis spectra for $[V(H_2O)_4Cl_2]^+$ also shows a shift towards higher wavelengths compared to $[V(H_2O)_6]^{3+}$, **Figure 3.4c**. Thus, in the HCl electrolyte we used for kinetic studies (1.6 M Cl^-), we have a distribution of V^{3+} complexes with chloride (either of the form $[V(H_2O)_5Cl]^{2+}$ or $[V(H_2O)_4Cl_2]^+$ based on previous DFT studies[9,11]) and water-only ($[V(H_2O)_6]^{3+}$), although the exact distribution cannot be determined without knowing the exact peak locations for the pure coordinated complex. The $^3T_{1g} \rightarrow {}^3T_{2g}$ peak location shows a second order dependence on $[Cl^-]$ as shown in **Figure 3.4d**, indicating that $[V(H_2O)_4Cl_2]^+$ forms in HCl rather than $[V(H_2O)_5Cl]^{2+}$, because the single chloride complex cannot show a second order dependence in $[Cl^-]$. This structural assignment requires the assumption that the peak location is proportional to the ratio of the chloride complex to the total amount of V^{3+}, as discussed in SI.

In H_2SO_4, with increasing SO_4^{2-} concentrations the $^3T_{1g} \rightarrow {}^3T_{2g}$ transition peak shifts towards higher wavelengths compared with HCl, **Figure 3.4b**, indicating SO_4^{2-} enters the first coordination sphere of V^{3+}. We hypothesize $[V(H_2O)_6]^{3+}$ undergoes ligand exchange to form $[V(H_2O)_5SO_4]^+$ in H_2SO_4, because the $^3T_{1g} \rightarrow {}^3T_{2g}$ peak location shows a first order dependence on $[SO_4^{2-}]$, **Figure 3.4d**, as opposed to the second order seen for chloride. The argument that $[V(H_2O)_5SO_4]^+$ is formed in H_2SO_4 rather than $[V(H_2O)_4(SO_4)_2]^-$ is further supported by the higher absolute absorbance of the $^3T_{1g}$ (F) $\rightarrow {}^3T_{1g}$ (P) and $^3T_{1g} \rightarrow {}^3T_{2g}$ transitions compared with the $[V(H_2O)_6]^{3+}$ complex in both experimental (**Figure 3.4a**) and computational (**Figure 3.4c**) UV-vis spectra, attributed to the loss of the inversion center and O_h symmetry by addition of a single sulfate ligand in the V^{3+} coordination sphere. The V^{3+} spectra in HCl/H_2SO_4 shows the same peak locations and intensity as H_2SO_4, **Figure 3.4a**, thus we infer a similar complex distribution is present (i.e., $[V(H_2O)_5SO_4]^+$

and $[V(H_2O)_6]^{3+}$) in both these electrolytes. The absence of the $[V(H_2O)_4Cl_2]^{+}$ complex in HCl/H_2SO_4 (and in other mixtures of Cl^{-}/SO_4^{2-} shown in **Figure S3.3**) as identified by UV-vis is likely due to the stronger complexation of sulfate than chloride.

We assume that at sufficiently low vanadium concentrations, the fraction of vanadium ions in dimers is minimal. However, as the vanadium concentration is increased, the formation of dimers becomes thermodynamically more favorable, and the increase in the fraction of dimers in solution would result in either the appearance of new transition peaks or new shoulders in existing transition peaks in the UV-vis spectra.[33] As we do not observe changes in peak shapes or the appearance of new transition peaks in the UV-vis spectra of V^{2+} and V^{3+} with increasing vanadium concentration, we assume no vanadium dimers are formed in our tested electrolytes.

Our analysis indicates the improvement in the kinetics in HCl only arises when the $[V(H_2O)_4Cl_2]^{+}$ complex is present. The appreciable decrease in apparent activation energies (~17 kJ mol^{-1} lower in HCl at 50% SoC evaluated by i_o), **Figure 3.3**, but rather modest increase in rate (~2.5 times) for HCl compared to H_2SO_4 or the HCl/H_2SO_4 mixture, **Figure 3.2a**, may be because there is only a small fraction of the more kinetically active $[V(H_2O)_4Cl_2]^{+}$ complex in HCl, with the balance being the less active $[V(H_2O)_6]^{3+}$. Thus, the pre-exponential factor may be different for the two mechanisms, i.e., lower in HCl, but because the apparent activation energies are lower, the overall kinetics are faster in HCl.

We hypothesize the higher V^{2+}/V^{3+} activity in HCl arises because the CT occurs through a chloride bridge (*Cl) in HCl, shown in **Scheme 3.1b**, as opposed to an OH bridge (*OH) in H_2SO_4 (**Scheme 3.1a**). Carbon electrodes are occupied with surface hydroxyl groups (*OH) groups in aqueous media,[21] which have been hypothesized to act as a bridge for electron transfer in H_2SO_4 for the V^{2+}/V^{3+} reaction,[20] consistent with the inner sphere mechanism behavior we observed here.

Chloride is known to adsorb on carbon electrodes,[34] and the *Cl bridge enhances the CT compared with the *OH bridge for metal ions because of the higher polarizability of *Cl compared with *OH.[22,35,36] A rate enhancement in the presence of Cl^- has been reported for Cr^{2+}/Cr^{3+},[37,38] Fe^{2+}/Fe^{3+},[39] and Cu^{2+}/Cu^{+} redox couples[40] on metal electrodes, hypothesized to be due to *Cl acting as a bridge for CT. To our knowledge, the apparent activation energies of a *Cl vs *OH bridge for an inner sphere CT over an electrode surface have not been previously reported for V^{2+}/V^{3+} or other similarly behaving redox couples like Cr^{2+}/Cr^{3+}, Fe^{2+}/Fe^{3+}, and Cu^{2+}/Cu^{+}.

To further test this mechanistic hypothesis involving bridges, we examined the V^{2+}/V^{3+} redox kinetics in HBr, where we postulated a greater kinetic enhancement due to the formation of a highly polarizable *Br bridge compared with a *Cl bridge.[22,36] Indeed, our current density measurements vs overvoltage show a ~1.5 times rate enhancement in HBr ($(9.82 \pm 0.04) \times 10^{-3}$ mA cm^{-2}) compared with HCl ($(6.49 \pm 0.09)) \times 10^{-3}$ mA cm^{-2}), and ~3.5 times rate enhancement compared with H_2SO_4 ($(2.89 \pm 0.01) \times 10^{-3}$ mA cm^{-2}) at 50% SoC. The dominant V^{2+} and V^{3+} complexes in HBr were the same as identified in HCl using UV-vis spectroscopy, i.e., $[V(H_2O)_6]^{2+}$ complex for V^{2+} and a distribution of complexes with the majority as $[V(H_2O)_6]^{3+}$ and a minority as $[V(H_2O)_5Br]^{2+}$ or $[V(H_2O)_4Br_2]^{+}$ for V^{3+}. Rate enhancement in HBr compared with HCl has been reported for the V^{2+}/V^{3+} redox couple on mercury electrodes due to bromide bridging,[41] but there have been no reports for this enhancement observed on carbon electrodes.

Ultimately, there are several pieces of evidence that support the formation of a chloride intermediate for the V^{2+}/V^{3+} reaction. In bulk solution, UV-vis shows the presence of small concentrations of $[V(H_2O)_4Cl_2]^{+}$ in HCl. When this complex is observed, the reaction has a lower apparent activation barrier, a higher exchange current density, and a change in the total number of electrons involved, implying a change in mechanism, which we attribute to the involvement of the

chloride species in the reaction. Previous kinetic studies of other redox couples like Cr^{2+}/Cr^{3+},[37,38] Fe^{2+}/Fe^{3+},[39] and Cu^{2+}/Cu^{+} in presence of chloride[40] show enhanced kinetics in comparison with non-interacting $HClO_4$, which were attributed to *Cl acting as a bridge instead of *OH. The faster electron transfer kinetics of the *Cl compared to the *OH were predicted to be due to better electronic coupling based on *ab initio* molecular orbital theory calculations.[40] The improved kinetics for the V^{2+}/V^{3+} reaction that we observe in HBr in comparison with HCl also imply the halide is part of a reaction intermediate. However, the chloride (or bromide) surface intermediate has not been detected in any of the systems mentioned above. In situ or operando spectroscopy techniques such as x-ray absorption, nuclear magnetic resonance, and Raman are necessary to identify the structure of the adsorbed intermediate. Computational studies using techniques such as *ab initio* metadynamics to compute adsorption and reaction free energies[9,21,42] could also help clarify the possibility of a chloride intermediate on the electrode surface which we discuss further in upcoming chapters.

As summarized in **Scheme 3.1a**, in H_2SO_4 and HCl/H_2SO_4 we propose that the hexa-aqua V^{2+} complex, $[V(H_2O)_6]^{2+}$, binds with the adsorbed *OH after shedding a water ligand, similar to trivalent chromium.[43] The V^{2+} adsorption process involves loss of a proton, forming an $*[O{-}V(H_2O)_5]^{2+}$ intermediate (i.e., V^{2+} adsorbed to glassy carbon via an *OH bridge). This intermediate then transfers an electron through the *OH bridge to oxidize V^{2+} to V^{3+}. After the CT, the $*[O{-}V(H_2O)_5]^{3+}$ intermediate desorbs, taking a water or sulfate ligand into the bulk electrolyte. In the bulk solution, $[V(H_2O)_6]^{3+}$ can undergo ligand exchange to replace the H_2O ligand by SO_4^{2-} or SO_4^{2-} is added directly during the desorption step, forming the $[V(H_2O)_5SO_4]^{+}$ seen by UV-vis in H_2SO_4 and HCl/H_2SO_4. We attribute the similar kinetics we observe in HCl/H_2SO_4 and H_2SO_4 to the high SO_4^{2-} concentration in HCl/H_2SO_4, which causes

$[V(H_2O)_5SO_4]^+$ to dominate as opposed to $[V(H_2O)_4Cl_2]^+$. We hypothesize that at sufficiently high Cl^- concentrations, even in mixed HCl/H_2SO_4 systems, there may be a catalytic effect such as that observed in HCl, possibly explaining the higher current densities in mixed-acid full cell systems, [4–6] where the Cl^- concentrations are much higher than those used in our work here. More work on the concentration dependence is needed to verify this hypothesis.

In HCl, the adsorbed Cl^- (*Cl) on glassy carbon can act as a bridge for CT (**Scheme 3.1b**). Based on the results from impedance and steady state current measurements, this mechanism is an overall two-electron transfer, with a one-electron RDS. Although we do not have definitive proof for a specific mechanism, we propose two mechanisms here that are consistent with our measured data. One possible mechanism is that two adsorbed vanadium intermediates form a dimer on the carbon surface to facilitate two electron transfer, after which the dimer desorbs/dissociates (no dimers were detected in bulk solution by UV-vis, as mentioned above). Another possible mechanism involves formation of V^{4+} as a reaction intermediate, which reacts with V^{2+} undergoing a comproportionation reaction observed in a previous study in perchlorate solutions[44] to give V^{3+}, facilitating an overall two electron transfer. A similar mechanism as that shown in **Scheme 3.1b** may occur in HBr, but additional tests are needed.

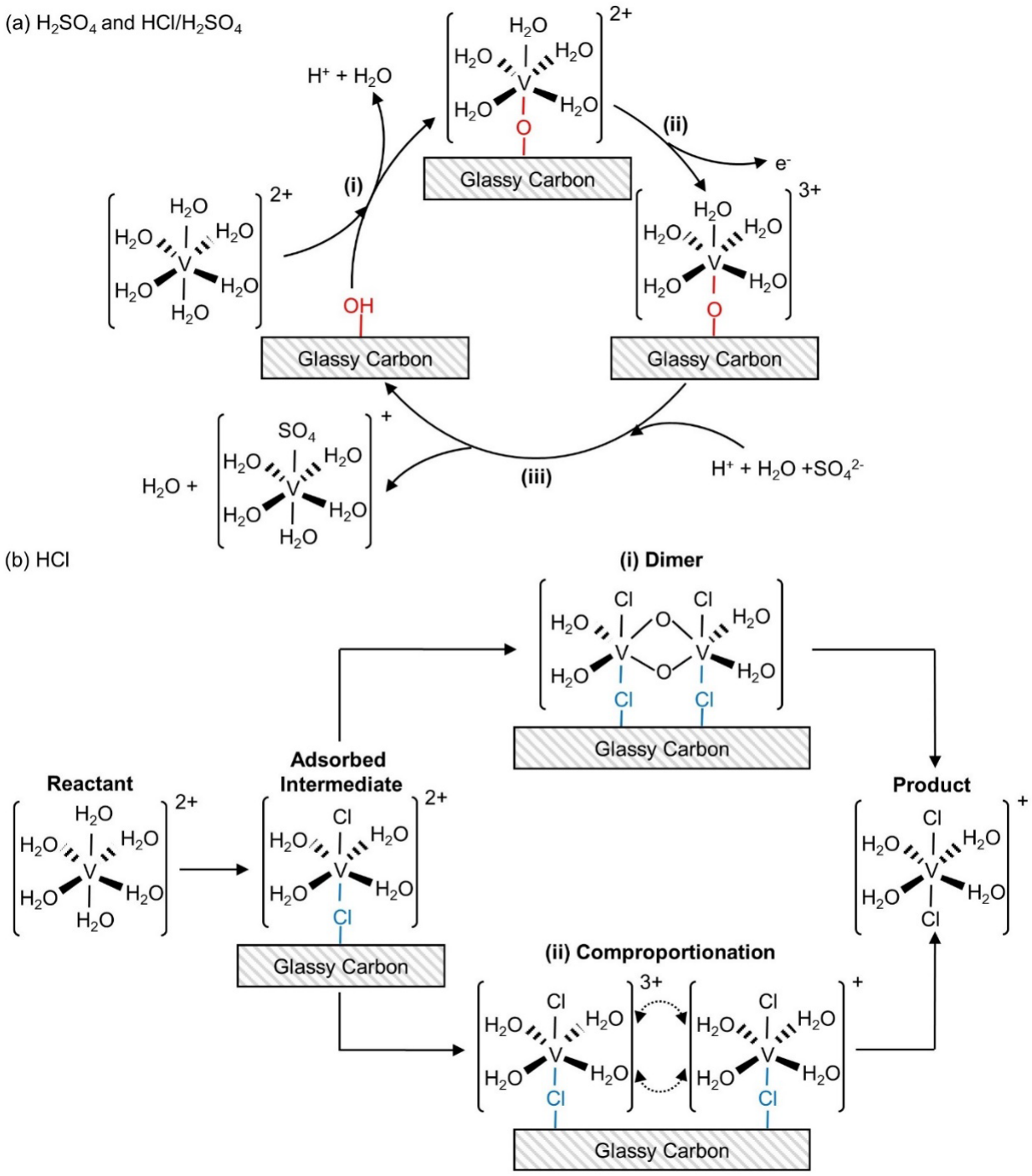

Scheme 3.1. Proposed Catalytic Cycle of V^{2+} Oxidation to V^{3+} on Glassy Carbon in H_2SO_4, HCl/H_2SO_4, and HCl Electrolytes. V^{3+} Reduction is Assumed to Follow the Reverse Reaction. **(a)** *In H_2SO_4 and HCl/H_2SO_4:* (i) V^{2+} ion as $[V(H_2O)_6]^{2+}$ adsorbs to *OH on the glassy carbon surface after shedding a water ligand. The adsorption of V^{2+} involves the loss of a proton, forming $*[O{-}V(H_2O)_5]^{2+}$; (ii) Electron transfer occurs through the *OH, acting as a bridge and leading to oxidation of V^{2+} to V^{3+}. We call the bridge here *OH by convention, although it may be an *O bridge due to the loss of the proton to the solution; (iii) The adsorbed intermediate $*[O{-}V(H_2O)_5]^{3+}$ desorbs (taking on a water or sulfate ligand), with addition of H^+ leading to regeneration of the adsorbed *OH species on the glassy carbon surface. $[V(H_2O)_6]^{3+}$ in the bulk electrolyte can exchange a water ligand with SO_4^{2-} to form $[V(H_2O)_5SO_4]^+$ or it may directly take the SO_4^{2-} ligand when desorbing. **(b)** *In HCl:* V^{2+} adsorbs onto the glassy carbon surface through

a *Cl bridge. The adsorbed species may undergo two-electron transfer via two possible postulated routes: (i) Two adsorbed vanadium intermediates can interact to form a dimer, facilitating two electron transfer, followed by desorption/dissociation to give $[V(H_2O)_4Cl_2]^+$; (ii) Adsorbed V^{2+} can undergo a comproportionation reaction with adsorbed V^{4+} formed as an intermediate to form V^{3+}, which desorbs to give product $[V(H_2O)_4Cl_2]^+$. Note that $[V(H_2O)_5SO_4]^+$ shown in **Scheme 3.1a** is the majority complex formed in H_2SO_4 and HCl/H_2SO_4, while $[V(H_2O)_4Cl_2]^+$ shown in **Scheme 3.1b** is the minority complex formed in HCl because we believe these are the kinetically most relevant species in the given electrolytes, as discussed in the main text.

3.4 Conclusions

The work in this chapter gives further evidence that the V^{2+}/V^{3+} reaction involves inner sphere charge transfer on glassy carbon, based on rate measurements in different electrolytes that confirm the presence of an adsorbed intermediate. The precise inner sphere CT mechanism is shown to depend on the choice of acidic electrolyte, based on different rates, activation energies, and the total number of electrons transferred. Two independent electrochemical techniques for estimating i_o indicate faster V^{2+}/V^{3+} redox kinetics with an overall two-electron transfer in HCl as opposed to a kinetically slower single-electron transfer in H_2SO_4 and HCl/H_2SO_4. UV-vis spectroscopy measurements confirm that V^{2+} is only complexed by water as $[V(H_2O)_6]^{2+}$ and identifies the V^{3+} complexes formed in the electrolytes in which we measured V^{2+}/V^{3+} kinetics. In HCl, the V^{3+} exists as a mixture of $[V(H_2O)_6]^{3+}$ and $[V(H_2O)_5Cl_2]^+$, whereas in H_2SO_4 and HCl/H_2SO_4, the V^{3+} exists as a mixture of $[V(H_2O)_5SO_4]^+$ and $[V(H_2O)_6]^{3+}$. We hypothesize that the CT in the V^{2+}/V^{3+} reaction goes through a bridging ligand, and the higher rate in HCl than H_2SO_4 or HCl/H_2SO_4 is due to the higher polarizability of the *Cl bridge than the *OH bridge, which leads to enhanced CT through the *Cl bridge. This is supported by testing the V^{2+}/V^{3+} redox kinetics in HBr, which shows higher activity than in HCl, attributed to the higher polarizability of *Br compared with *Cl. Electrolyte engineering to ensure the presence of more effective bridges to facilitate CT may be a method to improve VRFB kinetic performance in full cell systems. Overall this chapter highlights the importance of identifying the structures of complexed species in interpreting kinetics

and the use of multiple independent electrochemical techniques to gain valuable mechanistic insights into fundamental CT reactions.

3.5 Supporting Information

3.5.1 Starting Electrolyte Preparation

Solutions of the required concentrations are prepared by dissolving vanadium(III) chloride (VCl_3, 99% metals basis, Alfa Aesar), vanadium(IV) sulfate hydrate ($VOSO_4 \cdot xH_2O$ [x assumed to be 5], ≥ 99.99% trace metals basis, Sigma Aldrich) or vanadium(V) oxide (V_2O_5, ≥ 99.6% trace metals basis, Sigma Aldrich) in desired electrolyte concentrations of sulfuric acid (H_2SO_4, 99.999%, Sigma Aldrich), hydrochloric acid (HCl, ACS reagent 37%, Sigma Aldrich), hydrobromic acid (HBr, 48%, Sigma Aldrich) or perchloric acid ($HClO_4$, 60%, Fisher Chemical). All water used for preparing solutions and cleaning is purified using a MilliporeSigma Synergy UltrapureWater Purification System (18.2 MΩ cm resistivity).

VCl_3 is used as the vanadium source for HCl, $VOSO_4$ for H_2SO_4, and V_2O_5 for HBr and $HClO_4$ to avoid having a mixture of anions in those electrolytes. Desired concentrations of VCl_3 and $VOSO_4$ are completely soluble in HCl and H_2SO_4, however V_2O_5 is not completely soluble in $HClO_4$. V_2O_5 is dissolved in $HClO_4$ by pre-electrolysis (discussed below), which reduces the amount of vanadium in 5+ oxidation state, allowing more vanadium to dissolve in $HClO_4$ until V_2O_5 reaches its solubility limit in $HClO_4$. Eventually, all the V_2O_5 is dissolved and reduced to V^{2+} during pre-electrolysis. V_2O_5 is completely dissolved in HBr under continuous stirring after 48 hrs.

3.5.2 Electrochemical Cell Assembly and Setup

A two-compartment cell is used for all electrochemical measurements. The two compartments are separated by a Nafion N117 (Fuel Cell Store) proton conducting membrane,

which is presoaked in the supporting electrolyte for at least two hours prior to beginning of each experiment. The working electrode compartment is filled with 160 mL of prepared vanadium solution, and the counter electrode side is filled with 35 mL of supporting electrolyte (i.e., solution with no vanadium ions) with the same H^+ concentration as the prepared vanadium ion solution. H_2SO_4 is used on the counter electrode side instead of HCl for measurements of kinetics in HCl electrolyte to prevent Cl_2 evolution through oxidation of Cl^- during pre-electrolysis discussed below. A procedure similar to HCl is used to test in HBr. A graphite rod (99.9995% metals basis, Alfa Aesar) is used as the counter electrode and a single junction Ag/AgCl electrode (Pine Research) is used as the reference electrode. A VSP potentiostat/galvanostat with a built-in EIS analyzer (Biologic Science Instruments USA) is used for all electrochemical measurements. During all kinetic measurements a glassy carbon disk is used as the working electrode. For both pre-electrolysis and oxidizing to control the SoC, graphite felt (6.35 mm thick, 99.0%, Alfa Aesar) supported on a graphite rod (DFP grade, Pine Research) is used as the working electrode to increase the surface area of the electrode to minimize the time required for pre-electrolysis. During all electrochemical measurements, the electrochemical cell is continuously sparged and blanketed with N_2 gas (Ultra high purity grade, 99.999%, Cryogenic Gases) to prevent O_2 from reaching inside the cell and oxidizing the V^{2+}.

3.5.3 Pre-electrolysis to Produce V^{2+} and Oxidizing Back to V^{3+} to Reach Desired States of Charge

The potential is held constant at −1.13 V (vs Ag/AgCl) until all the vanadium ions are reduced to the V^{2+} oxidation state, regardless of the vanadium source. The current becomes nearly constant after all vanadium ions are reduced to V^{2+}, but never drops to zero because hydrogen evolution reaction continues to occur. The negative potential of −1.13 V vs Ag/AgCl is applied to

pass reducing currents until there is no change in the UV-vis spectrum of samples taken from the working electrode compartment, confirming all vanadium ions in solution are reduced to V^{2+}. The solution at the counter electrode side is replaced with freshly prepared H_2SO_4 with the same H^+ ion concentration as the working electrolyte in HCl and HCl/H_2SO_4 to prevent the contribution of currents from reduction of Cl_2. The Cl_2 can reach the working electrode compartment due to the crossover of the dissolved Cl_2 through the Nafion membrane from the counter electrode side, as is detected when the counter electrode compartment is not replaced with fresh H_2SO_4 solution. A similar process as for HCl is used for measurements in HBr.

To reach to a desired SoC, the working electrode potential is held constant at 0.08 V vs Ag/AgCl until the required amount of V^{2+} ions are oxidized to V^{3+}, which is confirmed by obtaining concentrations from UV-vis spectra by Gaussian curve fitting (discussed in **Chapter 2**) in the wavelength region from 350–1100 nm. The current decreases to zero once all the V^{2+} ions are oxidized to V^{3+}, which can also be confirmed by no absorbance between 700–1100 nm (in which both V^{2+} and V^{4+} have characteristic peaks).[45,46]

3.5.4 Theoretical UV-vis spectra Calculations

Theoretical UV-vis spectra of hexa-coordinated V^{3+} complexes (i.e., $[V(H_2O)_6]^{3+}$, $[V(H_2O)_5SO_4]^+$, or $[V(H_2O)_4Cl_2]^+$) are computed based on Time Dependent Density Functional Theory (TDDFT) in four steps, all carried out using the NWChem software.[47] In the first step, quantum mechanics/molecular mechanics[48] (QM/MM) based molecular dynamics simulations of V^{3+} complexes are performed in a 25 × 25 × 25 $Å^3$ periodic box for 50 ps in the NVT ensemble using the Berendsen thermostat[49] at 300 K. The QM region, treated using the B3LYP hybrid functional[15] and the 6-31G* basis set, contain the hexa-coordinated V^{3+} complexes. The MM region using Amber99 force field[50] contain 510 explicit H_2O molecules and one or three Cl^- anions

depending on the complex to neutralize the system's overall charge. Van der Waals parameters for the V^{3+} force field to treat the interactions between the QM and MM regions is taken from Ref. 51. After a 10 ps equilibration period,[52] geometry snapshots is taken every 1 ps (total of 50 geometry snapshots) from the QM/MM trajectories for further processing. Each snapshot is then truncated to include the V^{3+} complex, anions, and 40 explicit H_2O molecules for geometry optimization.

In the second step, all truncated snapshots are geometry optimized with the B3LYP functional corrected for van der Waals interactions using Grimme's D3 method (B3LYP-D3).[53] NWChem's COSMO solvation model[54] is also included to treat long-range implicit solvent effects of water (in steps 2–4). Note, the QM/MM simulations (step 1) are performed in periodic box, but steps 2–4 were all non-periodic calculations. To enable computational tractability while retaining high accuracy, a mixed Gaussian basis set is used during geometry optimizations, with Def2-TZVPPD[55] used for V^{3+} ion, 6-31G* for the first solvation shell (i.e., the six H_2O molecules and/or anion(s) complexed to the V^{3+} ion) and anions, and 3-21G for the solvent H_2O molecules (denoted as Def2-TZVPPD/6-31G*/3-21G).

In the third step, TDDFT calculations[56] are performed on all 50 of the optimized geometries using B3LYP-D3 to obtain the first 10 excited states and their oscillator strengths. The same Def2-TZVPPD/6-31G*/3-21G basis sets and COSMO settings used for ground-state geometry optimizations are employed for TDDFT calculations. Roots are Lorentzian broadened with a width of 0.3 eV to obtain a UV-vis spectrum for each optimized geometry. The width of Lorentzian broadening is selected to obtain broadening comparable with experimentally observed spectra.

Lastly, in the fourth step, the 50 UV-vis spectra for the corresponding V^{3+} complex are averaged to obtain the final spectrum. Benchmark calculations of B3LYP-D3 against the range

separated CAM-B3LYP-D3 functional show no difference in UV-vis spectra, indicating that long-range CT states are not critical to treat.[57] Additionally, TDDFT calculations including the first 50 excited states have no effect on the energies and a less than 0.2% effect on the oscillator strengths compared with using just the first 10 excited states.

3.5.5 Predicting the Number of Anions in V^{3+} Inner-Coordination Sphere Using UV-vis

Consider a ligand exchange reaction where x water ligands in the inner coordination sphere of V^{3+} are replaced by x anions, with each anion having a single negative charge:

$$[\mathrm{V(H_2O)_6}]^{3+} + x\ \mathrm{anion^-} \rightleftarrows \left[\mathrm{V(H_2O)_{(6-x)}(anion^-)_x}\right]^{(3-x)+} + x\ \mathrm{H_2O}$$

The equilibrium constant (K_{eq}) at standard conditions for the above reaction is related to the products and reactants as:

$$K_{eq} = \frac{\left[\mathrm{V(H_2O)_{(6-x)}(anion^-)_x}\right]^{(3-x)+}}{[\mathrm{V(H_2O)_6}]^{3+}\ (\mathrm{anion^-})^x}$$

The concentration of water (~55.5 M) in the electrolytes remain fairly constant due to the low anion concentrations used, so we assume the water concentration remains at its standard concentration and can thus be omitted in K_{eq} defined above. Re-arranging the above equation to obtain the ratio of anion complexed V^{3+} (i.e., $\left[\mathrm{V(H_2O)_{(6-x)}(anion^-)_x}\right]^{(3-x)+}$) to only water-complexed V^{3+} (i.e., $[\mathrm{V(H_2O)_6}]^{3+}$):

$$\frac{\left[\mathrm{V(H_2O)_{(6-x)}(anion^-)_x}\right]^{(3-x)+}}{[\mathrm{V(H_2O)_6}]^{3+}} = K_{eq}\ (\mathrm{anion^-})^x \qquad \text{(eq. S3.1)}$$

Thus, the ratio of anion-complexed V^{3+} and water-complexed V^{3+} is proportional to the concentration of anion raised to the power of x.

From the UV-vis spectra of V^{3+} at varied anion concentrations, we can relate the peak location (in nm) corresponding to $^3T_{1g} \rightarrow {}^3T_{2g}$ to concentrations of anion-complexed V^{3+} and water-complexed V^{3+} as:

$$P_{\left[V(H_2O)_{(6-x)}(anion^-)_x\right]^{(3-x)+}} = \gamma\left(\frac{\left[V(H_2O)_{(6-x)}(anion^-)_x\right]^{(3-x)+}}{[V(H_2O)_6]^{3+} + \left[V(H_2O)_{(6-x)}(anion^-)_x\right]^{(3-x)+}}\right) + P_{[V(H_2O)_6]^{3+}}$$

where $P_{\left[V(H_2O)_{(6-x)}(anion^-)_x\right]^{(3-x)+}}$ and $P_{[V(H_2O)_6]^{3+}}$ is the peak location of $^3T_{1g} \rightarrow {}^3T_{2g}$ transition for a solution containing only anion-complexed V^{3+} and water-complexed V^{3+}, respectively and γ is the shift in peak location of $^3T_{1g} \rightarrow {}^3T_{2g}$ transition of only anion-complexed V^{3+} relative to only water-complexed V^{3+}.

For low concentrations of anion-complexed V^{3+} (i.e., $[V(H_2O)_6]^{3+} \gg \left[V(H_2O)_{(6-x)}(anion^-)_x\right]^{(3-x)+}$), the above equation simplifies to:

$$P_{\left[V(H_2O)_{(6-x)}(anion^-)_x\right]^{(3-x)+}} = \gamma\left(\frac{\left[V(H_2O)_{(6-x)}(anion^-)_x\right]^{(3-x)+}}{[V(H_2O)_6]^{3+}}\right) + P_{[V(H_2O)_6]^{3+}} \quad \text{(eq. S3.2)}$$

Combining **eq. S3.1** and **S3.2** we get:

$$P_{\left[V(H_2O)_{(6-x)}(anion^-)_x\right]^{(3-x)+}} = \gamma\left(K_{eq}\,(anion^-)^x\right) + P_{[V(H_2O)_6]^{3+}} \quad \text{(eq. S3.3)}$$

Thus the dependency of peak location of $^3T_{1g} \rightarrow {}^3T_{2g}$ transition (at low concentrations of anion complexed V^{3+}) can be used to estimate the number of anions that are entering the V^{3+} inner coordination sphere.

3.5.6 Supporting Figures

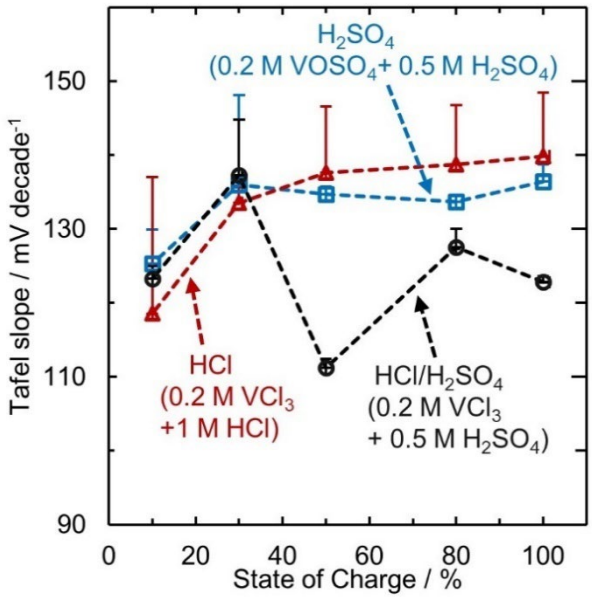

Figure S3.1. Tafel Slopes of V^{2+}/V^{3+} Reaction on Glassy Carbon in H_2SO_4, HCl/H_2SO_4, and HCl. Tafel slopes as a function of State of Charge for V^{2+}/V^{3+} reaction in H_2SO_4 (0.2 M $VOSO_4$ + 0.5 M H_2SO_4), HCl/H_2SO_4 (0.2 M VCl_3 + 0.5 M H_2SO_4), and HCl (0.2 M VCl_3 + 1M HCl).

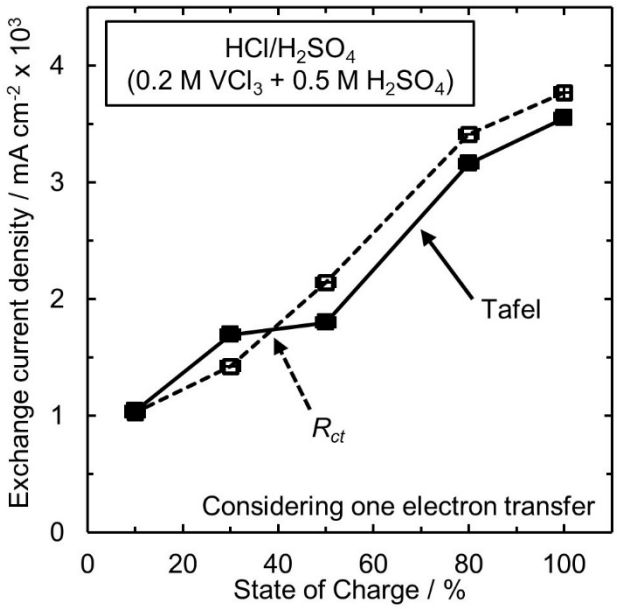

Figure S3.2. Exchange Current Density of V^{2+}/V^{3+} Reaction on Glassy Carbon in HCl/H_2SO_4 Using Two Independent Methods. Exchange current densities as a function of State of Charge for HCl/H_2SO_4 (0.2 M VCl_3 + 0.5 M H_2SO_4) obtained by: (i) (solid line) Using the Tafel equation, and (ii) (dashed line) Charge transfer resistance (R_{ct}) at open circuit voltage considering one electron transfer.

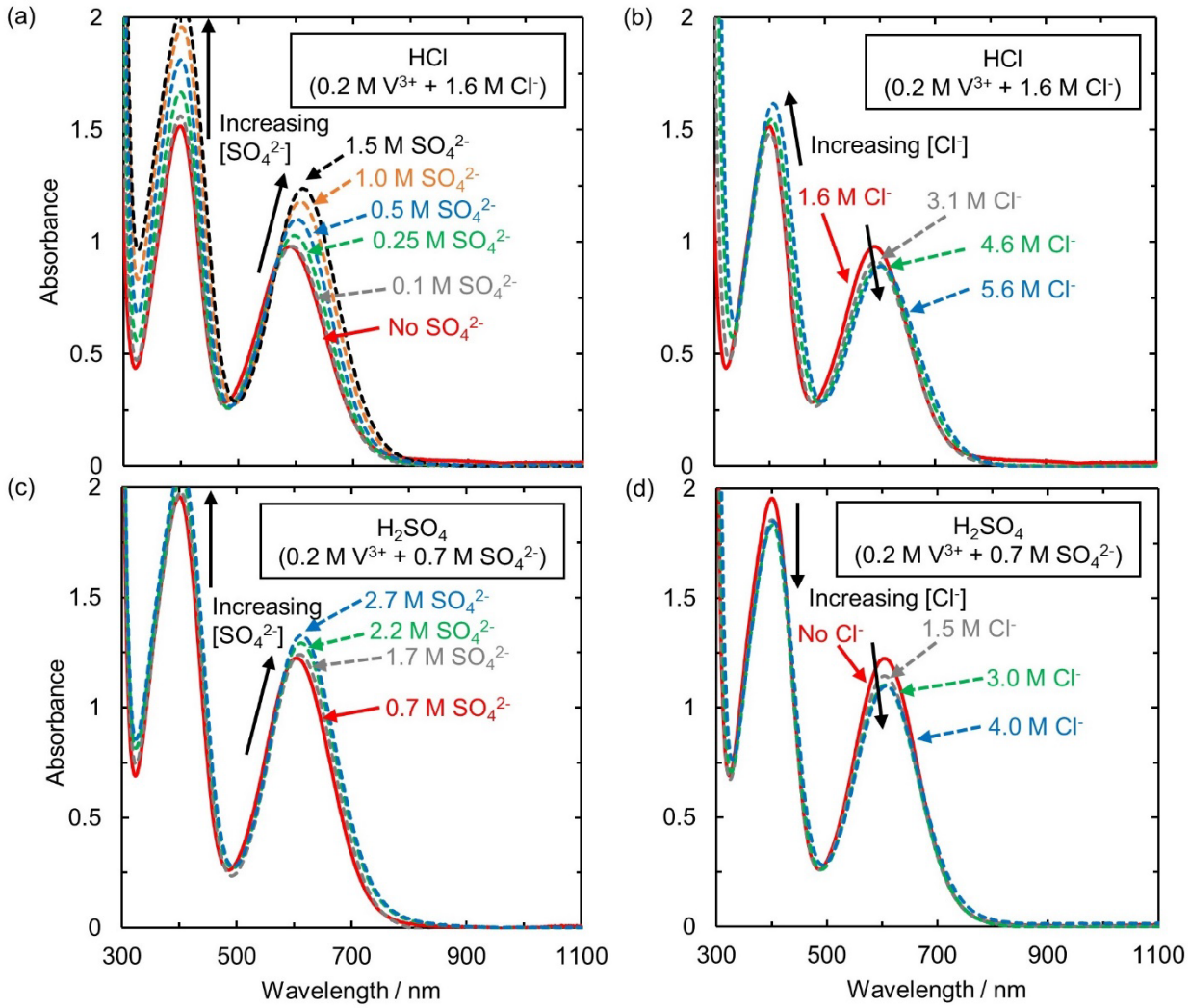

Figure S3.3. UV-vis Spectra of V^{3+} at Varying Concentrations of SO_4^{2-} and Cl^-. UV-vis absorbance of V^{3+} as a function of wavelength at room temperature (T = 23.3 °C) in the HCl (0.2 M VCl_3 + 1 M HCl) with increase in **(a)** SO_4^{2-} and **(b)** Cl^- anion concentration and H_2SO_4 (0.2 M $VOSO_4$ + 0.5 M H_2SO_4) with increase in **(c)** SO_4^{2-} and **(d)** Cl^- anion concentration. V^{3+} spectra are obtained by reducing vanadium salt completely to V^{2+} and oxidizing back to V^{3+} followed by the addition of sodium sulfate or sodium chloride to obtain spectra at high SO_4^{2-} (2.7 M SO_4^{2-}) and Cl^- (5.6 M Cl^-) concentrations.

3.6 References

(1) Kim, S.; Vijayakumar, M.; Wang, W.; Zhang, J.; Chen, B.; Nie, Z.; Chen, F.; Hu, J.; Li, L.; Yang, Z. Chloride Supporting Electrolytes for All-Vanadium Redox Flow Batteries. *Phys. Chem. Chem. Phys.* **2011**, *13*, 18186–18193.

(2) Skyllas-Kazacos, M. Novel Vanadium Chloride/Polyhalide Redox Flow Battery. *J. Power Sources* **2003**, *124*, 299–302.

(3) Wang, W.; Kim, S.; Chen, B.; Nie, Z.; Zhang, J.; Xia, G.-G.; Li, L.; Yang, Z. A New Redox Flow Battery Using Fe/V Redox Couples in Chloride Supporting Electrolyte. *Energy Environ. Sci.* **2011**, *4*, 4068–4073.

(4) Wang, W.; Nie, Z.; Chen, B.; Chen, F.; Luo, Q.; Wei, X.; Xia, G. G.; Skyllas-Kazacos, M.; Li, L.; Yang, Z. A New Fe/V Redox Flow Battery Using a Sulfuric/Chloric Mixed-Acid

Supporting Electrolyte. *Adv. Energy Mater.* **2012**, *2* (4), 487–493.
(5) Li, L.; Kim, S.; Wang, W.; Vijayakumar, M.; Nie, Z.; Chen, B.; Zhang, J.; Xia, G.; Hu, J.; Graff, G.; et al. A Stable Vanadium Redox-Flow Battery with High Energy Density for Large-Scale Energy Storage. *Adv. Energy Mater.* **2011**, *1* (3), 394–400.
(6) Vijayakumar, M.; Wang, W.; Nie, Z.; Sprenkle, V.; Hu, J. Elucidating the Higher Stability of Vanadium(V) Cations in Mixed Acid Based Redox Flow Battery Electrolytes. *J. Power Sources* **2013**, *241*, 173–177.
(7) Richens, D. T. Group 5 Elements: Vanadium, Niobium and Tantalum. In *The Chemistry of Aqua Ions: Synthesis, Structure and Reactivity*; John Wiley & Sons, Ltd: Chichester, UK, 1997; pp 230–235.
(8) Sepehr, F.; Paddison, S. J. The Solvation Structure and Thermodynamics of Aqueous Vanadium Cations. *Chem. Phys. Lett.* **2013**, *585*, 53–58.
(9) Bon, M.; Laino, T.; Curioni, A.; Parrinello, M. Characterization of Vanadium Species in Mixed Chloride−Sulfate Solutions: An Ab Initio Metadynamics Study. *J. Phys. Chem. C* **2016**, *120*, 10791–10798.
(10) Vijayakumar, M.; Li, L.; Nie, Z.; Yang, Z.; Hu, J. Structure and Stability of Hexa-Aqua V(III) Cations in Vanadium Redox Flow Battery Electrolytes. *Phys. Chem. Chem. Phys.* **2012**, *14*, 10233–10242.
(11) Gupta, S.; Lim, T. M.; Mushrif, S. H. Insights into the Solvation of Vanadium Ions in the Vanadium Redox Flow Battery Electrolyte Using Molecular Dynamics and Metadynamics. *Electrochim. Acta* **2018**, *270*, 471–479.
(12) Oldenburg, F. J.; Bon, M.; Perego, D.; Polino, D.; Laino, T.; Gubler, L.; Schmidt, T. J. Revealing the Role of Phosphoric Acid in All-Vanadium Redox Flow Batteries with DFT Calculations and In Situ Analysis. *Phys. Chem. Chem. Phys* **2018**, *20*, 23664–23673.
(13) Martin. Ernest L.; Bentley, K. E. Spectrophotometric Investigation of Vanadium(II), Vanadium(III), and Vanadium(IV) in Various Media. *Anal. Chem.* **1962**, *34* (3), 354–358.
(14) Li, B.; Gu, M.; Nie, Z.; Shao, Y.; Luo, Q.; Wei, X.; Li, X.; Xiao, J.; Wang, C.; Sprenkle, V.; et al. Bismuth Nanoparticle Decorating Graphite Felt as a High-Performance Electrode for an All-Vanadium Redox Flow Battery. *Nano Lett.* **2013**, *13* (3), 1330–1335.
(15) Yang, X.; Liu, T.; Xu, C.; Zhang, H.; Li, X.; Zhang, H. The Catalytic Effect of Bismuth for VO_2^+/VO^{2+} and V^{3+}/V^{2+} Redox Couples in Vanadium Flow Batteries. *J. Energy Chem.* **2017**, *26* (1), 1–7.
(16) Wei, L.; Zhao, T. S.; Zeng, L.; Zhou, X. L.; Zeng, Y. K. Copper Nanoparticle-Deposited Graphite Felt Electrodes for All Vanadium Redox Flow Batteries. *Appl. Energy* **2016**, *180*, 386–391.
(17) Mehboob, S.; Mehmood, A.; Lee, J.-Y.; Shin, H.-J.; Hwang, J.; Abbas, S.; Ha, H. Y. Excellent Electrocatalytic Effects of Tin Through In Situ Electrodeposition on the Performance of All-Vanadium Redox Flow Batteries. *J. Mater. Chem. A* **2017**, *5*, 17388–17400.
(18) Shen, J.; Liu, S.; He, Z.; Shi, L. Influence of Antimony Ions in Negative Electrolyte on the Electrochemical Performance of Vanadium Redox Flow Batteries. *Electrochim. Acta* **2015**, *151*, 297–305.
(19) Blasi, A. Di; Busacca, C.; Blasi, O. Di; Briguglio, N.; Antonucci, V. Synthesis and Characterization of Electrospun Nickel-Carbon Nanofibers as Electrodes for Vanadium Redox Flow Battery. *J. Electrochem. Soc.* **2018**, *165* (7), A1478–A1485.
(20) Sun, B.; Skyllas-Kazacos, M. Chemical Modification of Graphite Electrode Materials for

Vanadium Redox Flow Battery Application—Part II. Acid Treatments. *Electrochim. Acta* **1992**, *37* (13), 2459–2465.
(21) Jiang, Z.; Klyukin, K.; Alexandrov, V. First-Principles Study of Adsorption–Desorption Kinetics of Aqueous V^{2+}/V^{3+} Redox Species on Graphite in a Vanadium Redox Flow Battery. *Phys. Chem. Chem. Phys.* **2017**, *19*, 14897–14901.
(22) Anbar, M.; Hart, E. J. The Reactivity of Metal Ions and Some Oxy Anions toward Hydrated Electrons. *J. Phys. Chem.* **1965**, *69* (3), 973–977.
(23) Liu, Q. H.; Grim, G. M.; Papandrew, A. B.; Turhan, A.; Zawodzinski, T. A.; Mench, M. M. High Performance Vanadium Redox Flow Batteries with Optimized Electrode Configuration and Membrane Selection. *J. Electrochem. Soc.* **2012**, *159* (8), A1246–A1252.
(24) Darling, R. M.; Perry, M. L. The Influence of Electrode and Channel Configurations on Flow Battery Performance. *J. Electrochem. Soc.* **2014**, *161* (9), A1381–A1387.
(25) Aaron, D.; Sun, C.-N.; Bright, M.; Papandrew, A. B.; Mench, M. M.; Zawodzinski, T. A. In Situ Kinetics Studies in All-Vanadium Redox Flow Batteries. *ECS Electrochem. Lett.* **2013**, *2* (3), A29–A31.
(26) Fabjan, C.; Garche, J.; Harrer, B.; Jö Rissen, L.; Kolbeck, C.; Philippi, F.; Tomazic, G.; Wagner, F. The Vanadium Redox-Battery: An Efficient Storage Unit for Photovoltaic Systems. *Electrochim. Acta* **2001**, *47* (5), 825–831.
(27) Xiong, X. Y.; Poorten, H. Vander; Crappe, M. Impedance Parameters of Ni/Cd Batteries-Individual Electrode Characteristics. Application to Modelling and State of Charge Determinations. *Electrochim. Acta* **1996**, *41* (7–8), 1267–1275.
(28) Bard, A. J.; Faulkner, L. R. *Electrochemical Methods: Fundamentals and Applications*; John Wiley & Sons, Inc.: New York, 2001.
(29) Weaver, M. J. Activation Parameters for Simple Electrode Reactions. Application to the Elucidation of Ion-Solvent Interactions in the Transition State for Heterogeneous Electron Transfer. *J. Phys. Chem.* **1979**, *83* (13), 1748–1757.
(30) Landry-Hum, J.; Bussière, G.; Daniel, C.; Reber, C. Triplet Electronic States in d^2 and d^8 Complexes Probed by Absorption Spectroscopy: A CASSCF/CASPT2 Analysis of $[V(H_2O)_6]^{3+}$ and $[Ni(H_2O)_6]^{2+}$. *Inorg. Chem.* **2001**, *40* (11), 2595–2601.
(31) Bussière, G.; Beaulac, R.; Cardinal-David, B.; Reber, C. Coupled Electronic States in Trans-$MCl_2(H_2O)_4^{n+}$ Complexes (M: Ni^{2+}, Co^{2+}, V^{3+}, Cr^{3+}) Probed by Absorption and Luminescence Spectroscopy. *Coord. Chem. Rev.* **2001**, *219–221*, 509–543.
(32) Furman, S.; Garner, C. Absorption Spectra of Vanadium(III) and Vanadium(IV) Ions in Complexing and Non-Complexing Media. *J. Am. Chem. Soc.* **1950**, *72* (4), 1785–1789.
(33) Pajdowski, L. A Spectrophotometric Study of the Hydrolysis of Vanadium (III) Ion. *J. Inorg. Nucl. Chem.* **1966**, *28* (2), 433–442.
(34) Tanimoto, S.; Ichimura, A. Discrimination of Inner and Outer Sphere Electrode Reactions by Cyclic Voltammetry Experiments. *J. Chem. Educ.* **2013**, *90* (6), 778–781.
(35) Heyrovský, J. Retarded Electrodeposition of Metals Studied Oscillographically with Mercury Capillary Electrodes. *Discuss. Faraday Soc.* **1947**, *1*, 212–225.
(36) Sykes, A. G. Further Advances in the Study of Mechanisms of Redox Reactions. *Adv. Inorg. Chem. Radiochem.* **1968**, *10*, 153–245.
(37) Aikens, D. A.; Jr., J. W. R. Effect of Chloride on the Kinetics of Electroöxidation of Chromium (II) in Acidic Perchlorate Medium. *J. Phys. Chem.* **1961**, *65* (7), 1213–1216.
(38) Rodes, A.; Feliu, J. M.; Aldaz, A.; Clavilier, J. The Influence of Polyoriented Gold Electrodes Modified by Reversibly and Irreversibly Adsorbed Ad-Atoms on the Redox

Behaviour of the Cr(III) / Cr(II) Couple and the Effect of Chloride Ions. *J. Electroanal. Chem* **1989**, *271*, 127–139.
(39) Weber, J.; Samec, Z.; Mareček, V. The Effect of Anion Adsorption on the Kinetics of the Fe^{3+}/Fe^{2+} Reaction on Pt and Au Electrodes in $HClO_4$. *J. Electroanal. Chem. Interfacial Electrochem.* **1978**, *89* (2), 271–288.
(40) Nagy, Z.; Blaudeau, J. P.; Hung, N. C.; Curtiss, L. A.; Zurawski, D. J. Chloride Ion Catalysis of the Copper Deposition Reaction. *J. Electrochem. Soc.* **1995**, *142* (6), L87–L89.
(41) Niki, K.; Mizota, H. Effect of Specific Adsorbed Anions on the Electrode Kinetics of the V(III)/V(II) and Eu(III)/Eu(II) Couples. *J Electroanal. Chem* **1976**, *72*, 307–317.
(42) Jiang, Z.; Klyukin, K.; Miller, K.; Alexandrov, V. Mechanistic Theoretical Investigation of Self-Discharge Reactions in a Vanadium Redox Flow Battery. *J. Phys. Chem. B* **2019**, *123*, 3976–3983.
(43) Zeng, Z.; Sun, Y.; Zhang, J. The Electrochemical Reduction Mechanism of Trivalent Chromium in the Presence of Formic Acid. *Electrochem. commun.* **2009**, *11* (2), 331–334.
(44) Newton, T. W.; Baker, F. B. The Intermediate in the Reaction between Vanadium(II) and Vanadium(IV). *Inorg. Chem* **1964**, *3* (4), 569–573.
(45) Choi, N. H.; Kwon, S. -k.; Kim, H. Analysis of the Oxidation of the V(II) by Dissolved Oxygen Using UV-Visible Spectrophotometry in a Vanadium Redox Flow Battery. *J. Electrochem. Soc.* **2013**, *160* (6), A973–A979. https://doi.org/10.1149/2.145306jes.
(46) Brooker, R. P.; Bell, C. J.; Bonville, L. J.; Kunz, H. R.; Fenton, J. M. Determining Vanadium Concentrations Using the UV-Vis Response Method. *J. Electrochem. Soc.* **2015**, *162* (4), A608–A613.
(47) Valiev, M.; Bylaska, E. J.; Govind, N.; Kowalski, K.; Straatsma, T. P.; Van Dam, H. J. J.; Wang, D.; Nieplocha, J.; Apra, E.; Windus, T. L.; et al. NWChem: A Comprehensive and Scalable Open-Source Solution for Large Scale Molecular Simulations. *Comput. Phys. Commun.* **2010**, *181* (9), 1477–1489.
(48) Valiev, M.; Yang, J.; Adams, J. A.; Taylor, S. S.; Weare, J. H. Phosphorylation Reaction in CAPK Protein Kinase-Free Energy Quantum Mechanical/ Molecular Mechanics Simulations. *J. Phys. Chem. B* **2007**, *111* (47), 13455–13464.
(49) Berendsen, H. J. C.; Postma, J. P. M.; Van Gunsteren, W. F.; Dinola, A.; Haak, J. R. Molecular Dynamics with Coupling to an External Bath. *J. Chem. Phys.* **1984**, *81*, 3684–3690.
(50) Wang, J.; Cieplak, P.; Kollman, P. A. How Well Does a Restrained Electrostatic Potential (RESP) Model Perform in Calculating Conformational Energies of Organic and Biological Molecules? *J. Comput. Chem.* **2000**, *21* (12), 1049–1074.
(51) Gupta, S.; Wai, N.; Lim, T. M.; Mushrif, S. H. Corrigendum to "Force-Field Parameters for Vanadium Ions (+ 2, + 3, + 4, + 5) to Investigate Their Interactions Within the Vanadium Redox Flow Battery Electrolyte Solution" [Journal of Molecular Liquids, 215 (2016) 596–602]. *J. Mol. Liq.* **2016**, *219*, 1180.
(52) Dawson, W.; Gygi, F. Equilibration and Analysis of First-Principles Molecular Dynamics Simulations of Water. *J. Chem. Phys.* **2018**, *148*, 124501.
(53) Grimme, S.; Antony, J.; Ehrlich, S.; Krieg, H. A Consistent and Accurate Ab Initio Parametrization of Density Functional Dispersion Correction (DFT-D) for the 94 Elements H-Pu. *J. Chem. Phys.* **2010**, *132*, 154104.
(54) Klamt, A.; Schüürmann, G. COSMO: A New Approach to Dielectric Screening in Solvents with Explicit Expressions for the Screening Energy and Its Gradient. *J. Chem. Soc., Perkin*

Trans. 2 **1993**, 799–805.
(55) Rappoport, D.; Furche, F. Property-Optimized Gaussian Basis Sets for Molecular Response Calculations. *J. Chem. Phys* **2010**, *133*, 134105.
(56) Runge, E.; Gross, E. K. U. Density-Functional Theory for Time-Dependent Systems. *Phys. Rev. Lett.* **1984**, *52* (12), 997–1000.
(57) Yanai, T.; Tew, D. P.; Handy, N. C. A New Hybrid Exchange-Correlation Functional Using the Coulomb-Attenuating Method (CAM-B3LYP). *Chem. Phys. Lett.* **2004**, *393* (1–3), 51–57.

Chapter 4 : The Effect of Anion Bridging on V^{2+}/V^{3+} Charge Transfer*

* This chapter is adapted with permission from Agarwal, H.; Florian, J.; Goldsmith, B. R.; Singh, N. The Effect of Anion Bridging on Heterogeneous Charge Transfer for V^{2+}/V^{3+}. *Cell Reports Phys. Sci.* **2021**, *2* (1), 100307. The computational portion of the work is conducted by Jacob Florian.

4.1 Summary

In this chapter, we provide insights into the V^{2+}/V^{3+} reaction mechanism in $HClO_4$, H_2SO_4, HCl, HBr, and HI. We identify the V^{2+} and V^{3+} structures in these electrolytes using Extended X-ray Absorption Fine Structure, UV-vis, and density functional theory. We show that V^{2+}/V^{3+} kinetics correlate with the energy of vanadium intermediate bound to carbon through a bridging anion (*[bridge−V^{3+}]). The anion-induced kinetic enhancement is from a decreased activation energy because of changing *[bridge−V^{3+}] energy. The *[bridge−V^{3+}] energy increases in the order of anion polarizability (OH^- < Cl^- < Br^- < I^-), explaining previous reports that correlate anion polarizability with kinetics of other 3*d* transition metal ion redox couples.

4.2 Introduction

The enhancement in kinetics observed for V^{2+}/V^{3+} in the presence of Cl^- discussed in **Chapter 3** is also seen for Cr^{2+}/Cr^{3+},[1,2] Fe^{2+}/Fe^{3+},[3] and Cu^{+}/Cu^{2+} redox couples on metal electrodes.[4] Moreover, the extent of kinetic enhancement for Cr^{2+}/Cr^{3+} on mercury electrodes follows the order I^- > Br^- > Cl^- > OH^-.[1] Anion coverage, which mirrors the order of kinetic enhancement, is one explanation used to rationalize the effect of anions on charge transfer (CT) in Cr^{2+}/Cr^{3+}, Fe^{2+}/Fe^{3+}, and Cu^{+}/Cu^{2+} redox couples.[1,5] An increased anion coverage (**Scheme 4.1b**) would affect the

kinetics by increasing the concentration of active intermediates, resulting in a higher apparent frequency factor. The enhancement trend is also in the same order as increasing polarizability of the free anion (i.e., $I^- > Br^- > Cl^- > OH^-$); thus, the polarizability of the anion is also hypothesized as a cause of this enhancement.[6–8] Although anion polarizability correlates with the enhancement in kinetics, it is unclear why polarizability of the anion would describe the kinetics of various transition metal ion redox couples considering the anion polarizability is just the extent of electron cloud distortion in the presence of an electric field,[7,9,10] and neither accounts for the presence of the electrode surface nor the metal ion involved.

Anions can affect the structure of the adsorbed metal-anion intermediate or the metal ion complex in solution by entering the first coordination sphere. Therefore, rather than only considering anion polarizability or anion coverage (**Scheme 4.1b**), the metal ion itself should have a major effect on kinetics (**Scheme 4.1a**). Currently, the dearth of molecular level understanding of the CT pathway has made it difficult to explain how anions influence the redox kinetics for transition metal ions.

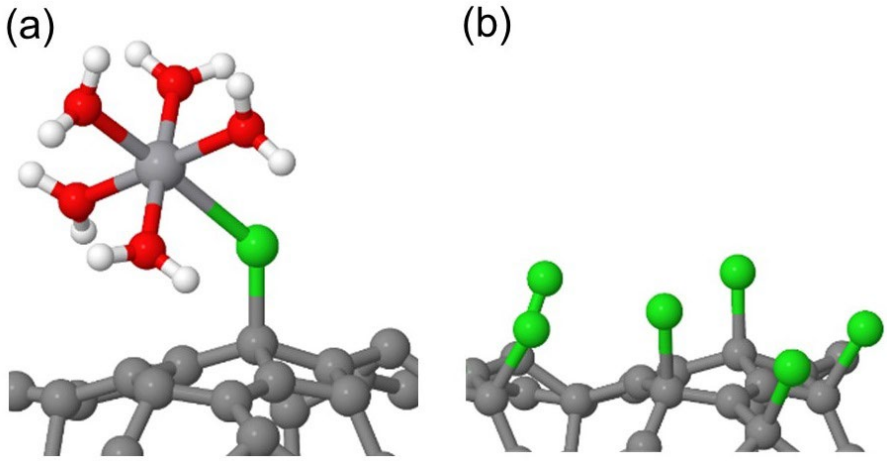

Scheme 4.1. Two Possible Causes for the Anion Effect on Charge Transfer Kinetics of Various Transition Metal Ion Redox Couples including V^{2+}/V^{3+} on Electrodes (e.g., Glassy Carbon). (a) Metal (M) ion complex adsorbed via an anion bridge (*[bridge−M]) whose energy controls the kinetics. **(b)** Anion coverage controlling the concentration of active intermediates. Atom color legend: dark gray = electrode (e.g., glassy carbon), light gray = metal (e.g., vanadium), red = oxygen, white = hydrogen, green = anion (e.g., chloride).

The challenge in understanding the role of anions on the kinetics and CT mechanism of metal ion redox couples arises from four shortcomings in the literature: (i) rates are not always measured under kinetic control and are often not normalized by electrochemical active surface area, (ii) apparent activation energies (E_a) and frequency factors are not evaluated, which makes it difficult to know if kinetic enhancement is related to lowered activation energy of the rate determining step (RDS) or increased coverages, (iii) the structure of the reacting species in different electrolytes is not known under electrochemical conditions, and (iv) first-principles modeling has not been utilized to understand the influence of anion coverage and adsorption strength of the metal-anion intermediates on CT. We address these four shortcomings in literature, focusing on the V^{2+}/V^{3+} redox couple, by a combined experimental and computational study. This combined analysis enables us to understand the energetics of the vanadium-anion adsorbed intermediate and propose a reaction mechanism that explains the kinetics of V^{2+}/V^{3+} in all tested electrolytes.

In this chapter, we demonstrate by operating under kinetically limiting regimes that the exchange current densities (i_o) of the V^{2+}/V^{3+} reaction on glassy carbon (GC) increase in the order H_2SO_4 < HCl < $HClO_4$ < HBr < HI, with the apparent activation energies (E_a) following the order H_2SO_4 > $HClO_4$ > HCl > HBr > HI. The reaction kinetics in a mixture of HI/H_2SO_4 is close to that of pure H_2SO_4, which we attribute to SO_4^{2-} preventing the formation of the active intermediate responsible for the high activity in HI. The decrease in E_a for V^{2+}/V^{3+} occurs in the order of increasing polarizability of the anion that forms the bridge for CT. However, the apparent frequency factor, which is proportional to the coverage of the active intermediate, follows an order that is opposite to the DFT-predicted anion coverages. This contradiction suggests that the kinetic enhancement does not result from higher anion coverage.

We use Extended X-ray Absorption Fine Structure spectroscopy (EXAFS), Molecular Dynamics EXAFS (MD-EXAFS), UV-vis spectroscopy, and ligand-exchange free energy calculations (ΔG_L) to identify the structures of V^{2+} and V^{3+} in these five electrolytes. We in particular report the structures of V^{2+} and V^{3+} in commercially used H_2SO_4 and HCl using EXAFS. V^{2+} exists in hydrated form as $[V(H_2O)_6]^{2+}$ in all the electrolytes, whereas V^{3+} complexes with anions. We find that the V^{2+}/V^{3+} reaction kinetics increases with decreasing adsorption strength of the *[bridge−V^{3+}] intermediate (i.e., increase in energy of the vanadium-anion intermediate). This finding is supported by a postulated mechanism that fits the observed experimental behavior.

We postulate the adsorption strength of the metal-anion intermediate, similar to V^{2+}/V^{3+}, can be used to control the heterogeneous CT for other reactions that obey a similar anion-bridging mechanism such as Cr^{2+}/Cr^{3+}, Fe^{2+}/Fe^{3+}, and Cu^{+}/Cu^{2+}. The structure of the reacting species, the identity of the anions, and the electrode surface all affect the energetics of the formed intermediate and should be considered when interpreting inner sphere CT kinetics.

4.3 Results and Discussions

4.3.1 V^{2+}/V^{3+} Reaction Kinetics on Glassy Carbon

We report the i_o, reaction orders, and E_a for the V^{2+}/V^{3+} reaction on GC in five acidic electrolytes obtained from steady state current (Tafel method) and impedance measurements (CT Resistance method). The data in **Figure 4.1** shows that the V^{2+}/V^{3+} reaction kinetics varies with State of Charge $\left(\text{SoC} = \frac{[V^{2+}]}{[V^{2+}]+[V^{3+}]}\right)$ in $HClO_4$, HBr, and HI, similar to HCl and H_2SO_4. The i_o increases (**Figure 4.1a**) and the E_a decreases (**Figure 4.1b**) with increasing SoC in HBr, HCl, and H_2SO_4. On the other hand, the i_o displays a maximum (and minimum in E_a) between 50−80% SoC in $HClO_4$ and HI. The i_o are evaluated in the kinetically limiting regime using the oxidation currents to prevent contributions from hydrogen evolution reaction (HER).

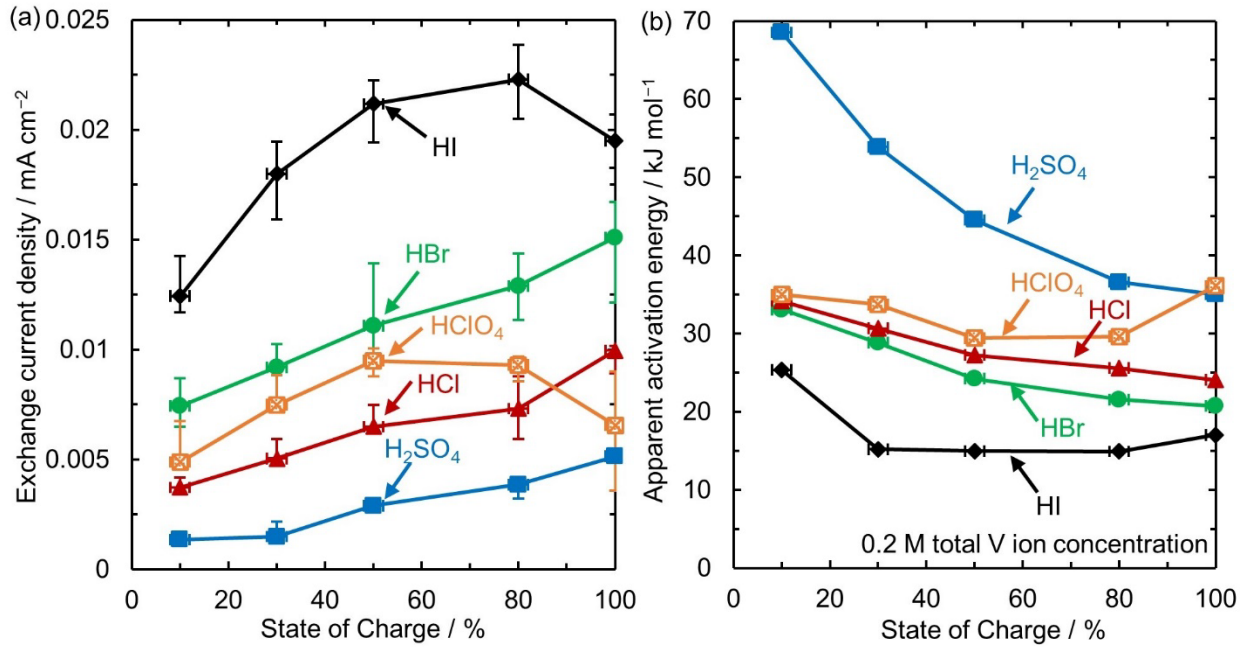

Figure 4.1. Kinetic Parameters for V^{2+}/V^{3+} Reaction on Glassy Carbon in $HClO_4$, H_2SO_4, HCl, HBr, and HI Acidic Electrolytes. (a) Exchange current densities and **(b)** Apparent activation energies as a function of State of Charge for the V^{2+}/V^{3+} redox reaction evaluated from the Tafel method in 1 M HI, 1 M HBr, 1 M $HClO_4$, 1 M HCl, and 0.5 M H_2SO_4 at 0.2 M total vanadium ion concentration. Values for H_2SO_4 and HCl are taken from reference 11. The exchange current densities are unchanged in 1 M H_2SO_4 in comparison to 0.5 M H_2SO_4. The counter electrolyte is $HClO_4$ instead of H_2SO_4 for studying HI to prevent contamination from SO_4^{2-} crossing through the membrane. The H^+ ion concentration in the electrolyte in the counter electrode compartment is the same as that of the working electrolyte. All measurements are conducted at room temperature (T = 23.3 °C).

By comparing exchange current density evaluated using the Tafel method (i_o) and CT Resistance method ($i_{o,R_{ct}}$), we show that the V^{2+}/V^{3+} reaction is an overall two-electron transfer reaction with one electron in the RDS in HBr, the same as in HCl (**Figure S4.1**). In contrast, the V^{2+}/V^{3+} reaction is overall one-electron transfer in $HClO_4$ and HI (**Figure S4.2**), the same as in H_2SO_4. This overall two-electron transfer behavior observed in HCl and HBr may arise either due to the formation of vanadium dimers on the electrode surface, a comproportionation reaction between adsorbed V^{2+} and V^{4+} on surface to form V^{3+},[11,12] or the partial CT from halide when vanadium di-halide (chloride and bromide) complexes are formed in solution as discussed in **Chapter 3**. Despite the difference in the overall number of electrons, the Tafel slopes (b) in all these electrolytes range from 120–150 mV decade^{-1} (**Figure S4.3**), corresponding to an RDS with one-electron transfer.

Because i_o includes the contribution of both apparent frequency factor and E_a, we measure both i_o and E_a to understand how anions influence the kinetics. These measurements enable us to distinguish if the kinetic enhancement is related to the apparent frequency factor or E_a. The i_o of the V^{2+}/V^{3+} reaction in these electrolytes increases in the order of H_2SO_4 < HCl < $HClO_4$ < HBr < HI. The E_a decreases in the order of $HClO_4$ > HCl > HBr > HI and follows the same order as the anion polarizability (OH^- < Cl^- < Br^- < I^-). The decreasing E_a with increasing anion polarizability implies that an adsorbed vanadium species with an anion bridge may act as an intermediate in the overall CT mechanism. The i_o in $HClO_4$ is higher compared with HCl (**Figure 4.1a**), despite its higher E_a (**Figure 4.1b**) because the i_o contains contributions from the apparent frequency factor in addition to E_a. We hypothesize the slow kinetics in H_2SO_4 arises from SO_4^{2-} preventing the formation of an active intermediate, because SO_4^{2-} cannot act as a bridge for CT reactions.[13]

To clarify the reaction mechanism, the reaction orders of V^{2+} and V^{3+} in different electrolytes are extracted by regression analysis on i_o and are given in **Table 4.1**. No dependence on the total vanadium concentration in H_2SO_4 was shown in **Chapter 3**, and the behavior with SoC was explained by V^{2+} and V^{3+} having equal and opposite reaction orders (i.e., positive order for V^{2+} and a negative order for V^{3+}).[11] Reaction orders evaluated in H_2SO_4 here (**Table 4.1**) corroborate this finding. Due to the same qualitative trend in i_o (and E_a) with SoC in HCl and HBr (**Figure 4.1**) as in H_2SO_4, the V^{2+} and V^{3+} orders in HCl and HBr are also evaluated assuming they are equal and opposite (**Table S4.1**). In contrast, both V^{2+} and V^{3+} have positive orders in HI and $HClO_4$ (**Table S4.1**), which explains the maxima observed in i_o around 50−80% SoC in **Figure 4.1**. Although an outer sphere CT reaction rationalizes the positive orders for both V^{2+} and V^{3+} in $HClO_4$ and HI, an outer sphere CT reaction cannot describe the observed negative reaction order of V^{3+} in H_2SO_4, HCl, and HBr as discussed in the Supporting Information (SI). Therefore, we

choose a single inner sphere CT reaction mechanism described below that explains the reaction order behavior in all electrolytes.

Table 4.1. Reaction Orders for V^{2+}/V^{3+} on Glassy Carbon in H_2SO_4 and HI by Regression. The orders are calculated from exchange current densities at different total vanadium concentrations (0.05, 0.1 and 0.2 M V) at room temperature using regression.

Electrolyte	$[V^{2+}]$ order (γ)		$[V^{3+}]$ order (ε)	
	i_o	$i_{o,R_{ct}}$	i_o	$i_{o,R_{ct}}$
H_2SO_4	0.25	0.22	−0.25	−0.23
HI with $HClO_4$ on counter electrode	0.67	0.68	0.28	0.32

The experimental V^{2+}/V^{3+} rate measurements in these electrolytes can be explained by a simple inner sphere microkinetic model involving adsorbed vanadium through an anion bridge as an intermediate (**Scheme 4.1a**):

$$V^{2+} + * \rightleftarrows *V^{2+} \quad (1)$$

$$*V^{2+} \rightleftarrows *V^{3+} + e^- \quad (2)$$

$$*V^{3+} \rightleftarrows V^{3+} + * \quad (3)$$

Here * represents a glassy carbon active site, which is either free or occupied by a reactive species. The i_o, assuming the single electron transfer in step 2 is the RDS (based on the measured Tafel slopes, **Figure S4.3**), can be written as (derived in the SI):

$$i_o = \frac{nFk_oK_1[V^{2+}]}{(K_1[V^{2+}] + K_3[V^{3+}] + 1)}\left(\frac{[V^{3+}]}{[V^{2+}]}\right)^{\left(\frac{n_k(1-\alpha)}{n}\right)} \quad \text{(eq. 4.1)}$$

where F = Faraday's constant, α = transfer coefficient, n_k = number of electrons involved in the RDS (1), n = total number of electrons involved in the reaction, k_o = standard rate constant for step 2 (i.e., rate constant at the V^{2+}/V^{3+} standard redox potential), and K_1 and K_3 are the adsorption constants for V^{2+} and V^{3+}, respectively.

A reaction model involving an adsorbed anion (**Scheme 4.1b**) can also explain the observed reaction orders of V^{2+} and V^{3+} in all the electrolytes as discussed in the SI, with the reaction kinetics proportional to the coverage of anions on the electrode surface.[1,5] Although the mechanisms associated with **Schemes 4.1a** and **4.1b** both explain the observed reaction orders, we will discuss further evidence to distinguish them in **Section 4.3.5**. Because the only evidence of an overall two electron transfer reaction is the comparison of i_o and $i_{o,R_{ct}}$ and there is a lack of spectroscopic evidence of an adsorbed surface intermediate, we choose a simple reaction model involving overall one electron transfer (in RDS), consistent with the observed Tafel slopes (**Figure S4.3**) in all electrolytes studied here. More complex multi-step reaction mechanisms could also describe the observed kinetic behavior, but we choose these two basic models to follow the principle of Occam's razor.[14]

We also investigate the V^{2+}/V^{3+} reaction kinetics in mixtures of anions to understand the relative energy of the formed vanadium-anion intermediates and the anion coverage. We expect the largest difference in the adsorption energy or concentration of the active intermediate between the electrolytes that have the largest difference in observed kinetics. Thus, we study the V^{2+}/V^{3+} kinetics in a mixture of I^- (highest activity) and SO_4^{2-} (lowest activity) in the following section. If the vanadium-sulfate intermediate is lower in energy than the vanadium-iodide intermediate, or the coverage of SO_4^{2-} is higher than I^- on GC, the kinetics in the HI/H_2SO_4 mixture will be more similar to H_2SO_4 than HI, and vice versa.

4.3.2 Influence of Sulfate Anions on V^{2+}/V^{3+} Reaction Kinetics

We observe that the presence of sulfate/bisulfate (SO_4^{2-}/HSO_4^-) decreases the V^{2+}/V^{3+} kinetics in HI. The i_o in HI with H_2SO_4 in the counter electrode (CE) compartment is much lower in comparison with non-interacting $HClO_4$ in the CE compartment (**Figure 4.2a**) and nearly

matches the i_o in pure H_2SO_4 at the same SoC, shown by the flat solid line in **Figure 4.2a**. In our experimental setup, we use a Nafion-117 proton-exchange membrane to separate cell compartments. We hypothesize that SO_4^{2-}/HSO_4^- anions cross through the membrane and suppress the kinetics. The data in **Figure 4.2a** supports this hypothesis, because the V^{2+}/V^{3+} kinetics decrease upon increasing the amount of $NaHSO_4$ in HI, even with $HClO_4$ in the CE compartment. At sufficiently high $NaHSO_4$ concentrations, the i_o is comparable to the case of HI with H_2SO_4 in the CE compartment. Even though the perchlorate anion will also cross-over to the working electrode compartment when using $HClO_4$ in the CE compartment, the kinetics in HI will be unaffected because of the non-interacting nature of perchlorate to complex with vanadium ions, contrary to the case of H_2SO_4 in the CE compartment. This effect of SO_4^{2-} suppressing the reaction kinetics is qualitatively captured by the larger E_a and smaller i_o for reaction in HI with H_2SO_4 compared to $HClO_4$ in the CE compartment, **Figure 4.2b**. The E_a in HI with H_2SO_4 in the CE compartment is comparable to that in pure H_2SO_4.

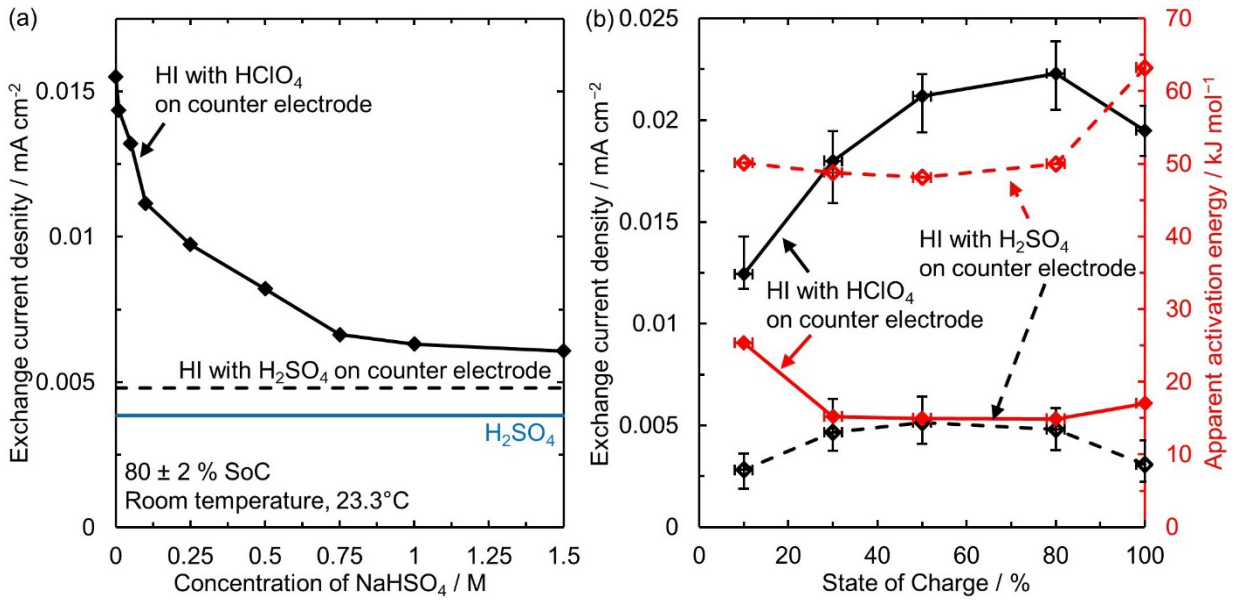

Figure 4.2. Influence of Sulfate on V^{2+}/V^{3+} Kinetics in HI on Glassy Carbon. (a) Exchange current densities at 80 ± 2% State of Charge for V^{2+}/V^{3+} reaction in 1 M HI with 1 M $HClO_4$ in counter electrode (CE) compartment with increasing concentration of $NaHSO_4$. The solid and dashed horizontal lines show the baseline exchange current densities in 0.5 M H_2SO_4 and 1 M HI with 0.5 M and 1 M H_2SO_4 in CE compartment, respectively. **(b)** Exchange current densities and apparent activation energies for V^{2+}/V^{3+} reaction in 1 M HI with 1 M $HClO_4$ (solid) and 1 M H_2SO_4 (dashed) in CE compartment.

These results that SO_4^{2-} decreases the V^{2+}/V^{3+} kinetics suggest that SO_4^{2-} prevents the formation of the active vanadium-iodide intermediate in HI. This kinetic inhibition may occur from adsorbed vanadium-sulfate complexes preventing the formation of active vanadium-iodide complexes or adsorbed sulfate blocking the adsorption of I^-. Understanding the reason for this catalytic inhibition requires knowledge of the structures of the vanadium species at the surface and the coverage of anions. To accomplish this task, we experimentally determine the structures of the species in solution, and then use DFT modeling to understand the interaction of species on carbon surface and the effect of anion coverage in the next sections.

4.3.3 Structures of V^{2+} and V^{3+} in $HClO_4$, H_2SO_4, and HCl, using EXAFS and MD-EXAFS

We use in-situ EXAFS measurements and MD-EXAFS of the V K-edge to elucidate the structures of vanadium ions in $HClO_4$, H_2SO_4, and HCl. We electrochemically control the oxidation state of vanadium in these electrolytes as either V^{2+} or V^{3+} during the measurements to

prevent any contamination from undesired oxidation to higher oxidation states. MD-EXAFS are computed by averaging the EXAFS spectra generated from *ab initio* molecular dynamics snapshots of vanadium complexes in explicit solvent.[15] All computational details for the MD-EXAFS are provided in the SI. By using both experimental EXAFS and MD-EXAFS, we are confident in attributing certain features of the spectra to specific vanadium complexes. We begin by identifying the structures of vanadium species in the absence of anion complexation by conducting EXAFS measurements in noncomplexing perchloric acid. The structural parameters in $HClO_4$ serve as a standard to identify complexed species in H_2SO_4 and HCl.

The data at the top of **Figure 4.3** shows the Img[$\tilde{\chi}$(R)] plots of hydrated $[V(H_2O)_6]^{2+}$ and $[V(H_2O)_6]^{3+}$ obtained from MD-EXAFS. Below the MD-EXAFS of $[V(H_2O)_6]^{2+}$ and $[V(H_2O)_6]^{3+}$ are the experimental EXAFS of V^{2+} and V^{3+} in $HClO_4$, where V^{2+} and V^{3+} are expected to be hydrated due to the non-interacting nature of perchlorate.[16,17] The MD-EXAFS of $[V(H_2O)_6]^{2+}$ and $[V(H_2O)_6]^{3+}$ match the dominant features of the first coordination sphere (< 3 Å) of the experimental measurements. Both MD-EXAFS and EXAFS show a shorter scattering distance of the first coordination sphere for V^{3+} compared to V^{2+}. The agreement between the MD-EXAFS and experimental EXAFS suggests that V^{2+} and V^{3+} exist in fully hydrated form in $HClO_4$. These results provide direct experimental verification of the V^{2+} and V^{3+} structures in water. No previous studies have accurately elucidated the structures of hydrated V^{2+} and V^{3+} complexes in aqueous phase. Although a previous study on the structure of hydrated V^{3+} in aqueous phase has been conducted, the V^{3+} solution used contained chloride anions along with concentrations of V^{4+}, as seen by their UV-vis spectra of the prepared solution.[18] The structural parameters of hydrated V^{2+} and V^{3+} we see here agrees with the *ab initio* calculations and experimental X-ray and neutron diffraction studies of solid $VSO_4 \bullet 6H_2O$ and $[V(H_2O)_6][H_5O_2](CF_3SO_3)_4$ crystals.[16,17,19–21]

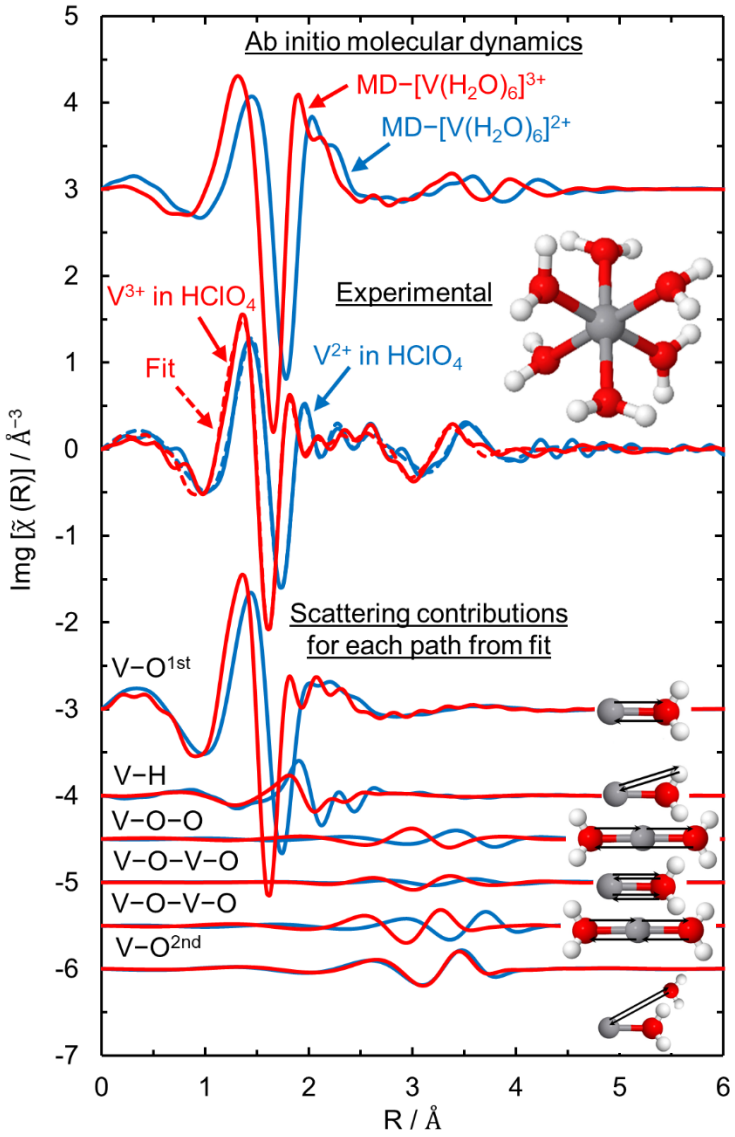

Figure 4.3. Structures of Hydrated V^{2+} and V^{3+} using EXAFS. The k^2-weighted Img[$\tilde{\chi}$(R)] plots for MD-EXAFS of vanadium complexes in pure water, that is, $[V(H_2O)_6]^{2+}$ (blue) and $[V(H_2O)_6]^{3+}$ (red). Below the MD-EXAFS, the experimental V K-edge EXAFS of V^{2+} (blue) and V^{3+} (red) in perchloric acid. The fit is shown by the dotted lines. The individual scattering paths that are used in the structural refinement are shown, along with their contributions in the resulting fit. Atom color legend: light gray = vanadium, red = oxygen, and white = hydrogen.

By fitting the EXAFS data, we identify the scattering paths that contribute to the different portions of the overall EXAFS spectra. We quantify distances of scattering paths for both V^{2+} and V^{3+} in perchloric acid and compare to the MD-EXAFS values. The individual path contributions obtained by fitting are shown at the bottom of **Figure 4.3**. The single leg scattering from the first shell (V-O and V-H) dominates the scattering in the region from 1−2 Å. The multiple leg

scatterings (V-O-O: 3-leg collinear path, V-O-V-O: double return and 4-leg collinear path) in the region from 2−4 Å are sensitive to first-shell symmetry and disorder. The paths used in the fit are based on previous studies for hydrated transition metal ions.[22] The V-O distance from experimental EXAFS of V^{2+} is 2.14 Å, while it is 2.0 Å for V^{3+}, within 0.01 Å of the previously reported V-O distances for V^{2+} and V^{3+} in $VSO_4 \bullet 6H_2O$ and $[V(H_2O)_6][H_5O_2](CF_3SO_3)_4$ crystals.[19–21] From MD-EXAFS, the V-O distance in V^{2+} and V^{3+} is 2.21 Å and 2.08 Å respectively, within 0.05 Å of the previously reported V-O distances for V^{2+} and V^{3+} from electronic structure calculations.[17] The fitting parameters for all single leg scattering paths are available in **Table S4.2**, and details of the electrochemical cell used for measurements along with processing and fitting of EXAFS data are discussed in **Chapter 2**. Using the structures of V^{2+} and V^{3+} and the associated scattering paths in noncomplexing solution, we will be able to identify the structures in different electrolytes by comparing their spectra to these standards.

The UV-vis spectra of V^{2+} are unaffected by the presence of different anions (SO_4^{2-}, Cl^-, Br^-, and I^- as shown in **Figure 2.1** and **2.2** of **Chapter 2**), indicating V^{2+} is present as $[V(H_2O)_6]^{2+}$ in all electrolytes.[11] Therefore, we assume the structural properties of V^{2+} in all of the electrolytes studied here are the same as in $HClO_4$ shown in **Figure 4.3**. Unlike V^{2+}, the UV-vis spectra of V^{3+} is different in the presence of interacting anions in solution (**Figure 2.1** and **2.2** of **Chapter 2**),[11,23–27] indicating a change in the first-coordination sphere. The UV-vis peak of V^{3+} corresponding to the $^3T_{1g} \rightarrow {}^3T_{2g}$ transition[28,29] shifts from that in noncomplexing $HClO_4$ most significantly in H_2SO_4, followed by HCl, HBr, and then least in HI.[11] As this shift is attributed to complexation, the anion complexation strength of V^{3+} follows this same order, which matches the spectrochemical series that provides an estimate of the strength of ligand interaction with transition metals (ligand strength: $SO_4^{2-} >> Cl^- > Br^- > I^-$).[13] However, the exact structural changes of V^{3+}

in the presence of anions have not been identified in aqueous phase. To identify the structures of V^{3+} complexes in H_2SO_4 and HCl, we conducted in-situ EXAFS measurements of V^{3+} in H_2SO_4 and HCl with increasing anion concentrations and compared them to the EXAFS of V^{3+} in $HClO_4$. Because weaker complexation of V^{3+} with Br^- and I^- than Cl^- and SO_4^{2-} is predicted from the spectrochemical series corroborated by our UV-vis measurements (**Figure S4.4**), we rely on DFT-calculated ΔG_L (**Table S4.3**) to identify the preferred complex in HBr and HI, rather than EXAFS measurements.

The data in **Figure 4.4a** provide evidence of V^{3+} complexation in H_2SO_4. The top of **Figure 4.4a** plots the Img[$\tilde{\chi}$(R)] of $[V(H_2O)_5SO_4]^+$ and $[V(H_2O)_6]^{3+}$ obtained by MD-EXAFS. There is a decline in the peak amplitude between 1.8 and 2.0 Å (**Inset 1**, **Figure 4.4a**) with the introduction of SO_4^{2-} in the first coordination sphere. The same peak occurs between 1.75 and 1.85 Å in the experimental EXAFS of V^{3+} in H_2SO_4 where we observe that the peak amplitude decreases with increasing SO_4^{2-} concentration (**Inset 2**, **Figure 4.4a**), which we attribute to the presence of $[V(H_2O)_5SO_4]^+$.

We fit the EXAFS data to determine the change in contribution of individual paths for V^{3+} with increasing SO_4^{2-}. The fittings are done considering an additional V-S single leg scattering path shown in **Figure 4.4a**, in addition to the paths utilized for fittings in perchloric acid shown in **Figure 4.3**. In sulfuric acid, the V-O path is shifted to the right (**Inset 3**, **Figure 4.4a**) with a change in the V-O distance in H_2SO_4 relative to $HClO_4$ (**Table S4.2**). The change in the average V-O distance with SO_4^{2-} complexation occurs due to an increasing contribution of the V-O bond (with O between V and S in sulfate anion). Further, at the bottom of **Figure 4.4a**, the increasing contribution of the V-S path and decreasing contribution of the V-H scattering path confirm increased V^{3+} complexation with SO_4^{2-} at higher SO_4^{2-} concentrations. This increased V^{3+}

complexation is quantified by the increase in the average coordination number of V-S path with increasing SO_4^{2-} concentration (**Table S4.2**). Therefore, V^{3+} exists as a mixture of $[V(H_2O)_5SO_4]^+$ and $[V(H_2O)_6]^{3+}$ in H_2SO_4, supporting our previous hypothesis by UV-vis spectroscopy.[11]

Our experimental EXAFS of V^{3+} in HCl shows clear evidence of Cl^- complexation, and by comparing to the MD-EXAFS Img[$\tilde{\chi}$(R)] plots of $[V(H_2O)_5Cl]^{2+}$, $[V(H_2O)_4Cl_2]^+$, and $[V(H_2O)_6]^{3+}$ (**Figure 4.4b**), we see that both mono-chloride and di-chloride V^{3+} complexes exist in HCl. The differences in experimental EXAFS are more subtle in HCl than in H_2SO_4 due to weaker complexation with Cl^- than SO_4^{2-}. The amplitudes of the peaks and troughs in the first coordination sphere of V^{3+} either monotonically increase or decrease with increasing Cl^- coordination in MD-EXAFS and Cl^- concentration in experimental EXAFS. However, for the amplitude of the feature between 2.05 and 2.20 Å in MD-EXAFS, the order is not monotonic, but instead $[V(H_2O)_6]^{3+} > [V(H_2O)_4Cl_2]^+ > [V(H_2O)_5Cl]^{2+}$ (**Inset 1**, **Figure 4.4b**). This same feature as identified in MD-EXAFS occurs between 1.85 and 2.05 Å in experimental EXAFS (**Inset 2**, **Figure 4.4b**), where the amplitude first decreases and then increases with increasing Cl^- concentration. This switch in order is not possible if only higher concentrations of $[V(H_2O)_5Cl]^{2+}$ are formed with increasing Cl^- concentration, indicating the presence of detectable concentrations of $[V(H_2O)_4Cl_2]^+$ along with $[V(H_2O)_5Cl]^{2+}$ at high concentrations of Cl^-.

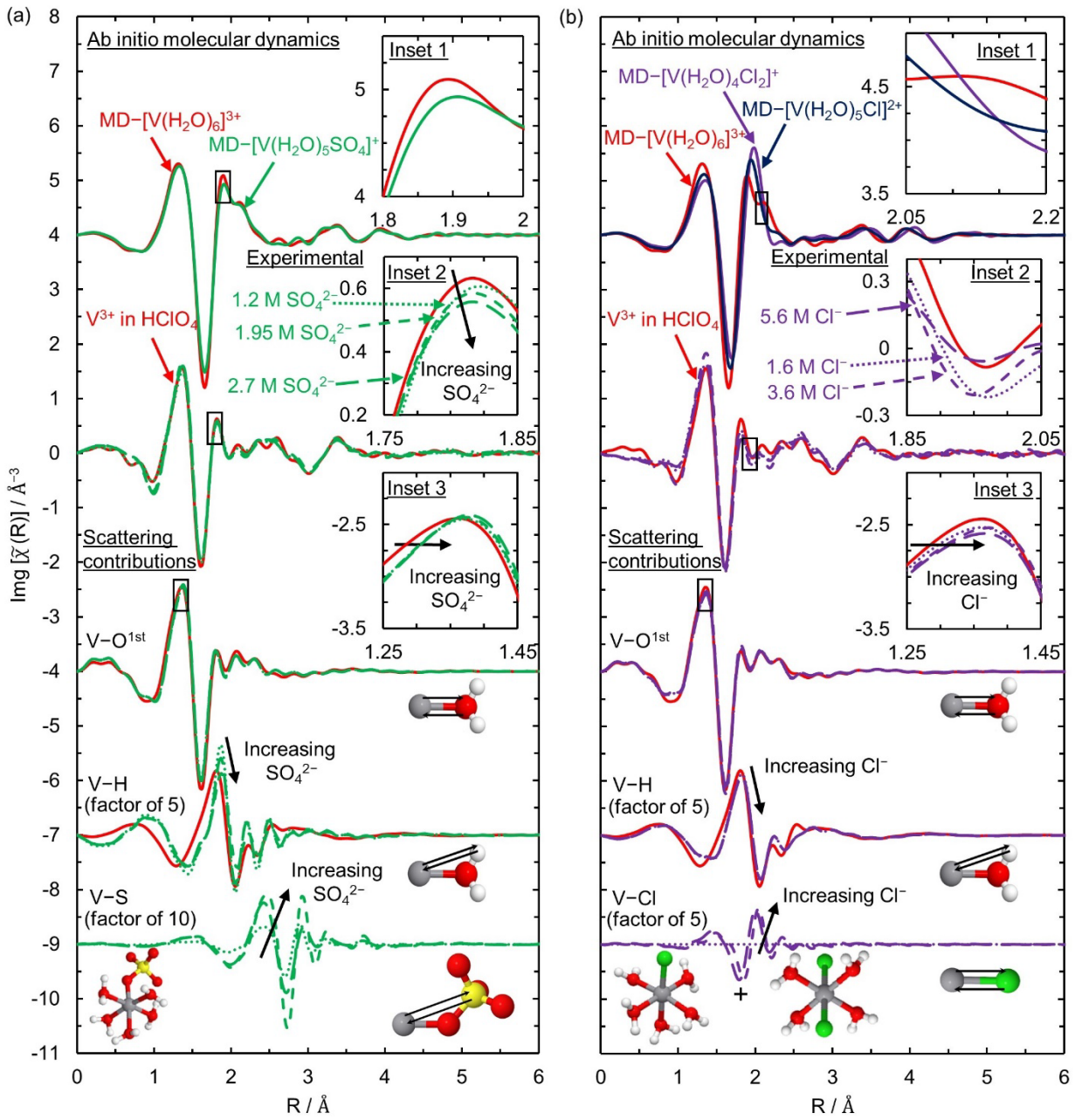

Figure 4.4. Structure of V^{3+} in H_2SO_4 and HCl with Changing Anion Concentrations using EXAFS. The V K-edge EXAFS k^2-weighted Img[$\tilde{\chi}$(R)] plots for V^{3+} with increasing concentrations of **(a)** SO_4^{2-} and **(b)** Cl^- anions compared with the case of hydrated V^{3+} ion in perchloric acid. The experimental spectrum is compared with the MD-EXAFS of $[V(H_2O)_5SO_4]^+$ in H_2SO_4, and $[V(H_2O)_5Cl]^{2+}$ and $[V(H_2O)_4Cl_2]^+$ in HCl, along with the hydrated V^{3+} ion (i.e., $[V(H_2O)_6]^{3+}$). The insets show the similarity in the relevant EXAFS region that are used to identify the presence of complexes in solutions at different concentration of anions. The contribution of the V-O, V-H, and V-S paths (in (a)), and V-Cl paths (in (b)) that are used in structural refinement are compared to the contribution of each of these paths in hydrated V^{3+}, obtained by fitting in Artemis. The contribution of V-H, V-S, and V-Cl paths are multiplied by a scaling factor to highlight the trends. Atom color legend: light gray = vanadium, red = oxygen, white = hydrogen, yellow = sulfur, and green = chloride.

We fit the EXAFS spectra of V^{3+} in HCl and deconvolute the contribution due to Cl^- complexation by including an additional single leg V-Cl scattering path during fitting as shown in **Figure 4.4b**. The V-O path contribution moves towards the right (**Inset 3**, **Figure 4.4b**) in HCl relative to $HClO_4$. Further, at the bottom of **Figure 4.4b**, the increasing contribution of the V-Cl path and decreasing contribution of the V-H scattering path with increasing Cl^- concentrations confirm V^{3+} complexation. The increasing coordination number of V-Cl with increasing Cl^- (**Table S4.2**) provide an estimate of the average number of anions in the first coordination sphere of V^{3+}. The V-Cl path is not included in fitting in 1.6 M Cl^- because introducing a V-Cl path worsened the obtained fits, indicating negligible complexation. We observe that the V-Cl distance is larger than the V-O distance, which we attribute to Jahn-Teller distortion in $[V(H_2O)_5Cl]^{2+}$ and $[V(H_2O)_4Cl_2]^+$ formed in HCl.[13] Therefore, V^{3+} exists predominantly as $[V(H_2O)_6]^{3+}$ with small concentrations of $[V(H_2O)_5Cl]^{2+}$ and $[V(H_2O)_4Cl_2]^+$ in HCl. The EXAFS analysis of the V^{3+} complex in HCl provides evidence of the formation of $[V(H_2O)_4Cl_2]^+$ hypothesized from UV-vis in our previous work.[11] The presence of $[V(H_2O)_4Cl_2]^+$ may also be related to the overall two-electron transfer behavior observed in HCl.

We were unable to identify the presence of vanadium dimers in the electrolytes studied by EXAFS. The absence of any intense peak ~3.1 Å attributed to V-V scattering in previous studies confirms the absence of dimers in our electrolytes.[30–32] The absence of dimers is also corroborated by UV-vis spectroscopy, which does not show any new transition peaks[31] or shoulders in the existing transition peaks with varying V^{3+} concentration.[11] However, the formation of vanadium dimers, comproportionation reaction between V^{2+} and V^{4+} on the surface,[11,12] or the vanadium di-halide complexes could explain the overall two-electron transfer behavior observed in HCl and HBr as discussed in **Chapter 3**. Since we have no direct evidence of V^{2+}/V^{3+} being a two electron

transfer reaction in HCl and HBr apart from comparing i_o and $i_{o,R_{ct}}$, we choose a simple reaction mechanism to avoid speculation.

$[V(H_2O)_5Br]^{2+}$ and $[V(H_2O)_4Br_2]^{+}$ are formed in HBr and $[V(H_2O)_5I]^{2+}$ and $[V(H_2O)_4I_2]^{+}$ are formed in HI, but in even lower concentrations than the V^{3+}-chloride complexes in HCl. Our prediction of the presence of these complexes is based on the exergonic DFT-calculated ΔG_L for $[V(H_2O)_5X]^{2+}$ and $[V(H_2O)_4X_2]^{+}$ (X = Cl, Br) from $[V(H_2O)_6]^{3+}$ (**Table S4.3**). Even though the ΔG_L of $[V(H_2O)_5I]^{2+}$ and $[V(H_2O)_4I_2]^{+}$ are slightly endergonic, we expect some of the V^{3+}-iodide complexes to form in solution based on changes in UV-vis with increasing I^- concentrations (**Figure S4.4**). The di-halide V^{3+} complex (X = Cl, Br) is more favorable than the mono-halide V^{3+} complex in HCl and HBr, while the mono-iodide V^{3+} complex is more favorable than the di-iodide V^{3+} complex, matching the overall two vs one-electron transfer observed in HCl and HBr compared to HI. With the kinetic information (**Sections 4.3.1** and **4.3.2**) combined with the vanadium structural information (**Section 4.3.3**) in the five electrolytes, we propose a microkinetic model in the following section.

4.3.4 Proposed Inner Sphere Mechanism and Kinetic Model for V^{2+}/V^{3+} Reaction in Different Electrolytes

The i_o (**eq. 4.1**) is simplified for three possible limiting conditions depending on the values of the V^{2+} and V^{3+} adsorption constants, yielding an expression of the form (**eq. 4.2**):

$$i_o = A \exp\left(-\frac{E_a}{RT}\right)[V^{2+}]^{\gamma}[V^{3+}]^{\varepsilon} \qquad \text{(eq. 4.2)}$$

When measuring i_o as a function of T and creating an Arrhenius plot, $A\,[V^{2+}]^{\gamma}[V^{3+}]^{\varepsilon}$ is the apparent (experimentally observed) frequency factor, γ and ε are reaction orders of V^{2+} and V^{3+}, respectively, and E_a is the apparent activation energy.

If $K_3[V^{3+}] \gg (1 + K_1[V^{2+}])$, that is, V^{3+} adsorbs strongly and much stronger than V^{2+}, then at a given temperature $i_o \propto [V^{2+}]^{\left(1-\frac{n_k(1-\alpha)}{n}\right)}[V^{3+}]^{-\left(1-\frac{n_k(1-\alpha)}{n}\right)}$. This rate law matches the positive order of V^{2+} and negative order of V^{3+} (with equal magnitude) observed in H_2SO_4, HCl, and HBr, indicating V^{3+} adsorbs stronger than V^{2+} in these three electrolytes. However, at a given temperature, if $1 \gg (K_1[V^{2+}] + K_3[V^{3+}])$, that is both V^{2+} and V^{3+} adsorb weakly, $i_o \propto [V^{2+}]^{\left(1-\frac{n_k(1-\alpha)}{n}\right)}[V^{3+}]^{\left(\frac{n_k(1-\alpha)}{n}\right)}$, explaining the positive reaction orders observed for both V^{2+} and V^{3+} in $HClO_4$ and HI ($\gamma, \varepsilon > 0$). The microkinetic model shows that the reaction kinetics is controlled by the V^{2+} and V^{3+} adsorption energies. With the reactant species in solution and reaction model identified, we next examine the energetics of adsorbed vanadium complexes and anions using DFT.

4.3.5 Energies of V^{2+}/V^{3+} Complexes and Anions Adsorbed on Glassy Carbon

To explain whether the kinetic enhancement of the V^{2+}/V^{3+} reaction in the presence of different anions is explained by the energy of the adsorbed vanadium-anion intermediate (**Scheme 4.1a**) or anion coverage (**Scheme 4.1b**), we compare the predicted kinetic behavior based on DFT-calculated adsorption energies of vanadium-anion intermediates and anions with experimental observations. We demonstrate that the energy of the adsorbed vanadium-anion intermediate follows the same trend as anion polarizability and explains the trend in kinetic enhancement (**Scheme 4.2a**). We show that the coverage of adsorbed anions follows the opposite trend of our experimental measurements (**Scheme 4.2b**), and thus cannot explain the observed kinetic behavior.

DFT calculations predict the trend in energy of the adsorbed vanadium-anion intermediate (i.e., *[bridge–V^{3+}]) on graphene matches the complexation strength of the free V^{3+} ion in solution. We calculate the energy of the *[bridge–V^{3+}] instead of *[bridge–V^{2+}] because barriers for

desorption are higher for V^{3+} than V^{2+} with OH bridge.[39,33] We assume that the desorption barrier is also higher for V^{3+} than V^{2+} for other bridges. We use a graphene cluster model as a representative model for GC because of challenges in accurately modelling amorphous surfaces. The details of modeling are available in the SI. The adsorption strength of *[bridge−V^{3+}] on graphene follows the order *[I−$V(H_2O)_5]^{2+}$ < *[Br−$V(H_2O)_5]^{2+}$ < *[Cl−$V(H_2O)_5]^{2+}$ < *[OH−$V(H_2O)_5]^{2+}$ < *[OH−$V(H_2O)_4SO_4$], reported in **Table S4.4** in the SI and shown qualitatively in **Scheme 4.2a**, where weaker adsorption means a higher energy intermediate. The order of adsorption strength is the same for the di-halide V^{3+} complexes as for mono-halide V^{3+} complexes. The order of the adsorption strength of the *[bridge−V^{3+}] on graphene, matches the ΔG_L of V^{3+} complex relative to $[V(H_2O)_6]^{3+}$ from our experimental UV-vis, DFT-calculations, and the spectrochemical series.

The relative adsorption strength of *[bridge−V^{3+}] species rationalizes the observed kinetic behavior by Sabatier's principle,[34] which states that the adsorbed intermediate should bind with medium strength. Assuming the energy of the transition state shifts the same amount as the desorption energy of the intermediate by Brønsted-Evans-Polanyi relations,[35,36] the E_a would be lowered with weakening of the adsorbed *[bridge−V^{3+}] intermediate. Weaker adsorption would also reduce the concentration of *[bridge−V^{3+}] on the surface, which would lower the apparent frequency factor. Based on the DFT-calculated adsorption free energy trends qualitatively shown in **Scheme 4.2a**, E_a and the apparent frequency factor for the V^{2+}/V^{3+} reaction should follow the order of $I^- < Br^- < Cl^- < OH^- < SO_4^{2-}$ if the electron transfer step through adsorbed vanadium acts as RDS, based on the rate law discussed in **Section 4.3.4**. This trend of E_a and apparent frequency factor with different anions matches the behavior observed in our experiments, which suggests the energy of the *[bridge−V^{3+}] controls the V^{2+}/V^{3+} kinetics.

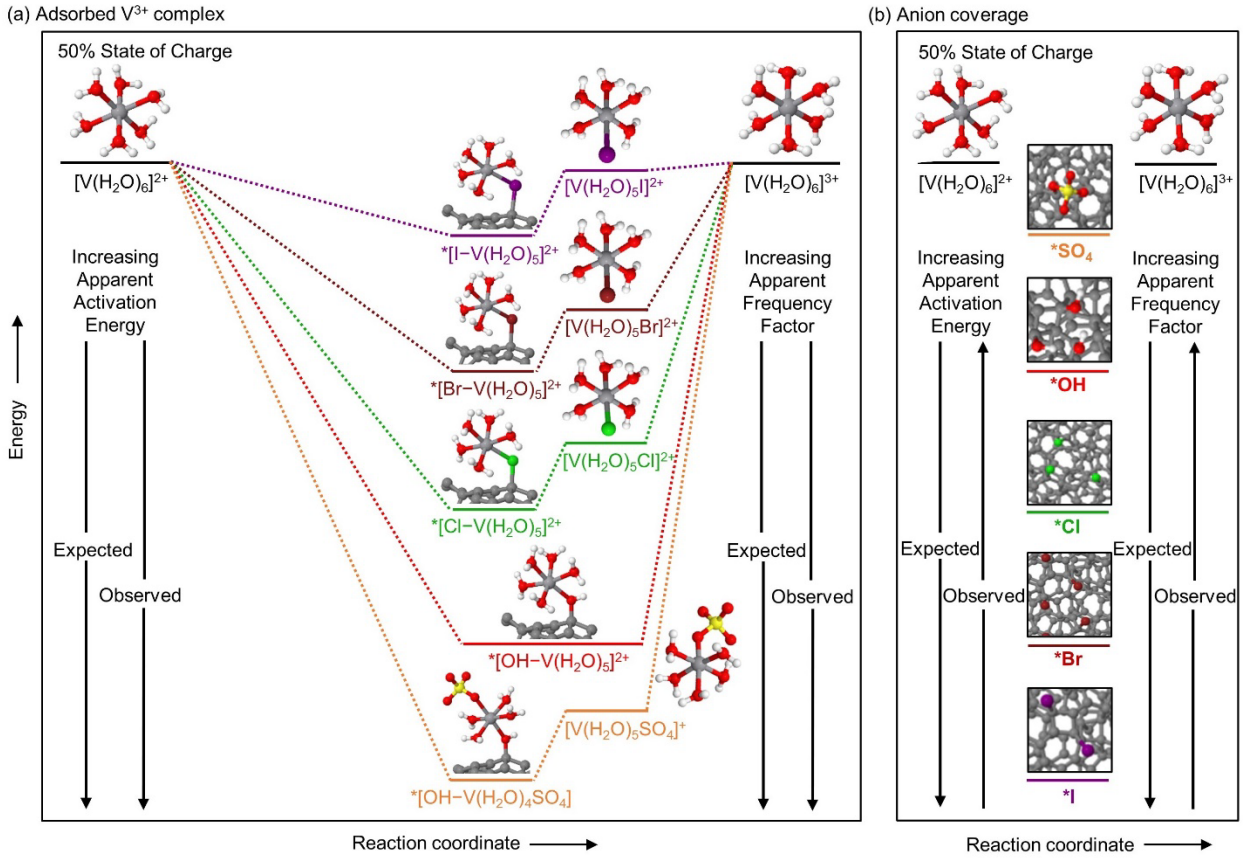

Scheme 4.2. Proposed Reaction Energy Diagram for the V^{2+}/V^{3+} Redox Reaction at 50% State of Charge and V^{2+}/V^{3+} Standard Redox Potential Considering Two Possible Mechanisms to Explain the Effect of Anions on Redox Kinetics. (a) Adsorbed V^{3+} complex (i.e., *[bridge−V^{3+}]) through anion bridge as reaction intermediate and **(b)** Anion coverage (i.e., *bridge). For simplicity, the energy diagram is not drawn to scale and does not show balancing anions and electrons involved in the reaction. Black arrows point in the direction of increasing apparent activation energy and apparent frequency factor based on expected and observed behavior. We show $[V(H_2O)_5X]^{2+}$ (X = Cl, Br, I) as the species formed in solution for consistency. However, in actuality there would be a combination of both $[V(H_2O)_4X_2]^{+}$ and $[V(H_2O)_5X]^{2+}$ in solution. We expect the adsorbed vanadium-anion intermediate to be closer to V^{3+} due to the easier desorption of V^{2+} than V^{3+}, as discussed in the text. Atom color legend: light gray = vanadium, red = oxygen, white = hydrogen, green = chloride, brown = bromide, purple = iodide, and dark gray = glassy carbon.

We propose anion polarizability acts as a useful descriptor for the kinetics of the numerous redox couples involving 3*d* transition metal ions[1–4] because anion polarizability correlates with the energy of the adsorbed metal-anion intermediate. The energy of the *[bridge−V^{3+}] in **Scheme 4.2a** follows the order of the anion polarizability. Consequently, the anion polarizability mimics the trends of observed V^{2+}/V^{3+} kinetics in different electrolytes.

The reaction pathway in **Scheme 4.2a** also captures the behavior of V^{2+}/V^{3+} reaction kinetics in mixtures of anions. The difference observed in kinetics in a mixture of I^- and SO_4^{2-} and

kinetics with only I^-, $\frac{i_{o,(I^-+SO_4^{2-})}}{i_{o,I^-}} \approx 0.3$ (**Figure 4.2**), implies the vanadium-sulfate intermediate is more energetically favorable than the vanadium-iodide intermediate. In contrast, the kinetics with Cl^- are comparable in the presence and absence of SO_4^{2-} $\left(\frac{i_{o,(Cl^-+SO_4^{2-})}}{i_{o,Cl^-}} \approx 0.9\right)$. The smaller effect of sulfate on kinetics with Cl^- compared with I^- implies that the vanadium-chloride intermediate is similar in energy to the vanadium-sulfate intermediate (i.e., more favorable than the vanadium-iodide intermediate). This order of energies qualitatively agrees with our calculations and is represented in **Scheme 4.2a**. Further the V^{2+}/V^{3+} kinetic behavior in mixtures of anions in presence of sulfate also correlates with the difference in the ΔG_L of the V^{3+}-halide complexes relative to the V^{3+}-sulfate complex. The more positive ΔG_L of V^{3+}-halide complexes relative to the V^{3+}-sulfate complex, the lower the concentration of reactive V^{3+}-halide complexes in solution, and higher the relative inhibition in V^{2+}/V^{3+} reaction kinetics with SO_4^{2-}. The large apparent frequency factor in the presence of SO_4^{2-} ($\sim 10^6$) in comparison to other tested halides ($\sim 10^2$), also indicates that small concentrations of SO_4^{2-} will prevent the formation of active V^{3+}-halide complexes.

The relatively minor changes in i_o compared to the changes in the E_a can be explained by the adsorbed *[bridge−V^{3+}] intermediates representing only a small fraction of the surface sites. While the i_o varies at most by a factor of 15 throughout the electrolytes, the E_a decreases by ~30 kJ mol^{-1} at 50% SoC in HI compared to H_2SO_4. Such a significant decrease in E_a would imply a much larger increase in i_o, all else being equal. The total rate includes contributions of reaction occurring both through the more active *[bridge−V^{3+}] intermediates on the surface and the less active sites comprising of vacant carbon sites, carbonyl, and carboxyl groups on the surface.[37,38] Due to the weak adsorption on GC, the coverage of the active *[bridge−V^{3+}] intermediates on the surface remains low. Consequently, the portion of the reaction going through the more active

*[bridge−V^{3+}] intermediates on the surface is small, rationalizing the minor increase in i_o. However, the E_a is dominated by the rapid charge transfer through the active *[bridge−V^{3+}] intermediates, explaining the large decline observed in E_a.

Our DFT calculations suggest the increasing anion coverage, often considered as the reason for enhancement observed in the presence of anions for other transition metal ion redox couples,[1,5] does not explain the V^{2+}/V^{3+} reaction. The coverage and adsorption strength of anions at the equilibrium V^{2+}/V^{3+} redox potential on GC follow the order: $I^- > Br^- > Cl^- > OH^- > SO_4^{2-}$ (**Figure S4.6**). If the anion coverage controls the V^{2+}/V^{3+} reaction, as depicted in **Scheme 4.2b**, the apparent frequency factor and E_a should increase with increasing anion adsorption strength, which is opposite to the experimentally observed behavior. This mismatch with the observed behavior allows us to conclude that anion coverages alone are not responsible for the observed kinetic trends. Also, the adsorption of SO_4^{2-} on GC is unfavorable with a negligible coverage, which suggests that SO_4^{2-} would not prevent I^- from adsorbing onto the electrode surface. Details of coverage calculations are available in the SI. These results do not mean that the reaction kinetics are not proportionally related to the coverage of a particular anion, but instead that the coverage is not the cause of the anion-enhancement trend observed here. Increasing the coverage of a particular anion enhances the reaction kinetics by increasing the concentration of that particular adsorbed vanadium-anion intermediate, as demonstrated in studies that oxidatively treat carbon electrodes and show improved V^{2+}/V^{3+} kinetics due to increased coverage of OH groups.[38]

4.4 Conclusions

The results discussed in this chapter reveal how the structure of formed vanadium complexes on the surface of glassy carbon influences kinetics for the V^{2+}/V^{3+} redox couple in five different acidic electrolytes. The energy of the formed vanadium-anion intermediate (i.e., *[bridge−V^{3+}])

controls V^{2+}/V^{3+} kinetics and correlates with free anion polarizability. The anions enhance the kinetics by forming active *[bridge−V^{3+}] intermediates that have a lower activation barrier, rather than by increasing the coverage of the intermediates. These results can explain the similar kinetic trends observed for other redox couples involving 3*d* transition metal ions in the presence of anions, such as Cr^{2+}/Cr^{3+}, Fe^{2+}/Fe^{3+}, and Cu^{+}/Cu^{2+} used for other RFBs. Our findings suggest that bridging anions may play a critical yet underexplored role in other RFB chemistries employing transition metal ions for use in energy storage applications. The understanding of the structure of the intermediate and its relation to the coverage and kinetics may lead to development of electrocatalysts that can adsorb vanadium ions with the desired energy for improved kinetics.

4.5 Supporting Information

4.5.1 Experimental Details

The V^{2+} and V^{3+} solutions in $HClO_4$, HBr, and hydriodic acid (HI, 57%, contains no stabilizer, Sigma Aldrich) are prepared using V_2O_5 following a similar process using the same electrochemical assembly as discussed in **Chapter 3**. For preparing solutions at different states of charge in HI, the potential of −0.2 V instead of 0.08 V (vs Ag/AgCl) is chosen because this is the most reducing potential at which we observe that all the V^{2+} gets converted to V^{3+}, with lowest contribution of I_3^- in the UV-vis spectra. More details regarding electrolyte preparation are discussed in the original publication.[39]

4.5.2 Rate Law for V^{2+}/V^{3+} Reaction in Presence of Anions

a) Inner sphere reaction mechanism for V^{2+}/V^{3+} reaction involving adsorbed vanadium-anion intermediate

The proposed inner sphere reaction mechanism involving an adsorbed vanadium-anion intermediate can be written as:

Step 1: $V^{2+} + * \rightleftarrows *V^{2+}$

Step 2: $*V^{2+} \rightleftarrows *V^{3+} + e^-$ RDS

Step 3: $*V^{3+} \rightleftarrows V^{3+} + *$

For the reaction model described above, conducting a total site balance yields:

$$\theta_{V^{2+}} + \theta_{V^{3+}} + \theta_* = 1 \qquad (\text{eq. S4.1})$$

where θ_i is the coverage of species, i. Because the electron transfer step is RDS, step 1 and step 3 are assumed to be quasi-equilibrated:

$$K_1 = \frac{\theta_{V^{2+}}}{\theta_*[V^{2+}]}$$

$$K_3 = \frac{\theta_{V^{3+}}}{\theta_*[V^{3+}]}$$

Here K_1 and K_3 are adsorption constants for V^{2+} and V^{3+}, respectively.

Substituting $\theta_{V^{2+}}$ and $\theta_{V^{3+}}$ in terms of θ_* in **eq. S4.1**, we retrieve:

$$K_1\theta_*[V^{2+}] + K_3\theta_*[V^{3+}] + \theta_* = 1$$

$$\theta_* = \frac{1}{(K_1[V^{2+}] + K_3[V^{3+}] + 1)}$$

The rate of reaction, i.e., rate of electron transfer in step 2 is:

$$i_k = nF(k_2\theta_{V^{2+}} - k_{-2}\theta_{V^{3+}}) \qquad (\text{eq. S4.2})$$

where k_2 and k_{-2} are the forward and backward rate constants for step 2.

k_2 and k_{-2} can be written from BV equation in terms of standard rate constant, k_o, defined at equilibrium:

$$k_2 = k_o e^{\left(\frac{n_k(1-\alpha)F\left(E-E^{o'}\right)}{RT}\right)}$$

$$k_{-2} = k_o e^{-\left(\frac{n_k \alpha F \left(E - E^{o'}\right)}{RT}\right)}$$

Here $E^{o'}$ is the formal potential of electrode. **Eq. S4.2** transforms to:

$$i_k = nFk_o \left(\theta_{V^{2+}} e^{\left(\frac{n_k(1-\alpha)F \left(E - E^{o'}\right)}{RT}\right)} - \theta_{V^{3+}} e^{-\left(\frac{n_k \alpha F \left(E - E^{o'}\right)}{RT}\right)} \right) \qquad \text{(eq. S4.3)}$$

Even though the net current density, i_k is zero at equilibrium, a balanced faradaic activity can be expressed in terms of exchange current density, i_o:

$$i_o = nFk_o \theta_{V^{2+}} e^{\left(\frac{n_k(1-\alpha)F \left(E_{eq} - E^{o'}\right)}{RT}\right)} = nFk_o \theta_{V^{3+}} e^{-\left(\frac{n_k \alpha F \left(E_{eq} - E^{o'}\right)}{RT}\right)} \qquad \text{(eq. S4.4)}$$

Using Nernst equation to remove the potential dependence:

$$E_{eq} - E^{o\prime} = \frac{RT}{nF} \ln \frac{[V^{3+}]}{[V^{2+}]}$$

Substituting the value of $\left(E_{eq} - E^{o'}\right)$ to **eq. S4.4** and simplifying, we get **eq. 4.1** reported in the results and discussions section:

$$\begin{aligned} i_o &= \frac{nFk_o K_1 [V^{2+}]}{(K_1[V^{2+}] + K_3[V^{3+}] + 1)} \left(\frac{[V^{3+}]}{[V^{2+}]}\right)^{\left(\frac{n_k(1-\alpha)}{n}\right)} \\ &= \frac{nFk_o K_3 [V^{3+}]}{(K_1[V^{2+}] + K_3[V^{3+}] + 1)} \left(\frac{[V^{3+}]}{[V^{2+}]}\right)^{-\left(\frac{n_k \alpha}{n}\right)} \end{aligned} \qquad \text{(eq. 4.1)}$$

Simplifying even further:

$$\frac{K_1}{K_3} = [V^{3+}]^{\left(1 - \frac{n_k}{n}\right)} [V^{2+}]^{-\left(1 - \frac{n_k}{n}\right)}$$

Using expressions for i_o, k_o, and the adsorption constant of species *i* (K_i):

$$i_o = A \exp\left(-\frac{E_a}{RT}\right)$$

$$k_o = A_o \exp\left(-\frac{E_{a,o}}{RT}\right) \quad \text{(eq. S4.5)}$$

$$\mathrm{K}_i = \exp\left(-\frac{\Delta G_{rxn,i}}{RT}\right) = \exp\left(-\frac{\Delta H_{rxn,i} - T\Delta S_{rxn,i}}{RT}\right)$$

$$= A_i \exp\left(-\frac{\Delta H_{rxn,i}}{RT}\right)$$

where $E_{a,o}$ is the activation energy of step 2, and $\Delta G_{rxn,i}$, $\Delta H_{rxn,i}$, and $\Delta S_{rxn,i}$ are free energy, enthalpy, and entropy of reaction *i*.

Eq. 4.1 can be rewritten by using **eq. S4.5** and simplified to:

$$i_o = A_o \exp\left(-\frac{E_{a,o}}{RT}\right) \frac{nF\mathrm{K}_1[\mathrm{V}^{2+}]^{\left(1-\frac{n_k(1-\alpha)}{n}\right)}[\mathrm{V}^{3+}]^{\left(\frac{n_k(1-\alpha)}{n}\right)}}{(1 + \mathrm{K}_1[\mathrm{V}^{2+}] + \mathrm{K}_3[\mathrm{V}^{3+}])} \quad \text{(eq. S4.6)}$$

Eq. S4.6 can be reduced under certain conditions to explain the behavior observed in all electrolytes:

Condition 1: When $\mathrm{K}_1[\mathrm{V}^{2+}] \gg (1 + \mathrm{K}_3[\mathrm{V}^{3+}])$

$$i_o = nFA_o \exp\left(-\frac{E_{a,o}}{RT}\right) [\mathrm{V}^{2+}]^{\left(-\frac{n_k(1-\alpha)}{n}\right)}[\mathrm{V}^{3+}]^{\left(\frac{n_k(1-\alpha)}{n}\right)}$$

$$= A \exp\left(-\frac{E_{a,o}}{RT}\right) [\mathrm{V}^{2+}]^{\left(-\frac{n_k(1-\alpha)}{n}\right)}[\mathrm{V}^{3+}]^{\left(\frac{n_k(1-\alpha)}{n}\right)}$$

where $A = nFA_o$ and $E_a = E_{a,o}$

Condition 2: When $\mathrm{K}_3[\mathrm{V}^{3+}] \gg (1 + \mathrm{K}_1[\mathrm{V}^{2+}])$

$$i_o = nFA_o \exp\left(-\frac{E_{a,o}}{RT}\right) \frac{\mathrm{K}_1}{\mathrm{K}_3} [\mathrm{V}^{2+}]^{\left(1-\frac{n_k(1-\alpha)}{n}\right)}[\mathrm{V}^{3+}]^{-\left(1-\frac{n_k(1-\alpha)}{n}\right)}$$

$$= A \exp\left(-\frac{E_a}{RT}\right) [\mathrm{V}^{2+}]^{\left(1-\frac{n_k(1-\alpha)}{n}\right)}[\mathrm{V}^{3+}]^{-\left(1-\frac{n_k(1-\alpha)}{n}\right)}$$

where $A = \frac{nFA_oA_1}{A_3}$ and $E_a = E_{a,o} + \Delta H_{rxn,1} - \Delta H_{rxn,3}$

Condition 3: When $1 \gg (\mathrm{K}_1[\mathrm{V}^{2+}] + \mathrm{K}_3[\mathrm{V}^{3+}])$

$$i_o = nFA_o \exp\left(-\frac{E_{a,o}}{RT}\right) \mathrm{K}_1 [\mathrm{V}^{2+}]^{\left(1-\frac{n_k(1-\alpha)}{n}\right)} [\mathrm{V}^{3+}]^{\left(\frac{n_k(1-\alpha)}{n}\right)}$$

$$= A \exp\left(-\frac{E_a}{RT}\right) [\mathrm{V}^{2+}]^{\left(1-\frac{n_k(1-\alpha)}{n}\right)} [\mathrm{V}^{3+}]^{\left(\frac{n_k(1-\alpha)}{n}\right)}$$

where $A = nFA_oA_1$ and $E_a = E_{a,o} + \Delta H_{rxn,1}$

Under Condition 2, the order of V^{2+} is positive and order of V^{3+} is negative, with equal in magnitude. This behavior is the same as observed experimentally for H_2SO_4, HCl, and HBr. Under Condition 3, the orders of both V^{2+} and V^{3+} are positive, which is same as observed experimentally in $HClO_4$ and HI.

b) Inner sphere V^{2+}/V^{3+} reaction mechanism involving adsorbed anion

If adsorbed anion ($* \mathrm{X}$) is involved, the reaction mechanism is modified to:

Step 1: $$\mathrm{X} + * \rightleftarrows * \mathrm{X}$$

Step 2: $$\mathrm{V}^{2+} + \mathrm{X} * \rightleftarrows * [\mathrm{X} - \mathrm{V}^{3+}] + \mathrm{e}^- \qquad \text{RDS}$$

Step 3: $$* [\mathrm{X} - \mathrm{V}^{3+}] \rightleftarrows [\mathrm{X} - \mathrm{V}^{3+}] + *$$

Following the same process of site balance and simplifying assuming the electron transfer step involving an adsorbed anion is RDS:

$$i_k = nFk_o \left(\theta_{\mathrm{X}} [\mathrm{V}^{2+}] \, e^{\left(\frac{n_k(1-\alpha)F\left(E-E^{o'}\right)}{RT}\right)} - \theta_{[\mathrm{X}-\mathrm{V}^{3+}]} \, e^{-\left(\frac{n_k\alpha F\left(E-E^{o'}\right)}{RT}\right)} \right)$$

where k_o is the standard rate constant defined at equilibrium, θ_{X} and $\theta_{[\mathrm{X}-\mathrm{V}^{3+}]}$ represent the coverage of anion (X) and complexed V^{3+} ($[\mathrm{X} - \mathrm{V}^{3+}]$) respectively.

Exchange current density, i_o can be written as:

$$i_o = nFk_o\theta_{\mathrm{X}}[\mathrm{V}^{2+}] e^{\left(\frac{n_k(1-\alpha)F\left(E_{eq}-E^{o'}\right)}{RT}\right)} = nFk_o\theta_{[\mathrm{X}-\mathrm{V}^{3+}]} \, e^{-\left(\frac{n_k\alpha F\left(E_{eq}-E^{o'}\right)}{RT}\right)} \qquad (\mathrm{eq.\,S4.7})$$

Thus, the reaction kinetics is directly proportional to θ_X (or $\theta_{[X-V^{3+}]}$) when an adsorbed anion is involved.

Removing the potential dependence by substituting the value of $\left(E_{eq} - E^{o'}\right)$ in **eq. S4.7**, and simplifying:

$$i_o = \frac{nFk_o K_1[X][V^{2+}]}{(K_3[X-V^{3+}] + K_1[X] + 1)}\left(\frac{[X-V^{3+}]}{[V^{2+}]}\right)^{\left(\frac{n_k(1-\alpha)}{n}\right)}$$
$$= \frac{nFk_o K_3[X-V^{3+}]}{(K_3[X-V^{3+}] + K_1[X] + 1)}\left(\frac{[X-V^{3+}]}{[V^{2+}]}\right)^{-\left(\frac{n_k\alpha}{n}\right)} \quad \text{(eq. S4.8)}$$

Here K_1 and K_3 are adsorption constants for X and $[X-V^{3+}]$ respectively.

Eq. S4.8 can be reduced under certain conditions to explain the behavior observed in all electrolytes:

Condition 1: When $1 \gg (K_3[X-V^{3+}] + K_1[X])$

$$i_o = nFk_o K_1[X][V^{2+}]^{\left(1-\frac{n_k(1-\alpha)}{n}\right)}[X-V^{3+}]^{\left(\frac{n_k(1-\alpha)}{n}\right)}$$

Condition 2: When $K_1[X] \gg (1 + K_3[X-V^{3+}])$

$$i_o = nFk_o[V^{2+}]^{\left(1-\frac{n_k(1-\alpha)}{n}\right)}[X-V^{3+}]^{\left(\frac{n_k(1-\alpha)}{n}\right)}$$

Condition 3: When $K_3[X-V^{3+}] \gg (1 + K_1[X])$

$$i_o = nFk_o(K_1/K_3)[X][V^{2+}]^{\left(1-\frac{n_k(1-\alpha)}{n}\right)}[X-V^{3+}]^{-\left(1-\frac{n_k(1-\alpha)}{n}\right)}$$

Under Condition 1 and Condition 2, the orders of both V^{2+} and V^{3+} are positive, which is same as observed experimentally in $HClO_4$ and HI. Under Condition 3, the order of V^{2+} is positive and order of V^{3+} is negative, with equal in magnitude. This behavior is same as observed experimentally for H_2SO_4, HCl, and HBr.

c) Outer sphere reaction mechanism for V^{2+}/V^{3+} reaction

Assuming V^{2+}/V^{3+} reaction is an outer sphere reaction, the reaction will include only one step in which electron transfer occurs:

$$V^{2+} \rightleftarrows V^{3+} + e^{-}$$

The rate of reaction can be written as:

$$i_k = nF(k_2[V^{2+}] - k_{-2}[V^{3+}])$$

where k_2 and k_{-2} are forward and backward rate constants for the reaction that can be written in terms of standard rate constant, k_o defined at equilibrium.

The kinetic current density, i_k, can be now written as:

$$i_k = nFk_o\left([V^{2+}]e^{\left(\frac{n_k(1-\alpha)F\left(E-E^{o'}\right)}{RT}\right)} - [V^{3+}]e^{-\left(\frac{n_k\alpha F\left(E-E^{o'}\right)}{RT}\right)}\right)$$

At equilibrium, exchange current density, i_o, can be written as:

$$i_o = nFk_o[V^{2+}]e^{\left(\frac{n_k(1-\alpha)F\left(E_{eq}-E^{o'}\right)}{RT}\right)} = nFk_o[V^{3+}]e^{-\left(\frac{n_k\alpha F\left(E_{eq}-E^{o'}\right)}{RT}\right)}$$

Using the Nernst equation to remove the potential dependence, and simplifying, we obtain:

$$i_o = nFk_o[V^{2+}]^{\left(1-\frac{n_k(1-\alpha)}{n}\right)}[V^{3+}]^{\left(\frac{n_k(1-\alpha)}{n}\right)} = nFk_o[V^{3+}]^{\left(1-\left(\frac{n_k\alpha}{n}\right)\right)}[V^{2+}]^{\left(\frac{n_k\alpha}{n}\right)} \qquad \text{(eq. S4.9)}$$

Thus, looking at **eq. S4.9**, the orders for both V^{2+} and V^{3+} are positive for an outer sphere reaction. This would not explain the negative orders observed for V^{3+} in H_2SO_4, contradicting our assumption that V^{2+}/V^{3+} reaction is an outer-sphere reaction.

4.5.3 Molecular Dynamics (MD) Simulations for Extended X-ray Absorption Fine Structure (EXAFS) for V^{2+} and V^{3+} Complexes

Ab initio Car-Parrinello Molecular Dynamics (CPMD) simulations are performed for different vanadium complexes: $[V(H_2O)_6]^{3+}$, $[V(H_2O)_5Cl]^{2+}$, $[V(H_2O)_4Cl_2]^{+}$, $[V(H_2O)_5SO_4]^{+}$, and

$[V(H_2O)_6]^{2+}$ to generate their MD-EXAFS spectra. The NWChem software package is used for CPMD simulations, and the PBE functional is employed.[40] The simulations are conducted in the NVT ensemble using the Nose-Hoover thermostat at 300 K with the period of ionic and electronic thermostats set to 1200 au. Besides the vanadium complex, 50 explicit water molecules are included in a periodic cell with side lengths of 12 Å, corresponding to a water density of 1 g cm^{-3}. A uniform background charge is added to neutralize charge of the periodic system, and all hydrogens are given a mass of 2 au to decrease the high frequency OH bond vibrations. After a 10 ps equilibration period, CPMD simulations are ran for 100 ps with a time step of 5 au (~0.121 fs) and fictitious electron mass of 600 au.

EXAFS spectra are calculated with the MD-EXAFS method.[41] The atomic coordinates of MD snapshots are collected every 1 ps, for a total of 100 snapshots for each vanadium complex (100 ps of total simulation time). For each snapshot, an EXAFS spectrum is calculated using the FEFF9 code with self-consistency field (SCF) using a cluster radius of 6 Å centered on vanadium.[42] About 1000 individual scattering paths are generated for each snapshot, and individual snapshots are then averaged to produce an average EXAFS spectrum for each complex.

4.5.4 Ligand-Exchange Free Energies for V^{2+}/V^{3+} Complexes

The structures of the V^{3+} complexes are geometry optimized using DFT with the B3LYP-D3 hybrid functional. No symmetry constraints are imposed during these geometry optimizations. The Def2-TZVPPD basis set is used for all atoms. Using dispersion corrected hybrid-functionals and diffuse basis functions is shown to give increased accuracy of anion binding.[43,44] Long-range solvation is treated implicitly during the geometry optimizations of all species using the COSMO solvation model (with default NWChem settings and a dielectric constant of 78.4 for water).

Computed free energies include the COSMO implicit solvation energy as well as zero-point, translational, rotational, and vibrational contributions obtained from ideal gas partition functions. Entropic and enthalpic contributions are evaluated at 298.15 K based on the output of harmonic vibrational frequency analysis. The Gibbs free energy of a species in the aqueous phase is computed as:

$$G(T) = E_{gas} + \Delta G_{solv} + H_{gas} - TS_{liq}$$

where E_{gas} is the total electronic energy of the species in the gas phase, ΔG_{solv} is the COSMO solvation free energy, H_{gas} is the thermal correction to the enthalpy, T is the temperature, and S_{liq} is the liquid phase entropy. Here, S_{liq} is approximated using the Wertz correction[45] to correct the gas phase entropy (S_{gas}) for solvation induced structural ordering in the aqueous electrolyte given as:

$$S_{liq} = S_{gas} + \Delta S_{solvation}$$

where $\Delta S_{solvation} = -0.46\left(S_{gas} - 14.3\right)$ for 1.0 M of solute. The reference state for all species is 1.0 M, besides water which is approximated as ~55.5 M.

To understand anion complexation strength, we perform a series of DFT calculations to compute the Gibbs free energy of reaction, ΔG_L (298.15 K), for various V^{3+} ligand exchange reactions. The free energy of each vanadium complex is calculated with only COSMO implicit solvent. In the case of anions, 12 explicit water molecules are added in addition to implicit COSMO solvation for improved accuracy.[46,47] The free energies of the non-vanadium species are thus computed as:

$$G_{X^-} = G_{[X(H_2O)_{12}]^-} - G_{(H_2O)_{12}}$$

$$G_{H_2O} = G_{(H_2O)_{13}} - G_{(H_2O)_{12}}$$

4.5.5 DFT Modeling of Adsorbed Intermediates

Adsorption energies for proposed vanadium-anion intermediates are computed on the edge site of a graphene cluster model capped with hydrogens. These graphene cluster models are shown to be representative of graphite in prior studies and demonstrated to be sufficiently large to not suffer from finite size effects.[48] One hydrogen is removed from the site that the vanadium complex will adsorb onto, and another is removed on the opposite site to maintain an even number of electrons (**Figure S4.5**). A cluster model of amorphous carbon would be more representative of the glassy carbon electrodes used in experiment, but it is challenging to accurately model due to its amorphous nature and heterogeneity of adsorption sites. In contrast, the graphene cluster models provide a controlled system to model trends in adsorption strength of vanadium-anion intermediates.

We predict that vanadium adsorbs to the carbon surface through an anion bridge (*OH, *Cl, *Br, or *I). The structures are geometry optimized using the B3LYP-D3 functional with COSMO implicit solvation as implemented in NWChem.[9,49] Select calculations are done using the M06-2X-D3 functional to compare trends with B3LYP-D3. The Def2-TZVPPD basis set is used to model the vanadium complex, whereas the Def2-SVP basis set is used to model the graphene cluster for computational tractability. To ensure that the correct spin state is considered, Constrained Density Functional Theory (CDFT) is used with a spin constraint on the vanadium complex.[50] A spin constraint of 2 spin up electrons is applied for V^{3+} complexes, and a spin constraint of 3 spin up electrons is applied for V^{2+} complexes. Free energies of the adsorbed

vanadium-anion intermediates are referenced to the vanadium-water complex (i.e., $[V(H_2O)_6]^{3+}$ or $[V(H_2O)_6]^{2+}$) and the bare graphene surface, as seen in **eq. S4.10**.

$$\Delta G_{ads}[\text{Complex}] = E[* \text{Complex}] - E[\text{Complex}] - E[*] + \Delta G_L \qquad (\text{eq. S4.10})$$

where $\Delta G_{ads}[\text{Complex}]$ is the free energy change upon adsorption of the vanadium-anion complex, $E[* \text{Complex}]$ is the energy of the adsorbed vanadium-anion complex, $E[\text{Complex}]$ is the energy of the vanadium-anion complex, and $E[*]$ is the energy of the graphene cluster model. COSMO implicit solvation is used to treat the solvent environment.

Calculations using M06-2X-D3 and B3LYP-D3 functionals agree that adsorption free energies follow the order *I > *Br > *Cl > *OH, with the weakest intermediates binding through *I and the strongest through *OH. In addition, the presence of sulfate in the first coordination sphere of V^{3+} leads to the strongest adsorption out of the complexes studied here. We also predict that the $*[OH{-}V(H_2O)_5]^{2+}$ complex (V^{3+} oxidation state) adsorbs stronger than the $*[OH{-}V(H_2O)_5]^{+}$ complex (V^{2+} oxidation state), which is consistent with a previous study of V^{2+}/V^{3+} adsorption on graphite.[51]

4.5.6 Coverage of Anions on Glassy Carbon

Surface coverages of adsorbed anions (i.e., *Cl, *Br, *I, *OH, and $*SO_4$) on glassy carbon are computed using periodic DFT as implemented in NWChem.[52] A 64-atom amorphous carbon slab from reference 53 is used as the glassy carbon surface model for our study. The glassy carbon surface is geometry optimized using the PBE0 hybrid functional corrected for dispersion interactions with Grimme's D3 method (PBE0-D3).[54,55] The bottom 3 Å of the glassy carbon surface is fixed at its optimized positions. The carbon model occupied a 7.53 × 7.53 × 27.53 $Å^3$ supercell with a 20 Å vacuum layer to prevent self-interaction in the *z* direction. A plane wave

kinetic energy cutoff of 817 eV (30 au) and an energy tolerance of 2.72×10^{-6} eV is used for all calculations.

To predict anion coverages (θ) as a function of electrode potential, we calculate the electronic adsorption energies of *Cl, *Br, *I, and *OH at different coverages on the glassy carbon model. The adsorbates are evenly spaced on the glassy carbon surface and the system is geometry optimized using PBE0-D3. The average adsorption energies of Cl, Br, and I are calculated using **eq. S4.11** at coverages up to 1/4, 1/6, and 1/12 monolayers (ML), respectively. Adsorption energies at higher coverages are not calculated because of spontaneous desorption from the surface during optimizations. The average adsorption energy of the halide, $\mathrm{E_{ads}}[* \mathrm{X}]$ is calculated as:

$$\mathrm{E_{ads}}[* \mathrm{X}] = \frac{1}{n}(\mathrm{E}[* + n\mathrm{X}] - \frac{n}{2}\mathrm{E}[\mathrm{X_2}] - \mathrm{E}[*]) \qquad (\mathrm{eq.\,S4.11})$$

where X is a halide, *n* is the number of adsorbates on the surface, $\mathrm{E}[* + n\mathrm{X}]$ denotes the energy of the glassy carbon surface with *n* halides adsorbed, and $\mathrm{E}[*]$ is the energy of the bare glassy carbon surface. Adsorption energies for *OH are referenced to liquid water and hydrogen gas using **eq. S4.12**. To calculate the energy of liquid water, we corrected the DFT-calculated electronic energy of a water molecule in the gas phase with enthalpy of vaporization, ΔH_{vap} = 40.6 kJ mol^{-1}.

$$\mathrm{E_{ads}}[* \mathrm{OH}] = \frac{1}{n}(\mathrm{E}[* + n\mathrm{OH}] + \frac{n}{2}\mathrm{E}[\mathrm{H_2}] - \mathrm{E}[*] - n\mathrm{E}[\mathrm{H_2O}]) \qquad (\mathrm{eq.\,S4.12})$$

In **eq. S4.11** and **4.12,** $\mathrm{E}[i]$ is the DFT-calculated energy of the species i (i = H_2, X_2, H_2O) in gas phase, whereas $\mathrm{E}[* i]$ is the DFT-calculated energy of an adsorbed species i (i = OH, X) in gas phase. Linear fits of the adsorption energy as a function of coverage are obtained.

To predict halide coverages at different potentials, we use the generalized computational hydrogen electrode (CHE) model combined with an equilibrium coverage model.[56,57] This

approximation has been shown to predict qualitative trends of halide coverage on metals.[56] The equations for a halide (X) adsorbing on a site (*) of glassy carbon are written as follows

$$\frac{1}{2}\mathrm{X_2(g)} + \mathrm{e^-} \rightleftharpoons \mathrm{X^-(aq)} \qquad (\mathrm{eq.\,S4.13})$$

$$\mathrm{X^-(aq)} + * \rightleftharpoons * \mathrm{X} + \mathrm{e^-} \qquad (\mathrm{eq.\,S4.14})$$

Adding **eq. S4.13** and **S4.14** together, we get **eq S4.15**, which is used to calculate halide adsorption free energies on the glassy carbon surface.

$$\frac{1}{2}\mathrm{X_2(g)} + * \rightleftharpoons * \mathrm{X} \qquad (\mathrm{eq.\,S4.15})$$

To model the adsorption of hydroxide (OH) onto the glassy carbon surface, we reference its equilibrium with water and a proton as follows[58]

$$\mathrm{H_2O(aq)} + * \rightleftharpoons * \mathrm{OH} + \mathrm{H^+(aq)} + \mathrm{e^-}$$

$$\mathrm{H^+(aq)} + \mathrm{e^-} \rightleftharpoons \frac{1}{2}\mathrm{H_2(g)}$$

For halide and hydroxide adsorption on glassy carbon with respect to the gas phase, the equilibrium constant (K_{eq}) expression is equal to the ratio of the number of sites occupied by a halide to the number of sites unoccupied sites, which can be written in terms of halide coverage (θ_X) assuming a standard state of 1 M for each species. This result gives **eq. S4.16**.

$$K_{eq} = \frac{[\theta_X]}{[1-\theta_X][X_2]^{1/2}} = \frac{[\theta_X]}{[1-\theta_X]} = \exp(-\frac{\Delta G}{k_b T}) \qquad (\mathrm{eq.\,S4.16})$$

where ΔG is the free energy of adsorption.

We calculate the free energy change as a function of applied potential, U, using the generalized CHE model.[59,60] Entropy and zero-point energy contributions are neglected. We next construct a coverage and potential dependent adsorption free energy model as shown in **eq. S4.17**.

$$\Delta G_{ads} = E_{ads}(\theta) - ne(U - U^o) \qquad (\mathrm{eq.\,S4.17})$$

Here $E_{ads}(\theta)$ is the adsorption energy of the anion as a function of the coverage, *n* is the number of electrons transferred, U^o is the standard reduction potential of the halide, and U is the electrode potential referenced to the SHE. The U^o of Cl_2, Br_2, I_2, and H_2 used in calculations are 1.36, 1.09, 0.54, and 0 V vs SHE, respectively.

We iteratively solve **eq. S4.16** and **S4.17** to obtain the coverage θ as a function of electrode potential U for OH, Cl, Br, and I adsorbed on glassy carbon. The results are shown in **Figure S4.6**.

4.5.7 Supporting Figures and Tables

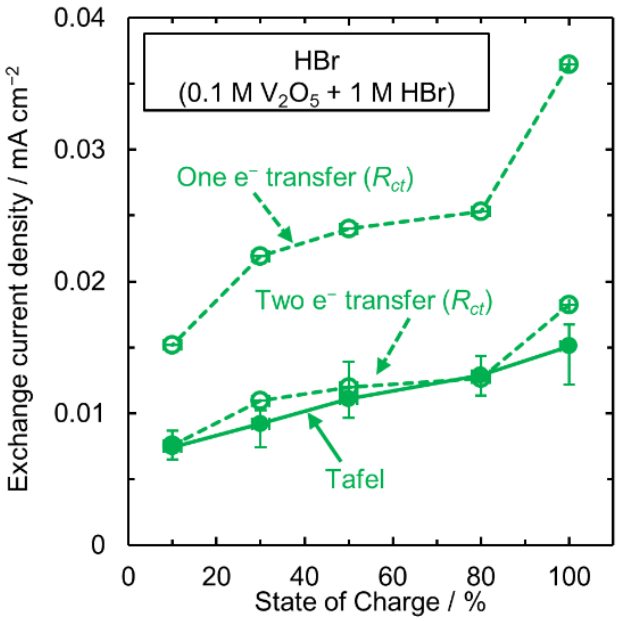

Figure S4.1. V^{2+}/V^{3+} Reaction Kinetics in HBr on Glassy Carbon using Two Independent Methods. Exchange current densities as a function of State of Charge for HBr (0.1 M V_2O_5 + 1 M HBr) obtained by two independent methods: (i) (solid lines) by extrapolating the *y*-intercept of log of oxidation current densities and using the Tafel equation for the reaction: $V^{2+} \rightarrow V^{3+} + e^-$, and (ii) (dashed lines) Charge transfer resistance (R_{ct}) at open circuit voltage using potentiostatic electrochemical impedance measurements assuming an overall one and two electron transfer (for R_{ct}).

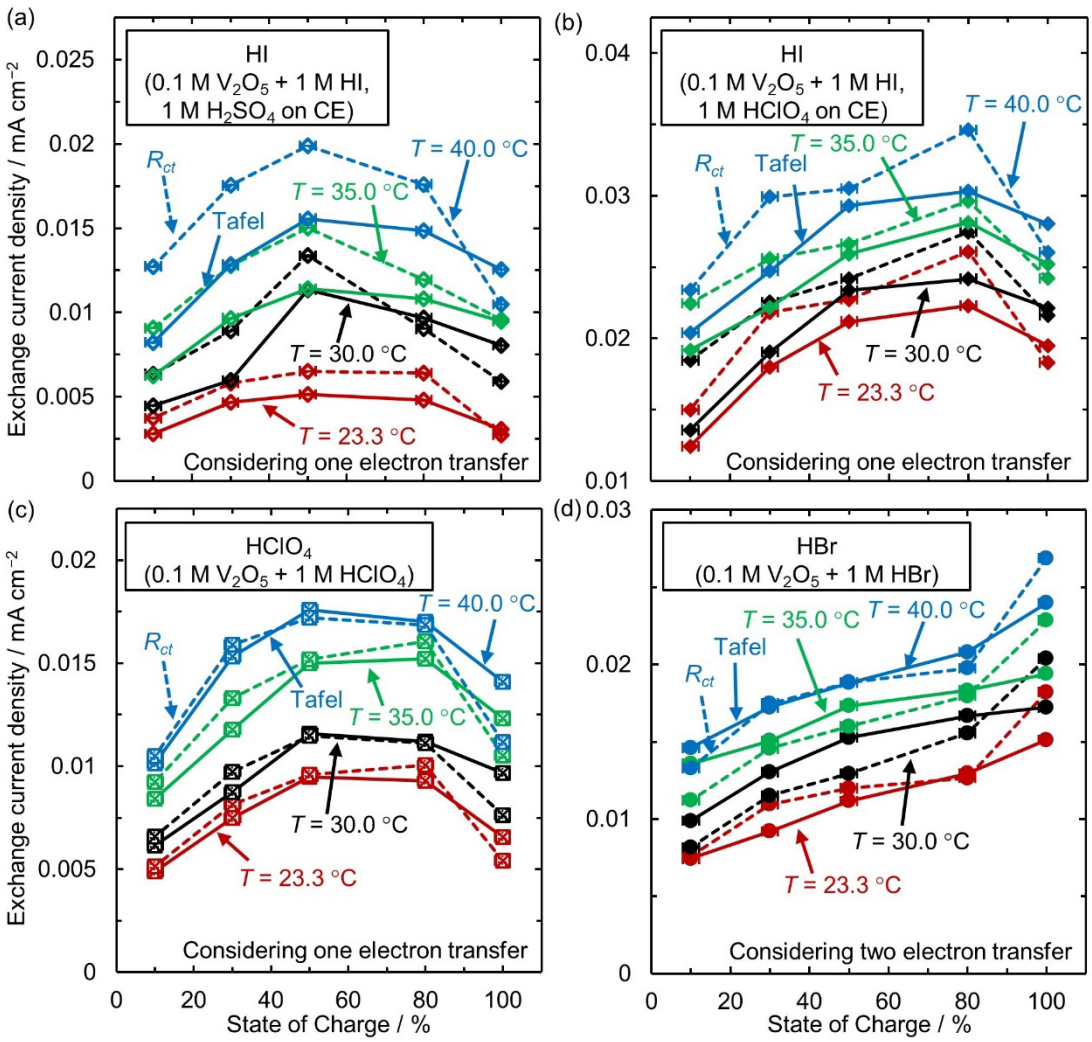

Figure S4.2. V^{2+}/V^{3+} Reaction Kinetics on Glassy Carbon in Various Acidic Electrolytes at Different Temperatures using Two Independent Methods. Exchange current densities as a function of State of Charge obtained by two independent methods: (solid line) using the Tafel equation and (dashed line) Charge transfer resistance (R_{ct}) at open circuit voltage for **(a)** HI with H_2SO_4 on CE (0.1 M V_2O_5 + 1 M HI, 1 M H_2SO_4 on CE) assuming an overall one electron transfer (for R_{ct}). **(b)** HI with $HClO_4$ on CE (0.1 M V_2O_5 + 1 M HI, 1 M $HClO_4$ on CE) assuming an overall one electron transfer (for R_{ct}). **(c)** $HClO_4$ (0.1 M V_2O_5 + 1 M $HClO_4$) assuming an overall one electron transfer (for R_{ct}). **(d)** HBr (0.1 M V_2O_5 + 1 M HBr, 1 M H_2SO_4 on CE) assuming an overall two electron transfer (for R_{ct}), at different temperatures.

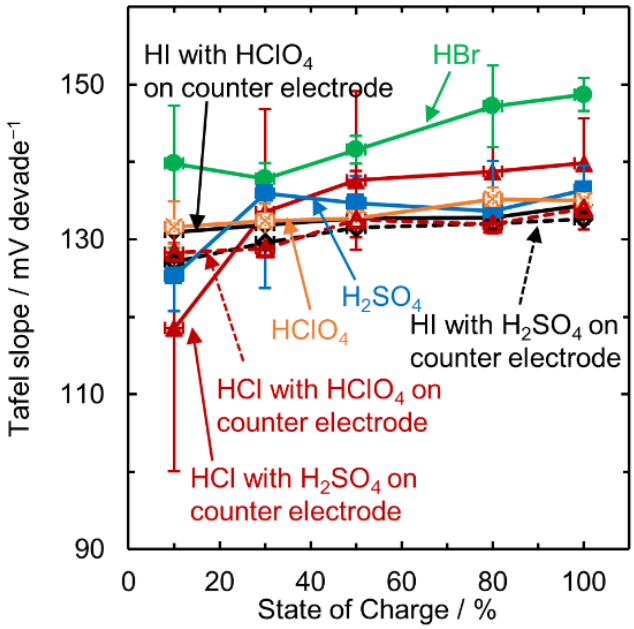

Figure S4.3. Tafel Slopes for V^{2+}/V^{3+} Reaction on Glassy Carbon in Various Acidic Electrolytes. Tafel slopes as a function of State of Charge in H_2SO_4 (0.2 M $VOSO_4$ + 0.5 M H_2SO_4), HCl with H_2SO_4 on CE (0.2 M VCl_3 + 1 M HCl, 1 M H_2SO_4 on counter electrode), HCl with $HClO_4$ on CE (0.2 M VCl_3 + 1 M HCl, 1 M $HClO_4$ on counter electrode), HBr (0.1 M V_2O_5 + 1 M HBr, 1 M H_2SO_4 on counter electrode), HI with H_2SO_4 on CE (0.1 M V_2O_5 + 1 M HI, 1 M H_2SO_4 on counter electrode), HI with $HClO_4$ on CE (0.1 M V_2O_5 + 1 M HI, 1 M $HClO_4$ on counter electrode), and $HClO_4$ (0.1 M V_2O_5 + 1 M $HClO_4$). The data for H_2SO_4 and HCl with H_2SO_4 on counter electrode has been reproduced from reference 11.

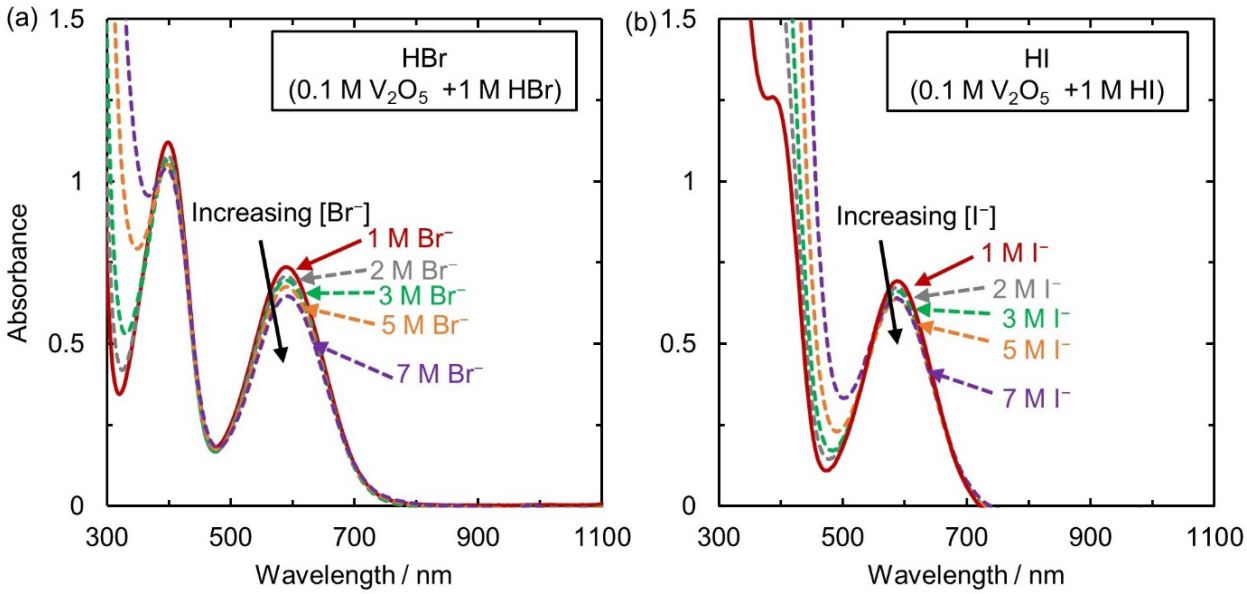

Figure S4.4. UV-vis Spectra of V^{3+} at High Concentrations of Br^- and I^-. UV-vis absorbance of V^{3+} as a function of wavelength at room temperature (T = 23.3 °C) in: **(a)** HBr (0.1 M V_2O_5 + 1 M HBr) with increasing [Br^-]. **(b)** HI (0.1 M V_2O_5 + 1 M HI) with increasing [I^-]. V^{3+} spectra is obtained by reducing V_2O_5 salt completely to V^{2+} and oxidizing back to V^{3+}, followed by the addition of sodium bromide (NaBr, BioXtra, ≥ 99.0%, Sigma Aldrich) or sodium iodide (NaI, ACS Reagent , ≥ 99.5%, Sigma Aldrich).

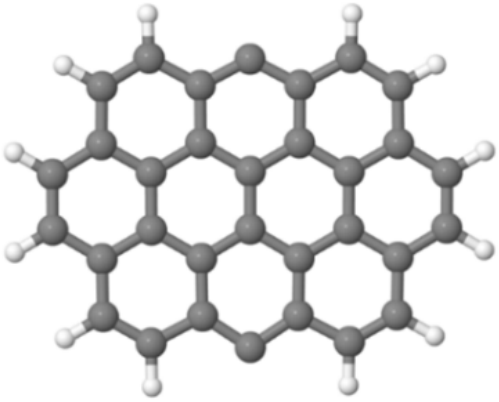

Figure S4.5. Graphene Cluster used as a Model Carbon Surface. The adsorption energies of vanadium-anion intermediate are calculated on graphene cluster instead of glassy carbon, due to the difficulty in modeling glassy carbon because of its amorphous nature.

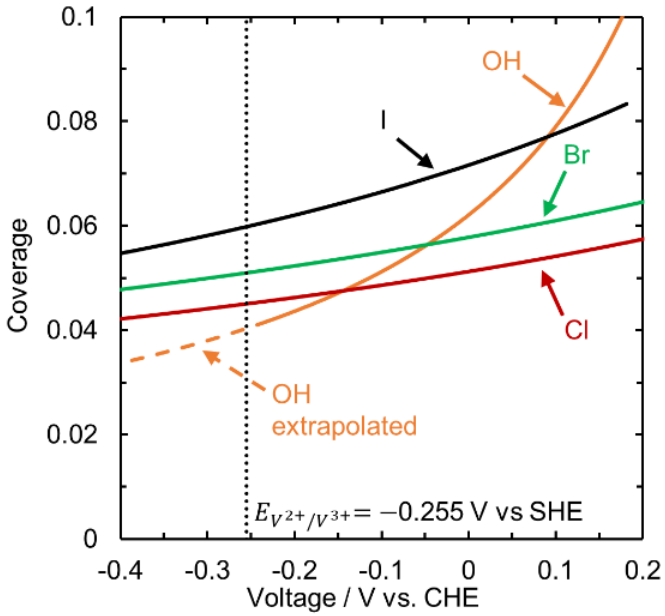

Figure S4.6. Coverage of Halides on Glassy Carbon as a Function of Electrode Potential. Coverage of anions evaluated using DFT with varying electrode potential. Dashed lines represent the coverage of OH when extrapolating the adsorption energy linear fit to low coverages.

Table S4.1. Reaction Orders for V^{2+}/V^{3+} in H_2SO_4, HCl, HBr, $HClO_4$, and HI with H_2SO_4 or $HClO_4$ on Counter Electrode Calculated using Regression. The orders are calculated using regression from exchange current densities for V^{2+}/V^{3+} reaction for 0.2 M vanadium concentration at various temperatures (23.3, 30, 35, and 40 °C). Average values over the four temperatures are reported. These are approximate orders because rate constants vary with changing temperature.

Electrolyte	$[V^{2+}]$ order (γ)		$[V^{3+}]$ order (ε)	
	i_o	$i_{o,R_{ct}}$	i_o	$i_{o,R_{ct}}$
H_2SO_4	0.19 ± 0.05	0.08 ± 0.04	Assuming $\varepsilon = -\gamma$	
HCl	0.13 ± 0.03	0.18 ± 0.05	Assuming $\varepsilon = -\gamma$	
HBr	0.09 ± 0.03	0.13 ± 0.02	Assuming $\varepsilon = -\gamma$	
HI with $HClO_4$ on CE	0.29 ± 0.07	0.25 ± 0.11	0.07 ± 0.03	0.11 ± 0.05
HI with H_2SO_4 on CE	0.46 ± 0.08	0.41 ± 0.11	0.18 ± 0.08	0.29 ± 0.10
$HClO_4$	0.44 ± 0.04	0.44 ± 0.08	0.19 ± 0.07	0.24 ± 0.05

Table S4.2. Structural Parameters from Model Fits to Experimental EXAFS Spectra of V^{2+} and V^{3+} in $HClO_4$, H_2SO_4, and HCl for Two and Multiple Leg Scattering Paths. CN is the coordination number, R is the distance, and σ^2 is the Debye-Waller factor. All parameters are allowed to vary during fitting, unless explicity stated as "set" in parenthesis after their value.

Path	Structural parameters	Perchloric acid		Sulfuric acid			Hydrochloric acid		
		0.2 M V^{2+} + 1 M ClO_4^-	0.2 M V^{3+} + 1 M ClO_4^-	0.2 M V^{3+} + 1.2 M SO_4^{2-}	0.2 M V^{3+} + 1.95 M SO_4^{2-}	0.2 M V^{3+} + 2.7 M SO_4^{2-}	0.2 M V^{3+} + 1.6 M Cl^-	0.2 M V^{3+} + 3.6 M Cl^-	0.2 M V^{3+} + 5.6 M Cl^-
V−O	CN	6 (set)	6 (set)	6 (set)	6 (set)	6 (set)	6 (set)	5.79 ± 0.35	5.70 ± 0.31
	R / Å	2.140 ± 0.011	2.002 ± 0.006	1.994 ± 0.003	1.994 ± 0.002	1.995 ± 0.002	2.008 ± 0.002	2.008 ± 0.005	2.010 ± 0.003
	$\sigma^2 \times 10^3$/ Å^2	8.7 ± 1.4	3.1 ± 0.6	2.9 ± 0.3	2.7 ± 0.3	2.4 ± 0.3	3.4 ± 0.3	2.4 ± 0.5	3.2 ± 0.4
V-H	CN	12	12	11.38 ± 0.70	10.09 ± 1.50	9.68 ± 2.06	12	11.57 ± 0.70	11.41 ± 0.61
	R / Å	2.407 ± 0.013	2.330 ± 0.029	2.324 ± 0.014	2.340 ± 0.023	2.324 ± 0.015	2.346 ± 0.029 (using same ΔR as obtained from V^{3+} in perchloric acid)		
	$\sigma^2 \times 10^3$/ Å^2	0.4 ± 1.5	5.1 ± 3.6	3.0 ± 1.6	2.8 ± 3.1	0.2 ± 2.2	5.1 (set, taken from V^{3+} in perchloric acid)		
V−S	CN	Not Applicable		0.31 ± 0.35	0.96 ± 0.75	1.16 ± 1.03	Not Applicable		
	R / Å			3.238 ± 0.078	3.273 ± 0.032	3.271 ± 0.062			
	$\sigma^2 \times 10^3$/ Å^2			3.0 ± 1.8	4.2 ± 6.8	12.4 ± 13.9			

V−Cl	CN	Not Applicable					--	0.21 ± 0.35	0.30 ± 0.31
	R / Å						--	2.401 ± 0.051	2.360 ± 0.038
	$\sigma^2 \times 10^3$/ Å^2						--	3.2 ± 10.7	3.5 ± 9.6
V−O−O 3-leg collinear	CN	6	6	6	6	6	6	5.58 ± 0.70	5.40 ± 0.62
	R / Å	4.399 ± 0.102	3.931 ± 0.088	4.063 ± 0.067	4.064 ± 0.083	4.103 ± 0.055	3.950 ± 0.082	3.944 ± 0.071	3.936 ± 0.046
	$\sigma^2 \times 10^3$/ Å^2	12.1 ± 19.2	10.7 ± 16.8	3.5 ± 2.3	2.5 ± 10.0	1.3 ± 9.2	9.4 ± 16.4	2.7 ± 12.5	2.5 ± 8.1
V−O−V−O 4-leg collinear	CN	6	6	6	6	6	6	5.58 ± 0.70	5.40 ± 0.62
	R / Å	4.399 ± 0.102	3.931 ± 0.088	4.072 ± 0.067	4.074 ± 0.083	4.112 ± 0.055	3.950 ± 0.082	3.944 ± 0.071	3.936 ± 0.046
	$\sigma^2 \times 10^3$/ Å^2	12.1 ± 19.2	10.7 ± 16.8	3.5 ± 2.3	2.5 ± 10.0	1.3 ± 9.2	9.4 ± 16.4	2.7 ± 12.5	2.5 ± 8.1
V−O−V−O 4-leg double return	CN	6	6	6	6	6	6	5.79 ± 0.35	5.70 ± 0.31
	R / Å	4.279 ± 0.022	4.004 ± 0.012	3.988 ± 0.006	3.988 ± 0.004	3.991 ± 0.004	4.016 ± 0.004	4.017 ± 0.010	4.019 ± 0.006
	$\sigma^2 \times 10^3$/ Å^2	34.8 ± 5.6	12.4 ± 2.4	11.6 ± 1.2	10.8 ± 1.2	9.6 ± 1.2	13.6 ± 1.2	9.6 ± 2.0	12.8 ± 1.6
V−O^{2nd} (2nd coordination sphere)	CN	12	12	12.31 ± 0.35	12.96 ± 0.75	13.16 ± 1.03	12	11.78 ± 0.35	11.70 ± 0.31
	R / Å	4.117 ± 0.072	4.043 ± 0.058	3.763 ± 0.032	3.810 ± 0.051	3.795 ± 0.036	4.049 ± 0.038	4.071 ± 0.071	4.066 ± 0.032
	$\sigma^2 \times 10^3$/ Å^2	26.4 ± 12.8	20.4 ± 12.8	25.3 ± 9.5	23.8 ± 11.5	21.2 ± 8.9	17.8 ± 10.9	14.7 ± 10.4	15.1 ± 6.7
Identified complex		$[V(H_2O)_6]^{2+}$	$[V(H_2O)_6]^{3+}$	$[V(H_2O)_6]^{3+}$ + $[V(H_2O)_5SO_4]^{+}$			$[V(H_2O)_6]^{3+}$ + $[V(H_2O)_5Cl]^{2+}$ + $[V(H_2O)_4Cl_2]^{+}$		

Table S4.3. DFT-calculated Free Energies of Ligand Exchange Reactions (ΔG_L) at 298 K and 1 M Solute Concentration.

Reaction	V oxidation state	ΔG_L / kJ mol^{-1}
$[V(H_2O)_6]^{3+} + Cl^- + SO_4^{2-} \rightleftarrows [V(H_2O)_4SO_4Cl] + 2\,H_2O$	3+	−82.4
$[V(H_2O)_6]^{3+} + SO_4^{2-} \rightleftarrows [V(H_2O)_5SO_4]^+ + H_2O$	3+	−70.7
$[V(H_2O)_6]^{3+} + Br^- + SO_4^{2-} \rightleftarrows [V(H_2O)_4SO_4Br] + 2\,H_2O$	3+	−67.2
$[V(H_2O)_6]^{3+} + HSO_4^- \rightleftarrows [V(H_2O)_5HSO_4]^{2+} + H_2O$	3+	−58.4
$[V(H_2O)_6]^{3+} + 2\,Cl^- \rightleftarrows [V(H_2O)_4Cl_2]^+ + 2\,H_2O$	3+	−48.2
$[V(H_2O)_6]^{3+} + I^- + SO_4^{2-} \rightleftarrows [V(H_2O)_4SO_4I] + 2\,H_2O$	3+	−48.1
$[V(H_2O)_6]^{3+} + Cl^- \rightleftarrows [V(H_2O)_5Cl]^{2+} + H_2O$	3+	−31.2
$[V(H_2O)_6]^{3+} + 2\,Br^- \rightleftarrows [V(H_2O)_4Br_2]^+ + 2\,H_2O$	3+	−19.8
$[V(H_2O)_6]^{3+} + Br^- \rightleftarrows [V(H_2O)_5Br]^{2+} + H_2O$	3+	−14.7
$[V(H_2O)_6]^{3+} + I^- \rightleftarrows [V(H_2O)_5I]^{2+} + H_2O$	3+	0.24
$[V(H_2O)_6]^{3+} + 2\,I^- \rightleftarrows [V(H_2O)_4I_2]^+ + 2\,H_2O$	3+	8.3
$[V(H_2O)_6]^{2+} + Cl^- \rightleftarrows [V(H_2O)_5Cl]^+ + H_2O$	2+	4.2
$[V(H_2O)_6]^{2+} + 2\,Cl^- \rightleftarrows [V(H_2O)_4Cl_2] + 2\,H_2O$	2+	7.7
$[V(H_2O)_6]^{2+} + SO_4^{2-} \rightleftarrows [V(H_2O)_5SO_4] + H_2O$	2+	24.0

Table S4.4. Free Energies for Proposed Vanadium-anion Intermediates Calculated with either the B3LYP-D3 or M06-2X-D3 Functional.

Intermediate	ΔG_{ads}[Complex] (B3LYP-D3) / eV	ΔG_{ads}[Complex] (M06-2X-D3) / eV
*[OH-V$(H_2O)_5]^+$	−2.97	−3.32
*[OH-V$(H_2O)_5]^{2+}$	−3.05	−3.39
*[OH-V$(H_2O)_4SO_4$]	−3.86	−4.18
*[Cl-V$(H_2O)_4Cl]^+$	−2.58	−3.01
*[Cl-V$(H_2O)_5]^{2+}$	−2.18	−2.55
*[Br-V$(H_2O)_4Br]^+$	−2.24	−2.43
*[Br-V$(H_2O)_5]^{2+}$	−1.99	−2.31
*[I-V$(H_2O)_4I]^+$	−2.06	−2.16
*[I-V$(H_2O)_5]^{2+}$	−1.99	−2.23

4.6 References

(1) Aikens, D. A.; Jr., J. W. R. Effect of Chloride on the Kinetics of Electroöxidation of Chromium (II) in Acidic Perchlorate Medium. *J. Phys. Chem.* **1961**, *65* (7), 1213–1216.

(2) Rodes, A.; Feliu, J. M.; Aldaz, A.; Clavilier, J. The Influence of Polyoriented Gold Electrodes Modified by Reversibly and Irreversibly Adsorbed Ad-Atoms on the Redox Behaviour of the Cr(III) / Cr(II) Couple and the Effect of Chloride Ions. *J. Electroanal. Chem* **1989**, *271*, 127–139.

(3) Weber, J.; Samec, Z.; Mareček, V. The Effect of Anion Adsorption on the Kinetics of the Fe^{3+}/Fe^{2+} Reaction on Pt and Au Electrodes in $HClO_4$. *J. Electroanal. Chem. Interfacial Electrochem.* **1978**, *89* (2), 271–288.

(4) Nagy, Z.; Blaudeau, J. P.; Hung, N. C.; Curtiss, L. A.; Zurawski, D. J. Chloride Ion Catalysis of the Copper Deposition Reaction. *J. Electrochem. Soc.* **1995**, *142* (6), L87–L89.

(5) de Levie, R. Anion Bridging and Anion Electrocatalysis on Mercury. *J. Electrochem. Soc.* **1971**, *118* (8), 185C-192C.

(6) Anbar, M.; Hart, E. J. The Reactivity of Metal Ions and Some Oxy Anions toward Hydrated Electrons. *J. Phys. Chem.* **1965**, *69* (3), 973–977.

(7) Heyrovský, J. Retarded Electrodeposition of Metals Studied Oscillographically with Mercury Capillary Electrodes. *Discuss. Faraday Soc.* **1947**, *1*, 212–225.

(8) Sykes, A. G. Further Advances in the Study of Mechanisms of Redox Reactions. *Adv. Inorg. Chem. Radiochem.* **1968**, *10*, 153–245.

(9) Nagle, J. K. Atomic Polarizability and Electronegativity. *J. Am. Chem. Soc.* **1990**, *112*, 4741–4747.

(10) Hati, S.; Datta, D. Electronegativity and Static Electric Dipole Polarizability of Atomic Species. A Semiempirical Relation. *J. Phys. Chem* **1995**, *99*, 10742–10746.

(11) Agarwal, H.; Florian, J.; R. Goldsmith, B.; Singh, N. V^{2+}/V^{3+} Redox Kinetics on Glassy Carbon in Acidic Electrolytes for Vanadium Redox Flow Batteries. *ACS Energy Lett.* **2019**, *4*, 2368–2377.

(12) Newton, T. W.; Baker, F. B. The Intermediate in the Reaction between Vanadium(II) and Vanadium(IV). *Inorg. Chem* **1964**, *3* (4), 569–573.

(13) Ribas Gispert, J. *Coordination Chemistry*, 1st ed.; Wiley-VCH: Weinheim, Germany, 2008.

(14) Scott, S. L. The Burden of Disproof. *ACS Catal.* **2019**, *9*, 4706–4708.

(15) Palmer, B. J.; Pfund, D. M.; Fulton, J. L. Direct Modeling of EXAFS Spectra from Molecular Dynamics Simulations. *J. Phys. Chem.* **1996**, *100*, 13393–13398.

(16) Richens, D. T. Group 5 Elements: Vanadium, Niobium and Tantalum. In *The Chemistry of Aqua Ions: Synthesis, Structure and Reactivity*; John Wiley & Sons, Ltd: Chichester, UK, 1997; pp 230–235.

(17) Sepehr, F.; Paddison, S. J. The Solvation Structure and Thermodynamics of Aqueous Vanadium Cations. *Chem. Phys. Lett.* **2013**, *585*, 53–58.

(18) Krakowiak, J.; Lundberg, D.; Persson, I. A Coordination Chemistry Study of Hydrated and Solvated Cationic Vanadium Ions in Oxidation States +III, +IV, and +V in Solution and Solid State. *Inorg. Chem.* **2012**, *51*, 9598–9609.

(19) Cotton, F. A.; Falvello, L. R.; Llusar, R.; Libby, E.; Murillo, C. A.; Schwotzer, W. Synthesis and Characterization of Four Vanadium(II) Compounds, Including Vanadium(II) Sulfate Hexahydrate and Vanadium(II) Saccharinates. *Inorg. Chem.* **1986**, *25*, 3423–3428.

(20) Cotton, F. A.; Fair, C. K.; Lewis, G. E.; Mott, G. N.; Ross, F. K.; Schultz, A. J.; Williams,

J. M. Precise Structural Characterizations of the Hexaaquovanadium(III) and Diaquohydrogen Ions. X-Ray and Neutron Diffraction Studies of $[V(H_2O)_6][H_5O_2](CF_3SO_3)_4$. *J. Am. Chem. Soc.* **1984**, *106* (18), 5319–5323.

(21) Cotton, F. A.; Falvello, L. R.; Murillo, C. A.; Pascual, I.; Schultz, A. J.; Tomás, M. Neutron and X-Ray Structural Characterization of the Hexaaquavanadium(II) Compound $VSO_4.7H_2O$. *Inorg. Chem* **1994**, *33*, 5391–5395.

(22) Fulton, J. L.; Bylaska, E. J.; Bogatko, S.; Balasubramanian, M.; Cauët, E.; Schenter, G. K.; Weare, J. H. Near-Quantitative Agreement of Model-Free DFT-MD Predictions with XAFS Observations of the Hydration Structure of Highly Charged Transition-Metal Ions. *J. Phys. Chem. Lett* **2012**, *3*, 2588–2593.

(23) Bon, M.; Laino, T.; Curioni, A.; Parrinello, M. Characterization of Vanadium Species in Mixed Chloride−Sulfate Solutions: An Ab Initio Metadynamics Study. *J. Phys. Chem. C* **2016**, *120*, 10791–10798.

(24) Vijayakumar, M.; Li, L.; Nie, Z.; Yang, Z.; Hu, J. Structure and Stability of Hexa-Aqua V(III) Cations in Vanadium Redox Flow Battery Electrolytes. *Phys. Chem. Chem. Phys.* **2012**, *14*, 10233–10242.

(25) Gupta, S.; Lim, T. M.; Mushrif, S. H. Insights into the Solvation of Vanadium Ions in the Vanadium Redox Flow Battery Electrolyte Using Molecular Dynamics and Metadynamics. *Electrochim. Acta* **2018**, *270*, 471–479.

(26) Oldenburg, F. J.; Bon, M.; Perego, D.; Polino, D.; Laino, T.; Gubler, L.; Schmidt, T. J. Revealing the Role of Phosphoric Acid in All-Vanadium Redox Flow Batteries with DFT Calculations and In Situ Analysis. *Phys. Chem. Chem. Phys* **2018**, *20*, 23664–23673.

(27) Martin. Ernest L.; Bentley, K. E. Spectrophotometric Investigation of Vanadium(II), Vanadium(III), and Vanadium(IV) in Various Media. *Anal. Chem.* **1962**, *34* (3), 354–358.

(28) Landry-Hum, J.; Bussière, G.; Daniel, C.; Reber, C. Triplet Electronic States in d^2 and d^8 Complexes Probed by Absorption Spectroscopy: A CASSCF/CASPT2 Analysis of $[V(H_2O)_6]^{3+}$ and $[Ni(H_2O)_6]^{2+}$. *Inorg. Chem.* **2001**, *40* (11), 2595–2601.

(29) Bussière, G.; Beaulac, R.; Cardinal-David, B.; Reber, C. Coupled Electronic States in Trans-$MCl_2(H_2O)_4^{n+}$ Complexes (M: Ni^{2+}, Co^{2+}, V^{3+}, Cr^{3+}) Probed by Absorption and Luminescence Spectroscopy. *Coord. Chem. Rev.* **2001**, *219–221*, 509–543.

(30) Frank, P.; Kustin, K.; Robinson, W. E.; Linebaugh, L.; Hodgson, K. O. Nature and Ligation of Vanadium within Whole Blood Cells and Henze Solution from the Tunicate Ascidia Ceratodes, As Investigated by Using X-Ray Absorption Spectroscopy. *Inorg. Chem* **1995**, *34*, 5942–5949.

(31) Chandrasekhar, P.; Bird, P. H. Synthesis and Characterization of an Oxygen-Bridged Vanadium(III) Dimer. *Inorg. Chem.* **1984**, *23*, 3677–3679.

(32) Hedman, B.; Sung Co, M.; Armstrong, W. H.; Hodgson, K. O.; Lippard, S. J. EXAFS Studies of Binuclear Iron Complexes as Models for Hemerythrin and Related Proteins. *Inorg. Chem.* **1986**, *25*, 3708–3711.

(33) Jiang, Z.; Alexandrov, V. Electrocatalytic Activity of Oxygen-Functionalized Carbon Electrodes for Vanadium Redox Flow Batteries from Free-Energy Calculations. *ACS Appl. Energy Mater.* **2020**, *3*, 7543–7549.

(34) Nørskov, J. K.; Studt, F.; Abild-Pedersen, F.; Bligaard, T. *Fundamental Concepts in Heterogeneous Catalysis*; John Wiley & Sons, Inc.: New Jersey, 2014.

(35) Nørskov, J. K.; Bligaard, T.; Logadottir, A.; Bahn, S.; Hansen, L. B.; Bollinger, M.; Bengaard, H.; Hammer, B.; Sljivancanin, Z.; Mavrikakis, M.; et al. Universality in

Heterogeneous Catalysis. *J. Catal.* **2002**, *209*, 275–278.
(36) Bligaard, T.; Nørskov, J. K.; Dahl, S.; Matthiesen, J.; Christensen, C. H.; Sehested, J. The Brønsted-Evans-Polanyi Relation and the Volcano Curve in Heterogeneous Catalysis. *J. Catal.* **2004**, *224*, 206–217.
(37) Fink, H.; Friedl, J.; Stimming, U. Composition of the Electrode Determines Which Half-Cell's Rate Constant Is Higher in a Vanadium Flow Battery. *J. Phys. Chem. C* **2016**, *120*, 15893–15901.
(38) Li, Y.; Parrondo, J.; Sankarasubramanian, S.; Ramani, V. Impact of Surface Carbonyl-and Hydroxyl-Group Concentrations on Electrode Kinetics in an All-Vanadium Redox Flow Battery. *J. Phys. Chem. C* **2019**, *123*, 6370–6378.
(39) Agarwal, H.; Florian, J.; Goldsmith, B. R.; Singh, N. The Effect of Anion Bridging on Heterogeneous Charge Transfer for V^{2+}/V^{3+}. *Cell Reports Phys. Sci.* **2021**, *2* (1), 100307.
(40) Perdew, J. P.; Burke, K.; Ernzerhof, M. Generalized Gradient Approximation Made Simple. *Phys. Rev. Lett.* **1996**, *77* (18), 3865–3868.
(41) Dang, L. X.; Schenter, G. K.; Glezakou, V.-A.; Fulton, J. L. Molecular Simulation Analysis and X-Ray Absorption Measurement of Ca^{2+}, K^{+} and Cl^{-} Ions in Solution. *J. Phys. Chem. B* **2006**, *110*, 23644–23654.
(42) Rehr, J. J.; Kas, J. J.; Vila, F. D.; Prange, M. P.; Jorissen, K. Parameter-Free Calculations of X-Ray Spectra with FEFF9. *Phys. Chem. Chem. Phys.* **2010**, *12*, 5503–5513.
(43) Young Lee, G.; Bay, K. L.; Houk, K. N. Evaluation of DFT Methods and Implicit Solvation Models for Anion-Binding Host-Guest Systems. *Helv. Chim. Acta* **2019**, *102* (5), e1900032.
(44) Jensen, F. Describing Anions by Density Functional Theory: Fractional Electron Affinity. *J. Chem. Theory Comput.* **2010**, *6* (9), 2726–2735.
(45) Wertz, D. H. Relationship Between the Gas-Phase Entropies of Molecules and Their Entropies of Solvation in Water and 1-Octanol. *J. Am. Chem. Soc.* **1980**, *102*, 5316–5322.
(46) Tawa, G. J.; Topol, I. A.; Burt, S. K.; Caldwell, R. A.; Rashin, A. A. Calculation of the Aqueous Solvation Free Energy of the Proton. *J. Chem. Phys.* **1998**, *109* (12), 4852–4863.
(47) Jinnouchi, R.; Hatanaka, T.; Morimoto, Y.; Osawa, M. First Principles Study of Sulfuric Acid Anion Adsorption on a Pt(111) Electrode. *Phys. Chem. Chem. Phys* **2012**, *14*, 3208–3218.
(48) Chen, N.; Yang, R. T. Ab Initio Molecular Orbital Calculation on Graphite: Selection of Molecular System and Model Chemistry. *Carbon N. Y.* **1998**, *36* (7–8), 1061–1070.
(49) Klamt, A.; Schüürmann, G. COSMO: A New Approach to Dielectric Screening in Solvents with Explicit Expressions for the Screening Energy and Its Gradient. *J. Chem. Soc., Perkin Trans. 2* **1993**, 799–805.
(50) Kaduk, B.; Kowalczyk, T.; Voorhis, T. Van. Constrained Density Functional Theory. *Chem. Rev* **2012**, *112* (1), 321–370.
(51) Jiang, Z.; Klyukin, K.; Alexandrov, V. First-Principles Study of Adsorption–Desorption Kinetics of Aqueous V^{2+}/V^{3+} Redox Species on Graphite in a Vanadium Redox Flow Battery. *Phys. Chem. Chem. Phys.* **2017**, *19*, 14897–14901.
(52) Valiev, M.; Bylaska, E. J.; Govind, N.; Kowalski, K.; Straatsma, T. P.; Van Dam, H. J. J.; Wang, D.; Nieplocha, J.; Apra, E.; Windus, T. L.; et al. NWChem: A Comprehensive and Scalable Open-Source Solution for Large Scale Molecular Simulations. *Comput. Phys. Commun.* **2010**, *181*, 1477–1489.
(53) Deringer, V. L.; Caro, M. A.; Jana, R.; Aarva, A.; Elliott, S. R.; Laurila, T.; Csányi, G.; Pastewka, L. Computational Surface Chemistry of Tetrahedral Amorphous Carbon by

Combining Machine Learning and Density Functional Theory. *Chem. Mater.* **2018**, *30*, 7438–7445.
(54) Grimme, S.; Antony, J.; Ehrlich, S.; Krieg, H. A Consistent and Accurate Ab Initio Parametrization of Density Functional Dispersion Correction (DFT-D) for the 94 Elements H-Pu. *J. Chem. Phys* **2010**, *132*, 154104.
(55) Grimme, S.; Ehrlich, S.; Goerigk, L. Effect of the Damping Function in Dispersion Corrected Density Functional Theory. *J. Comput. Chem.* **2011**, *32* (7), 1456–1465.
(56) Gossenberger, F.; Roman, T.; Groß, A. Equilibrium Coverage of Halides on Metal Electrodes. *Surf. Sci.* **2015**, *631*, 17–22.
(57) Goldsmith, B. R.; Sanderson, E. D.; Ouyang, R.; Li, W.-X. CO- and NO-Induced Disintegration and Redispersion of Three-Way Catalysts Rhodium, Palladium, and Platinum: An Ab Initio Thermodynamics Study. *J. Phys. Chem. C* **2014**, *118*, 9588–9597.
(58) Sakong, S.; Naderian, M.; Mathew, K.; Hennig, R. G.; Groß, A. Density Functional Theory Study of the Electrochemical Interface Between a Pt Electrode and an Aqueous Electrolyte Using an Implicit Solvent Method. *J. Chem. Phys.* **2015**, *142*, 234107.
(59) Nørskov, J. K.; Rossmeisl, J.; Logadottir, A.; Lindqvist, L.; Kitchin, J. R.; Bligaard, T.; Jónsson, H. Origin of the Overpotential for Oxygen Reduction at a Fuel-Cell Cathode. *J. Phys. Chem. B* **2004**, *108*, 17886–17892.
(60) Nørskov, J. K.; Bligaard, T.; Logadottir, A.; Kitchin, J. R.; Chen, J. G.; Pandelov, S.; Stimming, U. Trends in the Exchange Current for Hydrogen Evolution. *J. Electrochem. Soc.* **2005**, *152* (3), J23–J26.

Chapter 5 : Understanding Influence of Halides on Metal Ion Charge Transfer Reactions*

* This chapter is adapted with permission from Florian, J.; Agarwal, H.; Singh, N.; Goldsmith, B. R. Why Halides Enhance Heterogeneous Metal Ion Charge Transfer Reactions. *Chem. Sci.* **2021**, *12*, 12704–12710. The computational portion of the work is conducted by Jacob Florian.

5.1 Summary

The reaction kinetics of many metal redox couples on electrode surfaces are enhanced in the presence of halides (i.e., Cl^-, Br^-, I^-). In this chapter, using first-principles metadynamics simulations, we show a correlation between calculated desorption barriers of V^{3+}-anion complexes bound to graphite via an inner sphere anion bridge and experimental V^{2+}/V^{3+} kinetic measurements on edge plane pyrolytic graphite in H_2SO_4, HCl, and HI. We extend this analysis to V^{2+}/V^{3+}, Cr^{2+}/Cr^{3+}, and Cd^0/Cd^{2+} reactions on a mercury electrode and demonstrate that reported kinetics in acidic electrolytes for these redox couples also correlate with the predicted desorption barriers of metal-anion complexes. Therefore, the desorption barrier of the metal-anion intermediate is a descriptor of kinetics for many metal redox couple/electrode combinations in the presence of halides.

5.2 Introduction

Electrochemical charge transfer (CT) of metal ions has applications in energy storage,[1] wastewater remediation,[2] organic synthesis,[3] and chemical production.[4] Understanding and controlling CT at the electrode surface would increase energy efficiency, product selectivity, and reduce capital cost of devices. Interestingly, halides accelerate the kinetics of many

electrochemical reactions in aqueous solution as shown in **Figure 5.1**. For example, heterogeneous CT reactions including V^{2+}/V^{3+},[5,6] Cr^{2+}/Cr^{3+},[7,8] Fe^{2+}/Fe^{3+},[9,10] and Eu^{2+}/Eu^{3+},[11] and metal electrodeposition reactions, such as Cd^0/Cd^{2+} and Zn^0/Zn^{2+},[12,13] show rate constants (k) that are up to 10^3 higher in the presence of chloride (Cl^-), bromide (Br^-), or iodide (I^-). Kinetic enhancement by halides is observed on many electrodes, including glassy carbon (GC),[14] Hg,[15] Au,[7,10] and Pt,[9,16] where the increase in k typically is the largest for I^-, followed by Br^-, and then Cl^-. Thus, understanding the cause of these enhancements would guide electrolyte and electrode selection.

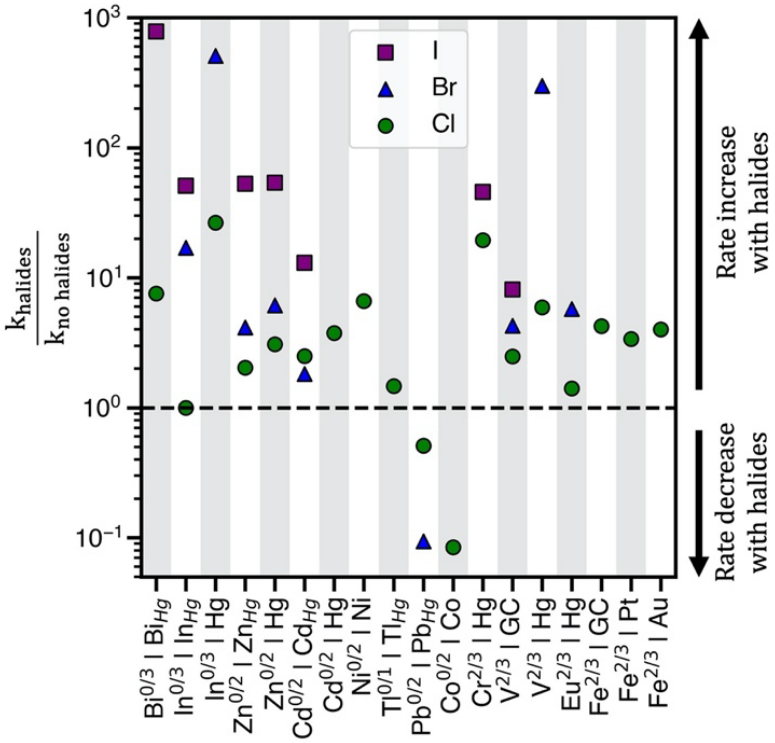

Figure 5.1. Effect of Halides on Metal Ion Charge Transfer Kinetics for Multitude of Redox Couples. The observed ratios of rate constants with and without halides for various redox couples and electrodes in aqueous electrolytes. $k_{halides}$ corresponds to the rate constant in the presence of halides, whereas $k_{no\ halides}$ corresponds to the rate constant in sulfate or perchlorate electrolytes. The abscissa shows 'redox couple | electrode surface' combinations where rate data has been reported. The halides present in the electrolytes considered are either chloride, bromide, or iodide. GC = Glassy carbon electrode and M_{Hg} = Metal-Hg amalgam alloy electrode. **Table S5.1** in the Supporting Information (SI) contains the standard rate constants for these redox couples.

Halide-induced rate enhancements may arise from the halide ions being adsorbed on electrodes to serve as sites for adsorption and CT of metal ions. This mechanism, whereby the halide anion adsorbed on the electrode acts as a bridge in the electron transfer between metal ion and electrode,

has been called anion bridging.[15] The anion bridging mechanism has been invoked to explain rate enhancements for Cr^{2+}/Cr^{3+}, V^{2+}/V^{3+}, Sb^{3+}/Sb^{5+}, and Fe^{2+}/Fe^{3+} redox couples.[10,14,15,17,18] A two-step inner sphere mechanism for how an adsorbed anion ($*X$) promotes oxidation of a metal ion (M^{n+}) through the formation of an adsorbed metal-anion intermediate ($*XM^{n+1}$) is written in **eq. 5.1** and **5.2**. Although here we write M^{n+1} as the product leaving behind $*X$, it is also possible that the halide becomes part of the desorbed complex as XM^{n+1}.

$$M^{n+} + *X \leftrightarrows *XM^{n+1} + e^- \quad \text{(eq. 5.1)}$$

$$*XM^{n+1} \leftrightarrows *X + M^{n+1} \quad \text{(eq. 5.2)}$$

Although this mechanism is plausible, there is little knowledge of how the metal ion and the bridging anion together promote CT and why the rate enhancement relative to non-complexing electrolytes (i.e., through *OH bridge) typically follows the order of $Cl^- < Br^- < I^-$. This order of rate enhancement correlates with increasing free anion polarizability,[19,20] that is, polarizable anions can more easily transfer one of their outer shell electrons to the metal cation while the other electron is being transferred from the electrode surface to the anion bridge. However, free anion polarizability does not account for the electrode and redox couple identity. Interfacial potential shifts due to anion adsorption can also increase the rate of metal ion redox couples, as has been reported previously.[21] However, some studies have found that electrostatic effects alone are insufficient to explain the large increases (> 10 $k_{\text{halide}}/k_{\text{no halides}}$) in the observed rate constants and postulated that anion bridging may be responsible.[8,10,15,18]

In this chapter, building up on our findings of **Chapters 3** and **4**, we test our hypothesis that anion bridging on electrodes increases the kinetics for many metal redox couples by changing the energy of the metal-anion surface intermediate ($*XM^{n+1}$) and its adsorption and desorption barriers. The energy of $*XM^{n+1}$ controls the fraction of active sites that the intermediate occupies

and the apparent activation barriers for the redox reaction. In **Scheme 5.1a** we show an energy diagram of a metal ion CT reaction involving the adsorbed intermediate written in **eq. 5.1** and **5.2**. We assume that electron transfer is fast so that it occurs concurrently with either adsorption or desorption. This assumption is consistent with observations that rate enhancements arise from changes in the barrier associated with the formation of adsorbed complexes as opposed to the intrinsic barrier for electron transfer.[15,17] At equilibrium, the reduced and oxidized species are the same energy, and the forward and reverse rates are equal and opposite. The magnitude of these rates is proportional to the experimental rate constant (k) and exchange current density (i_o).

The energy of the surface intermediate should correlate with the ease at which the intermediate desorbs from the surface, thus we hypothesize the desorption free energy barrier ($\Delta G_{des}^{\ddagger}$) is a descriptor for redox kinetics. For chemically similar surface reactions, the activation barrier of an elementary step is often linearly correlated to the reaction energy of that step, referred to as a Brønsted-Evans-Polanyi (BEP) relation.[22] Therefore, the adsorption barrier ($\Delta G_{ads}^{\ddagger}$) linearly correlates with the adsorption energy (ΔG_{ads}) and the desorption barrier ($\Delta G_{des}^{\ddagger}$) linearly correlates with the desorption energy (ΔG_{des}) if a BEP relation holds. If true, $\Delta G_{des}^{\ddagger}$ positively correlates with ΔG_{des} and negatively correlates with ΔG_{ads} (**Scheme 5.1b**). The oxidation rate is a function of the concentration of the reduced species ($[M^{n+}]$) and the rate constants for adsorption (k_{ads}) and desorption (k_{des}) on the surface. Adsorption is rate-limiting at low values of $\Delta G_{des}^{\ddagger}$, whereas desorption is rate-limiting at high values of $\Delta G_{des}^{\ddagger}$, thus the rate is maximized at intermediate $\Delta G_{des}^{\ddagger}$ values at the top of the volcano curve in **Scheme 5.1c**.[23] The rate has contributions from the apparent, or experimentally observed activation energy and frequency factor. The apparent activation energy (**Scheme 5.1d**) correlates with $\Delta G_{ads}^{\ddagger}$ ($\Delta G_{des}^{\ddagger}$) when $\Delta G_{des}^{\ddagger}$ is low (high).

Similarly, neglecting entropic changes, the apparent frequency factor (**Scheme 5.1e**) approaches the frequency factor for the adsorption step, A_1 (desorption step, A_2) at low (high) values of $\Delta G_{des}^{\ddagger}$.

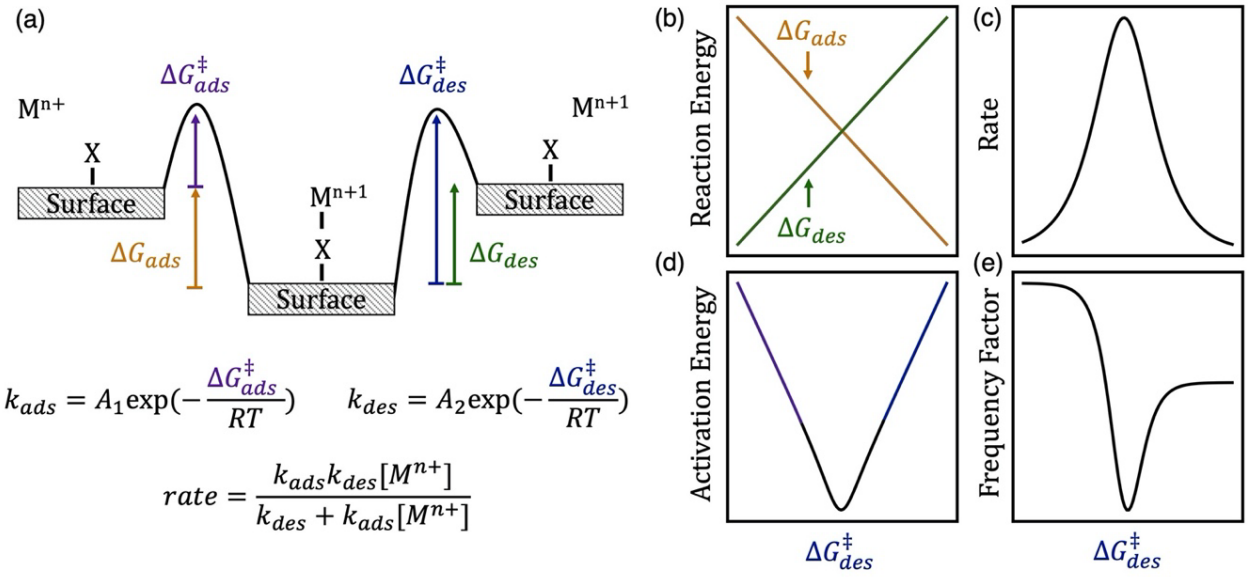

Scheme 5.1. Reaction Energy Diagram and Predicted Trends for Kinetic Parameters with Varying Desorption Barriers. (a) Energy diagram of a metal ion charge transfer reaction involving an adsorbed intermediate. The desorption free energy barrier ($\Delta G_{des}^{\ddagger}$) of the metal-anion surface intermediate can be a descriptor for kinetics of a M^{n+}/M^{n+1} redox couple. The diagrams on the right show the dependence of **(b)** reaction energy, **(c)** rate (proportional to exchange current density and observed rate constant), **(d)** apparent activation energy, and **(e)** apparent frequency factor on $\Delta G_{des}^{\ddagger}$, assuming Brønsted-Evans-Polanyi scaling relations hold. Here k_{ads} has units of s^{-1}, k_{des} has units of mol L^{-1} s^{-1}, and overall rate has units of mol L^{-1} s^{-1}.

We establish a relationship between desorption free energy barriers of metal-anion complexes and the kinetics of various redox reactions that rationalizes the enhancement by halides following the model discussed in **Scheme 5.1**. If BEP relations exist, any of the free energies in **Scheme 5.1** could be calculated, but here we focus on $\Delta G_{des}^{\ddagger}$ due to prior work showing its relevance to metal ion CT kinetics[24] and because it can be relatively straightforwardly computed. Using density functional theory (DFT)-based metadynamics simulations, we predict $\Delta G_{des}^{\ddagger}$ of V^{3+}-anion complexes on the graphite edge plane $(11\bar{2}0)$ [graphite$(11\bar{2}0)$] and compare to our V^{2+}/V^{3+} kinetic measurements on edge plane pyrolytic graphite (EPPG) in H_2SO_4 and hydrohalic acids. We evaluate V^{2+}/V^{3+} experimental exchange current densities (i_o), apparent frequency factors, and

apparent activation energies (E_a) on EPPG in sulfuric (H_2SO_4), hydrochloric (HCl), and hydriodic (HI) acids following the process described in **Chapters 2–4** and show that these parameters correlate with the predicted desorption barriers. Desorption barriers of V^{3+}-, Cr^{3+}-, and Cd^{2+}-anion complexes are also calculated on a model mercury Hg(111) electrode to examine whether $\Delta G_{des}^{\ddagger}$ correlates with rate constants across different redox couples and electrodes. These metal ions are chosen because of the availability of experimental rate data displaying an increase in activity in the presence of halides (**Figure 5.1**).

Our results show that desorption barriers of metal-anion complexes on model surfaces correlate with rate constants on polycrystalline electrodes, but inner sphere CT rates and adsorption of anions are also dependent on the surface structure of the electrode.[25] When rates of Fe^{2+}/Fe^{3+} CT on different facets of Pt[26] and Au[27] were examined in non-complexing perchloric acid, the rates correlated with the potential of zero charge (PZC) of the different facets. This finding suggests that the dependence of the rate constant on the local electrode structure comes, at least in part, from variations in the PZC, which affect the structure of the double layer. When Fe^{2+}/Fe^{3+} kinetics were measured in sulfuric acid, which is reported to follow an inner sphere mechanism,[28] a 30-fold increase in activity was observed at the grain boundaries of a polycrystalline Pt electrode compared to on the grains themselves.[26] Clearly, the rates for heterogeneous CT reactions are not uniform on a polycrystalline electrode, and corresponding desorption barriers of metal-anion complexes on different facets are likely to change. Although we limit our calculation of desorption barriers to a single facet for different electrodes, we elucidate qualitative trends by correlating desorption barriers of predicted metal-anion intermediates to experimental kinetic data on a given electrode surface. Our findings show that desorption barriers of metal-anion intermediates are descriptors for CT kinetics of redox couple across a constant electrode surface and support the hypothesis that

halides increase the CT in redox couples by changing the energy and transition states of the adsorbed metal-anion intermediate.

5.3 Results and Discussion

5.3.1 V^{2+}/V^{3+} Reaction on Graphite Edge Plane

We study the V^{2+}/V^{3+} reaction in this work because we have identified the solution-phase structure in various electrolytes as discussed in **Chapter 4**, and a prior study showed that the desorption barrier of the V^{3+} intermediate in non-complexing solution can be related to redox kinetics.[24] A metadynamics study predicted the adsorption and desorption barriers of $[V(H_2O)_6]^{2+}$ and $[V(H_2O)_6]^{3+}$ through an oxygen bridge on graphite$(11\bar{2}0)$ and found that $[V(H_2O)_6]^{3+}$ desorption had a larger barrier and was rate limiting.[24] Thus, a lower desorption barrier for the V^{3+}-complex should result in faster kinetics.

Our predicted desorption barriers of V^{3+}-anion complexes on graphite$(11\bar{2}0)$ and experimental kinetic parameters of V^{2+}/V^{3+} on EPPG in H_2SO_4, HCl, and HI are shown in **Figure 5.2**. The cell and graphite$(11\bar{2}0)$ model used in metadynamics simulations to predict $\Delta G_{des}^{\ddagger}$ are shown in **Figure 5.2a**. The EPPG used in experiments consists of multiple parallel edge facets, which resembles graphite$(11\bar{2}0)$. The kinetic measurements are conducted at various V^{2+} and V^{3+} concentrations using a rotating disk electrode setup to prevent mass transfer limitations and kinetic parameters are estimated using Tafel and CT resistance methods both of which show quantitative agreement. The change in E_a at various V^{2+} and V^{3+} concentrations in each electrolyte (**Figures S5.1** and **S5.2**) indicates that the V^{2+}/V^{3+} is an inner sphere CT reaction on EPPG that involves an adsorbed intermediate, as opposed to an outer sphere reaction where E_a is independent of vanadium concentration. This dependence of apparent activation energy on vanadium concentrations arises because of the dependence of coverage on temperature, which causes the

apparent activation energy to include contributions both from the rate constant and enthalpies of adsorption/desorption steps.[14]

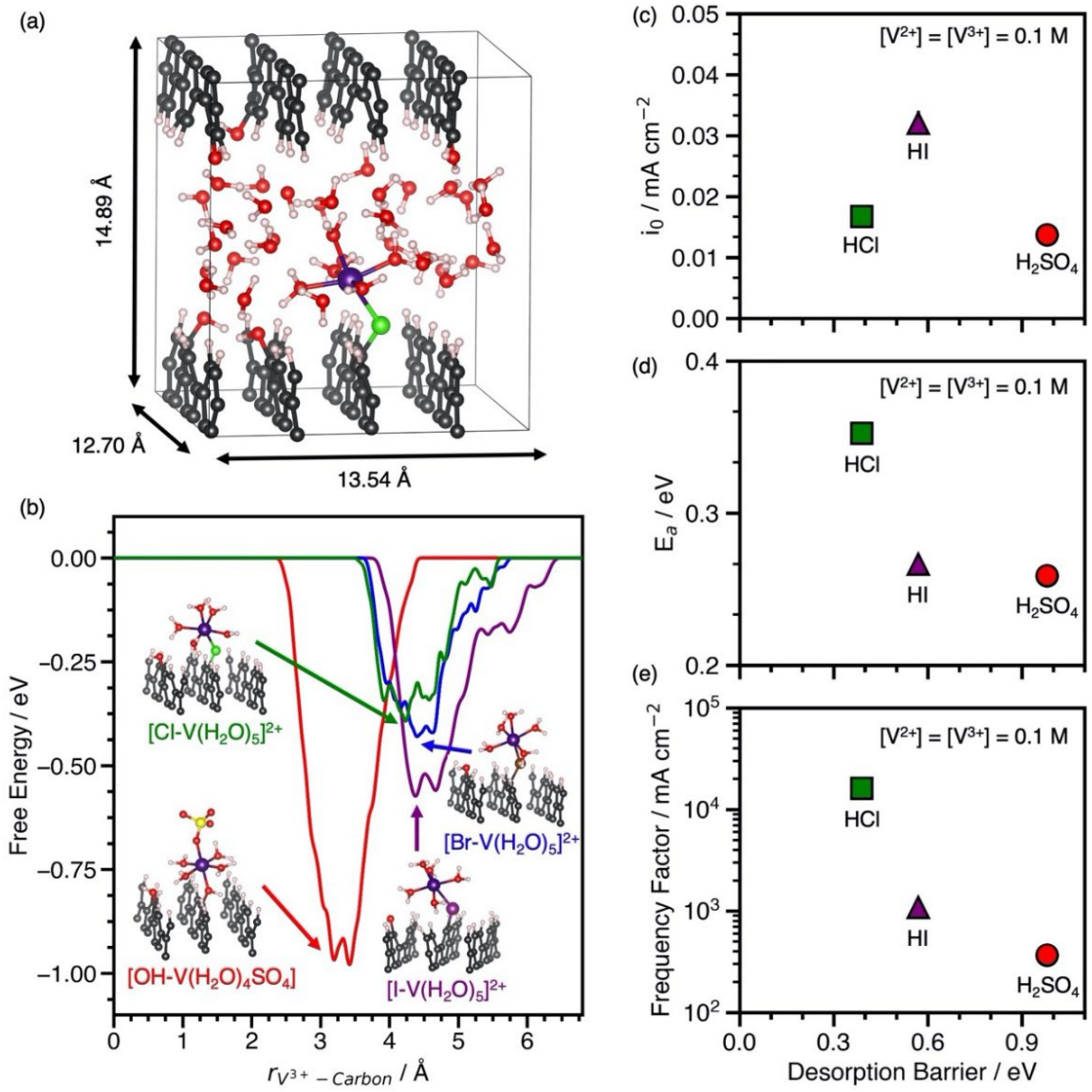

Figure 5.2. Computational Metadynamics of V^{3+}-anion Complexes on Graphite and Experimental Kinetic Measurements of V^{2+}/V^{3+} Reaction on Edge Plane Pyrolytic Graphite. (a) Cell used for metadynamics simulations of V^{3+}-anion complexes on graphite($11\bar{2}0$). **(b)** Free energy vs the distance between the V^{3+} ion and the carbon surface for V^{3+}-anion complexes adsorbed to graphite($11\bar{2}0$) through an *OH, *Cl, *Br, or *I bridge at 300 K. Geometries of adsorbed V^{3+}-anion complexes at the free energy minima are shown next to the corresponding free energy profile in H_2SO_4 (red line), HCl (green line), HBr (blue line), and HI (purple line). Atom color legend: C = gray, V = violet, O = red, S = yellow, H = white, Cl = green, Br = dark brown, I = purple. **(c)** V^{2+}/V^{3+} exchange current density (i_o) at room temperature ($T = 23.3$ °C) on EPPG in H_2SO_4, HCl, and HI from steady state current densities as a function of voltage extrapolated to equilibrium voltage using the Tafel equation vs. the V^{3+}-anion complex desorption barrier. **(d)** V^{2+}/V^{3+} apparent activation energy (E_a) in H_2SO_4, HCl, and HI extracted from the temperature dependence of i_o from measurements between 23.3−40 °C vs the V^{3+}-anion complex desorption barrier. **(e)** V^{2+}/V^{3+} frequency factors vs. the V^{3+}-anion complex desorption barrier. For all experimental measurements in (c−e), the acid concentration is 1 M and concentrations of both V^{2+} and V^{3+} are 0.1 M.

The adsorbed *[X-V(H_2O)$_5$] (where X = Cl, Br, or I) and *[OH-V(H_2O)$_4SO_4$] were used as models for the adsorbed metal-anion complex in hydrohalic acids and H_2SO_4, because they preserve the V^{3+} structure in solution and are adsorbed through an anion bridge. The *[OH−V(H_2O)$_4SO_4$] complex is modeled through an *OH bridge, because *SO_4 is unstable on carbon surfaces.[14] **Figure 5.2b** shows the desorption free energy profiles of V^{3+}-anion complexes from graphite$(11\bar{2}0)$ based on metadynamics simulations using spin-polarized DFT with the PBE functional. To calculate $\Delta G_{des}^{\ddagger}$, the distance between the metal ion and the surface was biased until the complex desorbs. Desorption barriers through halide bridges are lower than through an *OH bridge on graphite$(11\bar{2}0)$ in the order *OH > *I > *Br > *Cl. Additional DFT and metadynamics modeling details are given in the SI (**Figures S5.3–S5.5**).

The behavior between the measured i_o in each electrolyte and $\Delta G_{des}^{\ddagger}$ of the V^{3+}-anion complexes in **Figure 5.2c** matches the volcano-like relationship in **Scheme 5.1c**. V^{3+} adsorbs too strongly in H_2SO_4 such that desorption is rate-limiting, and as $\Delta G_{des}^{\ddagger}$ decreases due to weaker V^{3+} adsorption in HI, the rate begins to increase. However, once $\Delta G_{des}^{\ddagger}$ is too low, the adsorption of species become rate-limiting as suggested by rate measurements in HCl. The i_o has contributions from both E_a and the apparent frequency factor, which are shown in **Figure 5.2d** and **5.2e**. The data in **Figure 5.2d** resembles the inverse volcano in **Scheme 5.1d** with a hypothetical minimum between *[I−V(H_2O)$_5$]$^{2+}$ in HI and *[OH−V(H_2O)$_4SO_4$] in H_2SO_4. Assuming BEP relations hold, the ideal desorption barrier with the lowest E_a will be located at that minimum. Despite having the lowest measured E_a among the electrolytes studied, the V^{2+}/V^{3+} exchange current density is lowest in H_2SO_4 because it has a low frequency factor, as shown in **Figure 5.2e**. Using this as a model, we predict that the i_o, E_a, and apparent frequency factor of V^{2+}/V^{3+} in HBr will be between that in HCl and HI, because the desorption barrier of *[Br−V(H_2O)$_5$]$^{2+}$ is between *[Cl−V(H_2O)$_5$]$^{2+}$ and

*[I−V$(H_2O)_5$]$^{2+}$. We also find that the E_a observed on EPPG in the presence of halides does not correlate with increasing free anion polarizability. This finding highlights the importance of understanding the surface intermediate structure and that using anion physicochemical properties alone are insufficient to explain the observed kinetic behavior.

5.3.2 V^{2+}/V^{3+}, Cr^{2+}/Cr^{3+}, and Cd^0/Cd^{2+} Reaction on Mercury

To assess the transferability of the desorption barrier as a descriptor, we compare the $\Delta G_{des}^{\ddagger}$ of adsorbed V^{3+}-, Cr^{3+}-, and Cd^{2+}-anion complexes on a mercury (Hg) electrode to standard rate constants in sulfuric and hydrohalic acids. Mercury is the most widely reported electrode for anion-promoted electrocatalysis of metal redox couples with several experimental rate constants available in the literature (**Table S5.1**). Anion-promoted electrocatalysis has also been reported on surfaces such as Au, Pt, and carbon, but data is sparse and often consists of only one or two redox couple/electrolyte combinations. We predict the desorption barriers of V^{3+}-, Cr^{3+}-, and Cd^{2+}-anion complexes adsorbed on a Hg(111) electrode through halide and hydroxyl bridges, **Figure 5.3**. Hg(111) is often used as a model surface (**Figure S5.3**) for mercury electrodes to study qualitative trends.[30–33]

The effect of halides on the desorption barrier for V^{3+} complexes adsorbed on Hg(111) are different than on graphite$(11\bar{2}0)$. In the case of V^{3+} desorption on Hg(111) (**Figure 5.3a**), *[Br−V$(H_2O)_5$]$^{2+}$ has a desorption barrier of 1.91 eV, followed by *[Cl−V$(H_2O)_5$]$^{2+}$ at 1.28 eV, and *[OH−V$(H_2O)_4SO_4$] at 0.46 eV. This trend for V^{3+} complexes on Hg(111) is opposite to that of graphite$(11\bar{2}0)$, where $\Delta G_{des}^{\ddagger}$ is largest in sulfate electrolytes. This change in trends of desorption barriers for the same redox couple must arise due to the difference in nature of the interaction of the intermediate with Hg(111) and graphite$(11\bar{2}0)$. Hg, being noble, has chemisorption that is dominated by Pauli repulsion (especially for electronegative adsorbates such

as halides), while chemisorption on graphite is dominated by covalent interactions.[34] Generally, $\Delta G_{des}^{\ddagger}$ is much larger on Hg(111) than graphite($11\bar{2}0$).

Cr^{3+} complexes with anions in its first solvation sphere, and CT is predicted to take place through a adsorbed chromium-anion complex i.e., Cr^{3+}-anion bridge on Hg.[15,35] We predict that Cr^{3+} behaves similarly to V^{3+} on Hg(111), where halides increase the $\Delta G_{des}^{\ddagger}$ relative to sulfate in the same order (*OH < *Cl < *Br < *I), **Figure 5.3b**. The *[OH−$Cr(H_2O)_4SO_4$] complex only physisorbs on the surface, consistent with experiments suggesting that Cr^{2+}/Cr^{3+} CT is outer sphere in the presence of sulfate on Hg electrodes.[8]

We also model the desorption of Cd^{2+} on Hg(111), but only in H_2SO_4 and HCl, where rate data for Cd^0/Cd^{2+} is available.[12] Cd^{2+}-anion complexes have been proposed as the adsorbing species on Hg electrodes in hydrohalic acids.[36,37] From **Figure 5.3c**, the desorption barrier of the Cd^{2+}-chloride complex is 2.35 eV, which is much higher than the Cd^{2+}-sulfate complex at 0.64 eV. In the initial geometry, Cd^{2+} was coordinated with five water molecules and one chloride or sulfate ligand, consistent with a report that aqueous Cd^{2+} has a coordination number of six.[38] During the simulation, Cd^{2+} adsorbed directly onto Hg(111) and formed a *[Cl−$Cd(H_2O)_2$]$^+$ complex. After Cd^{2+} desorbed, the solvent waters were reincorporated into the first solvation sphere to form the [$Cd(H_2O)_5Cl$]$^+$ complex. The desorption barriers of Cd^{2+} complexes are higher than V^{3+} and Cr^{3+} complexes in the same electrolyte.

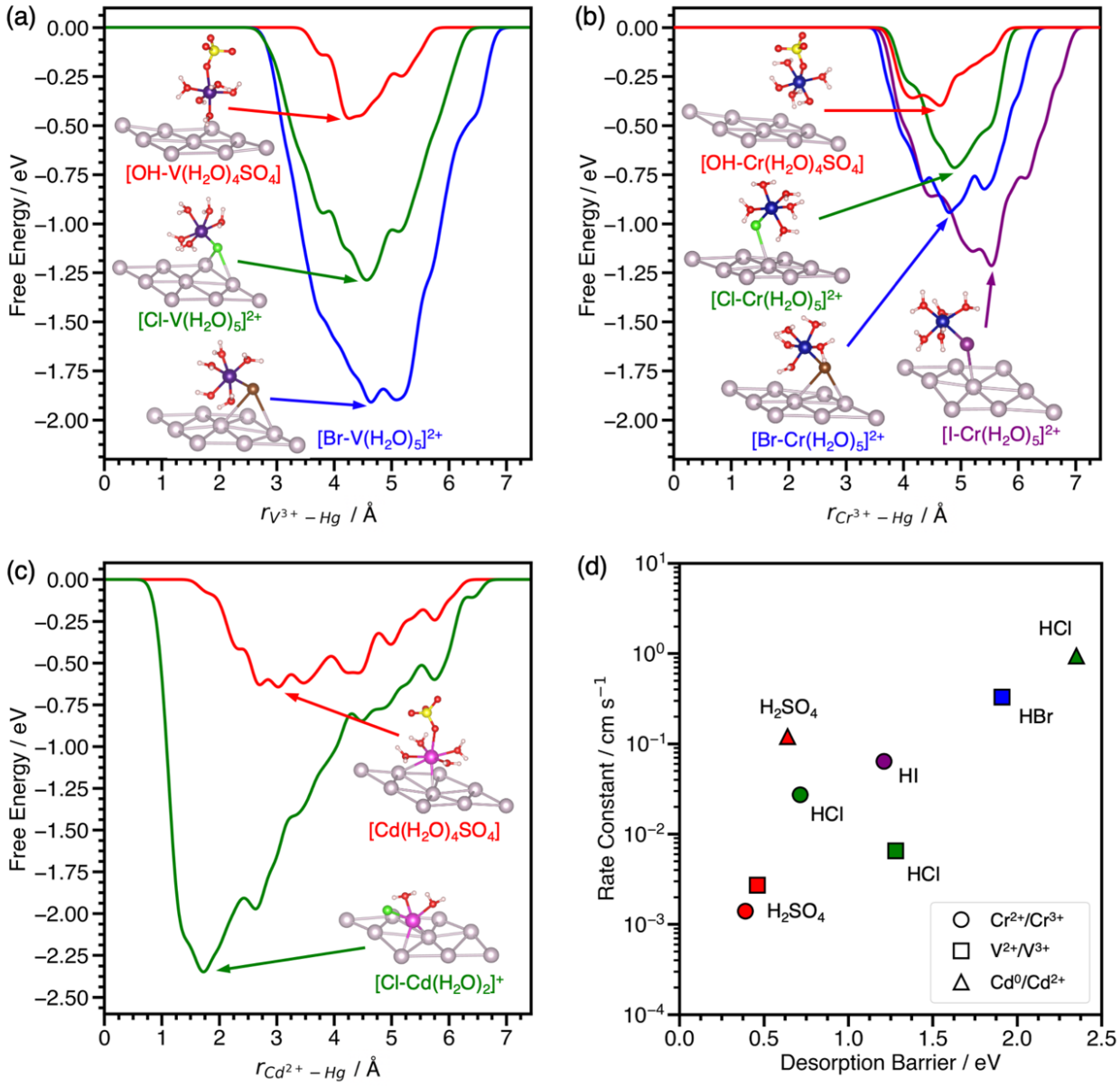

Figure 5.3. Desorption Barriers and Kinetics in the Presence of Halides of Metal Complexes on Mercury Electrode. Metadynamics-based free energy profiles for desorption of **(a)** V^{3+}-, **(b)** Cr^{3+}-, and **(c)** Cd^{2+}-anion complexes from Hg(111) through an *OH, *Cl, *Br, or *I bridge at 300 K. Snapshots of the adsorbed metal-anion complexes are shown at the free energy minima. **(d)** Experimental standard rate constants of the metal charge transfer reactions on mercury drop electrodes plotted against the corresponding predicted desorption barriers from (a−c). Colors denote the acid, namely H_2SO_4 (red), HCl (green), HBr (blue), and HI (purple). Rate constants for these reactions were reproduced from references 11,12,41 Atom color legend: Hg = gray, V = dark purple, Cr = blue, Cd = pink, O = red, S = yellow, H = white, Cl = green, Br = dark brown, I = purple.

The desorption barriers of V^{3+}, Cr^{3+}, and Cd^{2+} on Hg(111) show a positive correlation with previously measured standard rate constants of the V^{2+}/V^{3+}, Cr^{2+}/Cr^{3+}, and Cd^{0}/Cd^{2+} reactions on mercury drop electrodes in **Figure 5.3d**. Although Cd^{0}/Cd^{2+} metal electrodeposition is expected

to follow a different reaction mechanism than the inner sphere CT of aqueous ions, the correlation still holds. This may occur because the first electron transfer step (i.e., Cd^{+}/Cd^{2+}) is slower than the solid metal formation (i.e., Cd^{0}/Cd^{+}), making the kinetic trends more closely resemble that of aqueous CT.[39,40] This positive correlation between desorption barrier and rate constant suggests that these points are on the left side of the volcano curve in **Scheme 5.1c** where adsorption is rate limiting and not around the maximum like V^{2+}/V^{3+} on EPPG. For a given redox couple in **Figure 5.3d**, the CT rate constant and desorption barriers increase going from H_2SO_4 (*OH bridge) < HCl (*Cl bridge) < HBr (*Br bridge) < HI (*I bridge). This observation suggests that the more polarizable halides decrease the energy of the active metal-anion intermediate on Hg, thus increasing surface coverage and leading to higher reaction rates. Unlike V^{2+}/V^{3+} on EPPG, we do not have experimental apparent activation energies for a more detailed comparison of kinetics on Hg electrodes. We hypothesize that activation energies for V^{2+}/V^{3+}, Cr^{2+}/Cr^{3+}, and Cd^{0}/Cd^{2+} on Hg will negatively correlate with the desorption barrier and the rate constant.

We also compute desorption barriers of Fe^{2+}/Fe^{3+} on Au(111) through *OH, *Cl and *Br bridges (**Figure 5.4**). Qualitative enhancements in rate constants have been reported for Fe^{2+}/Fe^{3+} on gold with increasing concentrations of Cl^{-} and Br^{-} compared to H_2SO_4.[10] The desorption barriers for the $[OH{-}Fe(H_2O)_4SO_4]$, $[Cl{-}Fe(H_2O)_5]^{2+}$, and $[Br{-}Fe(H_2O)_5]^{2+}$ complexes are predicted to be 0.82, 0.67, and 0.55 eV, respectively, on Au(111). Thus, the rate enhancements in the presence of chloride and bromide may arise due to decreasing the desorption barrier. However, because the reports of enhancements with halides for Fe^{2+}/Fe^{3+} on Au(111) are only qualitative, we are unable to obtain quantitative correlations.

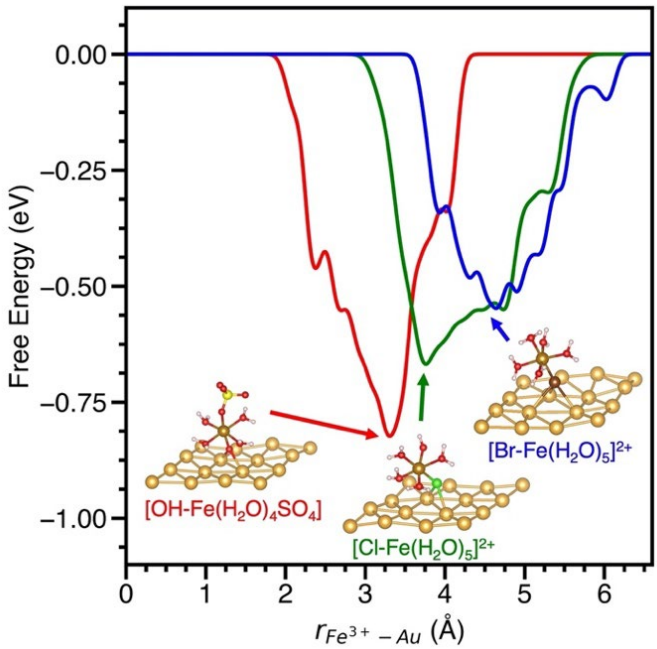

Figure 5.4. Desorption Barriers of Fe^{3+}-anion Complexes on Gold Electrode. Metadynamics-based free energy profiles for desorption of Fe^{3+}-anion complexes from Au(111) through an *OH, *Cl, *Br, or *I bridge at 300 K. Geometries of the adsorbed Fe^{3+}-anion complexes are shown at the lowest point on the free energy profile. Atom color legend: Au = gold, Fe = brown, O = red, S = yellow, H = white, Cl = green, Br = dark brown.

The desorption barrier of the electroactive species is a new way to rationalize and predict rate enhancement by halides for inner sphere aqueous metal ion CT reactions. However, we stress that the desorption barrier is only a valid descriptor among inner sphere reactions on chemically similar surfaces. When examined together, the rate constants for V^{2+}/V^{3+} on Hg(111) and graphite$(11\bar{2}0)$ in hydrohalic electrolytes do not correlate in the same way with $\Delta G_{des}^{\ddagger}$ (**Figure 5.5**).

The inability of $\Delta G_{des}^{\ddagger}$ to describe kinetics across different electrodes for a given redox couple can arise due to three major factors: (1) reactions on different surfaces do not necessarily obey the same BEP relations, (2) discrepancies exist between the modeled surface and the actual electrode active site, and (3) different mechanisms occur on different electrodes. By comparing desorption barriers of different metal-anion complexes on the same surface, these factors will be similar and qualitative insights can be gained. Different mechanisms and explanations for anion

enhancements may also be valid. Theories have been developed for how electrostatics can be used to explain outer sphere CT,[42] and how electrode modification can be used to enhance rates by changing the potential of zero charge.[43,44] Rate enhancements can also arise from a change in mechanism from outer sphere to inner sphere, as is reported to occur for Cr^{2+}/Cr^{3+} when halides are added to the electrolyte.[8] The applicability of using $\Delta G_{des}^{\ddagger}$ as a descriptor for kinetics of the same redox couple on multiple surfaces could be tested by conducting kinetic measurements for a fixed redox couple on chemically similar surfaces such as metal electrodes. **Figure 5.5** shows a possible correlation between the desorption barriers for vanadium-anion complex on two noble metals (Au and Hg) and V^{2+}/V^{3+} rate constants, but more data is needed for a conclusive analysis.

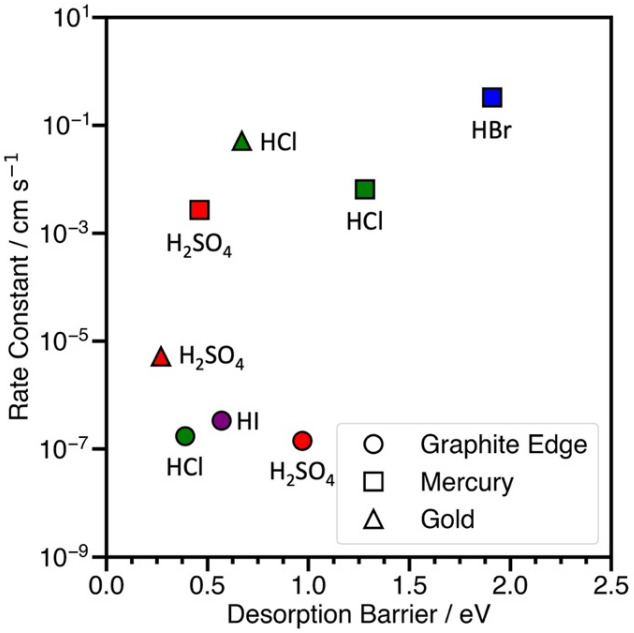

Figure 5.5. Rate Constants vs Desorption Barrier on Different Electrodes for V^{2+}/V^{3+} Redox Couple. Standard experimental rate constants on EPPG, mercury drop electrodes, and gold vs the predicted desorption barrier of V^{3+}-anion complex on graphite($11\bar{2}0$), Hg(111), and Au(111). Colors denote the sulfuric and hydrohalic acid, namely H_2SO_4 (red), HCl (green), HBr (blue), and HI (purple).

5.4 Conclusions

The work in this chapter demonstrates the role of halides in promoting inner sphere heterogeneous metal charge transfer by changing the transition state energies and energy of the adsorbed metal-anion intermediate. Experimental kinetic measurements combined with

metadynamics simulations show that halide bridges increase kinetics of the V^{2+}/V^{3+} redox couple on EPPG by decreasing the desorption barrier of the vanadium-anion complex intermediate (V^{3+}-anion), until an optimum is reached. For V^{2+}/V^{3+}, Cr^{2+}/Cr^{3+}, and Cd^{0}/Cd^{2+} on Hg, desorption is not rate limiting and halides stabilize the metal ion on the Hg surface, thus increasing surface coverage and promoting the reaction rate. When BEP relations hold for chemically similar reactions, desorption barriers correlate with redox kinetics. This knowledge can guide anion bridge design so reactive intermediates adsorb on electrodes with optimal strength. Because the CT kinetics of many metal ion redox couples are increased in the presence of halides, these findings apply broadly and highlight the importance of understanding the combined role of the redox couple, electrode, and electrolyte when engineering electrochemical systems.

5.5 Supporting Information

5.5.1 Rate Constants for Metal Ion Redox Couples

Rate constants in **Table S5.1** are calculated at room temperature using various methods. For comparing rate data to desorption barriers in **Figure 5.3**, rate constants in hydrohalic and sulfuric acid electrolytes were taken from a single reference for each redox couple to avoid discrepancies in the experimental method used.

Table S5.1. Standard Rate Constants for Metal Ion Redox Couples With and Without Halide Anions. *$Metal_{Hg}$ electrodes are metal-Hg amalgam alloy electrodes. **_(ref)_ indicates reference used for $k_{no\ halides}$ in **Figure 5.1**. The *ref* is chosen as a perchlorate- or sulfate-based salt solution (instead of acid) for the cases where the rate data in presence of halides is available only in halide-based salt solutions to eliminate the effect of pH on rate constants.

Redox Couple	Electrode*	Electrolyte**	Rate Constant / cm s^{-1}	Reference
Ag^{+}/Ag^{0}	Ag	$HClO_4$	5.18×10^{-3}	[45]
Bi^{3+}/Bi^{0}	Bi_{Hg}	$HClO_4$ *(ref)*	3.70×10^{-4}	[46]
Bi^{3+}/Bi^{0}	Bi_{Hg}	H_2SO_4	1.80×10^{-3}	[46]
Bi^{3+}/Bi^{0}	Bi_{Hg}	$HClO_4 + Cl^{-}$	2.80×10^{-3}	[46]
Bi^{3+}/Bi^{0}	Bi_{Hg}	$HClO_4 + I^{-}$	2.90×10^{-1}	[47]
Bi^{3+}/Bi^{0}	Hg	$HClO_4$	3.70×10^{-4}	[46]
Bi^{3+}/Bi^{0}	Hg	H_2SO_4	1.85×10^{-3}	[46]
Bi^{3+}/Bi^{0}	Hg	HCl	2.70×10^{-3}	[46]
Cd^{2+}/Cd^{0}	Cd_{Hg}	$HClO_4$	3.52×10^{-1}	[48]
Cd^{2+}/Cd^{0}	Cd_{Hg}	$NaClO_4$ *(ref)*	5.00×10^{-1}	[49]
Cd^{2+}/Cd^{0}	Cd_{Hg}	Na_2SO_4	5.50×10^{-1}	[49]
Cd^{2+}/Cd^{0}	Cd_{Hg}	KCl	1.25×10^{0}	[50]
Cd^{2+}/Cd^{0}	Cd_{Hg}	KBr	9.10×10^{-1}	[50]
Cd^{2+}/Cd^{0}	Cd_{Hg}	KI	6.50×10^{0}	[50]
Cd^{2+}/Cd^{0}	Hg	$HClO_4$ *(ref)*	2.50×10^{-1}	[12]
Cd^{2+}/Cd^{0}	Hg	H_2SO_4	1.20×10^{-1}	[12]
Cd^{2+}/Cd^{0}	Hg	HCl	9.40×10^{-1}	[12]
Ce^{4+}/Ce^{3+}	Au	$HClO_4$	4.70×10^{-5}	[51]
Ce^{4+}/Ce^{3+}	Pt	H_2SO_4	3.70×10^{-4}	[52]
Co^{2+}/Co^{0}	Co	$CoSO_4$ *(ref)*	6.74×10^{-8}	[53]
Co^{2+}/Co^{0}	Co	$CoSO_4 + Cl^{-}$	5.70×10^{-9}	[53]
Co^{2+}/Co^{0}	Co	$CoSO_4 + I^{-}$	5.18×10^{-10}	[53]
Cr^{2+}/Cr^{3+}	Hg	$HClO_4$ *(ref)*	1.40×10^{-3}	[41]
Cr^{2+}/Cr^{3+}	Hg	$HClO_4 + Cl^{-}$	2.73×10^{-2}	[41]
Cr^{2+}/Cr^{3+}	Hg	$HClO_4 + I^{-}$	6.40×10^{-2}	[41]
Cr^{3+}/Cr^{2+}	Hg	$NaClO_4$	8.00×10^{-6}	[54]
Cr^{3+}/Cr^{2+}	Hg	KCl	8.50×10^{-6}	[54]
Cr^{3+}/Cr^{2+}	Hg	KBr	1.70×10^{-5}	[54]
Cr^{3+}/Cr^{2+}	Hg	KI	9.80×10^{-5}	[54]
Cu^{2+}/Cu^{0}	Cu	H_2SO_4	4.20×10^{-4}	[55]
Eu^{2+}/Eu^{3+}	Hg	$HClO_4$ *(ref)*	1.70×10^{-4}	[11]
Eu^{2+}/Eu^{3+}	Hg	HCl	2.40×10^{-4}	[11]
Eu^{2+}/Eu^{3+}	Hg	HBr	9.80×10^{-4}	[11]
Fe^{2+}/Fe^{3+}	Au	$HClO_4$	8.00×10^{-5}	[56]

Fe^{2+}/Fe^{3+}	Au	H_2SO_4 *(ref)*	1.00×10^{-2}	[10,57]
Fe^{2+}/Fe^{3+}	Au	HCl	3.10×10^{-2}	[10]
Fe^{2+}/Fe^{3+}	Pt	H_2SO_4 *(ref)*	1.30×10^{-3}	[58]
Fe^{2+}/Fe^{3+}	Pt	HCl	4.40×10^{-3}	[58]
Fe^{2+}/Fe^{3+}	Ru	H_2SO_4	7.83×10^{-4}	[59]
Fe^{2+}/Fe^{3+}	Glassy Carbon	$HClO_4$	1.34×10^{-3}	[60]
Fe^{2+}/Fe^{3+}	Glassy Carbon	H_2SO_4 *(ref)*	1.20×10^{-3}	[60]
Fe^{2+}/Fe^{3+}	Glassy Carbon	HCl	5.70×10^{-3}	[60]
Fe^{3+}/Fe^{2+}	Rh	$HClO_4$	4.60×10^{-4}	[61]
Fe^{3+}/Fe^{2+}	Rh	H_2SO_4	2.28×10^{-3}	[62]
In^{3+}/In^{0}	In_{Hg}	$HClO_4 + SO_4^{2-}$ *(ref)*	5.87×10^{-5}	[63]
In^{3+}/In^{0}	In_{Hg}	$HClO_4 + Cl^-$	5.87×10^{-5}	[63]
In^{3+}/In^{0}	In_{Hg}	$HClO_4 + Br^-$	1.00×10^{-3}	[63]
In^{3+}/In^{0}	In_{Hg}	$HClO_4 + I^-$	3.01×10^{-3}	[63]
In^{3+}/In^{0}	Hg	$NaClO_4$ *(ref)*	1.28×10^{-3}	[64]
In^{3+}/In^{0}	Hg	NaCl	3.40×10^{-2}	[65]
In^{3+}/In^{0}	Hg	NaBr	6.50×10^{-1}	[65]
Ni^{2+}/Ni^{0}	Ni	H_2SO_4 *(ref)*	8.60×10^{-10}	[66]
Ni^{2+}/Ni^{0}	Ni	HCl	5.70×10^{-9}	[66]
Pb^{2+}/Pb^{0}	Pb_{Hg}	$HClO_4$	1.00×10^{0}	[67]
Pb^{2+}/Pb^{0}	Pb_{Hg}	$NaClO_4$ *(ref)*	1.02×10^{1}	[50]
Pb^{2+}/Pb^{0}	Pb_{Hg}	KCl	5.20×10^{0}	[50]
Pb^{2+}/Pb^{0}	Pb_{Hg}	KBr	9.60×10^{-1}	[50]
Pb^{2+}/Pb^{0}	Hg	NaCl	1.80×10^{-1}	[65]
Pb^{2+}/Pb^{0}	Hg	NaBr	4.80×10^{-1}	[65]
Pd^{2+}/Pd^{0}	Pd	HCl	2.49×10^{-6}	[68]
Pd^{2+}/Pd^{0}	Pd	HBr	4.04×10^{-6}	[68]
Pt^{4+}/Pt^{2+}	Pt	HCl	2.30×10^{-7}	[69]
Pt^{4+}/Pt^{2+}	Pt	HBr	6.30×10^{-6}	[69]
Pt^{4+}/Pt^{2+}	Pt	HI	7.20×10^{-5}	[69]
Tl^{+}/Tl^{0}	Tl_{Hg}	$NaClO_4$ *(ref)*	3.40×10^{0}	[50]
Tl^{+}/Tl^{0}	Tl_{Hg}	K_2SO_4	3.50×10^{0}	[50]
Tl^{+}/Tl^{0}	Tl_{Hg}	KCl	5.00×10^{0}	[50]
V^{2+}/V^{3+}	Hg	$HClO_4$ *(ref)*	1.10×10^{-3}	[11]
V^{2+}/V^{3+}	Hg	H_2SO_4	2.70×10^{-3}	[11]
V^{2+}/V^{3+}	Hg	HCl	6.50×10^{-3}	[11]
V^{2+}/V^{3+}	Hg	HBr	3.30×10^{-1}	[11]
V^{2+}/V^{3+}	Glassy Carbon	H_2SO_4 *(ref)*	2.70×10^{-8}	[14]
V^{2+}/V^{3+}	Glassy Carbon	HCl	6.73×10^{-8}	[14]
V^{2+}/V^{3+}	Glassy Carbon	HBr	1.16×10^{-7}	[14]
V^{2+}/V^{3+}	Glassy Carbon	HI	2.19×10^{-7}	[14]
Zn^{2+}/Zn^{0}	Zn_{Hg}	$NaClO_4$ *(ref)*	2.48×10^{-3}	[70]
Zn^{2+}/Zn^{0}	Zn_{Hg}	KCl	5.05×10^{-3}	[70]
Zn^{2+}/Zn^{0}	Zn_{Hg}	NaBr	1.03×10^{-2}	[70]
Zn^{2+}/Zn^{0}	Zn_{Hg}	NaI	1.31×10^{-1}	[70]
Zn^{2+}/Zn^{0}	Hg	K_2SO_4 *(ref)*	1.30×10^{-3}	[71]
Zn^{2+}/Zn^{0}	Hg	KCl	4.00×10^{-3}	[72]
Zn^{2+}/Zn^{0}	Hg	KBr	8.00×10^{-3}	[72]
Zn^{2+}/Zn^{0}	Hg	KI	7.00×10^{-2}	[72]

5.5.2 Electrochemical Kinetic Measurements on EPPG

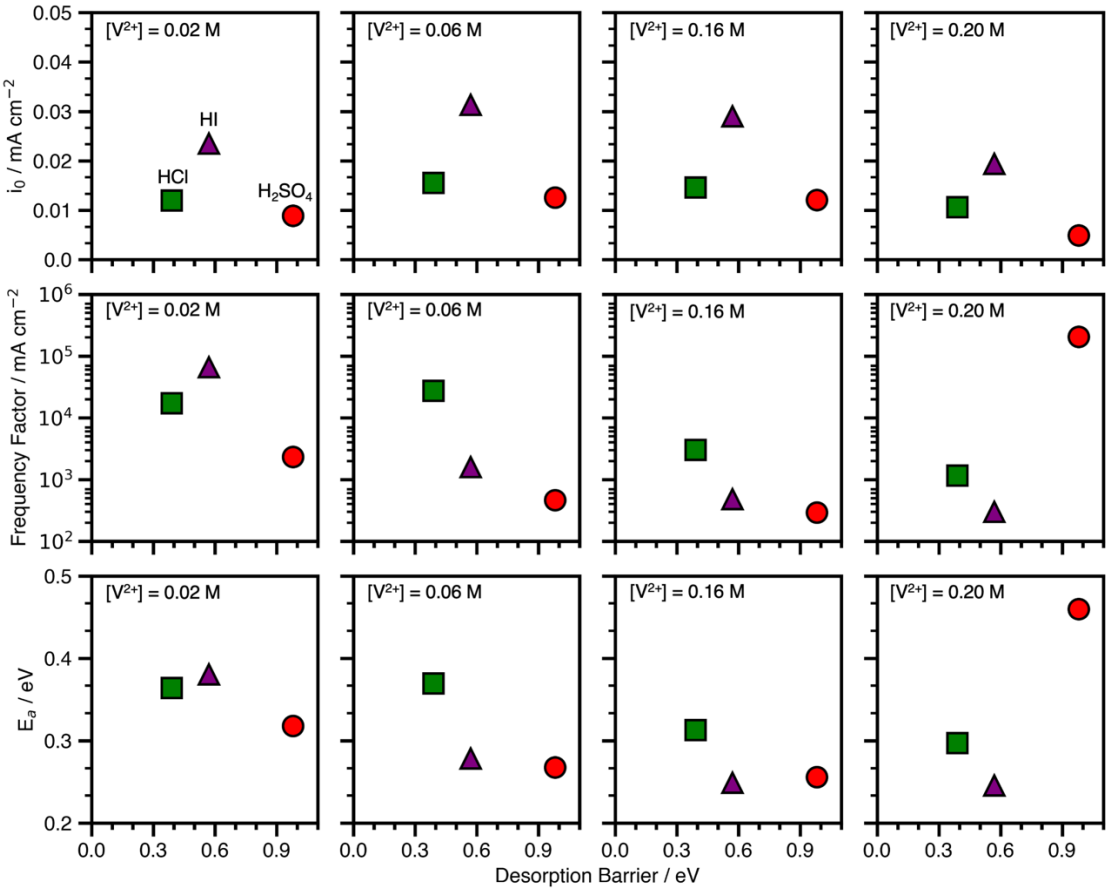

Figure S5.1. Kinetic Parameters of V^{2+}/V^{3+} Reaction on Edge Plane Pyrolytic Graphite in H_2SO_4, HCl, and HI Evaluated using Tafel Method vs Desorption Barriers. Experimentally evaluated exchange current densities (i_o) at room temperature, apparent frequency factors, and apparent activation energies (E_a) for V^{2+}/V^{3+} on EPPG plotted against the predicted desorption barriers. Experimental parameters are evaluated using the Tafel method at 0.02, 0.06, 0.16, and 0.2 M V^{2+} concentration, with corresponding concentrations of V^{3+} to make the total V ion concentration 0.2 M. Apparent frequency factors and apparent activation energies are from temperature measurements at 23.3, 30, 35, and 40 °C.

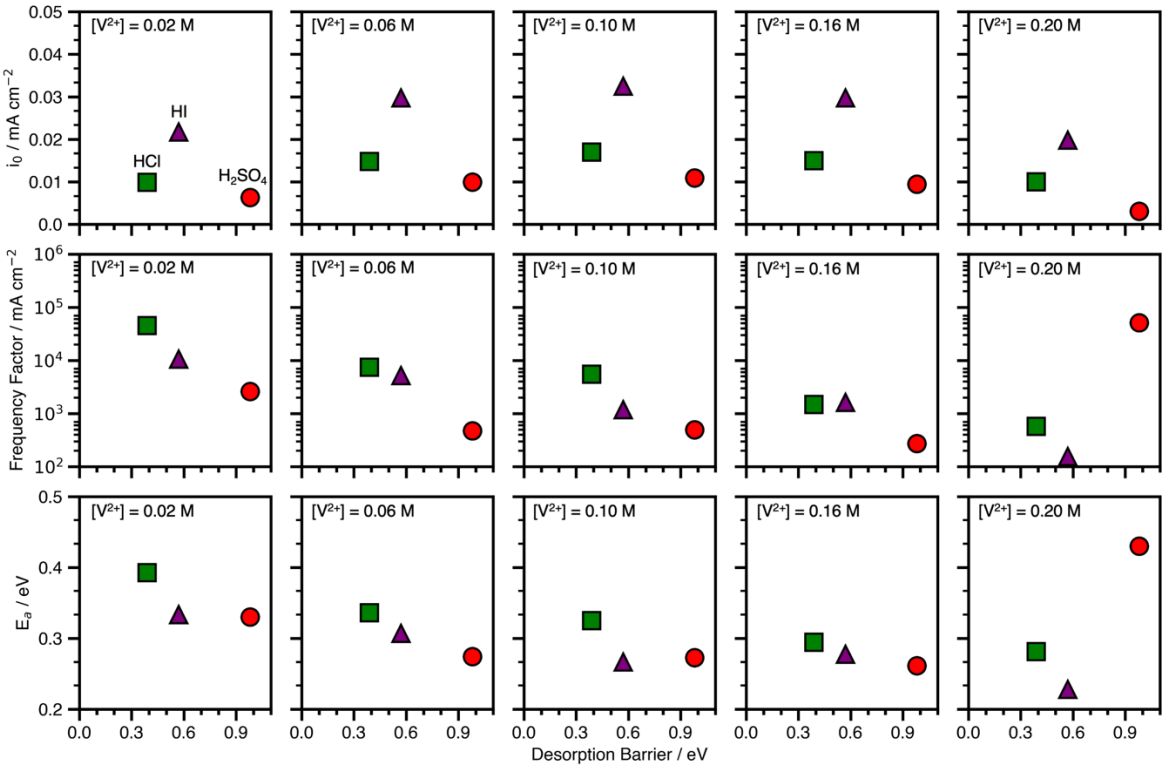

Figure S5.2. Kinetic Parameters of V^{2+}/V^{3+} Reaction on Edge Plane Pyrolytic Graphite in H_2SO_4, HCl, and HI Evaluated using Charge Transfer Resistance Method vs Desorption Barriers. Experimentally measured exchange current densities (i_o) at room temperature, apparent frequency factors, and apparent activation energies (E_a) for V^{2+}/V^{3+} on EPPG as a function of the predicted desorption barrier. Experimental parameters are evaluated using the Charge Transfer Resistance method at 0.02, 0.06, 0.10, 0.16, and 0.2 M V^{2+} concentration, with corresponding concentration of V^{3+} to make the total V ion concentration 0.2 M. Apparent frequency factors and apparent activation energies are from temperature measurements at 23.3, 30, 35, and 40 °C.

5.5.3 Computational Methods and Simulation Cell Setup for Metadynamics

Spin-polarized density functional theory (DFT) calculations are performed using Vienna Ab Initio Simulation Package (VASP).[77–79] The PBE functional is used for all metadynamics simulations.[80] The projector augmented wave method is chosen to describe electron-ion interactions.[81] A 400 eV plane wave kinetic energy cutoff is set for all systems. A Γ-centered 1×1×1 *k*-point grid is used. The systems modeled are V^{3+}-anion complexes on the graphite edge plane $(11\bar{2}0)$, V^{3+}-, Cr^{3+}-, and Cd^{2+}-anion complexes on Hg(111), and Fe^{3+}-anion complexes on Au(111).

Details of the unit cell dimensions and compositions for NVT metadynamics simulations are shown in **Figure 5.2a** and **Figures S5.3–S5.4**. Graphite$(11\bar{2}0)$ with lattice constants of a =

2.45 Å and c = 6.77 Å (**Figure 5.2a**) is used as a model surface for EPPG. The graphite surface is passivated with 42 adsorbed *H and five adsorbed *OH. In addition to vanadium, 38 explicit water molecules are added to maintain an aqueous environment with a density of 1 g/cm^3. The middle layer of carbon atoms is fixed to their bulk positions. Spin-polarized DFT is used with a spin density of 2 spin-up electrons to model the V^{3+} ion. A three-layer 3×3 Hg(111) surface with an Hg interatomic distance of 3.60 Å (**Figure S5.3**) is used to model a mercury drop electrode. In addition to the Cr^{3+} ion, 48 explicit water molecules are added to maintain an aqueous environment with a density of 1 g/cm^3. The middle layer of Hg atoms is fixed to their bulk positions. Spin-polarized DFT is used with a spin density of 3 spin-up electrons to model the Cr^{3+} ion. The same procedure is used for the V^{3+} and Cd^{2+} on Hg(111) with 2 spin-up electrons for V^{3+} and 0 spin-up electrons for Cd^{2+}.

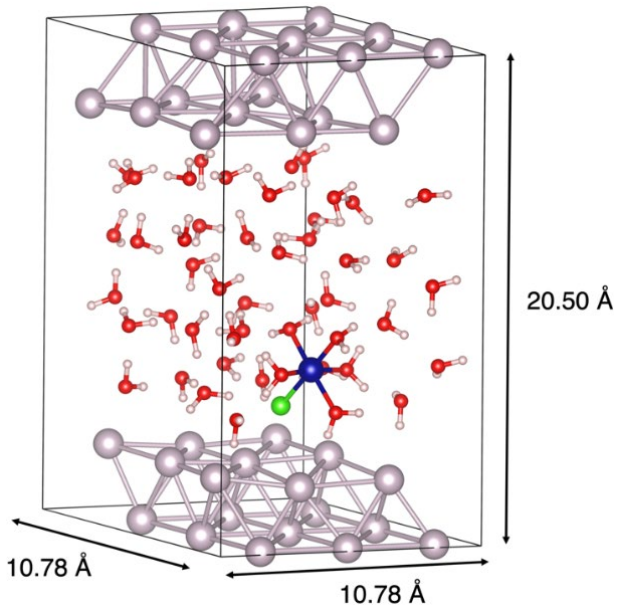

Figure S5.3. Simulation Cell for $[X{-}Cr(H_2O)_5]^{2+}$ Complex on Hg(111) used for Calculating Desorption Barriers. Atom color legend: red = O, gray = Hg, green = anion, beige = H, blue = Cr.

A three-layer 4×4 Au(111) surface with lattice constant a = 4.17 Å (**Figure S5.4**) is used as a model for a polycrystalline gold electrode. In addition to the $[Fe(H_2O)_5X]^{2+}$ complex, 48 explicit water molecules are added to the simulation cell to maintain an aqueous environment with

a density of 1 g/cm^3. To prevent system translation and maintain a symmetric simulation cell, the middle layer of Au atoms is fixed to their bulk positions during the simulation. Spin-polarized DFT was used with a spin density of five spin-up electrons to model the high-spin Fe^{3+} ion.

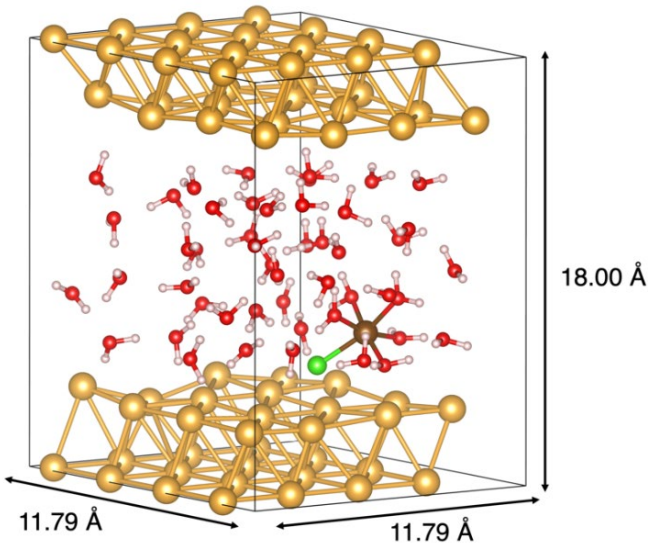

Figure S5.4. Simulation cell for [X−Fe(H$_2$O)$_5$]$^{2+}$ complex on Au(111) used for Calculating Desorption Barriers. Atom color legend: red = O, gold = Au, green = anion, beige = H, brown = Fe.

A Nosé-Hoover thermostat is used to equilibrate the system at 300 K.[82,83] Equations of motion are integrated with a time step of 0.5 fs, and all hydrogen atoms are replaced with deuterium to dampen the high frequency OH bond vibrations. To calculate desorption free energy barriers, the distance between the metal ion and the surface (*z* coordinate) is chosen as the collective variable. Adding an additional collective variable that biases the coordination number between the metal ion and solvent water molecules, which occurs on a longer timescale than desorption, did not affect the desorption barriers and thus is not further considered (**Figure S5.5**).

The free energy barrier for *[I−Cr(H$_2$O)$_5$]$^{2+}$ desorption on Hg(111) when biasing both the coordination number of Cr^{3+} with water and the Cr^{3+} distance from the surface is 1.24 eV (**Figure S5.5**). The most stable *[I−Cr(H$_2$O)$_5$]$^{2+}$ configuration occurs at a Cr^{3+}-Hg distance of 5.2 Å and a coordination number of five and is described by the dark blue energy well. This prediction is similar to the desorption barrier when only biasing the Cr^{3+} distance from the surface, which is

1.21 eV as shown in the free energy profile in **Figure 5.3b**. The second collective variable biasing the coordination number of water with the metal ion did not change the desorption barriers by more than three percent.

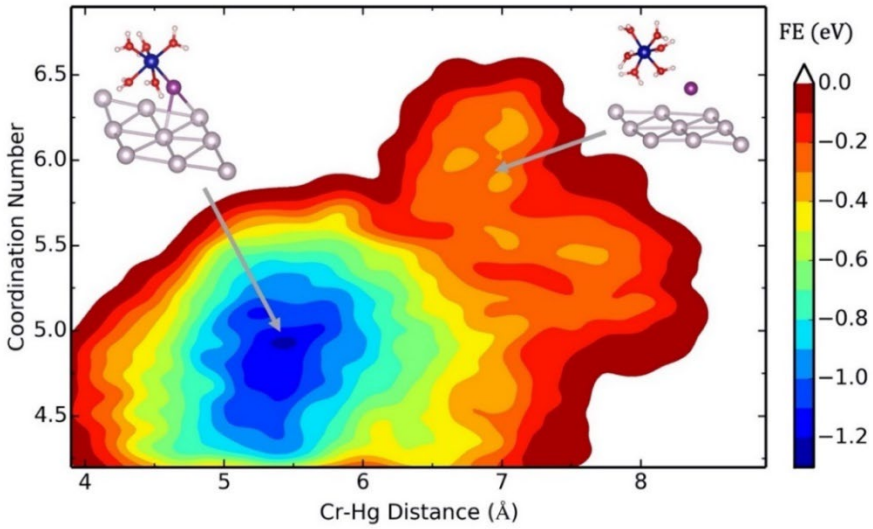

Figure S5.5. Two-dimensional Contour Plot Showing the Free Energy Surface of the Desorption of *[I−Cr(H₂O)₅]$^{2+}$ when Biasing Both Coordination Number of Water and Cr^{3+}-Hg Distance. Snapshots of the adsorbed and desorbed complexes with solvent water molecules removed are shown, and the arrows show their position on the free energy surface. The reference state is the desorbed state. Atom color legend: gray = Hg, blue = Cr, purple = I, red = O, white = H.

After at least a 5 ps equilibration period, gaussian bias potentials with height 0.01 eV and width 0.10 Å are deposited every 15 fs to bias the collective variable. The width of the gaussian hills is based on the standard deviation of changes in the collective variable during equilibration. Metadynamics simulations are stopped once the distance of the desorbed metal ion complex exceeded $1.5R_{S-X} + R_{X-M}$ from the surface for more than 0.3 ps, where R_{S-X} is the surface-anion bond distance in the gas phase and R_{X-M} is the bond distance between the anion-metal ion of the gas-phase complex. The effect of applied potential is not considered in these simulations.

5.6 References

(1) Sánchez-Díez, E.; Ventosa, E.; Guarnieri, M.; Trovò, A.; Flox, C.; Marcilla, R.; Soavi, F.; Mazur, P.; Aranzabe, E.; Ferret, R. Redox Flow Batteries: Status and Perspective towards Sustainable Stationary Energy Storage. *J. Power Sources* **2021**, *481*.

(2) Srimuk, P.; Su, X.; Yoon, J.; Aurbach, D.; Presser, V. Charge-Transfer Materials for Electrochemical Water Desalination, Ion Separation and the Recovery of Elements. *Nat.*

Rev. Mater. **2020**, *5* (7), 517–538.
(3) Möhle, S.; Zirbes, M.; Rodrigo, E.; Gieshoff, T.; Wiebe, A.; Waldvogel, S. R. Modern Electrochemical Aspects for the Synthesis of Value-Added Organic Products. *Angew. Chemie - Int. Ed.* **2018**, *57* (21), 6018–6041.
(4) Orella, M. J.; Román-Leshkov, Y.; Brushett, F. R. Emerging Opportunities for Electrochemical Processing to Enable Sustainable Chemical Manufacturing. *Curr. Opin. Chem. Eng.* **2018**, *20*, 159–167.
(5) Agarwal, H.; Florian, J.; R. Goldsmith, B.; Singh, N. V^{2+}/V^{3+} Redox Kinetics on Glassy Carbon in Acidic Electrolytes for Vanadium Redox Flow Batteries. *ACS Energy Lett.* **2019**, *4*, 2368–2377.
(6) Park, M.; Jeon, I. Y.; Ryu, J.; Jang, H.; Back, J. B.; Cho, J. Edge-Halogenated Graphene Nanoplatelets with F, Cl, or Br as Electrocatalysts for All-Vanadium Redox Flow Batteries. *Nano Energy* **2016**, *26*, 233–240.
(7) Rodes, A.; Feliu, J. M.; Aldaz, A.; Clavilier, J. The Influence of Polyoriented Gold Electrodes Modified by Reversibly and Irreversibly Adsorbed Ad-Atoms on the Redox Behaviour of the Cr(III) / Cr(II). *J. Electroanal. Chem.* **1989**, *271* (1–2), 127–139.
(8) Weaver, M. J.; Anson, F. C. Distinguishing between Inner- and Outer-Sphere Electrode Reactions. Reactivity Patterns for Some Chromium(III)-Chromium(II) Electron-Transfer Reactions at Mercury Electrodes. *Inorg. Chem.* **1976**, *15* (8), 1871–1881.
(9) Johnson, D. C.; Resnlck, E. W. Electrocatalysis of the Reduction of Iron(III) by Halides Adsorbed at Platinum Electrodes in Perchloric Acid Solutions. *Anal. Chem.* **1977**, *49* (13), 1918–1924.
(10) Weber, J.; Samec, Z.; Mareček, V. The Effect of Anion Adsorption on the Kinetics of the Fe^{3+}/Fe^{2+} Reaction on Pt and Au Electrodes in $HClO_4$. *J. Electroanal. Chem.* **1978**, *89* (2), 271–288.
(11) Niki, K.; Mizota, H. Effect of Specific Adsorbed Anions on the Electrode Kinetics of the V(III)/V(II) and Eu(III)/Eu(II) Couples. *J. Electroanal. Chem.* **1976**, *72* (3), 307–317.
(12) Frischmann, J. K.; Timnick, A. Transfer Coefficients and Heterogeneous Rate Constants for Cadmium(II) in Various Supporting Electrolytes Evaluated by Phase-Angle Measurements with an A.C. Polarograph. *Anal. Chem.* **1967**, *39* (4), 507–511.
(13) Eriksrud, E. Effect of Halides and Alkali Cations on the Zn(Hg)/Zn(II) Electrode Reactions. *J. Electroanal. Chem.* **1977**, *76* (1), 27–49.
(14) Agarwal, H.; Florian, J.; Goldsmith, B. R.; Singh, N. The Effect of Anion Bridging on Heterogeneous Charge Transfer for V^{2+}/V^{3+}. *Cell Reports Phys. Sci.* **2021**, *2* (1), 100307.
(15) de Levie, R. Anion Bridging and Anion Electrocatalysis on Mercury. *J. Electrochem. Soc.* **1971**, *118* (8), 185–192.
(16) Davenport, R. J.; Johnson, D. C. Electrocatalysis of the Oxidation of Antimony(III) at Platinum Electrodes in 2M Hydrogen Chloride by Adsorbed Iodide. *Anal. Chem.* **1973**, *45* (9), 1755–1756.
(17) Weaver, M. J. Some Recent Approaches to the Study of Heterogeneous Redox Kinetics of Metal Complexes. Comparisons with Homogeneous Redox Processes. *Isr. J. Chem.* **1979**, *18* (1–2), 35–44.
(18) Taylor, L. R.; Parkinson, B. A.; Johnson, D. C. Electrocatalysis of the Charge-Transfer Process for the Sb(III)/Sb(V) Couple at a Platinum Electrode in Concentrated HCl. *Electrochim. Acta* **1975**, *20* (12), 1005–1009.
(19) Sykes, A. G. Further Advances in the Study of Mechanisms of Redox Reactions. *Adv. Inorg.*

Chem. Radiochem. **1968**, *10* (C), 153–245.
(20) Heyrovsky, J. Retarded Electrodeposition of Metals Studied Oscillographically with Mercury Capillary Electrodes. *Discuss. Faraday Soc.* **1947**, *1*, 212–225.
(21) Weaver, M. J.; Anson, F. C. Double-Layer Effects on Simple Electrode Reactions. *J. Electroanal. Chem.* **1975**, *65*, 737–758.
(22) Bligaard, T.; Nørskov, J. K.; Dahl, S.; Matthiesen, J.; Christensen, C. H.; Sehested, J. The Brønsted-Evans-Polanyi Relation and the Volcano Curve in Heterogeneous Catalysis. *J. Catal.* **2004**, *224*, 206–217.
(23) Norskov, J. K.; Studt, F.; Ablid-Pederson, F.; Bligaard, T. *Fundamental Concepts in Heterogeneous Catalysis*; John Wiley & Sons: Hoboken, New Jersey, 2014.
(24) Jiang, Z.; Klyukin; Vitaly Alexandrov. First-Principles Study of Adsorption–Desorption Kinetics of Aqueous $V^{2+}/V^{3}+$ Redox Species on Graphite in a Vanadium Redox Flow Battery. *Phys. Chem. Chem. Phys.* **2017**, *19*, 14897–14901.
(25) Vogel, Y. B.; Zhang, J.; Darwish, N.; Ciampi, S. Switching of Current Rectification Ratios within a Single Nanocrystal by Facet-Resolved Electrical Wiring. *ACS Nano* **2018**, *12* (8), 8071–8080.
(26) Aaronson, B. D. B.; Chen, C. H.; Li, H.; Koper, M. T. M.; Lai, S. C. S.; Unwin, P. R. Pseudo-Single-Crystal Electrochemistry on Polycrystalline Electrodes: Visualizing Activity at Grains and Grain Boundaries on Platinum for the Fe^{2+}/Fe^{3+} Redox Reaction. *J. Am. Chem. Soc.* **2013**, *135* (10), 3873–3880.
(27) Hromadová, M.; Fawcett, W. R. Studies of Double-Layer Effects at Single Crystal Gold Electrodes II. The Reduction Kinetics of Hexaaquairon(III) Ion in Aqueous Solutions. *J. Phys. Chem. A* **2001**, *105* (1), 104–111.
(28) Bochmann, H. G.; Vielstich, W. On the Reaction Rate of the Fe(II)/Fe(III) Redox Couple in Sulfate Solution. *Electrochim. Acta* **1987**, *33* (6), 805–809.
(29) Oldenburg, F. J.; Bon, M.; Perego, D.; Polino, D.; Laino, T.; Gubler, L.; Schmidt, T. J. Revealing the Role of Phosphoric Acid in All-Vanadium Redox Flow Batteries with DFT Calculations and In Situ Analysis. *Phys. Chem. Chem. Phys* **2018**, *20*, 23664–23673.
(30) Wasileski, S. A.; Weaver, M. J. Electrode Potential-Dependent Anion Chemisorption and Surface Bond Polarization as Assessed by Density Functional Theory. *J. Phys. Chem. B* **2002**, *106* (18), 4782–4788.
(31) Dimitrov, D. I.; Raev, N. D. Molecular Dynamics Simulations of the Electrical Double Layer at the 1 M KCl Solution | Hg Electrode Interface. *J. Electroanal. Chem.* **2000**, *486* (1), 1–8.
(32) Ivaništšev, V.; Nazmutdinov, R. R.; Lust, E. A Comparative DFT Study of the Adsorption of H_2O Molecules at Bi, Hg, and Ga Surfaces. *Surf. Sci.* **2013**, *609*, 91–99.
(33) Tóth, G.; Spohr, E.; Heinzinger, K. SCF Calculations of the Interactions of Alkali and Halide Ions with the Mercury Surface. *Chem. Phys.* **1995**, *200* (3), 347–355.
(34) Xin, H.; Linic, S. Exceptions to the *d*-band Model of Chemisorption on Metal Surfaces: The Dominant Role of Repulsion between Adsorbate States and Metal d-States. *J. Chem. Phys.* **2010**, *132* (22), 12–15.
(35) Dellien, I.; Hepler, L. G. Enthalpies of Formation of Cr^{3+} (aq) and the Inner Sphere Complexes CrF_2^+ (aq), $CrCl_2^+$ (aq), $CrBr_2^+$ (aq), and $CrSO_4^+$ (aq). *Can. J. Chem.* **1976**, *54* (9), 1383–1387.
(36) Anson, F. C.; Barclay, D. J. Anion Induced Adsorption of Cadmium(II) on Mercury from Iodide and Bromide Media. *Anal. Chem.* **1968**, *40* (12), 1791–1798.

(37) Ackerman, J. J. H.; Orr, T. V.; Bartuska, V. J.; Maciel, G. E. Effect of Halide Complexation of Cadmium(II) on Cadmium-113 Chemical Shifts. *J. Am. Chem. Soc.* **1979**, *101* (2), 341–347.
(38) Frick, R. J.; Hofer, T. S.; Pribil, A. B.; Randolf, B. R.; Rode, B. M. Structure and Dynamics of the Cd(II) Ion in Aqueous Solution: An Ab Initio QMCF-MD Study. *Phys. Chem. Chem. Phys.* **2010**, *12* (37), 11736–11743.
(39) Van der Pol, F.; Sluyters-Rehbach, M.; Sluyters, J. H. On the Elucidation of Mechanisms of Electrode Reactions by Combination of a.c.-and Faradaic Rectification Polarography. Application to the Zn^{2+}/Zn(Hg) and Cd^{2+}/Cd(Hg) Reduction. *J. Electroanal. Chem.* **1975**, *58* (1), 177–188.
(40) Bongenaar, C. P. M.; Remijnse, A. G.; Sluyters-Rehbach, M.; Sluyters, J. H. On the Selection of the Most Probable Mechanism of the Cd(II) Reduction at Mercury from 1 M KF Solution. *J. Electroanal. Chem.* **1980**, *111* (2–3), 139–153.
(41) Jones Ulrich, J.; Anson, F. C. Ligand Bridging by Halide in the Electrochemical Oxidation of Chromium(II) at Mercury Electrodes. *Inorg. Chem.* **1969**, *8* (2), 195–200.
(42) Kant, R.; Kaur, J.; Mishra, G. K. Theory for Influence of the Metal Electrolyte Interface on Heterogeneous Electron Transfer Rate Constant: Fractional Electron Transferred Transition State Approach. *J. Phys. Chem. C* **2020**, *124* (4), 2273–2288.
(43) Kaur, J.; Kant, R. Theory of Work Function and Potential of Zero Charge for Metal Nanostructured and Rough Electrodes. *J. Phys. Chem. C* **2017**, *121* (24), 13059–13069.
(44) Kaur, J.; Kant, R. Model of Local Work Function and PZC for Molecular Self Assembly over Nanostructured Metal Electrode. *J. Phys. Chem. C* **2018**, *122* (1), 911–918.
(45) Mehl, W.; Bockris, J. O. M. Mechanism of Electrolytic Silver Deposition and Dissolution. *J. Chem. Phys.* **1957**, *27* (3), 818–819.
(46) Moussa, A. A.; Sammour, H. M. Reactivity of Anions towards Electron Transfer in the Bismuth - Teravalent Bismuth Exchange Reaction. *J. Chem. Soc.* **1960**, 2151–2157.
(47) Gorodetskii, V. V.; Losev, V. *Elektrokhimiya* **1966**, *2*, 656.
(48) Salié, G. Experimental Investigation of Intermediate States of Electrochemical Amalgam Reactions. *Zeitschrift Fur Phys. Chemie* **1970**, *244*, 1.
(49) Kooijman, D. J.; Sluyters, J. H. The Galvanostatic Single-Pulse and the Coulostatic Impulse Methods for the Determination of the Rate Constants of Electrode Reactions. *Electrochim. Acta* **1967**, *12* (12), 1579–1592.
(50) Agarwal, H. P. Electrode Kinetics Studies Using Faradaic Rectification. *Electrochim. Acta* **1971**, *16* (9), 1395–1414.
(51) Ferro, S.; De Battisti, A. Electron Transfer Reactions at Conductive Diamond Electrodes. *Electrochim. Acta* **2002**, *47* (10), 1641–1649.
(52) Galus, Z.; Adams, R. N. The Investigation of the Kinetics of Moderately Rapid Electrode Reactions Using Rotating Disk Electrodes. *J. Phys. Chem. A* **1962**, *43* (3), 5–10.
(53) Sheinin, A. B.; Zinovev, V. A.; Kheifets, V. L. Oscillographic Studies of the Kinetics of Electrode Processes. 3. Cobalt Electrode in Solutions of Various Composition. *Russ. J. Phys. Chem. A* **1961**, *35* (3), 513–516.
(54) Anson, F. C.; Rathjen, N.; Frisbee, R. D. The Absence of a Detectable Potential-Dependence of the Transfer Coefficient in the Cr^{3+}/Cr^{2+} Reaction. *J. Electrochem. Soc.* **1970**, *117* (4), 477.
(55) Hurlen, T. Heats of Activation at the Cu/Cu(II) Electrode. *Acta Chem. Scand.* **1961**, *15* (3), 621–629.

(56) Curtiss, L. A.; Halley, J. W.; Hautman, J.; Hung, N. C.; Nagy, Z.; Rhee, Y. -J.; Yonco, R. M. Temperature Dependence of the Heterogeneous Ferrous-Ferric Electron Transfer Reaction Rate: Comparison of Experiment and Theory. *J. Electrochem. Soc.* **1991**, *138* (7), 2032–2040.
(57) Angell, D. H.; Dickinson, T. The Kinetics of the Ferrous/Ferric and Ferro/Ferricyanide Reactions at Platinum and Gold Electrodes. *J. Electroanal. Chem.* **1972**, *35* (1), 55–72.
(58) Stulikova, M.; Vydra, F. The Voltammetry of Iron(III) at the Glassy Carbon Rotating Disk Electrode in Acid Media. **1972**, *38* (2), 349–357.
(59) Galizzioli, D.; Trasatti, S. Simple Electron Exchange Reactions. Fe(II)/Fe(III) Redox Couple. *J. Electroanal. Chem.* **1973**, *44* (3), 367–388.
(60) Gross, M.; Jordan, J. Voltammetry at Glassy Carbon Electrodes. *Pure Appl. Chem.* **1985**, *57* (4), 633–638.
(61) Everett, K. G.; Drew, L. A.; Ericson, S. J.; Schmid, G. M. The Fe(II)-Fe(III) and Hydroquinone-Quinone Reactions on Oxygen-Covered Rhodium Electrodes. *J. Electrochem. Soc.* **1978**, *125* (3), 389–394.
(62) Bockris, J. O.; Mannan, R. J.; Damjanovic, A. Dependence of Rate of Electrodic Redox Reactions on the Substrate. *J. Chem. Phys.* **1968**, *48*, 1898–1904.
(63) Losev, V. V.; Molodov, A. I. The Influence of Fluorine Ions on the Anode Solution of Indium Amalgam and Certain Regularities in Electrode Processes Involving Complexes. *Dokl. Akad. Nauk SSSR* **1963**, *148* (5), 1114–1117.
(64) Gaur, J. N.; Jain, D. S. Reduction of Indium at the Dropping Mercury Electrode in Non-Complexing Media. *Electrochim. Acta* **1966**, *11* (11), 1661–1665.
(65) Moussa, A. A.; Abou Romia, M. M.; El-Taib Heakal, F. Reactivity of the Azide Ion Compared with That of Chloride and Bromide Ions towards Electron Transfer at Electrodes. *Electrochim. Acta* **1970**, *15* (8), 1391–1397.
(66) Hollnahel, M.; Landsberg, B. Non-Stationary Anodic Voltage Curves on Nickel. *Zeitschrift Fur Phys. Chemie* **1959**, *212*, 94.
(67) Randles, J. E. B. *Progress in Polarography 1*; Interscience: New York, 1962.
(68) Kravtsov, V. I. Kinetics and Mechanism of Electrode Reactions of Metal Complexes in Aqueous Electrolyte Solutions. *Russ. Chem. Rev.* **1976**, *45* (4), 284–297.
(69) Hubbard, A. T.; Anson, F. C. *The Theory and Practice of Electrochemistry with Thin Layer Cells, in Electroanalytical Chemistry A.J. Bard (Vol. 4), A Series of Advances.*; Marcel Dekker: New York, 1970.
(70) Blackledge, J.; Hush, N. S. Mechanism of the Zn(II)/Zn(Hg) Exchange Part 2: Catalysis by Halide and Thiocyanate Ions. *J. Electroanal. Chem.* **1963**, *5* (6), 435–449.
(71) Koryta, J. Kinetics of Discharge of Zinc at the Dropping Mercury Electrode. *Electrochim. Acta* **1962**, *6* (1–4), 67–74.
(72) Kambara, T.; Ishii, T. A.C. Polarographic Determination of the Rate Constant of Electrode Reaction. *Rev. Polarogr.* **1961**, *9* (1), 30–35.
(73) Bard, A. J.; Faulkner, L. R. *Electrochemical Methods: Fundamentals and Applications*; John Wiley & Sons, Inc., 2001.
(74) *EC-Lab Software User's Manual*; 10.38, Ed.; BioLogic Science Instruments, 2014.
(75) Randin, J. P.; Yeager, E. Differential Capacitance Study on the Edge Orientation of Pyrolytic Graphite and Glassy Carbon Electrodes. *J. Electroanal. Chem.* **1975**, *58* (2), 313–322.
(76) Iamprasertkun, P.; Hirunpinyopas, W.; Keerthi, A.; Wang, B.; Radha, B.; Bissett, M. A.;

Dryfe, R. A. W. Capacitance of Basal Plane and Edge-Oriented Highly Ordered Pyrolytic Graphite: Specific Ion Effects. *J. Phys. Chem. Lett.* **2019**, *10*, 617–623.
(77) Kresse, G.; Furthmüller, J. Efficient Iterative Schemes for Ab Initio Total-Energy Calculations Using a Plane-Wave Basis Set. *Phys. Rev. B* **1996**, *54* (16), 11169–11186.
(78) Kresse, G.; Furthmüller, J. Efficiency of Ab-Initio Total Energy Calculations for Metals and Semiconductors Using a Plane-Wave Basis Set. *Comput. Mater. Sci.* **1996**, *6* (1), 15–50.
(79) Kresse, G. Ab Initio Molecular Dynamics for Liquid Metals. *J. Non. Cryst. Solids* **1995**, *192–193*, 222–229.
(80) Perdew, J. P.; Burke, K.; Ernzerhof, M. Generalized Gradient Approximation Made Simple. *Phys. Rev. Lett.* **1996**, *77* (18), 3865–3868.
(81) Joubert, D. From Ultrasoft Pseudopotentials to the Projector Augmented-Wave Method. *Phys. Rev. B - Condens. Matter Mater. Phys.* **1999**, *59* (3), 1758–1775.
(82) Hoover, W. G. Canonical Dynamics: Equilibrium Phase-Space Distributions. *Phys. Rev. A* **1985**, *31* (3), 1695–1697.
(83) Nosé, S. A Unified Formulation of the Constant Temperature Molecular Dynamics Methods. *J. Chem. Phys.* **1984**, *81* (1), 511–519.

Chapter 6 : Understanding Influence of Electrode on Charge Transfer Reactions of Transition Metal Ions*

* This chapter is adapted from Agarwal, H.; Florian, J.; Goldsmith, B. R.; Singh, N. Explaining Kinetic Trends of Inner-Sphere Transition Metal Ion Redox Reactions at Electrodes Using the *d*-band Model. *Submitted* **2022**. The computational portion of the work is conducted by Jacob Florian.

6.1 Summary

In this chapter, we report that the average energy of the *d* electrons (i.e., *d*-band center) of a transition metal electrode rationalizes the kinetic trends of heterogeneous inner sphere charge transfer (CT) of transition metal ions. We show that V^{2+}/V^{3+} is an inner sphere reaction and that the kinetic parameters correlate with the energy of an adsorbed vanadium intermediate on Au, Ag, Cu, Bi, and W electrodes, with W being the most active. We demonstrate that the energy of the adsorbed vanadium intermediate linearly correlates with the *d*-band center, such that the *d*-band center serves as a simple descriptor for the V^{2+}/V^{3+} kinetics. We extract kinetic data from the literature for four other inner sphere CT reactions of transition metal ions involving Cr, Fe, Co-based complexes to show that the *d*-band center also linearly correlates with kinetic trends for these systems. The *d*-band center of the electrode is a general descriptor for heterogeneous inner sphere CT because it correlates with the adsorption strength of the metal ion intermediate. The *d*-band center descriptor is analogous to the *d*-electron configuration of transition metal ions serving as a descriptor for homogeneous inner sphere CT because the *d*-electron configuration controls bond strengths of intermediate metal ion complexes.

6.2 Introduction

The large effect of the electrode on the kinetics of heterogeneous inner sphere CT (het-CT) reactions of transition metal ions is poorly understood. Inner sphere CT of transition metal ions generally involves formation of a chemical bond between the two redox centers through a bridging ligand. The bridging ligand mediates the electron transfer between the redox centers. Bridging ligands (denoted by X) are typically molecules containing *p*-block elements like C, N, O, P, S, and halides.[1–3] For het-CT, the exchange current densities (i_o) or rate constants (k) vary by several orders of magnitude on different electrodes.[4–7] Changes of this magnitude in i_o and k cannot be attributed solely to double layer changes at the electrode-electrolyte interface, so the electrode's electronic structure must have an effect on the energy of intermediate steps.[8,9] The i_o and k have been shown to correlate with electrode properties such as point of zero charge,[10,11] work function,[10,12] electronegativity,[12,13] and polarizability for inner sphere CT reactions of Fe^{2+}/Fe^{3+} complexes;[14] but there is a lack of physical understanding of why these properties correlate with kinetics and how universally these correlations hold.

We hypothesize that the large effect of the electrode in het-CT is because of the electrode's influence on the adsorption energy of the intermediate. We denote this intermediate species as *[X─M], where * represents the electrode surface, and X is the ligand through which metal ion M adsorbs. In the previous chapters, we have shown that for the V^{2+}/V^{3+} reaction on carbon electrodes, the i_o, apparent activation energy (E_a), and apparent frequency factor are related to the adsorption strength and desorption barrier of an adsorbed vanadium intermediate (*[X─V^{3+}]).[2,3] We investigate whether this relationship between V^{2+}/V^{3+} kinetics and desorption barrier extends to metal electrodes here and whether an electrode property can universally describe the trends in kinetics for het-CT reactions of transition metal ions.

It is critical to understand what metal ion and electrode properties control the reaction energetics and mechanism to rationalize kinetic trends of heterogeneous inner sphere CT reactions. Here we discuss how the kinetic parameters, that is, i_o or k, E_a, and apparent frequency factor, depend on a general reaction free energy diagram as depicted in **Scheme 6.1a**. We then discuss the corresponding reaction steps, intermediates, and transition states of homogeneous inner sphere CT (hom-CT, **Scheme 6.1b**) and het-CT (**Scheme 6.1c**) and identify similarities in reaction mechanism.

Both homogeneous and heterogeneous inner sphere CT generally involve the formation of three intermediates (I_1, I_2, and I_3). For the case where electron transfer to form I_3 is the rate determining step (RDS), the apparent frequency factor is related to the concentration of the intermediates (I_1 and I_2) formed in steps before the RDS and depends on the free energies of forming I_1 (ΔG_1) and I_2 (ΔG_2). The E_a is related to the difference in the transition states ($\ddagger_{RDS}$) energy and the energy of I_2, denoted by $E^{\ddagger_{RDS}}$. Therefore, with ΔG_1, ΔG_2, and $E^{\ddagger_{RDS}}$, one can in principle predict the kinetics of charge transfer. If the electron transfer step is not the RDS or multiple reaction steps are rate-controlling, the kinetics of CT will depend on the free energies of relevant intermediates and transition state energies. Experimentally measuring ΔG_1, ΔG_2, and $E^{\ddagger_{RDS}}$ is difficult and evaluating these energies from first-principles atomistic modeling requires structural knowledge of these species and calculating the reaction energy profile, which is computationally expensive. By identifying similarities in the mechanisms of hom-CT and het-CT and properties that control ΔG_1, ΔG_2, and $E^{\ddagger_{RDS}}$ in hom-CT, we can predict what electrode properties may control het-CT of transition metal ions.

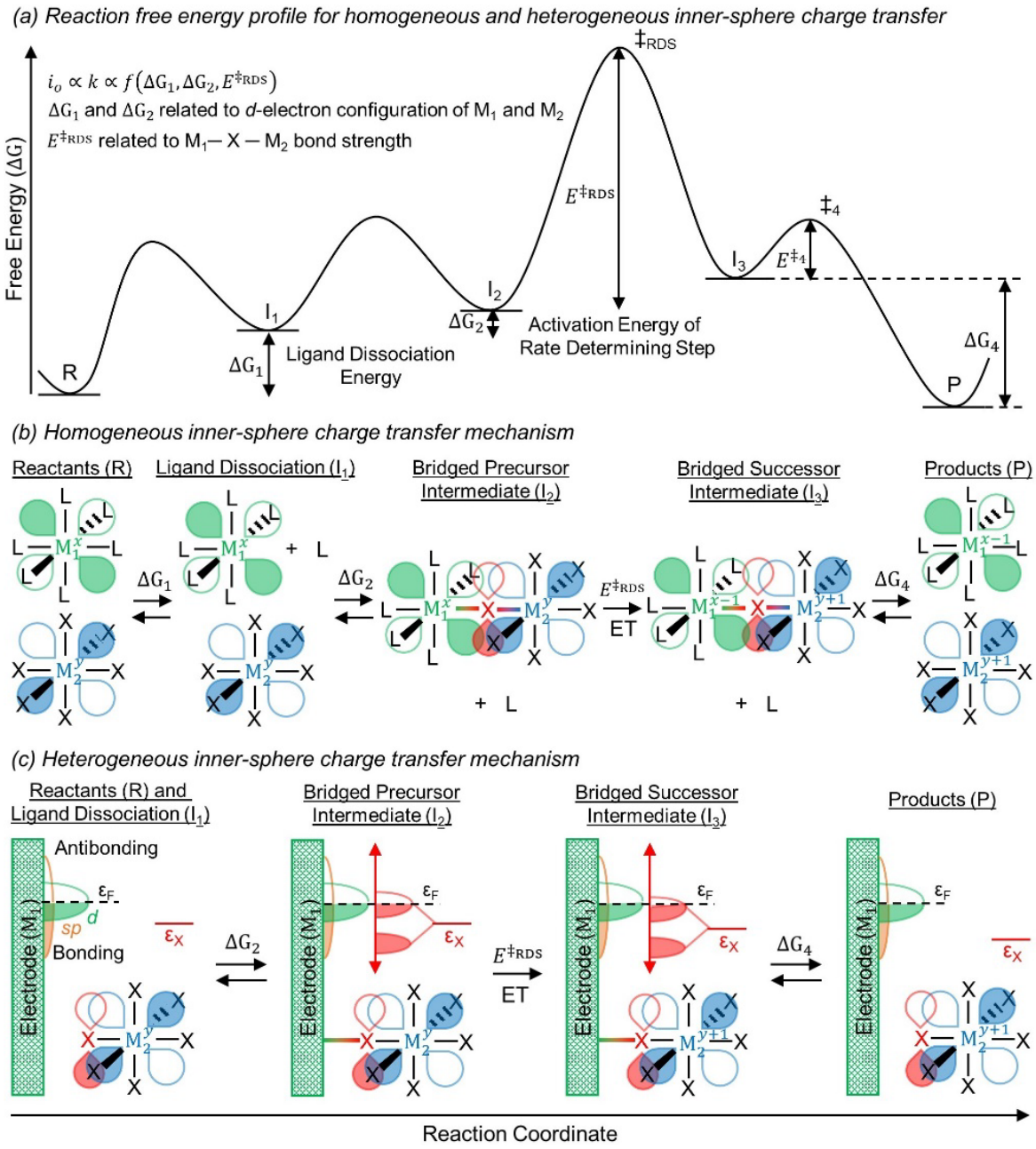

Scheme 6.1. Inner Sphere Charge Transfer Reactions of Transition Metal Ions in Solution and at Electrode. **(a)** Free energy diagram showing typical steps involved in inner sphere CT of transition metal ions. Reactant (R), intermediates (I_1, I_2, and I_3), and products (P) are denoted. The exchange current density and rate constant are a function of the reaction energetics. ΔG_i is the free energy change of step i, $E^{\ddagger RDS}$ is the activation energy of the rate determining step, and $E^{\ddagger 4}$ is activation energy to form the product (e.g., the desorption barrier in heterogeneous inner sphere CT). Corresponding reaction steps for **(b)** homogeneous and **(c)** heterogeneous inner sphere CT involving transition metals M_1 and M_2. Here x is the oxidation state of M_1 in homogeneous CT, and y is the oxidation state of M_2 in homogeneous and heterogenous CT. L and X are neutral ligands. The *d*-orbitals of metal ions M_1 and M_2 in homogeneous CT and density of states of electrode M_1 and *d*-orbitals of metal ion M_2 is shown for het-CT. The *p*-orbitals of bridging ligand X is also shown. ET is electron transfer, ε_X is the electronic energy of the *p*-orbital of ligand X, and ε_F is the electrode Fermi-level energy with respect to the vacuum.

For hom-CT (**Scheme 6.1b**) the properties that control ΔG_1, ΔG_2 and $E^{\ddagger_{RDS}}$ include the *d*-electron configuration of the transition metal ion redox centers and the ligand field strength. Here, the reactants undergo CT as two metal ions in solution, $M_1^x L_6$ and $M_2^y X_6$. We assume that $M_1^x L_6$ first loses ligand L to form I_1, with energy ΔG_1.[1] Next, $M_1^x L_5$ and $M_2^y X_6$ form a bridged precursor intermediate I_2 ($L_5 M_1^x - X - M_2^y X_5$) with free energy of reaction ΔG_2.[1] I_2 subsequently undergoes electron transfer in the RDS through transition state $\ddagger_{RDS}$ to form a bridged successor intermediate I_3, which proceeds to form the products. The *d*-electron configuration of metal ions M_1 and M_2 and the ligand field strength of ligand X govern the *d*-orbitals involved in forming I_1 and I_2 and control ΔG_1 and ΔG_2. The symmetry of the *d*-orbitals of the metal ions available for overlapping with the *p*-orbitals of the bridging ligand controls the $M_1 - X - M_2$ bond strength, and hence $E^{\ddagger_{RDS}}$ and E_a.[1] Thus, the rate of hom-CT can be controlled by tuning the *d*-electron configuration of the metal ions and ligand field strength.

For het-CT, in addition to the *d*-electron configuration of the metal ion and the ligand field strength, the coupling of the energy levels between the metal ion and the electrode affects ΔG_1, ΔG_2 and $E^{\ddagger_{RDS}}$. In het-CT, one of the redox centers is an electrode (M_1), so in **Scheme 6.1c** we depict the density of states and Fermi-level (ε_F) for M_1. We also show the electronic energy (ε_X) of the *p*-orbital of the ligand X in metal ion complex $M_2^y X_6$. $M_2^y X_6$ adsorbs on M_1 to form I_2. Analogous to hom-CT, ΔG_1 ($M_2^y X_6$ ligand dissociation) and ΔG_2 ($M_2^y X_6$ adsorption to M_1) depend on the *d*-electron configuration of M_2 and the ligand field strength of X. Additionally, ΔG_2 also depends on the electronic structure of M_1. I_2 undergoes electron transfer to form $M_1 - X - M_2^{y+1} X_5$ (that is, I_3 or $*[X - M_2^{y+1}]$). I_3 desorbs to form the product. The adsorption energy of the metal ion on the electrode through the bridging ligand ($*[X - M_2^{y+1}]$) depends on the electronic structure of the electrode and controls $E^{\ddagger_{RDS}}$. Thus, the electronic structure of the electrode

influences het-CT analogous to the *d*-electron configuration of transition metal ions for hom-CT. For a reaction where adsorbate scaling relations exist,[15] the energy of all intermediates will vary linearly, i.e., an electrode that adsorbs one intermediate strongly relative to other electrode materials will also adsorb other intermediates strongly. If Brønsted-Evans-Polanyi (BEP) relations hold for any reaction,[15,16] the transition state energies will be linearly related to the reaction energies of the elementary steps. Thus, for reactions with adsorbate scaling and BEP relations, the entire reaction energy profile can be defined by a single intermediate or transition state energy, where all other energies would be related linearly. We showed in previous chapters that for het-CT of metal ions in acidic electrolytes on carbon electrodes, i_o, E_a, apparent frequency factors scaled with the computationally predicted energies of I_3 or desorption barrier $E^{\ddagger_4}$ in **Scheme 6.1a**.

We hypothesize the *d*-band center of the electrode is related to the adsorption energies of the intermediates and transition states for het-CT reactions of transition metal ions. From a molecular perspective, for a fixed ligand X and metal ion M_2, the adsorption strength of X on electrode M_1 is dictated by the occupancy of the antibonding states of X, which depends on the position of antibonding states relative to ε_F. The position of antibonding states of atomic adsorbates such as H, N, O, S and molecular adsorbates such as CO, NO, C_2H_4 are described well by the *d*-band center of the electrode (i.e., average energy of the *d*-electrons with respect to ε_F).[17–20] The occupancy of antibonding states of X is higher with a lower *d*-band center, which leads to a weaker adsorption of X. The weaker adsorption of X leads to weaker adsorption of the $*[X-M_2^{y+1}]$ intermediate for fixed X and M_2 and vice versa. This *d*-band model has successfully rationalized kinetic trends of several inner sphere reactions in heterogeneous catalysis that involve the formation of an adsorbed intermediate such as hydrogen evolution reaction (HER)[18,19] and the oxygen reduction reaction.[20] If similar trends between the *d*-band center and adsorption energies are seen for metal ion

adsorbates, the *d*-band center will capture the effect of the electrode on the kinetics of het-CT of transition metal ions if the bridging ligand is unchanged.

In this chapter, we demonstrate that the *d*-band electronic structure of the electrode is related to the heterogeneous inner sphere CT kinetics of transition metal ions. We use the V^{2+}/V^{3+} reaction as a probe system and evaluate kinetic parameters on five different metal electrodes to show V^{2+}/V^{3+} kinetics linearly correlates with the *d*-band center of the different electrodes. The *d*-band center controls the kinetics by changing the adsorption strength of the metal ion CT intermediate. We extend this analysis to show that the *d*-band center also linearly correlates with the kinetics of het-CT reactions involving Cr, Fe, Co-based complexes. The *d*-band correlation is stronger than those of other electrode properties proposed to explain kinetic trends. Our demonstration that the *d*-band model rationalizes kinetic trends for several inner sphere CT reactions of transition metal ions on various electrodes provides links between concepts from heterogeneous catalysis and homogeneous inner sphere CT.

6.3 Results and Discussion

6.3.1 V^{2+}/V^{3+} Reaction Kinetics on Metal Electrodes

Although Bi,[21–25] Ag,[26] Sb,[27] W,[28] Cu,[29] and Sn[30] on carbon supports have shown improved kinetics for the V^{2+}/V^{3+} reaction, there is little understanding of the reason behind this kinetic enhancement and whether there are any trends in the kinetics with electrode properties. Various challenges have prevented a fair comparison of activity among electrodes and understanding of the reaction mechanism, including the absence of reaction rates normalized by the electrochemically active surface area (ECSA), differences in experimental techniques (cyclic voltammetry at different scan rates, CT resistance at different voltages) and testing conditions (mass transfer limitations), and not capturing the effect of metal deposition and functionalization

on properties of the carbon support. Similar challenges have prevented comparing activities of different metal electrodes for other transition metal ion redox couples.[31–33] We address these challenges in this work by: (i) using unsupported metals as electrodes in a single electrolyte to ensure any changes in activity are coming solely from the metal itself, (ii) measuring ECSA normalized kinetics, and (iii) measuring kinetic parameters using steady-state current measurements and CT resistance at open circuit voltages using a rotating disk electrode that provides control over mass transfer limitations. Mitigating these challenges allows us to understand the V^{2+}/V^{3+} reaction mechanism and identify physicochemical descriptors that explain kinetic trends for several het-CT reactions.

We measure the V^{2+}/V^{3+} kinetic parameters on Au, Ag, Cu, Bi, and W metal electrodes in H_2SO_4 to isolate the effect of the electrode on charge transfer. The preparation of these electrodes are discussed in the Supporting Information (SI). We choose these five metal electrodes for our analysis because of their varying *d*-band center and other electronic properties like work function, polarizability, and electronegativity. Because V^{3+} interacts with anions present in the electrolyte and often forms complexed species, we use the same electrolyte to ensure the structure of reacting vanadium ions remains unchanged and the role of the metal electrode on V^{2+}/V^{3+} redox kinetics is isolated.[2,3,34] We have shown in previous chapters that V^{2+} exists as $[V(H_2O)_6]^{2+}$ and V^{3+} exists as a mixture of $[V(H_2O)_5SO_4]^{+}$ and $[V(H_2O)_6]^{3+}$ in H_2SO_4.

We measure the ECSA to ensure normalized intrinsic V^{2+}/V^{3+} kinetics on Au, Ag, Cu, Bi, and W metal electrodes. We determine the ECSA of Au using Cu underpotential deposition (UPD) and the ECSA of Ag and Cu using Pb UPD. We observe that Cu and Pb UPD do not occur on Bi and W. To our knowledge, there is not any other UPD technique previously shown to estimate ECSA for Bi and W. A previous study used HER currents to determine the ECSA of W electrodes,

however, it is unclear if the measured HER currents were mass-transfer limited and the roughness of the W electrodes was not considered.[35] Here, we measure the ECSA of Bi and W electrodes by determining the HER current at a fixed voltage on our disk electrode and normalizing to the HER current on Bi and W electrodes deposited to have a roughness factor of one. The details of the ECSA measurements are discussed in **Chapter 2**. We ensure that the HER currents are not mass transfer limited by operating at sufficiently high rotation or stir rates where the current is independent of mass transfer. This is the first time that HER current is used to measure ECSA of Bi electrodes.

We evaluate the i_o, Tafel slopes, E_a, and apparent frequency factors for the V^{2+}/V^{3+} reaction on Au, Ag, Cu, Bi, and W electrodes using steady state current measurements (Tafel method) and impedance measurements (CT resistance method). We record the steady state measurements at different rotation rates for a range of overpotentials using a rotating disk electrode setup, and use Koutecky-Levich analysis to deconvolute the contributions of kinetic and diffusive current.[36] The kinetic currents of the oxidation reaction are used to estimate i_o and Tafel slopes using the Tafel equation for all metal electrodes except W. We use the Butler-Volmer equation instead of the Tafel equation to estimate i_o on W because the limiting currents are reached at low overpotentials on W. Analyzing only the oxidation region ensures the contribution of HER on the estimated i_o is minimal.[3,34] Electrochemical impedance spectroscopy measurements at open circuit voltage are fitted to a modified Randles circuit to estimate exchange current densities from CT resistance method ($i_{o,R_{ct}}$). The variation of i_o with temperature is fitted to the Arrhenius equation to estimate E_a and apparent frequency factors by Tafel method. Similarly, the variation of $i_{o,R_{ct}}$ with temperature is used to estimate apparent activation energies ($E_{a,R_{ct}}$), and CT apparent frequency factors. The agreement between the kinetic parameters obtained from the independent

Tafel and CT resistance methods assists in ensuring reproducibility and provides information pertaining to the number of electrons involved in the reaction as shown in **Figure S6.1** of the SI. This experimental procedure to estimate kinetic parameters is the same as used in previous chapters and is discussed in detail in **Chapter 2**.

The large effect of the electrode surface on the exchange current density in **Figure 6.1a** shows that the V^{2+}/V^{3+} reaction is inner sphere. The i_o of the V^{2+}/V^{3+} reaction on all five electrodes (Au, Ag, Cu, Bi, and W) measured in this work are compared with i_o on glassy carbon (GC) and edge plane pyrolytic graphite (EPPG) from our prior chapters and are shown as a function of State of Charge $\left(\mathrm{SoC} = \frac{[V^{2+}]}{[V^{2+}]+[V^{3+}]}\right)$ in **Figure 6.1a**. We measure the SoC by deconvoluting the contributions of V^{2+} and V^{3+} using UV-vis spectroscopy as discussed in **Chapter 2**.[34] The i_o on metal electrodes follow the order W > Cu > Ag > Au > Bi at 50% SoC. The three orders of magnitude variation in i_o between the most active (W) and least active (GC) electrode in **Figure 6.1a** is much larger than the factor of 3–8 times observed for different electrodes for outer sphere reactions of transition metal ions,[4–7] suggesting that the V^{2+}/V^{3+} is an inner sphere reaction. Additionally, the three orders of magnitude rate enhancement on metals compared to carbon confirm that the catalyzing effect observed previously for metals deposited on carbon supports for V^{2+}/V^{3+} reaction is largely due to the metals themselves and not due to changes in the properties of carbon supports because of metal deposition. By comparing i_o and $i_{o,R_{ct}}$ on different metal electrodes except W, we show that the RDS of V^{2+}/V^{3+} reaction involves one electron transfer on all metals (**Figure S6.1**), similar to GC and EPPG in H_2SO_4.[2,34]

The dependence of V^{2+}/V^{3+} kinetics on SoC for all metal and carbon electrodes indicates that V^{2+}/V^{3+} is an inner sphere reaction, and matches the kinetic trends predicted by a rate law with electron transfer step as RDS. W, Cu, Ag, and Bi show a maximum in i_o between 30–80% SoC

similar to EPPG, whereas i_o on Au decreases with decreasing SoC similar to GC as shown in **Figure 6.1a**. An outer sphere reaction would not have a decreasing i_o with SoC, as we have previously discussed on GC.[3] The rate law for inner sphere CT reaction with electron transfer step as the RDS (**eq. S6.17**) captures the i_o behavior with SoC on all metal and carbon electrodes. On the contrary, rate laws assuming either the adsorption or desorption of the vanadium intermediate as the RDS are unable to capture the i_o behavior on all electrodes (**Tables S6.1** and **S6.2**).

The Tafel slopes on all metal and carbon electrodes in **Figure 6.1b** indicate that the V^{2+}/V^{3+} reaction is asymmetric with electron transfer as the RDS. For a reaction involving one electron transfer in RDS and completely symmetric (transfer coefficient, $\alpha_{ox} = \alpha_{red} = 0.5$), the Tafel slope is ~117 mV decade^{-1} at room temperature ($T = 23.3$ °C) and independent of SoC.[36] The Tafel slopes are between 130–170 mV decade^{-1} on Au, Bi, EPPG, and GC and between 200–250 mV decade^{-1} on Cu and Ag. On the contrary, Tafel slopes are close to 60 mV decade^{-1} on W. The use of V^{2+}/V^{3+} oxidation region to estimate i_o and Tafel slopes greater than 117 mV decade^{-1} on all metal and carbon electrodes except W indicate that the V^{2+}/V^{3+} reaction is asymmetric with α_{ox} lower than 0.5. The relatively constant Tafel slopes with varying SoC confirms that the electron transfer is the RDS on all metal and carbon electrodes. The Tafel slopes decrease with decreasing SoC if the adsorption or desorption of the vanadium intermediate are considered as RDS, as shown in the SI. However, the reaction mechanisms with adsorption, electron transfer, or desorption steps as RDS do not explain the very low Tafel slopes on W indicating the possibility of a more complex reaction mechanism on W. Asymmetric transfer coefficients have been previously reported for several redox reactions including Fe^{2+}/Fe^{3+}, Co^{3+}/Co^{2+}, and Cr^{2+}/Cr^{3+} on metal electrodes.[8,9,37–40]

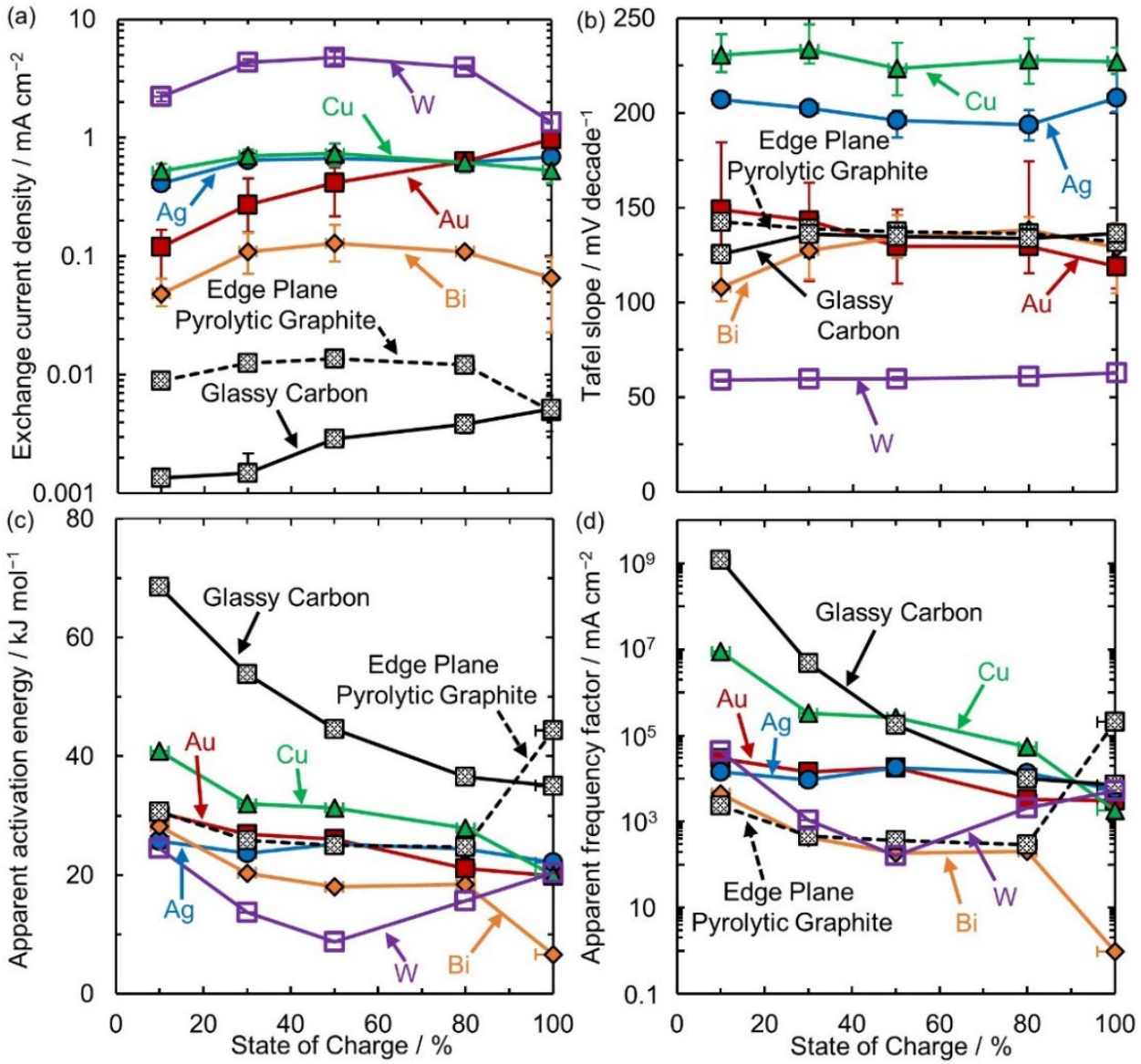

Figure 6.1. Kinetic Parameters for the V^{2+}/V^{3+} Reaction in H_2SO_4 on Metal and Carbon Electrodes. (a) Exchange current densities (i_o) from the Tafel method at room temperature ($T = 23.3$ °C). **(b)** Tafel slopes at $T = 23.3$ °C. **(c)** Apparent activation energies (E_a) and **(d)** Apparent frequency factors. All kinetic parameters are plotted as a function of state of charge for V^{2+}/V^{3+} reaction on Au, Ag, Cu, Bi, and W metal electrodes and edge plane pyrolytic graphite (EPPG) and glassy carbon (GC) electrodes. The E_a and apparent frequency factors are evaluated using the i_o at $T =$ 23.3, 30.0, 35.0, and 40.0 °C for all metals except W. We use i_o at $T = 5.0$, 10.0, 15.0, and 23.3 °C to evaluate E_a and apparent frequency factors for W because of the difficulty in obtaining accurate i_o at higher T. The vanadium ion concentration is 0.2 M dissolved in 1 M H_2SO_4, except for GC (0.5 M H_2SO_4). All kinetic parameters of GC and EPPG are reproduced from our prior works.[2,34]

The variation of E_a and apparent frequency factor with SoC also indicates that the electron transfer step is the RDS for V^{2+}/V^{3+} reaction on all electrodes except W and EPPG. On all metals except W, the E_a and apparent frequency factor continuously increase with decreasing SoC as

shown in **Figure 6.1c** and **Figure 6.1d**, respectively. Similar trends in E_a and apparent frequency factor with SoC are also observed on GC. The increasing E_a and apparent frequency factor with decreasing SoC agrees with predicted trends for a reaction mechanism with electron transfer step as the RDS (**Figure S6.3**). W and EPPG shows a minimum in both E_a and apparent frequency factor with SoC as shown in **Figure 6.1c** and **6.1d**. The reaction mechanisms with adsorption, desorption, or electron transfer step as the RDS (**Figures S6.2–S6.4**) do not predict a minimum in E_a and apparent frequency factor with SoC indicating the reaction mechanism on W and EPPG is different than the other metals or on GC. The rate laws showing the trends in kinetic parameters with SoC are summarized in **Table S6.2** and available in the SI.

Based on the kinetic data and comparison to our previous work on GC, we hypothesize that the CT intermediate is a vanadium species adsorbed through an *O bridge, and the energy of this intermediate affects the i_o for metals. On GC, we showed V^{2+} adsorbs as $*[OH{-}V(H_2O)_5]^+$ bridged intermediate, which corresponds to I_2 in **Scheme 6.1**.[3,34] Alternatively, the bridging ligand may come from *OH on the surface. The $*[OH{-}V(H_2O)_5]^+$ undergoes electron transfer and a ligand exchange to form $*[OH{-}V(H_2O)_4SO_4]$, corresponding to I_3 in **Scheme 6.1c**. We expect ligand exchange to occur during the electron transfer step in the RDS because the ligand exchange of V^{3+} with SO_4^{2-} is thermodynamically preferred.[3,34] We observe in our density functional theory-based metadynamics calculations that $*[O{-}V(H_2O)_4SO_4]$ is more favorable to form on metals compared to $*[OH{-}V(H_2O)_4SO_4]$. Because we see similar kinetic trends in **Figure 6.1** on metals as on GC, we postulate a reaction mechanism similar to GC on metals involving the $*[O{-}V(H_2O)_4SO_4]$ intermediate (corresponding to I_3). Further, because we have shown that the energy of the $*[X{-}V^{3+}]$ intermediate or its desorption barrier, $E^{\ddagger_4}$, correlates with kinetics in various acidic electrolytes on GC and EPPG,[2,3] we hypothesize that the adsorption strength of $*[O{-}V(H_2O)_4SO_4]$

(i.e., I_3) will correlate with the apparent frequency factor and E_a for metals as well. As discussed in the Introduction, if BEP relations hold for a given reaction, a single intermediate or transition state energy (e.g., $E^{\ddagger_4}$) can be used to describe the entire reaction energy profile. Resultantly, we compute the $E^{\ddagger_4}$ for *[O−V(H$_2$O)$_4$SO$_4$] on metals to compare to our kinetic data here.

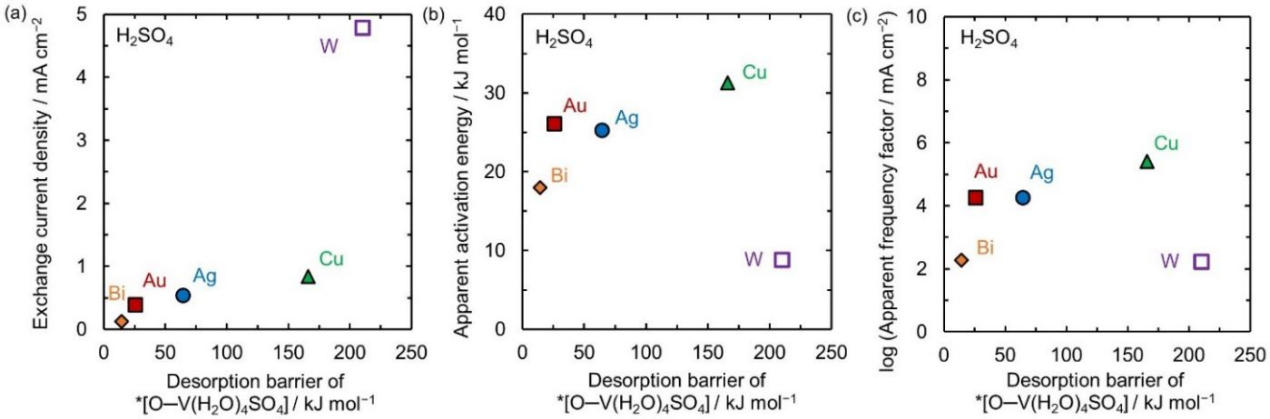

Figure 6.2. V^{2+}/V^{3+} Kinetic Parameters in H_2SO_4 Compared to Desorption Barrier of Proposed Intermediate on Metals. (a) Exchange current density at room temperature (T = 23.3 °C), **(b)** Apparent activation energy, and **(c)** Logarithmic of apparent frequency factor at 50% state of charge in H_2SO_4 as a function of calculated desorption barrier ($E^{\ddagger_4}$) of *[O—V(H$_2$O)$_4$SO$_4$] on Au, Ag, Cu, Bi, and W electrodes for V^{2+}/V^{3+} reaction.

The computed desorption barrier of *[O−V(H$_2$O)$_4$SO$_4$] rationalizes the kinetic trends of the V^{2+}/V^{3+} reaction on metal electrodes. We calculate the $E^{\ddagger_4}$ of *[O−V(H$_2$O)$_4$SO$_4$] using metadynamics and show the i_o, E_a, and apparent frequency factor at 50% SoC vs $E^{\ddagger_4}$ in **Figure 6.2**. The $E^{\ddagger_4}$ increases in the order W > Cu > Ag > Au > Bi and the i_o in **Figure 6.2a** follow a similar trend confirming our hypothesis that changing the metal electrode alters the reaction energy profile. Based on a reaction profile where BEP relations hold for different conditions/electrodes,[21] we would expect that as $E^{\ddagger_4}$ increases, due to stronger intermediate adsorption, the E_a and the intermediate coverage would increase. The higher intermediate coverage would lead to a larger apparent frequency factor. All metals except W obey these trends expected from BEP relations, as shown by the increasing E_a and apparent frequency factor with increasing $E^{\ddagger_4}$ in **Figure 6.2b** and **Figure 6.2c** respectively. However, W has different Tafel slopes and different dependence of E_a

and apparent frequency factor on SoC compared to other metals and is most active with lowest E_a. The different dependence on SoC and low E_a on W for high $E^{\ddagger_4}$ indicates that the V^{2+}/V^{3+} reaction occurs either through a different reaction mechanism or that BEP relations don't hold on W. Regardless, the i_o increases with $E^{\ddagger_4}$, indicating that the electrodes that binds *[O−V$(H_2O)_4SO_4$] more strongly are more active. The simulation cell used and process of evaluating desorption barrier from the metadynamics calculations is the same a discussed in **Chapter 5**. The free energy profiles of the adsorbed vanadium intermediate on metals are shown in **Figure S6.5**.

Our studies for the V^{2+}/V^{3+} reaction on metal electrodes highlight the importance of measuring kinetic parameters and coupling them with the understanding of the reaction energy profile to identify how the intermediate energies correlate with reaction kinetics. However, the desorption barrier of the *[O−V$(H_2O)_4SO_4$] intermediate requires metadynamics calculations and does not provide direct information about the electrode property influencing kinetics. Next, we show that the *d*-band center of the electrode correlates with the adsorption strength and desorption barrier of *[O−V$(H_2O)_4SO_4$], opening an avenue to directly predict active materials for V^{2+}/V^{3+} reaction.

6.3.2 Correlating V^{2+}/V^{3+} Reaction Kinetics with the *d*-band Center of the Electrode

The V^{2+}/V^{3+} kinetics on transition metal electrodes in H_2SO_4 at 50% SoC linearly correlate with the *d*-band center. The i_o correlates strongly to the *d*-band center (Pearson correlation coefficient, $r = 0.97$) of the four *d*-block metal electrodes as shown in **Figure 6.3a**. The linear correlation between i_o and *d*-band center arises because the desorption barrier of *[O−V$(H_2O)_4SO_4$] correlates with the *d*-band center ($r = 0.84$), as shown in **Figure 6.3b**. The correlation of i_o with the *d*-band center has a higher r and lower mean absolute error (MAE) than the correlation of desorption barrier with the *d*-band center indicating that the *d*-band center can

be used to predict kinetics with higher accuracy than the desorption barrier. The MAE of 0.41 mA cm^{-2} for the linear correlation between i_o and the *d*-band center in **Figure 6.3a** is much smaller than the maximum i_o observed on metals indicating small errors in i_o will not affect the quality of correlations.

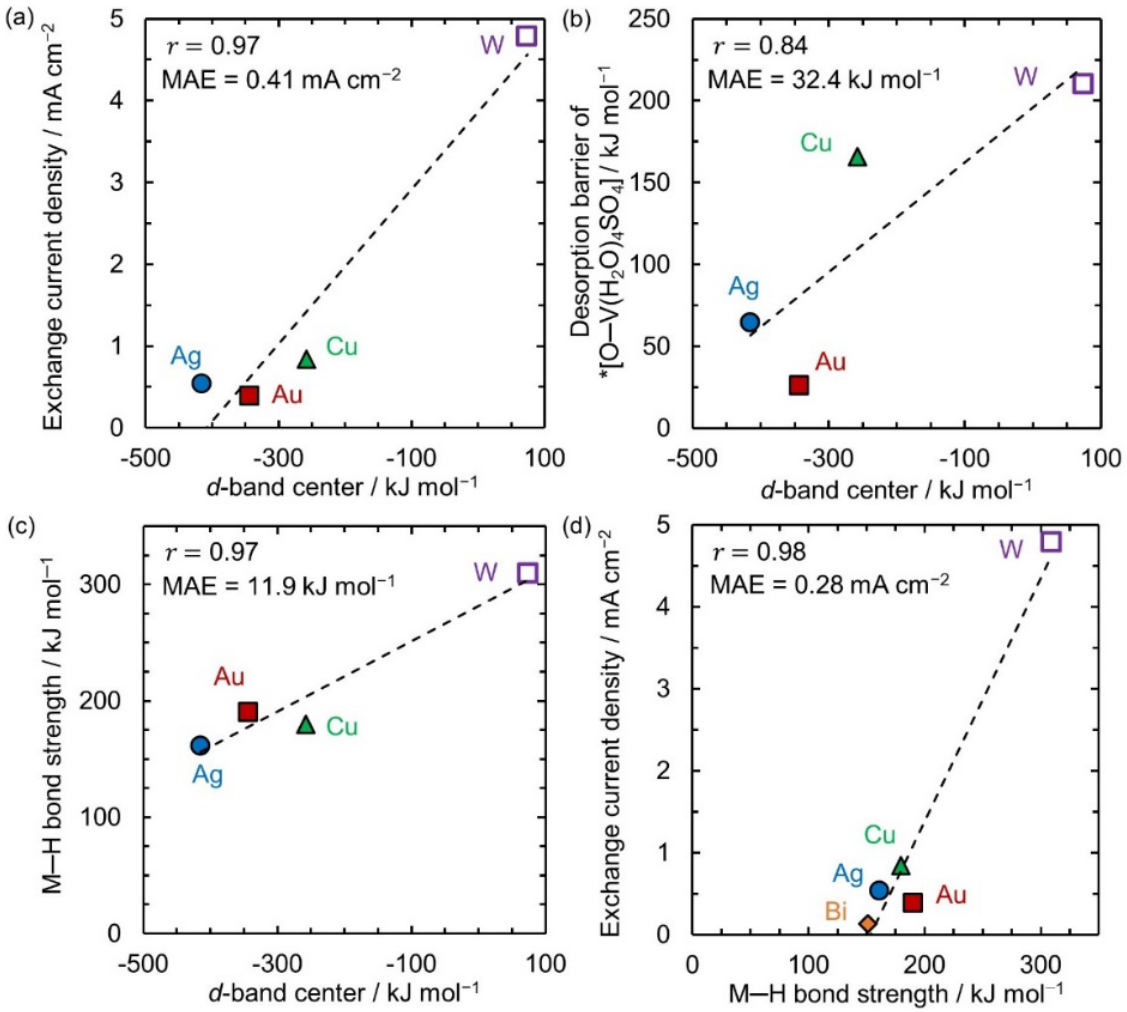

Figure 6.3. Relationship between Exchange Current Density of V^{2+}/V^{3+} Reaction in H_2SO_4, *d*-Band Center, Desorption Barrier, and Metal-Hydrogen Bond Strength. (a) Exchange current density of V^{2+}/V^{3+} reaction plotted against *d*-band center. **(b)** Desorption barrier of *[O−V$(H_2O)_4SO_4$] plotted against the *d*-band center. **(c)** Metal−hydrogen (M−H) bond strength plotted against the *d*-band center. **(d)** Exchange current density of V^{2+}/V^{3+} reaction plotted against M−H bond strength. Exchange current densities for the V^{2+}/V^{3+} reaction is obtained at 50% state of charge and room temperature (T = 23.3 °C). Linear trendlines are indicated for each. r is the Pearson correlation coefficient and MAE is the mean absolute error. The *d*-band center and M−H bond strength values for metals are taken from references 17 and 41, respectively.

Because Bi is not a *d*-block element, we use another material property, the metal−hydrogen (M−H) bond strength, to include Bi in the analysis. M−H bond strength also linearly correlates

with the *d*-band center ($r = 0.97$) as shown in **Figure 6.3c**. The i_o of V^{2+}/V^{3+} reaction on all five metals linearly correlates with the M−H bond strength as shown in **Figure 6.3d** ($r = 0.98$). Even though the MAE for linear correlation of i_o with M−H bond strength in **Figure 6.3d** is lower than that of i_o with *d*-band center in **Figure 6.3a**, we do not believe the M−H bond strength itself impacts the kinetics. The M−H bond strength instead is representative of the electronic structure of the electrode. Thus, i_o of V^{2+}/V^{3+} reaction on all five tested metals correlates with the electronic structure of the electrode. The *d*-band center controls the electrode−oxygen adsorption strength of the vanadium intermediate on metal electrodes, explaining trends in V^{2+}/V^{3+} kinetics. The *d*-band center and the M−H bond strength of the electrode can be used as descriptors to identify materials with desired properties for the V^{2+}/V^{3+} reaction. The *d*-band center of materials can be altered by alloying with different metals and introducing defects, opening avenues to identify low-cost materials that are active for V^{2+}/V^{3+} reaction.

6.3.3 *d*-band Center as a Descriptor for Heterogeneous Inner Sphere Charge Transfer of Fe-, Co-, Cr- Metal Ions

To explore if the *d*-band center or other electrode properties explain kinetic trends of het-CT of various transition metal ions, we extract kinetic data for four het-CT reactions from literature to add to our V^{2+}/V^{3+} work here. To avoid lab-to-lab variations in the reported k or i_o for a redox couple on the same electrode we only compare kinetic data from the same laboratory measured using the same methods.[42] Additionally, to control for the effect of the anion on rate constants, we only compare kinetic data in the same electrolyte. To ensure sufficient points to draw a correlation, we only select CT reactions where a minimum of three metals are used as electrodes. These criteria result in six sets of data to add to ours for V^{2+}/V^{3+} in H_2SO_4. Three of those sets of data are for the same redox couple (Fe^{2+}/Fe^{3+}) but done in different laboratories with varying total Fe

concentration and supporting electrolyte. The six data sets include the kinetic rate constants of $[Fe(H_2O)_6]^{2+/3+}$ in H_2SO_4 (with total [Fe] = 0.1 and 0.01 M) and mixture of K_2SO_4 and H_2SO_4 (Fe^{2+}/Fe^{3+}),[10,11] $[Co(NH_3)_5]NCS^{2+/1+}$ and *cis*-$([Co(en)_2](NCS)_2)^{1+/0}$ in mixture of $NaClO_4$ and $HClO_4$ (Co^{3+}/Co^{2+}),[9] and Cr^{2+}/Cr^{3+} in $NaClO_4$.[8] The anions present in the electrolyte or part of the coordination sphere, e.g., OH^-, NCS^-, SO_4^{2-}, act as bridging ligands to form adsorbed metal ion intermediate for these redox reactions undergoing het-CT similar to V^{2+}/V^{3+}.[1]

The kinetics of all five het-CT reactions linearly correlate best with the *d*-band center of the electrode in comparison to other electrode properties proposed to influence het-CT kinetics in the literature. The data in **Figure 6.4a** shows that r for kinetics is largest for the *d*-band center compared to electrode polarizability, electronegativity, and work function. The high r for kinetics with M−H bond strength for these CT reactions confirm the strong correlation between the M−H bond strength and *d*-band center as also observed in **Figure 6.3c**. The kinetics might also correlate to several combinations of electrodes properties, however, in this work we choose a single electrode property to follow the principle of Occam's razor.[43] Even though the electrode electronegativity for $[Fe(H_2O)_6]^{2+/3+}$, electrode work function for *cis*-$([Co(en)_2](NCS)_2)^{1+/0}$, and electrode polarizability for V^{2+}/V^{3+} also lead to good linear correlations ($|r| > 0.5$), *d*-band center and M−H bond strength are the only electrode properties that shows good correlations for all analyzed CT reactions as depicted in **Figure 6.4a**. Although our analysis is limited to only five inner sphere CT reactions due to limited availability of rate constants, the high r value for the *d*-band center of the electrode for all CT reactions suggests that the *d*-band center can be used as a descriptor for understanding and capturing the effect of electrode on the het-CT reactions. The availability of more kinetic data for inner sphere CT reactions on multiple metal electrodes in the same electrolyte will help in further confirming this analysis.

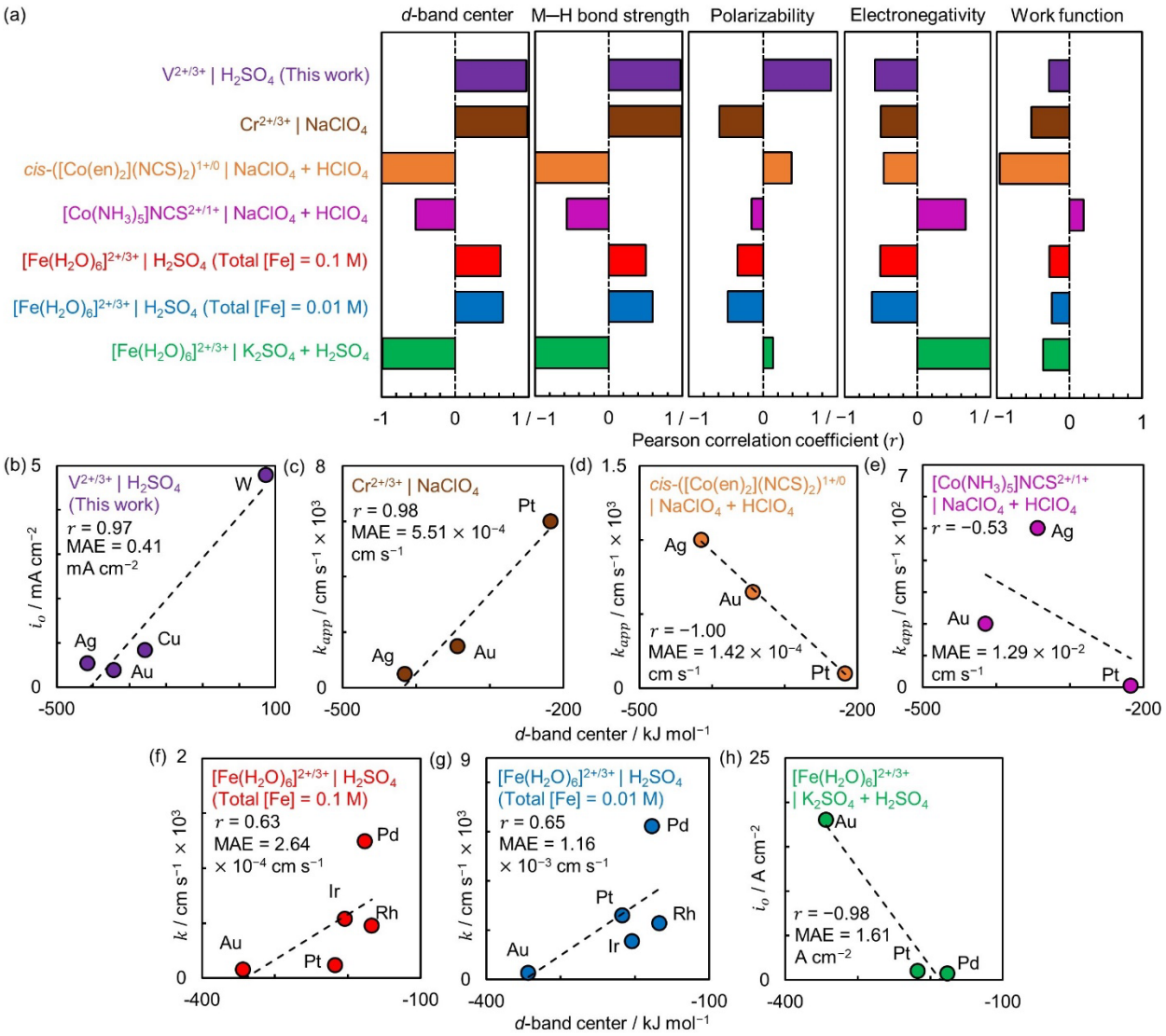

Figure 6.4. Correlation between Kinetics of Inner Sphere Charge Transfer Reactions of Transition Metal Ions and Electrode Properties. (a) Pearson correlation coefficient (r) for linear correlations of exchange current densities (i_o) or standard (k) or apparent (k_{app}) rate constants for various inner sphere redox couple | electrolyte combinations vs *d*-band center of the electrode, metal–hydrogen (M–H) bond strength, electrode polarizability, electronegativity, and work function. **(b–h)** i_o or k or k_{app} for various inner sphere redox couple | electrolyte combinations linearly correlating with the *d*-band center of the electrode with r and mean absolute error (MAE) shown in inset. The metal electrode properties used to determine the correlations are available in **Table S6.3**.

The kinetics linearly correlate either positively or negatively with the *d*-band center for all five het-CT reactions. The kinetics of V^{2+}/V^{3+} in H_2SO_4 (**Figure 6.4b**), Cr^{2+}/Cr^{3+} (**Figure 6.4c**), and $[Fe(H_2O)_6]^{2+/3+}$ in H_2SO_4 (**Figure 6.4f** and **6.4g**) correlate positively with the *d*-band center. On the other hand, the kinetics of *cis*-$([Co(en)_2](NCS)_2)^{1+/0}$ (**Figure 6.4d**), $[Co(NH_3)_5]NCS^{2+/1+}$ (**Figure 6.4e**), and $[Fe(H_2O)_6]^{2+/3+}$ in a mixture of K_2SO_4 and H_2SO_4 (**Figure 6.4h**) correlate

negatively with the *d*-band center. We propose the sign of the correlation depends on whether increasing the adsorption strength of the metal ion intermediate increases or decreases the rate. For V^{2+}/V^{3+} and the others with positive correlations, a higher *d*-band center increases the adsorption strength of the intermediates, increasing the rate. If the intermediate adsorbs too strongly, the kinetics will decrease with higher *d*-band center leading to a negative correlation because the electrode will adsorb the intermediate even more strongly, and desorption becomes more difficult. Resultantly, there is an optimum value for intermediate adsorption strength or *d*-band center of the electrode, that would maximize the CT kinetics based on Sabatier's principle.[15] **Figure 6.4e** shows the kinetics of $[Co(NH_3)_5]NCS^{2+/1+}$ are faster on Ag compared to Au and Pt indicating that possibly the *d*-band center of Ag allows the intermediate to adsorb with optimum adsorption strength, maximizing the kinetics. However, kinetics of $[Co(NH_3)_5]NCS^{2+/1+}$ on more metal electrodes is needed to confirm this. The positive *d*-band center correlation of $[Fe(H_2O)_6]^{2+/3+}$ kinetics in H_2SO_4 vs the negative correlation of kinetics in K_2SO_4 and H_2SO_4 may arise because of differences in complexation of Fe^{2+} and Fe^{3+} species in these electrolytes, which affect the bridge involved in formation of the adsorbed metal ion intermediate. Regardless of the changing sign of correlations, the MAE for correlations of kinetics of all five het-CT reactions vs *d*-band center is at least an order of magnitude smaller in comparison to the kinetics on most active metal as shown in **Figures 6.4b–6.4h**, indicating the correlations capture the kinetic trends on metals quantitatively.

The use of the *d*-band center as a descriptor to understand the electrode effect on het-CT confirms our hypothesis of analogous reaction mechanisms for inner sphere CT in the homogeneous and heterogeneous phase. As discussed, the kinetics in homogeneous inner sphere CT depends on the *d*-electron configuration that controls the orbital overlap between the bridging ligand and metal ions in the bridged intermediates, which in turn controls the intermediate's bond

strength for a fixed bridging ligand. Similarly, the kinetics of het-CT depends on the adsorption strength of the bridged intermediate on electrode surface, which is controlled by the *d*-band center of the electrode for a fixed metal ion and bridging ligand. Compared to the *d*-band center, the smaller r value for all other electrode properties like polarizability, electronegativity, and work function is expected because none of these electrode properties govern the adsorption strength of the bridged intermediate. The identification of the *d*-band center as a descriptor will enable the rational design of bimetallic alloys or core-shell catalysts with a desired *d*-band center to improve redox kinetics for het-CT reactions.

6.4 Conclusions

The work presented in this chapter demonstrates a relationship between the *d*-band center of a transition metal electrode and kinetic trends for heterogeneous inner sphere charge transfer reactions of transition metal ions. The *d*-band center controls the adsorption strength of the metal ion intermediate, which rationalizes the trends in heterogeneous inner sphere CT kinetics. The linear correlation of the redox kinetics with the *d*-band center observed here for reactions involving transition metal ion adsorbates is similar to the linear correlations found with the *d*-band center and reaction kinetics for many chemical reactions in heterogeneous catalysis involving atomic and molecular adsorbates. The observation that the *d*-band center controls the heterogeneous inner sphere CT rate is also analogous to the *d*-electron configurations of transition metal ions controlling rates in homogeneous inner sphere CT. The importance of the energy of *d* orbitals highlights the similarity in the intermediate steps between homogeneous and heterogeneous inner sphere CT. The *d*-band center of a metal electrode can be tuned by alloying with different metals at various compositions, nano structuring (e.g., changing the fraction of exposed surface facets),

or introducing lattice strains, opening an avenue to rationally design electrodes for heterogeneous inner sphere charge transfer reactions.

6.5 Supporting Information

6.5.1 Preparation of Metal Electrodes

The Ag, Cu, and W metal disk inserts (5 mm outer diameter × 4 mm thick) used for rate measurements are purchased from Pine Research. The Au films (300 nm thick) are deposited using electron beam evaporation on a glassy carbon disk insert (5 mm outer diameter × 4 mm thick, Pine Research). Ti (10 nm thick) is used as a seed layer and the glassy carbon disk insert is cleaned with ion implantation prior to deposition for proper adhesion of the seed layer. The deposition rate used is 2 Å s^{-1}. These metal depositions are conducted using the Angstrom Engineering Evaporator in the Lurie Nanofabrication Facility at the University of Michigan, Ann Arbor (UofM). The Bi disk insert (5 mm outer diameter × 4 mm thick) is prepared by machining a Bi rod (11 mm diameter, 99.99% metals basis, Fisher Scientific) at the Instrumentation shop of UofM according to the design used by Pine Research for making their disk inserts.[44]

6.5.2 Rate Laws to Identify Rate Determining Step of V^{2+}/V^{3+} Reaction

The overall reaction can be written as a series of elementary steps:

Step 1 (Adsorption): $V^{2+} + * \rightleftarrows *V^{2+}$

Step 2 (Electron Transfer): $*V^{2+} \rightleftarrows *V^{3+} + e^-$

Step 3 (Desorption): $*V^{3+} \rightleftarrows V^{3+} + *$

The rate laws for all the above considered discusses is derived below and findings of which rate laws match the observed kinetic trends from experiments are summarized in **Table S6.2**.

a) Rate Law Assuming Desorption of V^{3+} (Step 3) is RDS

The measured current density can be written as shown in **eq. S6.1**:

$$i = nF(k_3\theta_{V^{3+}} - k_{-3}[V^{3+}]\theta_*) \quad \text{(eq. S6.1)}$$

Here n is the total number of electrons involved in the reaction, k_3 and k_{-3} are the forward and backward rate constants of Step 3, and $\theta_{V^{3+}}$ and θ_* are the coverage of sites that are occupied by V^{3+} and are empty, respectively. Since Steps 2 and 3 are quasi-equilibrated, we can write **eq. S6.2**:

$$K_1 = \frac{\theta_{V^{2+}}}{[V^{2+}]\theta_*}$$
$$K_2 = \frac{\theta_{V^{3+}}}{\theta_{V^{2+}}} \quad \text{(eq. S6.2)}$$

Here K_1 is the adsorption constant of Step 1, K_2 is the equilibrium constant of Step 2, and $\theta_{V^{2+}}$ is the coverage of V^{2+}. The forward and backward rate constants of Step 2 (k_2 and k_{-2}) are written in terms of applied overvoltage (η) and standard rate constant at equilibrium (k_o) using the Butler-Volmer equation (**eq. S6.3**):

$$k_2 = k_o e^{\left(\frac{n\alpha_{ox}F\,\eta}{RT}\right)}$$
$$k_{-2} = k_o e^{-\left(\frac{n(1-\alpha_{ox})\,F\,\eta}{RT}\right)} \quad \text{(eq. S6.3)}$$
$$K_2 = \frac{k_2}{k_{-2}} = e^{\frac{nF\,\eta}{RT}}$$

Conducting a total site balance and simplifying, we get **eq. S6.4**:

$$\theta_* + \theta_{V^{2+}} + \theta_{V^{3+}} = 1$$
$$\theta_* + K_1[V^{2+}]\theta_* + K_2K_1[V^{2+}]\theta_* = 1 \quad \text{(eq. S6.4)}$$

$$\theta_* = \frac{1}{(1 + K_1[\mathrm{V}^{2+}] + K_2K_1[\mathrm{V}^{2+}])}$$

Substituting coverage terms from **eq. S6.4** in **eq. S6.1** and simplifying the measured current density, we get **eq. S6.5**:

$$i = nF\left(\frac{k_3K_2K_1[\mathrm{V}^{2+}] - k_{-3}[\mathrm{V}^{3+}]}{1 + K_1[\mathrm{V}^{2+}] + K_2K_1[\mathrm{V}^{2+}]}\right) \qquad (\mathrm{eq.\,S6.5})$$

Substituting K_2 in terms of η from **eq. S6.3**, **eq. S6.5** reduces to **eq. S6.6**:

$$i = nF\left(\frac{k_3K_1[\mathrm{V}^{2+}]e^{\frac{nF\eta}{RT}} - k_{-3}[\mathrm{V}^{3+}]}{1 + K_1[\mathrm{V}^{2+}] + e^{\frac{nF\eta}{RT}}K_1[\mathrm{V}^{2+}]}\right) \qquad (\mathrm{eq.\,S6.6})$$

Tafel slope is obtained as by taking the derivative of η with respect to $\log(i)$. Considering the oxidation Tafel slope that is measured in experiments, we get **eq. S6.7**:

$$b = \frac{d\eta}{d(\log i)} = \frac{2.303\ RT\left(1 + K_1[\mathrm{V}^{2+}] + e^{\frac{nF\eta}{RT}}K_1[\mathrm{V}^{2+}]\right)}{nF\ (1 + K_1[\mathrm{V}^{2+}])} \qquad (\mathrm{eq.\,S6.7})$$

The Tafel slopes are written in terms of SoC $\left(\mathrm{SoC} = \frac{[\mathrm{V}^{2+}]}{[\mathrm{V}]_{\mathrm{total}}}\right)$, **eq. S6.8**, to compare with experimental data in **Figure 6.1b** of the chapter:

$$b = \frac{d\eta}{d(\log i)} = \frac{2.303\ RT\left(1 + K_1[\mathrm{V}]_{\mathrm{total}}\mathrm{SoC} + e^{\frac{nF\eta}{RT}}K_1[\mathrm{V}]_{\mathrm{total}}\mathrm{SoC}\right)}{nF\ (1 + K_1[\mathrm{V}]_{\mathrm{total}}\mathrm{SoC})} \qquad (\mathrm{eq.\,S6.8})$$

b decreases with decreasing SoC for a constant $[V]_{total}$*, which is not observed on any of the metal and carbon electrodes.*

The Nernst equation (**eq. S6.9**) is used to simplify further to reduce i in terms of V^{2+} and V^{3+} concentrations in **eq. S6.10**:

$$\eta = \frac{RT}{nF}\ln\left(\frac{[\mathrm{V}^{3+}]}{[\mathrm{V}^{2+}]}\right) \qquad \text{(eq. S6.9)}$$

$$i = nF\left(\frac{k_3K_1[\mathrm{V}^{3+}] - k_{-3}[\mathrm{V}^{3+}]}{1 + K_1[\mathrm{V}^{2+}] + K_1[\mathrm{V}^{3+}]}\right) \qquad \text{(eq. S6.10)}$$

i is zero at equilibrium, however a balanced faradaic activity can be expressed in terms of i_o as depicted in **eq. S6.11**:

$$i_o = \frac{nFk_3K_1[\mathrm{V}^{3+}]}{(1 + K_1[\mathrm{V}^{2+}] + K_1[\mathrm{V}^{3+}])} = \frac{k_{-3}[\mathrm{V}^{3+}]}{(1 + K_1[\mathrm{V}^{2+}] + K_1[\mathrm{V}^{3+}])} \qquad \text{(eq. S6.11)}$$

Case 1: When $1 \gg (K_1[\mathrm{V}^{2+}] + K_1[\mathrm{V}^{3+}])$

$$i_o = nFk_3K_1[\mathrm{V}^{3+}] = k_{-3}[\mathrm{V}^{3+}]$$

Case 2: When $K_1[\mathrm{V}^{2+}] \gg (1 + K_1[\mathrm{V}^{3+}])$

$$i_o = nFk_3[\mathrm{V}^{3+}][\mathrm{V}^{2+}]^{-1} = \frac{k_{-3}}{K_1}[\mathrm{V}^{3+}][\mathrm{V}^{2+}]^{-1}$$

Case 3: When $K_1[\mathrm{V}^{3+}] \gg (1 + K_1[\mathrm{V}^{2+}])$

$$i_o = nFk_3 = \frac{k_{-3}}{K_1}$$

The sign of V^{2+} and V^{3+} orders for none of the cases above match with the orders observed in experiments on all metal and carbon electrodes.

Using the temperature dependence of adsorption constant K_1 $\left(\propto \exp\left(-\frac{\Delta G_1}{RT}\right)\right)$ and rate constant k_3 $\left(\propto \exp\left(\frac{-E_{a,3}}{RT}\right)\right)$ in **eq. S6.11**, we obtain the trends in E_a and apparent frequency factor with SoC as shown in **Figure S6.2**. Here ΔG_1 is the free energy of Step 1 and $E_{a,3}$ is the activation energy of Step 3.

b) Rate Law Assuming Electron Transfer Step Involving Adsorbed Vanadium Intermediate (Step 2) is RDS

The measured current density is described by **eq. S6.12**:

$$i = nF(k_2\theta_{V^{2+}} - k_{-2}\theta_{V^{3+}}) \qquad \text{(eq. S6.12)}$$

Assuming Steps 1 and 3 are in quasi-equilibrated and following the same process of site balance, we get **eq. S6.13**:

$$i = nF\left(\frac{k_2K_1[V^{2+}] - k_{-2}K_3[V^{3+}]}{1 + K_1[V^{2+}] + K_3[V^{3+}]}\right) \qquad \text{(eq. S6.13)}$$

Here K_3 is the adsorption constant of Step 3.

Substituting k_2 and k_{-2} in terms of η from **eq. S6.3**, we get **eq. S6.14**:

$$i = nFk_o\left(\frac{e^{\left(\frac{n\alpha_{ox}F\eta}{RT}\right)}K_1[V^{2+}] - e^{-\left(\frac{n(1-\alpha_{ox})F\eta}{RT}\right)}K_3[V^{3+}]}{1 + K_1[V^{2+}] + K_3[V^{3+}]}\right) \qquad \text{(eq. S6.14)}$$

Anodic Tafel slopes are obtained in terms of SoC and $[V]_{total}$ in **eq. S6.15**, using the same process as above:

$$b = \frac{d\eta}{d(\log i)} = \frac{2.303\,RT}{n\alpha_{ox}F} \qquad \text{(eq. S6.15)}$$

b remains constant with SoC for a constant $[V]_{total}$*, which is observed on all the metal and carbon electrodes*. Since the Tafel slopes on W are very different compared to other metals, we anticipate a more complex reaction mechanism on W.

Using the Nernst equation (**eq. S6.9**), i_o simplifies to **eq. S6.16**:

$$i_o = \frac{nFk_oK_1[\mathrm{V}^{2+}]}{(1+K_1[\mathrm{V}^{2+}]+K_3[\mathrm{V}^{3+}])}\left(\frac{[\mathrm{V}^{3+}]}{[\mathrm{V}^{2+}]}\right)^{\alpha_{ox}}$$
$$= \frac{nFk_oK_3[\mathrm{V}^{3+}]}{(1+K_1[\mathrm{V}^{2+}]+K_3[\mathrm{V}^{3+}])}\left(\frac{[\mathrm{V}^{3+}]}{[\mathrm{V}^{2+}]}\right)^{-(1-\alpha_{ox})} \quad \text{(eq. S6.16)}$$

Case 1: When $1 \gg (K_1[\mathrm{V}^{2+}] + K_3[\mathrm{V}^{3+}])$

$$i_o = nFk_oK_1[\mathrm{V}^{2+}]^{(1-\alpha_{ox})}[\mathrm{V}^{3+}]^{\alpha_{ox}} = nFk_oK_3[\mathrm{V}^{2+}]^{(1-\alpha_{ox})}[\mathrm{V}^{3+}]^{\alpha_{ox}}$$

Case 2: When $K_1[\mathrm{V}^{2+}] \gg (1 + K_3[\mathrm{V}^{3+}])$

$$i_o = nFk_o[\mathrm{V}^{2+}]^{-\alpha_{ox}}[\mathrm{V}^{3+}]^{\alpha_{ox}} = \frac{nFk_oK_3}{K_1}[\mathrm{V}^{2+}]^{-\alpha_{ox}}[\mathrm{V}^{3+}]^{\alpha_{ox}}$$

Case 3: When $K_3[\mathrm{V}^{3+}] \gg (1 + K_1[\mathrm{V}^{2+}])$

$$i_o = \frac{nFk_oK_1}{K_3}[\mathrm{V}^{2+}]^{(1-\alpha_{ox})}[\mathrm{V}^{3+}]^{-(1-\alpha_{ox})} = nFk_o[\mathrm{V}^{2+}]^{(1-\alpha_{ox})}[\mathrm{V}^{3+}]^{-(1-\alpha_{ox})}$$

In Case 1, both V^{2+} and V^{3+} orders are positive. This behavior is the same as observed experimentally for Ag, Cu, Bi, and W electrodes. In Case 3, the V^{2+} order is positive and V^{3+} order is negative, which is experimentally observed for Au electrode.

Using the temperature dependence of adsorption constant K_1 $\left(\propto \exp\left(-\frac{\Delta G_1}{RT}\right)\right)$ and K_3 $\left(\propto \exp\left(-\frac{\Delta G_3}{RT}\right)\right)$ and standard rate constant k_o $\left(\propto \exp\left(\frac{-E_{a,o}}{RT}\right)\right)$ in **eq. S6.16**, we obtain the trends in E_a and apparent frequency factor with SoC as shown in **Figure S6.3**. Here ΔG_1 and ΔG_3 is the free energy of Step 1 and 3 respectively and $E_{a,o}$ is the activation energy of Step 2.

c) Raw Law Assuming Adsorption of V^{2+} (Step 1) is RDS

The measured current density is described by **eq. S6.17**:

$$i = nF(k_1[\mathrm{V}^{2+}]\theta_* - k_{-1}\theta_{\mathrm{V}^{2+}}) \quad \text{(eq. S6.17)}$$

Here k_1 and k_{-1} are the forward and backward rate constants of Step 1.

Assuming Steps 2 and 3 are quasi-equilibrated and following the same process of site balance as described above, we get **eq. S6.18**:

$$i = nF\left(\frac{k_1[\mathrm{V}^{2+}] - \left(\frac{k_{-1}}{K_2}\right)K_3[\mathrm{V}^{3+}]}{1 + K_3[\mathrm{V}^{3+}] + \left(\frac{K_3}{K_2}\right)[\mathrm{V}^{3+}]}\right) \qquad \text{(eq. S6.18)}$$

Here K_2 is the equilibrium constant of Step 2 and K_3 is the adsorption constant of Step 3.

Substituting k_2 and k_{-2} in terms of η from **eq. S6.3**, **eq. S6.18** transforms to **eq. S6.19**:

$$i = nF\left(\frac{k_1[\mathrm{V}^{2+}] - k_{-1}K_3[\mathrm{V}^{3+}]e^{-\left(\frac{nF\eta}{RT}\right)}}{1 + K_3[\mathrm{V}^{3+}] + K_3[\mathrm{V}^{3+}]e^{-\left(\frac{nF\eta}{RT}\right)}}\right) \qquad \text{(eq. S6.19)}$$

Anodic Tafel slopes are obtained in terms of SoC and $[\mathrm{V}]_{\mathrm{total}}$ in **eq. S6.20**, using the same process as followed for deriving other rate laws:

$$b = \frac{d\eta}{d(\log i)}$$
$$= \frac{2.303\,RT\left(1 + K_3[\mathrm{V}]_{\mathrm{total}}(1 - \mathrm{SoC}) + K_3[\mathrm{V}]_{\mathrm{total}}(1 - \mathrm{SoC})e^{-\left(\frac{nF\eta}{RT}\right)}\right)}{nFK_3[\mathrm{V}]_{\mathrm{total}}(1 - \mathrm{SoC})\,e^{-\left(\frac{nF\eta}{RT}\right)}} \qquad \text{(eq. S6.20)}$$

b decreases with decreasing SoC for a constant $[V]_{total}$*, which is not observed experimentally on metal and carbon electrodes.*

Using the Nernst equation, i_o is reduced to **eq. S6.21**:

$$i_o = \frac{nFk_1[\mathrm{V}^{2+}]}{1 + K_3[\mathrm{V}^{3+}] + K_3[\mathrm{V}^{2+}]} = \frac{nFk_{-1}K_3[\mathrm{V}^{2+}]}{1 + K_3[\mathrm{V}^{3+}] + K_3[\mathrm{V}^{2+}]} \qquad \text{(eq. S6.21)}$$

Case 1: When $1 \gg (K_3[\mathrm{V}^{3+}] + K_3[\mathrm{V}^{2+}])$

$$i_o = nFk_1[\mathrm{V}^{2+}] = nFk_{-1}K_3[\mathrm{V}^{2+}]$$

Case 2: When $K_3[\mathrm{V}^{3+}] \gg (1 + K_3[\mathrm{V}^{2+}])$

$$i_o = \frac{nFk_1}{K_3}[\mathrm{V}^{2+}][\mathrm{V}^{3+}]^{-1} = nFk_{-1}[\mathrm{V}^{2+}][\mathrm{V}^{3+}]^{-1}$$

Case 3: When $K_3[\mathrm{V}^{2+}] \gg (1 + K_3[\mathrm{V}^{3+}])$

$$i_o = \frac{nFk_1}{K_3} = nFk_{-1}$$

In Case 2, the V^{2+} order is positive and V^{3+} order is negative, which is experimentally observed for Au electrode. However, none of the remaining cases explain positive orders of V^{2+} and V^{3+} as experimentally observed for Ag, Cu, Bi, and W electrodes.

Using the temperature dependence of rate constant k_1 $\left(\propto \exp\left(\frac{-E_{a,1}}{RT}\right)\right)$ and adsorption constant K_3 $\left(\propto \exp\left(-\frac{\Delta G_3}{RT}\right)\right)$ in **eq. S6.21**, we obtain the trends in E_a and apparent frequency factor with SoC as shown in **Figure S6.4**. Here $E_{a,1}$ is the activation energy of Step 1 and ΔG_3 is the free energy of Step 3.

6.5.3 Supporting Figures and Tables

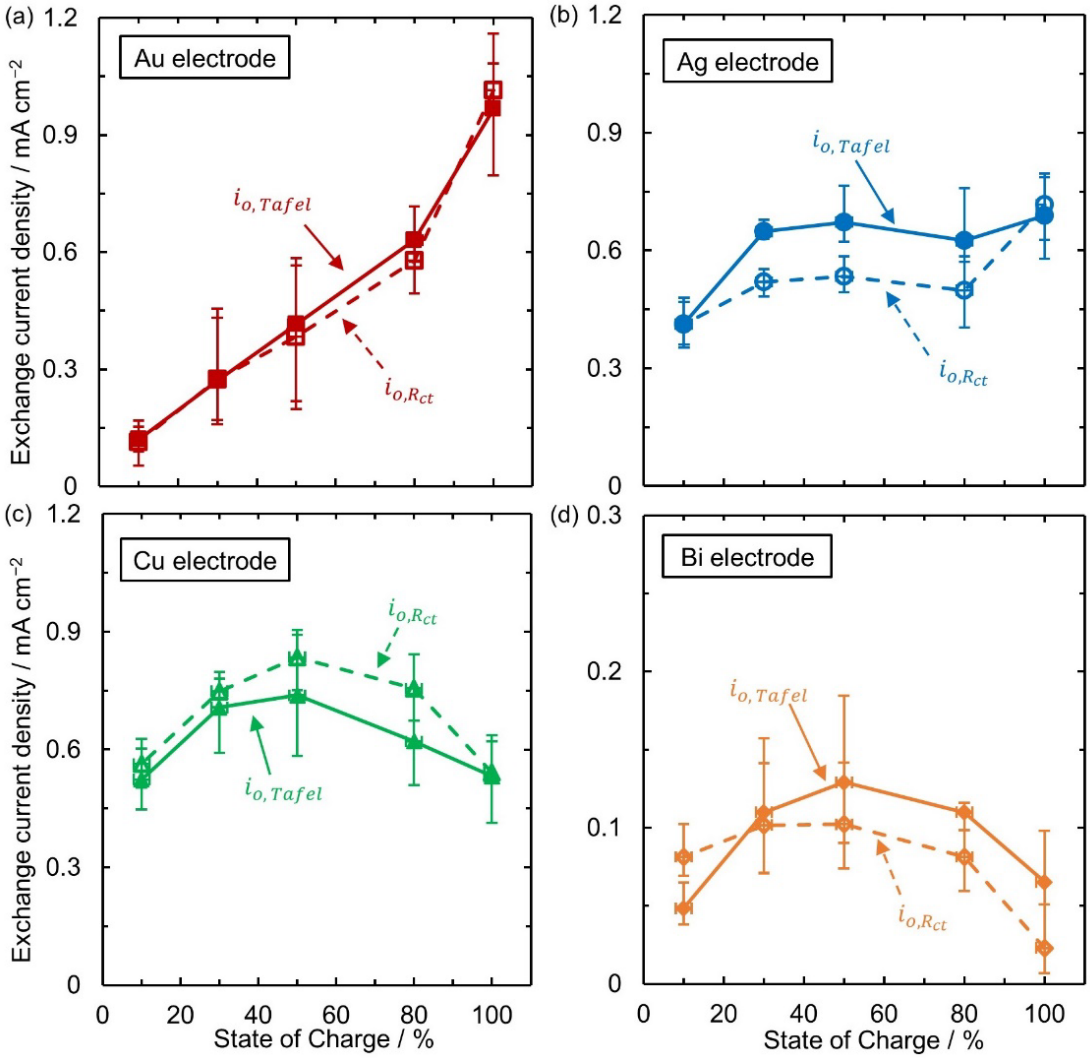

Figure S6.1. Exchange Current Density of V^{2+}/V^{3+} Reaction in H_2SO_4 for Au, Ag, Cu, and Bi Metal Electrodes by Two Independent Methods. Exchange current densities (i_o) as a function of state of charge obtained by (solid line) using the Tafel equation and (dashed line) Charge transfer resistance (R_{ct}) at open circuit voltage for **(a)** Au, **(b)** Ag, **(c)** Cu, and **(d)** Bi electrodes at room temperature. $i_{o,R_{ct}}$ is obtained by considering overall one electron transfer. The i_o and $i_{o,R_{ct}}$ agree at higher temperatures as well for all electrodes.

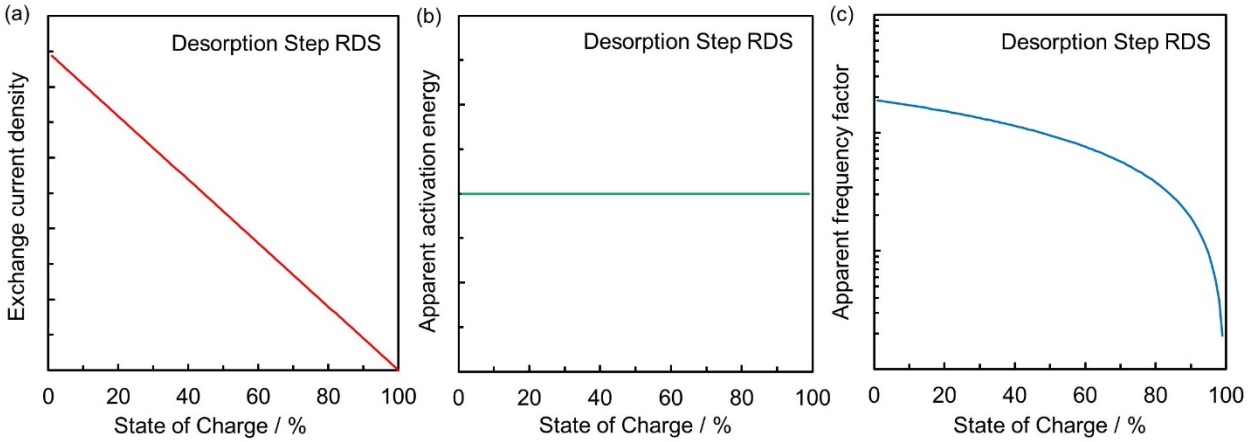

Figure S6.2. Kinetic Trends for a Reaction Mechanism with Desorption Step as RDS. Predicted trends of **(a)** i_o, **(b)** E_a, and **(c)** Apparent frequency factor with SoC considering desorption step as the rate determining step. The trends of kinetic parameters with SoC are independent of the chosen values of ΔG_1 and $E_{a,3}$. Here ΔG_1 is the free energy of Step 1 (adsorption) and $E_{a,3}$ is the activation energy of Step 3 (desorption).

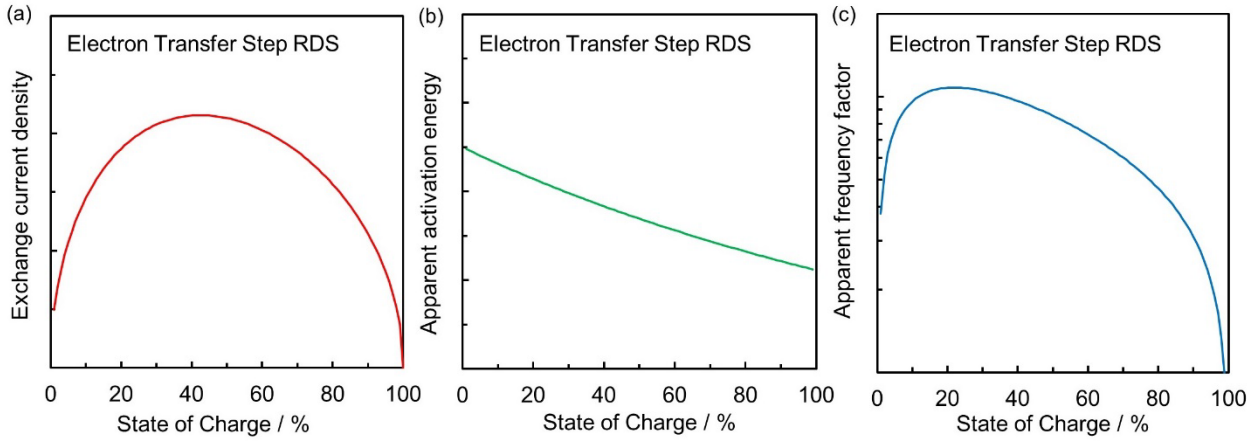

Figure S6.3. Kinetic Trends for Reaction Mechanism with Electron Transfer Step as RDS. Predicted trends of **(a)** i_o, **(b)** E_a, and **(c)** Apparent frequency factor with SoC considering electron transfer step as the rate determining step. The trends of kinetic parameters with SoC are dependent of the chosen values of ΔG_1, ΔG_3 and $E_{a,o}$. For some combinations of ΔG_1, ΔG_3 and $E_{a,o}$; i_o continuously decreases, E_a and apparent frequency factor continuously increases with increasing SoC. However, we choose these parameters such that the trends in kinetic parameters with SoC match with experiments. Here ΔG_1 and ΔG_3 is the free energy of Step 1 (adsorption) and 3 (desorption) respectively and $E_{a,o}$ is the activation energy of Step 2 (electron transfer).

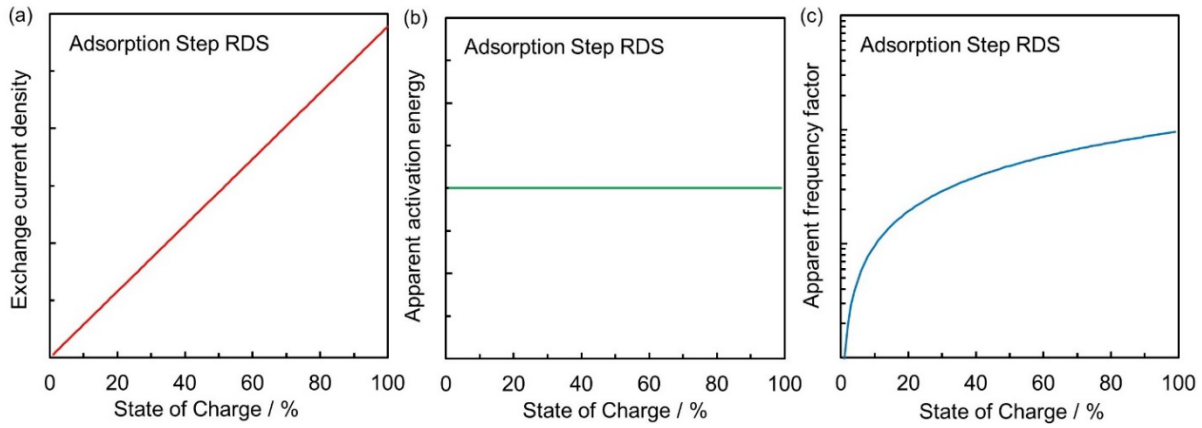

Figure S6.4. Kinetic Trends for Reaction Mechanism with Adsorption Step as RDS. Predicted trends of **(a)** i_o, **(b)** E_a, and **(c)** Apparent frequency factor with SoC considering adsorption step as the rate determining step. The trends of kinetic parameters with SoC are independent of the chosen values of ΔG_3 and $E_{a,1}$. Here $E_{a,1}$ is the activation energy of Step 1 (adsorption) and ΔG_3 is the free energy of Step 3 (desorption).

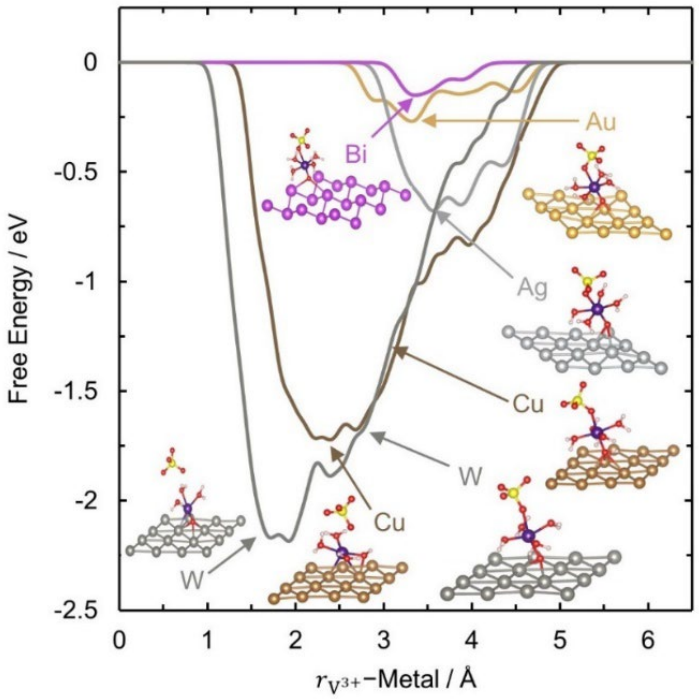

Figure S6.5. Free Energy Profiles of *[O−V(H₂O)₄SO₄] Intermediate on Au, Ag, Cu, Bi, and W Metals. Free energy profile of adsorbed vanadium intermediate on Bi (111), Au (111), Ag (111), Cu (111), and W(110) in order from top to bottom. These surface facets are chosen because they have the lowest surface energy. Snapshots of the adsorbed V^{3+} complex is shown at different points on the free energy profile, as indicated by the arrows. Atom color legend: red = O, light yellow = S, purple = V, white = H, violet = Bi, yellow = Au, light gray = Ag, brown = Cu, and dark gray = W.

Table S6.1. Reaction Orders for V^{2+}/V^{3+} Reaction in H_2SO_4 on Au, Ag, Cu, Bi, and W Metal Electrodes using Regression. Reaction orders of V^{2+} and V^{3+} on different metal electrodes obtained by fitting i_o using non-linear regression for both the Tafel and Charge Transfer Resistance methods.

Metal	$[V^{2+}]$ order (γ)		$[V^{3+}]$ order (δ)	
	i_o	$i_{o,R_{ct}}$	i_o	$i_{o,R_{ct}}$
Au	0.56 ± 0.14	0.55 ± 0.09	-0.23 ± 0.10	-0.25 ± 0.07
Ag	0.27 ± 0.10	0.18 ± 0.11	0.05 ± 0.04	0.01 ± 0.02
Cu	0.24 ± 0.22	0.28 ± 0.06	0.13 ± 0.08	0.19 ± 0.04
Bi	0.64 ± 0.06	0.39 ± 0.13	0.28 ± 0.15	0.59 ± 0.24
W	0.64 ± 0.09	R_{ct} data not fitted	0.53 ± 0.04	R_{ct} data not fitted

Table S6.2. Experimental Observed and Predicted Trends for Various Reaction Mechanisms of V^{2+}/V^{3+} Reaction. Reaction mechanisms predicting or not predicting experimentally observed reaction orders of V^{2+} and V^{3+} and trends in kinetics on metal and carbon electrodes. * denotes that the trends are satisfied on all tested electrodes except W and edge plane pyrolytic graphite (EPPG), and # denotes that trends are satisfied only on Au and glassy carbon (GC).

Condition	Rate Determining Step		
	Desorption	Electron Transfer	Adsorption
V^{2+} and V^{3+} Orders	No	Yes	Yes#
i_o with SoC	No	Yes	Yes#
b with SoC	No	Yes	No
E_a with SoC	No	Yes*	No
Apparent frequency factor with SoC	Yes*	Yes*	No

Table S6.3. Electronic Properties of Different Metal Electrodes. The facet for which the electronic property corresponds to is shown in parenthesis (if applicable). 'Poly' and 'Liq' denotes polycrystalline and liquid respectively.

Metal	Electronic Property[a]				
	d-band center[17] / eV	M–H bond strength[41] / kcal mol^{-1}	Atomic Polarizability ($\times 10^{-24}$) [45] / cm^3	Atomic Electronegativity[45]	Work Function[45] / eV
Au	−3.56 (111)	45.44 (Poly)	5.8	2.40	5.31 (111)
Pd	−1.83 (111)	60.00 (Poly)	4.8	2.20	5.22 (Poly)
Pt	−2.25 (111)	59.71 (Poly)	6.5	2.20	5.64 (Poly)
Ir	−2.11 (111)	59.70 (Poly)	7.6	2.20	5.76 (111)
Rh	−1.73 (111)	60.01 (Poly)	8.6	2.28	4.98 (111)
Ag	−4.30 (111)	38.60 (Poly)	7.2	1.93	4.74 (111)
Hg	Not Applicable	Not Available	5.7	1.90	4.48 (Liq)
Cu	−2.67 (111)	42.96 (Poly)	6.1	1.90	4.94 (111)
Bi	Not Applicable	36.17 (Poly)	7.4	1.90	4.34 (Poly)
W	0.77 (110)	73.98 (Poly)	11.1	1.70	4.55 (Poly)

[a] The conversion factor of 1 eV = 96.48 kJ mol^{-1} is used to convert *d*-band center and work function to units of kJ mol^{-1} for all metals. Similarly, 1 kcal = 4.184 kJ is used for converting all M–H bond strength to units of kJ mol^{-1}.

6.6 References

(1) Ribas Gispert, J. *Coordination Chemistry*, 1st ed.; Wiley-VCH: Weinheim, Germany, 2008.
(2) Florian, J.; Agarwal, H.; Singh, N.; Goldsmith, B. R. Why Halides Enhance Heterogeneous Metal Ion Charge Transfer Reactions. *Chem. Sci.* **2021**, *12*, 12704–12710.
(3) Agarwal, H.; Florian, J.; Goldsmith, B. R.; Singh, N. The Effect of Anion Bridging on Heterogeneous Charge Transfer for V^{2+}/V^{3+}. *Cell Reports Phys. Sci.* **2021**, *2* (1), 100307.
(4) Kuhn, A. T.; Randle, T. H. Effect of Oxide Thickness on the Rates of Some Redox Reactions on a Platinum Electrode. *J. Chem. Soc., Faraday Trans. I* **1985**, *81*, 403–419.
(5) Tanimoto, S.; Ichimura, A. Discrimination of Inner and Outer Sphere Electrode Reactions by Cyclic Voltammetry Experiments. *J. Chem. Educ.* **2013**, *90* (6), 778–781.
(6) Iwasita, T.; Schmickler, W.; Schultze, J. W. The Influence of the Metal on the Kinetics of Outer Sphere Redox Reactions. *Ber. Bunsenges. Phys. Chem.* **1985**, *89* (2), 138–142.
(7) Velmurugan, J.; Sun, P.; Mirkin, M. V. Scanning Electrochemical Microscopy with Gold Nanotips: The Effect of Electrode Material on Electron Transfer Rates. *J. Phys. Chem. C* **2009**, *113*, 459–464.
(8) Barr, S. W.; Guyer, K. L.; Weaver, M. J. The Dependence of the Kinetics of Some Simple Outer-Sphere Electrode Reactions on the Nature of the Electrode Material. *J. Electroanal. Chem.* **1980**, *111*, 41–59.
(9) Barr, S. W.; Weaver, M. J. Intramolecular Electron Transfer at Metal Surfaces. 1. Relative Energetics of Some Corresponding Outer-and Inner-Sphere Pathways Involving Halide and Pseudohalide Bridging Ligands. *Inorg. Chem* **1984**, *23*, 1657–1663.
(10) Bockris, J. O.; Mannan, R. J.; Damjanovic, A. Dependence of Rate of Electrodic Redox Reactions on the Substrate. *J. Chem. Phys.* **1968**, *48*, 1898–1904.
(11) Bochmann, H. G.; Vielstich, W. On the Reaction Rate of the Fe^{2+}/Fe^{3+} Redox Couple in Sulfate Solution. *Electrochim. Acta* **1988**, *33* (6), 805–809.
(12) Galizzioli, D.; Trasatti, S. Work Function, Electronegativity, and Electrochemical Behaviour of Metals IV. Simple Electron Exchange Reactions. Fe^{2+}/Fe^{3+} Redox Couple. *J. Electroanal. Chem. Interfacial Electrochem.* **1973**, *44*, 367–388.
(13) Trasatti, S. Work Function, Electronegativity, and Electrochemical Behaviour of Metals: II. Potentials of Zero Charge and "Electrochemical" Work Functions. *J. Electroanal. Chem. Interfacial Electrochem.* **1971**, *33* (2), 351–378.
(14) Weber, J.; Samec, Z.; Mareček, V. The Effect of Anion Adsorption on the Kinetics of the Fe3+/Fe2+ Reaction on Pt and Au Electrodes in $HClO_4$. *J. Electroanal. Chem. Interfacial Electrochem.* **1978**, *89* (2), 271–288.
(15) Nørskov, J. K.; Studt, F.; Abild-Pedersen, F.; Bligaard, T. *Fundamental Concepts in Heterogeneous Catalysis*; John Wiley & Sons, Inc.: New Jersey, 2014.
(16) Bligaard, T.; Nørskov, J. K.; Dahl, S.; Matthiesen, J.; Christensen, C. H.; Sehested, J. The Brønsted-Evans-Polanyi Relation and the Volcano Curve in Heterogeneous Catalysis. *J. Catal.* **2004**, *224*, 206–217.
(17) Hammer, B.; Nørskov, J. K. Theoretical Surface Science and Catalysis—Calculations and Concepts. *Adv. Catal.* **1972**, *45*, 71–129.
(18) Leonard, K. C.; Bard, A. J. Pattern Recognition Correlating Materials Properties of the Elements to Their Kinetics for the Hydrogen Evolution Reaction. *J. Am. Chem. Soc* **2013**, *135*, 15885–15889.
(19) Greeley, J.; Nørskov, J. K.; Kibler, L. A.; El-Aziz, A. M.; Kolb, D. M. Hydrogen Evolution

Over Bimetallic Systems: Understanding the Trends. *ChemPhysChem* **2006**, *7*, 1032–1035.
(20) Lima, F. H. B.; Zhang, J.; Shao, M. H.; Sasaki, K.; Vukmirovic, M. B.; Ticianelli, E. A.; Adzic, R. R. Catalytic Activity-*d*-Band Center Correlation for the O_2 Reduction Reaction on Platinum in Alkaline Solutions. *J. Phys. Chem. C* **2007**, *111*, 404–410.
(21) Liu, Y.; Liang, F.; Zhao, Y.; Yu, L.; Liu, L.; Xi, J. Broad Temperature Adaptability of Vanadium Redox Flow Battery–Part 4: Unraveling Wide Temperature Promotion Mechanism of Bismuth for V^{2+}/V^{3+} Couple. *J. Energy Chem.* **2018**, *27* (5), 1333–1340.
(22) Liu, T.; Li, X.; Nie, H.; Xu, C.; Zhang, H. Investigation on the Effect of Catalyst on the Electrochemical Performance of Carbon Felt and Graphite Felt for Vanadium Flow Batteries. *J. Power Sources* **2015**, *286*, 73–81.
(23) Lv, Y.; Zhang, J.; Lv, Z.; Wu, C.; Liu, Y.; Wang, H.; Lu, S.; Xiang, Y. Enhanced Electrochemical Activity of Carbon Felt for V^{2+}/V^{3+} Redox Reaction via Combining KOH-Etched Pretreatment with Uniform Deposition of Bi Nanoparticles. *Electrochim. Acta* **2017**, *253*, 78–84.
(24) Yang, X.; Liu, T.; Xu, C.; Zhang, H.; Li, X.; Zhang, H. The Catalytic Effect of Bismuth for VO_2^+/VO^{2+} and V^{3+}/V^{2+} Redox Couples in Vanadium Flow Batteries. *J. Energy Chem.* **2017**, *26* (1), 1–7.
(25) Li, B.; Gu, M.; Nie, Z.; Shao, Y.; Luo, Q.; Wei, X.; Li, X.; Xiao, J.; Wang, C.; Sprenkle, V.; et al. Bismuth Nanoparticle Decorating Graphite Felt as a High-Performance Electrode for an All-Vanadium Redox Flow Battery. *Nano Lett.* **2013**, *13* (3), 1330–1335.
(26) Zhang, Q.; Liu, T.; Zhang, H.; Li, X. Highly Active Ag Nanoparticle Electrocatalysts toward V^{2+}/V^{3+} Redox Reaction. *ACS Appl. Energy Mater.* **2021**, *4*, 3913–3920.
(27) Shen, J.; Liu, S.; He, Z.; Shi, L. Influence of Antimony Ions in Negative Electrolyte on the Electrochemical Performance of Vanadium Redox Flow Batteries. *Electrochim. Acta* **2015**, *151*, 297–305.
(28) Kim, M.; Yoo, H.; Lee, G.; Choi, J. Enhanced VRB Electrochemical Performance Using Tungsten as an Electrolyte Additive. *Electrochim. Acta* **2017**, *246*, 190–196.
(29) Wei, L.; Zhao, T. S.; Zeng, L.; Zhou, X. L.; Zeng, Y. K. Copper Nanoparticle-Deposited Graphite Felt Electrodes for All Vanadium Redox Flow Batteries. *Appl. Energy* **2016**, *180*, 386–391.
(30) Mehboob, S.; Mehmood, A.; Lee, J.-Y.; Shin, H.-J.; Hwang, J.; Abbas, S.; Ha, H. Y. Excellent Electrocatalytic Effects of Tin Through In Situ Electrodeposition on the Performance of All-Vanadium Redox Flow Batteries. *J. Mater. Chem. A* **2017**, *5*, 17388–17400.
(31) Gaha, R. F.; Hagdorn, N. H. Negative Electrode Catalyst for the Iron Chromium Redox Energy Storage System, 1985.
(32) Wu, C. D.; Scherson, D. A.; Calvo, E. J.; Yeager, E. B.; Reid, M. A. A Bismuth-Based Electrocatalyst for the Chromous-Chromic Couple in Acid Electrolytes. *J. Electrochem. Soc.* **1986**, *133* (10), 2109–2112.
(33) Arenas, L. F.; Loh, A.; Trudgeon, D. P.; Li, X.; Ponce de León, C.; Walsh, F. C. The Characteristics and Performance of Hybrid Redox Flow Batteries with Zinc Negative Electrodes for Energy Storage. *Renew. Sustain. Energy Rev.* **2018**, *90*, 992–1016.
(34) Agarwal, H.; Florian, J.; R. Goldsmith, B.; Singh, N. V^{2+}/V^{3+} Redox Kinetics on Glassy Carbon in Acidic Electrolytes for Vanadium Redox Flow Batteries. *ACS Energy Lett.* **2019**, *4*, 2368–2377.
(35) Park, I. T.; Kim, W.; Kim, E. J.; Bae, S. E.; Kim, J. Y.; Shin, H. C. Electrochemical

Reactivity of Chemically Roughened Tungsten Electrodes. *Asian J. Chem.* **2013**, *25* (12), 7037–7040.
(36) Bard, A. J.; Faulkner, L. R. *Electrochemical Methods: Fundamentals and Applications*; John Wiley & Sons, Inc.: New York, 2001.
(37) Makrides, A. C. Kinetics of Redox Reactions on Passive Electrodes. *J. Electrochem. Soc.* **1964**, *111* (3), 392–400.
(38) Agarwal, H. P.; Qureshi, S. Faradaic Rectification Studies of the Ferrous-Ferric Redox Couple in the Acid Media. *Electrochim. Acta* **1974**, *19* (10), 607–610.
(39) Hamelin, A.; Weaver, M. J. Metal Substrate Effects upon the Kinetics of Simple Electrochemical Reactions: The Reduction of Cobalt(III) Ammines at Single-Crystal Gold Faces. *J. Electroanal. Chem. Interfacial Electrochem.* **1986**, *209* (1), 109–124.
(40) Sawant, T. V; Mckone, J. R. Flow Battery Electroanalysis: Hydrodynamic Voltammetry of Aqueous Fe(III/II) Redox Couples at Polycrystalline Pt and Au. *ACS Appl. Energy Mater.* **2018**, *1*, 4743–4753.
(41) Trasatti, S. Work Function, Electronegativity, and Electrochemical Behavior of Metals III. Electrolytic Hydrogen Evolution in Acid Solutions. *J. Electroanal. Chem. Interfacial Electrochem.* **1972**, *39* (1), 163–184.
(42) Holze, R. Table 5.1. Exchange Current Densities and Rate Constants in Aqueous Systems. In *Electrochemistry·Electrochemical Thermodynamics and Kinetics*; Lechner, M. D., Ed.; Springer, 2007; pp 276–378.
(43) Scott, S. L. The Burden of Disproof. *ACS Catal.* **2019**, *9*, 4706–4708.
(44) Disk Insert Mechanical Drawing, Pine Instrument Company https://pineresearch.com/shop/products/electrodes/disk-inserts/elemental/#documentation (accessed Feb 7, 2022).
(45) Lide, D. R. *CRC Handbook of Chemistry and Physics*, 84th ed.; Lide, D. R., Ed.; CRC Press, 2003.

Chapter 7 : Conclusions, Future Directions, and Outlook

7.1 Summary and Conclusions

Redox flow batteries (RFBs) are one of the most promising technologies for grid scale long duration energy storage due to their high electrode lifetimes and scalability. Even though the origin of inorganic RFBs that store/release energy based on charge transfer (CT) of transition metal ions dates to the early 1970s, there is still a lack of fundamental understanding of how these CT reactions occur at electrode surfaces. As discussed in **Chapter 1**, the slow CT kinetics of transition metal ions at electrode surface introduces voltage losses that reduce the overall efficiency of RFBs, increasing their costs.

The overall goal of this dissertation was to understand CT mechanism of transition metal ions used in RFBs and identify electrode and electrolyte properties that can be tailored to design materials with improved CT kinetics for the development of low-cost RFBs. I used V^{2+}/V^{3+} as the probe redox couple in this dissertation to understand CT mechanism of transition metal ions due to widespread importance of V^{2+}/V^{3+} at the negative half in most commercialized vanadium RFBs (VRFBs) and demonstrated that the findings for V^{2+}/V^{3+} also rationalize kinetic trends of several transition metal ion redox couples used in RFBs. By identifying the structure of ions in solution, isolating the effect of anions and electrodes on CT kinetics, microkinetic modeling, and adsorption energy calculations of proposed intermediates, I showed that the desorption barrier of the metal ion intermediate (*[bridge−M], with generally anions as the bridge for CT) explains the influence

of anions on CT kinetics and the *d*-band center of the electrode correlates with CT kinetics of transition metal ions on different electrodes.

In **Chapters 3** and **4**, I isolated the effect of anions on V^{2+}/V^{3+} reaction kinetics on a glassy carbon (GC) electrode to show that the anion-induced kinetic enhancement arises due to decrease in activation energy because of changes in the energy of the adsorbed vanadium intermediate (*[bridge–V^{3+}]), as depicted in **Scheme 7.1**. I conducted V^{2+}/V^{3+} kinetic studies in $HClO_4$, H_2SO_4, HCl, mixed HCl/H_2SO_4, HBr, and HI to show that V^{2+}/V^{3+} is an inner sphere reaction. Using UV-vis spectroscopy, extended x-ray absorption spectroscopy, and density functional theory (DFT) evaluated ligand exchange energies, I identified that V^{2+} exists as $[V(H_2O)_6]^{2+}$ in all electrolytes, while V^{3+} complexes with anions and exists as a mixture of $[V(H_2O)_6]^{3+}$ and $[V(H_2O)_5SO_4]^{+}$ in H_2SO_4 and mixed HCl/H_2SO_4, and a mixture of $[V(H_2O)_6]^{3+}$, $[V(H_2O)_5X]^{2+}$, and $[V(H_2O)_4X_2]^{+}$ (X = Cl, Br, and I) in HCl, HBr, and HI. By evaluating the coverage of anions using DFT, I confirmed that the changes in coverage are not responsible for anion-induced kinetic enhancement.

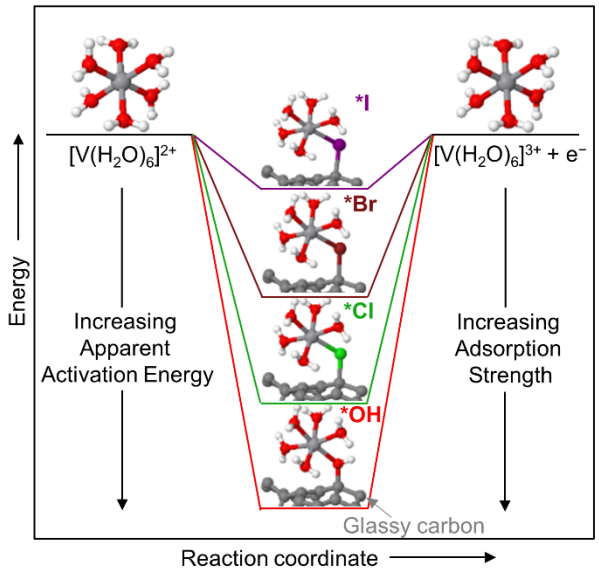

Scheme 7.1. Effect of Anions on the Reaction Energy Profile of V^{2+}/V^{3+} on Glassy Carbon. Both $[V(H_2O)_6]^{2+}$ (reactant) and $[V(H_2O)6]^{3+}$ (product) have the same energy at equilibrium. During the charge transfer reaction, adsorbed vanadium intermediate (*[bridge–V^{3+}], bridge = OH, Cl, Br, and I) is formed. The adsorption strength of the *[bridge–V^{3+}] intermediate correlates with activation energy of V^{2+}/V^{3+} reaction explaining the influence of anions on charge transfer kinetics. Atom color legend: light gray = vanadium, red = oxygen, white = hydrogen, green = chloride, brown = bromide, purple = iodide, and dark gray = glassy carbon.

In **Chapter 5**, I showed that the desorption barrier of the metal ion intermediate (*[bridge−M]) correlates with kinetic trends in the presence of halides for multitude of metal ion redox couples. The desorption barrier is linearly related with the adsorption energy of the *[bridge−M] intermediate (which is identified to be important in **Chapters 3** and **4**) by Brønsted-Evans-Polanyi relationships and can be calculated using metadynamics. I conducted V^{2+}/V^{3+} kinetic measurements on edge plane pyrolytic graphite (EPPG) in various electrolytes and calculated desorption barriers of *[bridge−V^{3+}] intermediate on graphite($11\bar{2}0$) that is structurally similar to EPPG, to show that the V^{2+}/V^{3+} kinetics correlates with the desorption barrier. The V^{2+}/V^{3+} kinetics on EPPG is maximum when the desorption barrier of the *[bridge−V^{3+}] intermediate is between that of *[I−V^{3+}] and *[OH−V^{3+}], as depicted in **Scheme 7.2**. I also demonstrate that the kinetics of V^{2+}/V^{3+}, Cr^{2+}/Cr^{3+}, and Cd^{0}/Cd^{2+} on Hg and Fe^{2+}/Fe^{3+} on Au in various electrolytes also correlates with desorption barrier of corresponding *[bridge−M] intermediates.

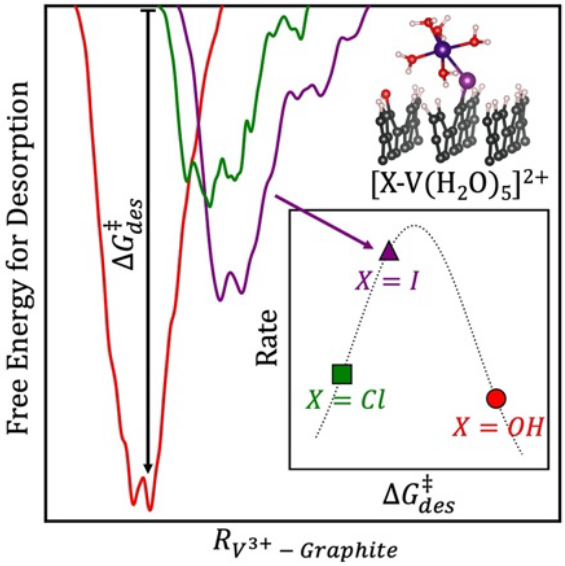

Scheme 7.2. Influence of Desorption Barriers on V^{2+}/V^{3+} Reaction Kinetics on Edge Plane Pyrolytic Graphite. Free energy vs the distance between the V^{3+} ion and the carbon surface for V^{3+}-anion complexes adsorbed to graphite($11\bar{2}0$) through an *OH (red), *Cl (green), and *I (purple) bridge. The free energy minimum in the energy profile is the desorption barrier and denoted by $\Delta G^{\ddagger}_{des}$. A sample geometry of adsorbed V^{3+}-anion complex at the free energy minimum is shown in the inset. The variation of V^{2+}/V^{3+} rate in different electrolytes on edge plane pyrolytic graphite with $\Delta G^{\ddagger}_{des}$ of V^{3+}-anion complexes adsorbed through different bridges is also shown in the inset. Atom color legend: C = gray, V = violet, O = red, H = white, Cl = green, Br = dark brown, I = purple.

In **Chapter 6**, I showed that the CT kinetics of transition metal ions at electrodes are dependent on the electronic structure of the electrode. The *d*-band electronic structure of the electrode dictates the occupancy of antibonding orbitals of the adsorbate ligand of metal ion intermediate, which in turn controls the adsorption strength of the intermediate at the electrode as depicted in **Scheme 7.3**. Resultantly, the CT kinetics correlates with the *d*-band center of the electrode. I conducted V^{2+}/V^{3+} kinetic measurements on five metal electrodes (Au, Ag, Cu, Bi, and W) and extracted the kinetic data of several Cr, Fe, and Co-based complexes undergoing CT on metal electrodes from literature to show that the *d*-band center of the electrode linearly correlates with the CT kinetics as shown in **Scheme 7.3**. The use of *d*-band center as a descriptor for CT reactions of transition metal ions at electrodes is analogous to the *d*-electron configuration of transition metal ions controlling CT kinetics in solution phase.

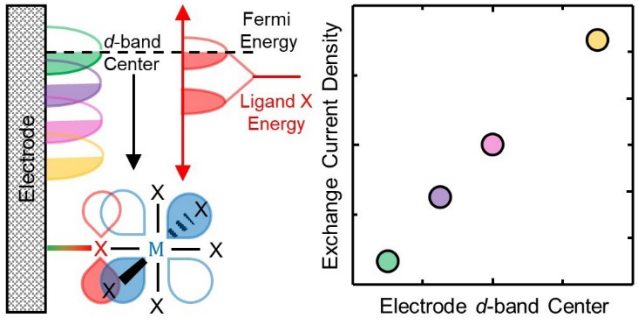

Scheme 7.3. Effect of the Electronic Structure of Electrode on Heterogeneous Charge Transfer Kinetics of Transition Metal Ions. During the charge transfer process, metal ion intermediate (*[X−MX_5]) is formed on the surface of the electrode. Resultantly, the *p* orbitals of ligand X (denoted by red) are split into bonding and antibonding states. The adsorption strength of the *[X−MX_5] depends on the occupancy of the antibonding states of X. The schematic on the left shows that the occupancy of the antibonding states of X is dictated by the *d*-band center of the electrode. With increase in the *d*-band center of the electrode (green lowest, then purple, pink, and yellow highest), more antibonding states are occupied due to which the *[X−MX_5] intermediate adsorbs weakly. The direct consequence of decreasing adsorption strength of *[X−MX_5] intermediate is either increase in the exchange current density as show by schematic on the right or vice versa. The *d* orbitals of M are shown by blue and the density of states of different electrodes are shown by green, purple, pink, and yellow.

The identification of the desorption barrier of metal ion intermediate to explain the influence of anions and *d*-band center of the electrode to rationalize the influence of electrode on CT kinetics of transition metal ions in this dissertation opens a wide avenue of electrolyte and electrode

engineering for RFBs. Carefully chosen additives that alter the coordination structure of transition metal ions or alloying and nano structuring to modify the electrodes' *d*-band center such that adsorption strength of the metal ion intermediate is optimized can lead to development of more efficient RFBs that have lower cost due to faster CT kinetics. Since CT reactions of transition metal ions at electrodes are also critical in many natural phenomena and applications, including photosynthesis,[1,2] biological systems,[3–5] electrodeposition,[6–8] corrosion,[9–11] and chemical sensors,[3,12] I expect that the findings of this dissertation can also help in making these processes more efficient.

7.2 Limitations of the Work and Future Directions

This dissertation has made significant contributions in the field of understanding CT of transition metal ions at electrodes. Even though the work provided new insights and identified relevant electrolyte and electrode properties that can be tuned to enhance CT kinetics of transition metal ions at electrodes, there are a few limitations of the work that are highlighted below and form the basis of future work. Pursuing work in the proposed directions will allow the findings of this dissertation to be more broadly accepted by the scientific community and test if these findings can provide mechanistic insights of more complicated reactions.

7.2.1 Experimental Evidence of Adsorbed Metal Ion Intermediate

The adsorbed metal ion intermediate (*[bridge−M]) that is hypothesized to form during CT reactions of transition metal ions is based on the structure of transition metal ions in solution, possible mechanism of CT through anion bridging proposed in literature, and favorable free energy of relevant adsorbed intermediates calculated using computational modeling. However, there is no spectroscopic evidence that *[bridge−M] is formed under reaction conditions at the electrode

surface. Since the adsorbed intermediates are generally formed in low concentrations for short time scales during the reaction, the detection of these intermediates is extremely challenging.

Surface enhanced Raman spectroscopy (SERS), a label-free analytical technique with single-molecule detection sensitivity,[13–15] can be used to obtain used to obtain rich vibrational molecular information of the adsorbed intermediate formed in CT reactions. The enhanced sensitivity of SERS stems from the fact that when an appropriately nanostructured material (such as gold, silver, or copper) that can sustain high-quality localized surface plasmon resonances is illuminated with light of an appropriate wavelength, the optical fields re-radiated by the nanostructure and the incident field can coherently superimpose, to create regions of concentrated electromagnetic energy (hot spots) where the field amplitude can be enhanced by factors of tens or even hundreds.[13–16] In recent years, *in situ* SERS has been used to interrogate adsorbate molecule reactants, intermediates, products, and thereby follow reaction dynamics at electrocatalyst surfaces for several reactions like oxygen and carbon dioxide reduction.[17–19]

In situ SERS can be used to confirm the formation of *[bridge−V^{3+}] intermediate during V^{2+}/V^{3+} reaction. Anions that serve as bridges adsorb on the surface of Au and can be detected using SERS, with Au−OH stretch at 580 cm^{-1}, Au−Cl stretch at 260 cm^{-1}, and Au−Br stretch at 180 cm^{-1}.[20–22] If the *[bridge−V^{3+}] intermediate is formed under reaction conditions, on addition of V^{3+} ions in different acidic electrolytes, the Au−anion stretch will no longer be the same (Au−anion−V stretch) and will shift from its original location due to the interaction with vanadium ions. Since the adsorbed *[bridge−V^{3+}] intermediate will also have other vibrations associated with surrounding ligands, preliminary work to understand the structure of vanadium ions in different acidic electrolytes from Raman is required for correct assignment of vibrations.

7.2.2 Extension of Findings to Carbon Felt Electrodes

The V^{2+}/V^{3+} kinetic studies in different electrolytes discussed in **Chapter 3−5** are conducted on GC and EPPG. Both GC and EPPG are structurally very different from carbon felts that are commercially used as electrodes in RFBs. Conducting V^{2+}/V^{3+} kinetic studies on carbon felts and showing the findings in this dissertation can explain kinetic trends on carbon felts in the presence of anions will allow the work to be widely accepted with a potential of direct implementation in RFBs.

Carbon felts are very porous with high surface area, which introduces additional challenges to quantify reaction kinetics due to mass transfer limitations. Recently, a new strategy to measure reaction kinetics on porous electrodes has been proposed, which involves the pores of carbon felts to be filled with epoxy. The cross-section of this composite is a planar electrode with kinetics representative of what happens inside the porous electrode.[23] These planar electrodes prepared from carbon felts can be attached to rotating disk electrode assembly for measuring reaction kinetics.

7.2.3 Similarity in Charge Transfer Mechanism of Transition Metal Ion and Organic Redox Couples

Several electrode treatments have been shown to improve the CT kinetics of organic redox couples used in aqueous organic RFBs. Thermal treatment,[24–37] acid/base treatment,[31,32,37–41] plasma treatment,[42,43] electrochemical oxidation treatment,[44] doping with elements,[31,32,45,46] carbon-based electrocatalysts,[47–52] and metals and metal oxides[53–56] are shown to improve CT in aqueous organic RFBs and are the same treatments shown to improve CT for VRFBs as discussed in **Chapter 1**. The improvement in performance of aqueous organic RFBs by similar treatments

as VRFBs on carbon electrodes can arise due to a similarity in the CT mechanism of organic and vanadium redox couples.

The proposed CT mechanism for organic redox couples used in aqueous organic RFBs is the same as that of transition metal ion redox couples used for RFBs including V^{2+}/V^{3+}. Quinones, which form the most popular class of organic molecules used in aqueous organic RFBs, undergo CT as shown in **Scheme 7.4**. The quinone molecule approaches and interacts with the functional groups introduced by treatments on the electrodes' surface. The quinone molecule then gets adsorbed on the surface forming a quinone bridged intermediate. The adsorbed intermediate undergoes CT followed by desorption, leading to regeneration of the electrode surface.[32] These steps are repeated until a stable reduced/oxidized organic molecule is formed after several charge transfers. This mechanism of CT in quinones is similar to other transition metal ion redox couples discussed in **Chapter 3-5** where the functional groups introduced by electrode treatments or anions adsorbed on electrode act as active sites for forming a metal ion bridged intermediate during CT.

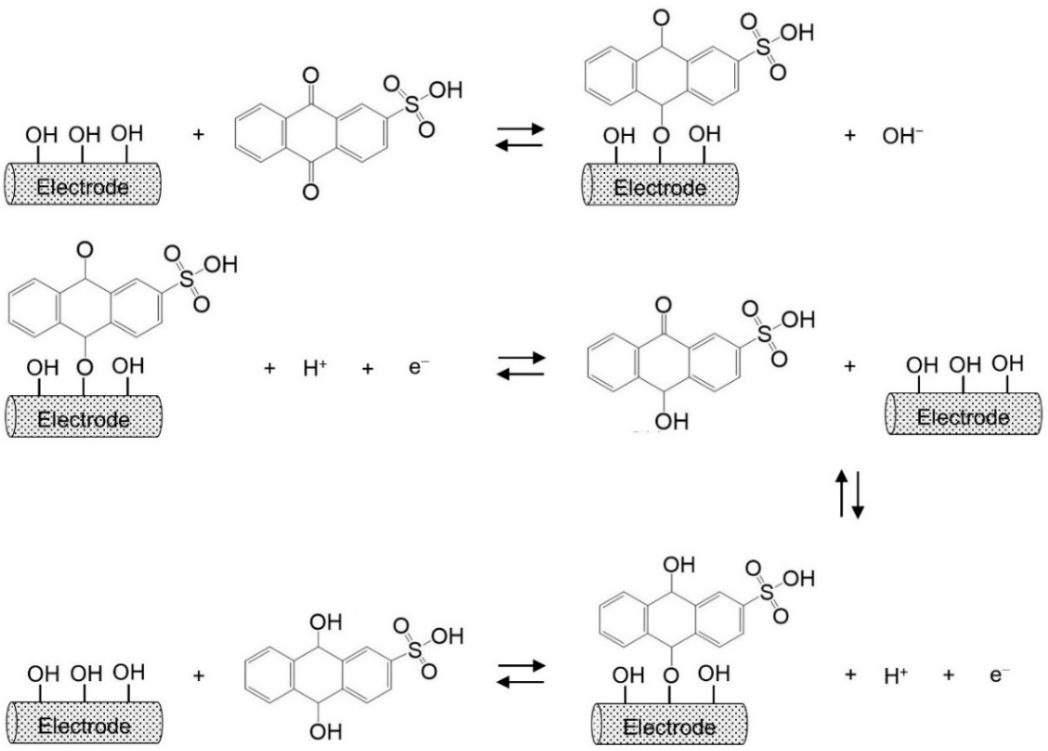

Scheme 7.4. Proposed Charge Transfer Mechanism in Quinones Used in Aqueous Organic Redox Flow Batteries. The treatment of the electrode introduces hydroxyls (*OH) on the surface which act as bridges for charge transfer. The quinone molecule approaches the electrode surface and adsorbs to form a quinone bridged intermediate, which undergoes charge transfer(s) to store or release energy. Finally, the quinone molecule desorbs from the surface. The scheme is adapted from reference 32.

Due to the similarity in CT mechanism of organic molecules and transition metal ion redox couples and based on the findings of this dissertation, there is a possibility that the energy of a similar organic bridged intermediate can be tailored to control the CT kinetics and the stability of organic molecules. If true, this would allow us to understand the CT mechanism and control the degradation of organic molecules that often limit the performance of aqueous organic RFBs. It is possible that the mechanism might change or become more complex depending on the nature of the quinone derivatives and for other classes of the aqueous organic molecules due to their different orientations on the electrode surface, steric hindrance, stability, and degradation products. Hence, fundamental work that captures the effect of specific functional groups and molecular structure on the CT in organic molecules is needed to validate if the mechanisms are indeed similar and the findings of this dissertation can be extended to organic molecules.

7.3 Outlook

As the RFB community moves forward with the continued exploration of old and identification of new chemistries, a more structured approach with standardization of testing procedures for measuring CT kinetics and RFB performance is needed to be adapted by researchers around the globe, so that the findings are transferable and can be put to immediate use. In this dissertation, I evaluated the kinetic parameters of V^{2+}/V^{3+} reaction for 15 electrode-electrolyte combinations over the course of five years. Even though a lot of electrolyte and electrode treatments are shown to improve CT kinetics of vanadium redox couples (as discussed in **Chapter 1**), the reported kinetic data could not be utilized due to widely varying experimental conditions and techniques. I had to be very watchful while extracting the kinetic data of other metal ion redox couples from literature, as discussed in **Chapters 5** and **6**, due to huge lab-to-lab variations in reported kinetic parameters. All these kinetic studies combined allowed me to identify two key properties of the electrolyte and the electrode that can be tuned to control CT of transition metal ions. However, this process could have been accelerated significantly if there was a standardized protocol adapted by researchers worldwide for testing CT kinetics of redox couples and RFBs performance. The availability of a large database of kinetic and performance data collected under same conditions can allow the use of machine learning models to identify patterns and insights onto the important properties that can guide future experiments.

I recommend the use of steady state measurements and electrochemical impedance spectroscopy (EIS) instead of cyclic voltammetry (CV), wherever possible, to estimate kinetic parameters of redox couples since the instantaneous currents obtained in CVs are shown to yield erroneous kinetic parameters.[57] CVs can however serve as a good tool for looking at qualitative kinetic trends if done under same conditions. I propose CVs to be conducted at a fixed scan rate

of 100 mV s^{-1} since 100 mV s^{-1} is most widely used scan rate in VRFB literature and EIS should be conducted at open circuit voltage (OCV) since charge transfer resistance at OCV only represents CT kinetics.[58]

I recommend the RFB performance at a fixed current density with minimum number of cycles to be reported in all academic publications. This (current density, cycle) combination must be considered as a universal for testing performance across different redox couples, so that the performance of various chemistries with same electrolytes and electrode treatments can be compared. From the widespread studies of VRFBs in literature, current density of 100 mA cm^{-2} with at least 100 cycles can be used a benchmark for comparisons. Additionally, carbon felts used as electrodes differ in performance when purchased from different vendors, partly due to the differences in synthesizing process which alters physical properties of carbon felts. The physical properties of carbon felts like porosity, conductivity, thickness, and wetness should be clearly reported, so that their effects on performance are accounted for wherever possible. Solid-state batteries and solar photovoltaics are a step ahead from RFBs in the topic of standardization, with several leading academic journals requiring the researchers to report performance metrics under specific conditions with complete experimental details.[59,60] A recent article was published where established researchers across the globe recommended experimental protocols in organic-based RFBs,[61] however standardized conditions for measuring CT kinetics and testing RFBs performance is yet to be proposed.

7.4 References

(1) Yruela, I. Transition Metals in Plant Photosynthesis. *Metallomics* **2013**, *5*, 1109.
(2) Kärkäs, M. D.; Johnston, E. V.; Verho, O.; Akermark, B. Artificial Photosynthesis: From Nanosecond Electron Transfer to Catalytic Water Oxidation. *Acc. Chem. Res.* **2014**, *47* (1), 100–111.
(3) Iovan, D. A.; Jia, S.; Chang, C. J. Inorganic Chemistry Approaches to Activity-Based Sensing: From Metal Sensors to Bioorthogonal Metal Chemistry. *Inorg. Chem* **2019**, *58*,

13546–13560.
(4) Alday, J.; Mazzeo, A.; Suarez, S. Selective Detection of Gasotransmitters Using Fluorescent Probes Based on Transition Metal Complexes. *Inorganica Chim. Acta* **2020**, *510*, 119696.
(5) Paul, B. T.; Manz, D. H.; Torti, F. M.; Torti, S. V. Mitochondria and Iron: Current Questions. *Expert Rev. Hematol.* **2017**, *10* (1), 65–79.
(6) Bhat, M. A.; Nioradze, N.; Kim, J.; Amemiya, S.; Bard, A. J. In Situ Detection of the Adsorbed Fe(II) Intermediate and the Mechanism of Magnetite Electrodeposition by Scanning Electrochemical Microscopy. *J. Am. Chem. Soc.* **2017**, *139*, 15891–15899.
(7) Gimenez-Romero, D.; Juan García-Jareño, J.; Agrisuelas, J.; Gabrielli, C.; Perrot, H.; Vicente, F. Formation of a Copper Oxide Layer as a Key Step in the Metallic Copper Deposition Mechanism. *J. Phys. Chem. C* **2008**, *112*, 4275–4280.
(8) Morales-Guio, C. G.; Liardet, L.; Hu, X. Oxidatively Electrodeposited Thin-Film Transition Metal (Oxy)Hydroxides as Oxygen Evolution Catalysts. *J. Am. Chem. Soc.* **2016**, *138*, 8946–8957.
(9) Newman, R. C.; Sieradzki, K. Metallic Corrosion. *Science.* **1994**, *263* (5154), 1708–1709.
(10) Jeon, B.; Sankaranarayanan, S. K. R. S.; van Duin, A. C. T.; Ramanathan, S. Atomistic Insights into Aqueous Corrosion of Copper. *J. Chem. Phys.* **2011**, *134*, 234706.
(11) Frankel, G. S. Pitting Corrosion of Metals: A Review of the Critical Factors. *J. Electrochem. Soc.* **1998**, *145* (6), 2186–2198.
(12) Morstein, J.; Höfler, D.; Ueno, K.; Jurss, J. W.; Walvoord, R. R.; Bruemmer, K. J.; Rezgui, S. P.; Brewer, T. F.; Saitoe, M.; Michel, B. W.; et al. Ligand-Directed Approach to Activity-Based Sensing: Developing Palladacycle Fluorescent Probes That Enable Endogenous Carbon Monoxide Detection. *J. Am. Chem. Soc.* **2020**, *142*, 15917–15930.
(13) Li, M.-D.; Cui, Y.; Gao, M.-X.; Luo, J.; Ren, B.; Tian, Z.-Q. Clean Substrates Prepared by Chemical Adsorption of Iodide Followed by Electrochemical Oxidation for Surface-Enhanced Raman Spectroscopic Study of Cell Membrane. *Anal. Chem.* **2008**, *80*, 5118–5125.
(14) De, R.; Shin, Y. S.; Lee, C. L.; Oh, M. K. Long-Standing Stability of Silver Nanorod Array Substrates Functionalized Using a Series of Thiols for a SERS-Based Sensing Application. *Appl. Spectrosc.* **2016**, *70* (7), 1137–1149.
(15) Gonçalves, M. R.; Enderle, F.; Marti, O. Surface-Enhanced Raman Spectroscopy of Dye and Thiol Molecules Adsorbed on Triangular Silver Nanostructures: A Study of Near-Field Enhancement, Localization of Hot-Spots, and Passivation of Adsorbed Carbonaceous Species. *J. Nanotechnol.* **2012**, *2012*, 173273.
(16) Moran, C. H.; Xia, X.; Xia, Y. Improving Correlated SERS Measurements with Scanning Electron Microscopy: An Assessment of the Problem Arising from the Deposition of Amorphous Carbon. *Phys. Chem. Chem. Phys.* **2013**, *15*, 5400–5406.
(17) Wang, Y.-H.; Zheng, S.; Yang, W.-M.; Zhou, R.-Y.; He, Q.-F.; Radjenovic, P.; Dong, J.-C.; Li, S.; Zheng, J.; Yang, Z.-L.; et al. In Situ Raman Spectroscopy Reveals the Structure and Dissociation of Interfacial Water. *Nature* **2021**, *600*, 81–86.
(18) Dix, S. T.; Linic, S. In-Operando Surface-Sensitive Probing of Electrochemical Reactions on Nanoparticle Electrocatalysts: Spectroscopic Characterization of Reaction Intermediates and Elementary Steps of Oxygen Reduction Reaction on Pt. *J. Catal.* **2021**, *396*, 32–39.
(19) Meng, Y.; Zhang, X.; Hung, W.-H.; He, J.; Tsai, Y.-S.; Kuang, Y.; Kenney, M. J.; Shyue, J.-J.; Liu, Y.; Stone, K. H.; et al. Highly Active Oxygen Evolution Integrated with Efficient CO_2 to CO Electroreduction. *Proc. Natl. Acad. Sci.* **2019**, *116* (48), 23915–23922.

(20) Gao, P.; Weaver, M. J. Metal-Adsorbate Vibrational Frequencies as a Probe of Surface Bonding: Halides and Pseudohalides at Gold Electrodes. *J. Phys. Chem.* **1986**, *90*, 4057–4063.
(21) Gao, P.; Patterson, M. L.; Tadayyoni, A.; Weaver, M. J. Gold as a Ubiquitous Substrate for Intense Surface-Enhanced Raman Scattering. *Langmuir* **1985**, *1* (1), 173–176.
(22) Desilvestro, J.; Weaver, M. J. Surface Structural Changes during Oxidation of Gold Electrodes in Aqueous Media as Detected Using Surface Enhanced Raman Spectroscopy. *J. Electroanal. Chem* **1986**, *209*, 377–386.
(23) Yang, S.; Chen, Q. Quantifying Electron Transfer Kinetics on Porous Carbon Electrodes for Redox Flow Batteries. *J. Electrochem. Soc.* **2020**, *167*, 160501.
(24) Gerhardt, M. R.; Tong, L.; Gómez-Bombarelli, R.; Chen, Q.; Marshak, M. P.; Galvin, C. J.; Aspuru-Guzik, A.; Gordon, R. G.; Aziz, M. J. Anthraquinone Derivatives in Aqueous Flow Batteries. *Adv. Energy Mater.* **2017**, *7* (8), 1601488.
(25) Lin, K.; Chen, Q.; Gerhardt, M. R.; Tong, L.; Kim, S. B.; Eisenach, L.; Valle, A. W.; Hardee, D.; Gordon, R. G.; Aziz, M. J.; et al. Alkaline Quinone Flow Battery. *Science (80-.).* **2015**, *349* (6255), 1529–1532.
(26) Mirle, C.; Medabalmi, V.; Ramanujam, K. Crossover-Free Hydroxy-Substituted Quinone Anolyte and Potassium Ferrocyanide Catholyte for Aqueous Alkaline Organic Redox Flow Battery. *Catal. Today* **2021**, *370*, 173–180.
(27) Tong, L.; Goulet, M.-A.; Tabor, D. P.; Kerr, E. F.; Porcellinis, D. De; Fell, E. M.; Aspuru-Guzik, A.; Gordon, R. G.; Aziz, M. J. Molecular Engineering of an Alkaline Naphthoquinone Flow Battery. *ACS Energy Lett.* **2019**, *4* (8), 1880–1887.
(28) Drazevic, E.; Szabo, C.; Konya, D.; Lund, T.; Wedege, K.; Bentien, A. Investigation of Tetramorpholinohydroquinone as a Potential Catholyte in a Flow Battery. *ACS Appl. Energy Mater.* **2019**, *2* (7), 4745–4754.
(29) Wang, C.; Yang, Z.; Wang, Y.; Zhao, P.; Yan, W.; Zhu, G.; Ma, L.; Yu, B.; Wang, L.; Li, G.; et al. High-Performance Alkaline Organic Redox Flow Batteries Based on 2-Hydroxy-3-Carboxy-1,4-Naphthoquinone. *ACS Energy Lett.* **2018**, *3* (10), 2404–2409.
(30) Beh, E. S.; De Porcellinis, D.; Gracia, R. L.; Xia, K. T.; Gordon, R. G.; Aziz, M. J.; Paulson, J. A. A Neutral PH Aqueous Organic− Organometallic Redox Flow Battery with Extremely High Capacity Retention. *ACS Energy Lett.* **2017**, *2*, 639–644.
(31) Zhang, Y.; Qian, G.; Huang, C.; Wang, Y. Effect of Modification of Polyacrylonitrile-Based Graphite Felts on Their Performance in Redox Fuel Cell and Redox Flow Battery. *J. Power Sources* **2016**, *324*, 528–537.
(32) Gao, F.; Li, X.; Zhang, Y.; Huang, C.; Zhang, W. Electrocatalytic Activity of Modified Graphite Felt in Five Anthraquinone Derivative Solutions for Redox Flow Batteries. *ACS Omega* **2019**, *4* (9), 13721–13732.
(33) Kwabi, D. G.; Lin, K.; Ji, Y.; Aspuru-Guzik, A.; Gordon, R. G.; Aziz, M. J.; Kerr, E. F.; Goulet, M.-A.; De Porcellinis, D.; Tabor, D. P.; et al. Alkaline Quinone Flow Battery with Long Lifetime at PH 12. *Joule* **2018**, *2*, 1894–1906.
(34) Ji, Y.; Goulet, M.-A.; Pollack, D. A.; Kwabi, D. G.; Jin, S.; Porcellinis, D. De; Kerr, E. F.; Gordon, R. G.; Aziz, M. J. A Phosphonate-Functionalized Quinone Redox Flow Battery at Near-Neutral PH with Record Capacity Retention Rate. *Adv. Energy Mater.* **2019**, *9* (12), 1900039.
(35) Goulet, M.-A.; Aziz, M. J. Flow Battery Molecular Reactant Stability Determined by Symmetric Cell Cycling Methods. *J. Electrochem. Soc.* **2018**, *165* (7), A1466–A1477.

(36) Yang, Z.; Tong, L.; Tabor, D. P.; Beh, E. S.; Goulet, M.-A.; Porcellinis, D. De; Aspuru-Guzik, A.; Gordon, R. G.; Aziz, M. J. Alkaline Benzoquinone Aqueous Flow Battery for Large-Scale Storage of Electrical Energy. *Adv. Energy Mater.* **2018**, *8* (8), 1702056.
(37) Chen, Q.; Gerhardt, M. R.; Hartle, L.; Aziz, M. J. A Quinone-Bromide Flow Battery with 1 W/cm^2 Power Density. *J. Electrochem. Soc.* **2015**, *163* (1), A5010.
(38) Huskinson, B.; Marshak, M. P.; Suh, C.; Er, S.; Gerhardt, M. R.; Galvin, C. J.; Chen, X.; Aspuru-Guzik, A.; Gordon, R. G.; Aziz, M. J. A Metal-Free Organic-Inorganic Aqueous Flow Battery. *Nature* **2014**, *505*, 195.
(39) Huskinson, B.; Marshak, M. P.; Gerhardt, M. R.; Aziz, M. J. Cycling of a Quinone-Bromide Flow Battery for Large-Scale Electrochemical Energy Storage. *ECS Trans.* **2014**, *16*, 27.
(40) Li, G.; Jia, Y.; Zhang, S.; Li, X.; Li, J.; Li, L. The Crossover Behavior of Bromine Species in the Metal-Free Flow Battery. *J. Appl. Electrochem.* **2017**, *47*, 261–272.
(41) Hoober-Burkhardt, L.; Krishnamoorthy, S.; Yang, B.; Murali, A.; Nirmalchandar, A.; Prakash, G. K. S.; Narayanan, S. R. A New Michael-Reaction-Resistant Benzoquinone for Aqueous Organic Redox Flow Batteries. *J. Electrochem. Soc.* **2017**, *164* (4), A600.
(42) Permatasari, A.; Shin, J. W.; Lee, W.; An, J.; Kwon, Y. The Effect of Plasma Treated Carbon Felt on the Performance of Aqueous Quinone-Based Redox Flow Batteries. *Int. J. Energy Res.* **2021**, 1–10.
(43) Wong, A. A.; Aziz, M. J. Method for Comparing Porous Carbon Electrode Performance in Redox Flow Batteries. *J. Electrochem. Soc.* **2020**, *167* (11), 110542.
(44) Kepley, L. J.; Bard, A. J. Ellipsometric, Electrochemical, and Elemental Characterization of the Surface Phase Produced on Glassy Carbon Electrodes by Electrochemical Activation. *Anal. Chem.* **1988**, *60*, 1459–1467.
(45) Gao, F.; Cai, X.; Huang, C. The Impact of Modified Electrode on the Performance of an DHAQ/ $K_4Fe(CN)_6$ Redox Flow Battery. *Electrochim. Acta* **2021**, *390*, 138847.
(46) Li, X.; Li, J.; Huang, C.; Zhang, W. Modification of a Carbon Paper Electrode by Three-Dimensional Reduced Graphene Oxide in a MV/4-HO-TEMPO Flow Battery. *Electrochim. Acta* **2019**, *301*, 240–250.
(47) Yang, B.; Hoober-Burkhardt, L.; Krishnamoorthy, S.; Murali, A.; Surya Prakash, G. K.; Narayanan, S. R. High-Performance Aqueous Organic Flow Battery with Quinone-Based Redox Couples at Both Electrodes. *J. Electrochem. Soc.* **2016**, *163* (7), A1442–A1449.
(48) Yang, B.; Hoober-Burkhardt, L.; Wang, F.; Prakash, G. K. S.; Narayanan, S. R. An Inexpensive Aqueous Flow Battery for Large-Scale Electrical Energy Storage Based on Water-Soluble Organic Redox Couples. *J. Electrochem. Soc.* **2014**, *161* (9), A1371.
(49) Lee, W.; Kwon, B. W.; Kwon, Y. Effect of Carboxylic Acid-Doped Carbon Nanotube Catalyst on the Performance of Aqueous Organic Redox Flow Battery Using the Modified Alloxazine and Ferrocyanide Redox Couple. *ACS Appl. Mater. Interfaces* **2018**, *10* (43), 36882–36891.
(50) Chu, C.; Kwon, W.; Lee, W.; Kwon, Y. Effect of Temperature on the Performance of Aqueous Redox Flow Battery Using Carboxylic Acid Functionalized Alloxazine and Ferrocyanide Redox Couple. *Korean J. Chem. Eng* **2019**, *36* (10), 1732–1739.
(51) Li, X.; Huang, C. A New Modification Method for Graphite Felt Electrodes in a MV/4-HO-TEMPO Flow Battery. *RSC Adv.* **2020**, *10* (11), 6333–6341.
(52) Qi, H.; Zhang, C. Simultaneous Determination of Hydroquinone and Catechol at a Glassy Carbon Electrode Modified with Multiwall Carbon Nanotubes. *Electroanalysis* **2005**, *17* (10), 832–838.

(53) Park, M.; Beh, E. S.; Fell, E. M.; Jing, Y.; Kerr, E. F.; Porcellinis, D. De; Goulet, M.-A.; Ryu, J.; Wong, A. A.; Gordon, R. G.; et al. A High Voltage Aqueous Zinc–Organic Hybrid Flow Battery. *Adv. Energy Mater.* **2019**, *9* (25), 1900694.
(54) Wang, H.; Li, D.; Chen, L.; Han, H. La and Sr Composite Oxides-Modified Graphite Felt for Aqueous Organic Redox Flow Batteries. *Chem. Res. Chinese Univ.* **2020**, *36* (6), 1255–1260.
(55) Preger, Y.; Gerken, J. B.; Biswas, S.; Anson, C. W.; Johnson, M. R.; Root, T. W.; Stahl, S. S. Quinone-Mediated Electrochemical O_2 Reduction Accessing High Power Density with an Off-Electrode Co-N/C Catalyst. *Joule* **2018**, *2* (12), 2722–2731.
(56) Rosanske, T. W.; Evans, D. H. Rate Constants for the Electrode Reactions of Some Quinones in Aprotic Media at Platinum, Gold and Mercury Electrodes. *J. Electroanal. Chem. Interfacial Electrochem.* **1976**, *72* (3), 277–285.
(57) Anantharaj, S.; Noda, S.; Driess, M.; Menezes, P. The Pitfalls of Using Potentiodynamic Polarization Curves for Tafel Analysis in Electrocatalytic Water Splitting . *ACS Energy Lett.* **2021**, *6*, 1607–1611.
(58) Bard, A. J.; Faulkner, L. R. *Electrochemical Methods: Fundamentals and Applications*; John Wiley & Sons, Inc.: New York, 2001.
(59) Stephan, A. K. Standardized Battery Reporting Guidelines. *Joule* **2021**, *5*, 1–2.
(60) Sun, Y.-K. An Experimental Checklist for Reporting Battery Performances. *ACS Energy Lett.* **2021**, *6*, 2187–2189.
(61) Li, M.; Odom, S. A.; Pancoast, A. R.; Robertson, L. A.; Vaid, T. P.; Agarwal, G.; Doan, H. A.; Wang, Y.; Suduwella, T. M.; Bheemireddy, S. R.; et al. Experimental Protocols for Studying Organic Non-Aqueous Redox Flow Batteries. *ACS Energy Lett.* **2021**, *6*, 3932–3943.